In-situ Plasma Analysis of Ion Kinetics in the Solar Wind and Hermean Magnetosphere

by

Patrick J. Tracy

A dissertation submitted in partial fulfillment
of the requirements for the degree of
Doctor of Philosophy
(Atmospheric Oceanic and Space Sciences)
in the University of Michigan
2016

Doctoral Committee:

Professor Thomas H. Zurbuchen, Co-Chair
Assistant Research Scientist Jim M. Raines, Co-Chair
Professor John E. Foster
Associate Professor Justin C. Kasper

To my wife, Paige

Acknowledgements

It is the task of this disproportionately small section to acknowledge the contributions that made this PhD possible. A PhD is not just the culmination of an individual’s graduate journey, but also a compilation of the many toils from a large supporting cast.

I will start the many thanks that need to be given out with some to my advisors, Jim Raines and Thomas Zurbuchen. Jim bears the primary responsibility for my undertaking of this thesis, having served as my advisor since that first REU program back in 2010. Jim has continued to support me week in and week out, giving practical advice over a broad range of topics. Although with the completion of this thesis, it is very possible he will have to find someone else to feed his fish! Thomas I would like to thank for providing that extra little push that made all the difference in some projects. Those challenges paved the way for me to grow as a scientist. In addition to my advisors, I also need to thank Justin Kasper, who served as a much appreciated mentor and proxy advisor during my time at Michigan. Justin was the primary reason for my success on several occasions during this thesis work and provided a much appreciated infusion of expertise and enthusiasm. I am also thankful to the final member of my committee, John Foster, who has only known me through coursework but still signed on for the arduous task of seeing this thesis to completion.

Next, I would like to thank my academic peers and cohorts who supported me during my time at UM. This begins with the members of the Solar and Heliospheric Research Group, including but not limited to, Dan Gershman, Jacob Gruesbeck, Gina Riemer, Aledia Higginson, Mark Stakhiv, Gang Kai Poh, Nicole Portier, Manan Kocher, Ryan Dewey, Mojtaba Akhavantafti, Robert Alexander, Jason Gilbert, Liang Zhao, Jon Thomas, Paul Shearer, and Austin Glass. Special shout out to Dan for his incredible insight into scientific details that eluded me. To Gina for finding me a place to live my first summer of grad school and making me feel welcome. To Jason for sacrificing many hours to the lab deities trying to get my projects to work. To Jon for always having an answer to my many FIPS library software questions. To Micah for many lively discourses, scientific and otherwise. To Paul for his invaluable overhaul of and help with the SWICS data analysis. And to Austin for doing a tremendous job with his UROP and summer research that greatly improved the foreshock work presented in this thesis. I am forever indebted to this bunch for being slogging with me through the trial and tribulations of coursework and graduate research.

In addition to my academic peers, I also need to thank some of that staff in the CLaSP department. Debbie Eddy, for always having an answer to the deluge of questions I sent her way. Rick Baker, for making sure all the funding flowed the way it should, and

Sandra Pytlinski for deciphering the paperwork requirements that always baffled me. A special acknowledgement to the engineers in the SPRL group, in particular Curt Cooper, Ken Arnett, Brad Angelocci, Michael Long, Dave Boprie, Ava Dupre, and Steve Rogacki. Thank you for all your efforts (especially Curt) in trying to sort out a spare FIPS instrument that just didn't want to work.

I would also like to recognize the contributions from my friends outside the office. First and foremost amongst them are my roommates through the first years in graduate school, Kevin Fisher and later his wife Sydney Fisher. Kevin was the good friend I never saw coming from a chance pairing of new grad students looking for a roommate. I am forever grateful for the healthy dose of bad movies, frisbee golf, and grad school commiseration they provided (and also for putting up with me for two years!).

The final and most important person during this process has been my wife, Paige. She has been with me every step of the way through graduate school. From scheduling our wedding around my qualification exams, coming with to the yearly AGU conference, some late nights at the office, all the way to working out what treats go best with a thesis defense. I cannot imagine how I would have made it through without her support, and I can never fully express how grateful I am for her every day of my life.

This work was supported, in part, by NASA Grants No. NNX13AH66G and No.NNX13AO68H.

Table of Contents

List of Figures

List of Tables

List of Appendices

Appendix

List of Acronyms

ACE	Advanced Composition Explorer
AU	Astronomical Unit
FAB	Field-aligned beam
FIPS	Fast Imaging Plasma Spectrometer
GSE	Geocentric Solar Ecliptic
IMF	Interplanetary Magnetic Field
MCP	Microchannel Plate
MSO	Mercury Solar Orbital
NASA	National Aeronautics and Space Administration
PA	Pitch Angle
PAHV	Post Acceleration High Voltage
RTN	Radial Tangential Normal
SEP	Solar Energetic Particles
SWEPAM	Solar Wind Electron, Proton, and Alpha Monitor
SWICS	Solar Wind Ion Composition Spectrometer
SWOOPS	Solar Wind Observations Over the Poles of the Sun
TOF	Time of flight
TRIM	TRansport of Ions in Matter

Abstract

The heating of the solar wind and its interaction with the planetary magnetosphere of Mercury is the primary focus of this work. The first aspect of this study is focused on the heavy ion population of the solar wind (A > 4 amu) and how information that cannot be recovered from the bulk plasma properties can be readily recovered from this valuable trace population. In particular, the signature of the heating process that is responsible for creating the solar wind is preserved in this heavy ion population, provided it is not erased by other processes. One result of this work is that this signature in the heavy ion population is primarily erased (thermalized) via Coulomb collisional interactions with solar wind protons. The heavy ion temperatures observed in collisionally young solar wind, where the initial heating profiles should be best preserved, reveal a clear, stable dependence on mass. Furthermore, this young solar wind shows non-thermal heating that is not in quantitative or qualitative agreement with current model predictions based on turbulent transport and kinetic dissipation.

Due to its weak magnetic dipole, the solar wind can impinge on the surface of Mercury, one of the processes contributing to the desorption of neutrals and ions that make up the planet's exosphere. The ionization of these neutrals in turn provides one of the primary sources of planetary ions in Mercury's magnetosphere. Differentiating between surface mechanisms and analyzing magnetospheric plasma dynamics requires the quantification of a variety of ion species. A detailed forward model and a robust statistical method are created to identify new ion signatures in the measurement space of the FIPS instrument, formerly orbiting Mercury onboard the MESSENGER spacecraft. The recovery of new heavy ions species, including Al, Ne, Si, and Mg, along with tentative recoveries of S, Ar, K, and C, enable in depth studies of plasma sources and dynamics in the Hermean magnetosphere. Assuming ion production primarily via photoionization for these species, the neutral abundance ratio relative to Na is also recovered. Comparison of the exospheric neutral ratios to surface abundances at Mercury is a critical constraint in determining the dominant desorption mechanism at the planet’s surface.

The interaction of the solar wind with the bow shock of the Hermean magnetosphere leads to the creation of a foreshock region. The unique parameter regime of this foreshock, relative to that at Earth, provides a compelling reason to study the foreshock plasma populations and their energization mechanisms. New tools and methods were created to enable the analysis of the diffuse and Field Aligned Beam (FAB) foreshock populations at Mercury. One result suggests that the energization process for the observed FABs can be explained by Shock Drift Acceleration, which is not limited by the small spatial size of Mercury’s bow shock. For diffuse populations it is shown, through estimates of the diffusion coefficient, IMF-bow shock connection times, and the Fermi acceleration time scale, that a connection time limited diffusive shock acceleration is likely responsible for the behavior of the observed energy distributions.

Chapter 1 -Introduction

The unifying theme of this dissertation is the study of particle energization and heating in the solar wind and its interaction with the Hermean magnetosphere. In the study of the solar wind this involved a detailed analysis of heavy ion ($A > 4$ amu) kinetics as tracers for underlying heating mechanisms in the solar wind. As this solar wind propagates through the heliosphere its interaction with planetary magnetospheres is also of interest. In particular, the interaction of the solar wind with the relatively weak dipole magnetic field of the planet Mercury can allow for solar wind impingement on the planet's surface. This contributes to the desorption of neutrals and, through photoionization, ions that populate Mercury's magnetosphere. Quantifying the relative importance of different surface desorption mechanisms and studies of ion motion through the magnetosphere requires the identification of a variety of ion species. Last, the interaction of the solar wind with the Hermean magnetic field also leads to the creation of a population of particles upstream of Mercury's bow shock, called a foreshock region. The foreshock region at Mercury is unique in the heliosphere, and provides a prime opportunity to advance the particle acceleration mechanisms developed from observations of the terrestrial foreshock. Throughout this introduction, the key ideas and remaining questions pertinent to the kinetic properties of heavy ions in the solar wind and Mercury's magnetospheric environment will be elucidated.

1.1 Solar wind heating problem and heavy ions

1.1.1 Source of the Solar Wind

The solar wind is the plasma extending from the corona to very large distances from the Sun. Basically, this solar wind exists because of the huge pressure difference between the hot plasma at the base of the corona and the interstellar medium. The heating and kinetic processes that occur in the solar wind are of central importance in this work.

To understand the problem of the heating of the solar wind, a brief description of the layers of the Sun is helpful. A sketch of these layers can be seen in Figure 1.1, and further parameters can be found in Gombosi (1998). In the central core of the Sun (< 0.25 R_S), exists a region of extremely high density and temperature (> 15 MK). This region contains roughly half of the total solar mass and is where thermonuclear fusion combines H into He. Outside the core there are the radiative (0.25-0.71 R_S) and convection (0.71-1.0 R_S) zones. These zones are named for the dominant form of heat transfer within that region.

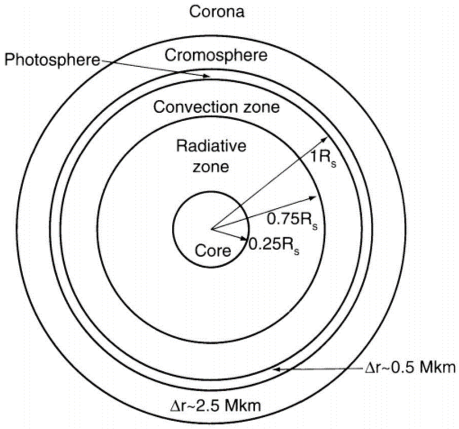

Figure 1.1: A sketch of the structure of the solar interior. Adapted from Gombosi, T.I. (1998).

The temperature and density of the solar plasma largely decreases from the core outward to the visible surface. This visible surface is named the photosphere and has an average temperature of about 5770 K, and a density of about 10^{23} m^{-3}. Moving out from the photosphere is the chromosphere, a layer in which the temperature increases to about 10^4 K. After the chromosphere, the temperature rises rapidly from 10^4K to a few MK in what is called the transition region. The transition region is still a very active region of research and many theories exist to attempt to explain the temperature increase (Hammer 1982; Parker 1988; Priest et al. 2000).

A profile showing this sharp increase in temperature is shown in Figure 1.2. After the transition layer comes the last layer of the solar atmosphere, the corona, which extends out to a few solar radii. This corona is where a number of interesting physical processes take place which heat, accelerate and ultimately release plasma into the heliosphere where is it known as solar wind. The study of the heating processes that create this solar wind forms one of the focuses of this work.

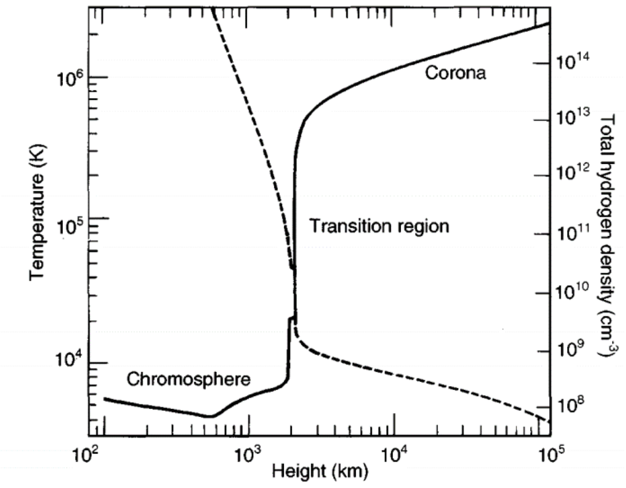

Figure 1.2: Calculated temperature (solid line) and density (dashed line) profiles in the Sun's transition region. Adapted from Gabriel, A.H. (1976).

After the solar wind is released to the heliosphere it presents itself as a supersonic plasma with densities of a few particles per cm^3 by the time it reaches 1 AU. For a more detailed list of typical solar wind parameters see Gombosi 1998. The solar wind is a quasi-neutral plasma composed primarily of H^+ (95-98%) and He^{2+} (2-4%). Bulk dynamics seen in the solar wind are dominated by the density and velocity of H+. There is however, much that can be learned by studied the less abundant components of the solar wind.

1.1.2 Heavy ions in the solar wind

The study of heavy ions, which consists of elements heavier than He, has been an active research area since the first observation of oxygen charge states by the Vela 3 satellites in 1965 (Bame et al. 1968). Heavy ions make up less than 1% of the total mass in the solar wind, but provide a wealth of information unattainable from studies of H+ and He2+.

Heavy ions have been shown to be invaluable tracers of physical processes in the solar wind and provide crucial information about both the origin and evolutionary processes of the wind from the corona into the heliosphere (i.e., Zurbuchen 2007; von Steiger et al 2000; Raymond et al. 1997). For example, it has been demonstrated that elemental abundance ratios of heavy ions are powerful indicators of solar wind source regions on the Sun (von Steiger et al. 2000). Furthermore, the ionic charge state ratios observed in the solar wind are connected to the temperature and density profiles where a parcel of solar wind originated from (Geiss et al. 1995). Finally, due to their low abundances relative to the hydrogen and helium ions that govern the bulk parameters of the coronal and solar wind plasma, the kinetic properties of heavy ions reflect the initial state of the solar wind and can respond to wave-particle interactions throughout the inner heliosphere without significantly modifying the expansion and acceleration of the solar wind itself (von Steiger & Zurbuchen 2006).

Solar wind with its origin in coronal holes exhibits low ionic charge states, reflecting the cooler (lower) electron temperatures in those regions. These coronal-hole associated plasmas are observed to undergo rapid heating near the Sun, preferentially heating heavy ions to very large kinetic temperatures (Landi and Cranmer 2009). In contrast, solar wind associated with the streamer belt exhibits elemental composition that is comparable to that of the closed corona, with an enhanced abundance of ions with low First Ionization Potential (FIP) relative to the photospheric value, and an ionic composition that reflects electron temperatures that are significantly higher than those of coronal holes. The plasma heating in these streams, reflected in their kinetic temperatures, is less pronounced than that of fast, coronal hole associated streams (Kohl et al. 2006). A summary table of the abundances of solar wind ions for these sources is shown in Table 1.1.

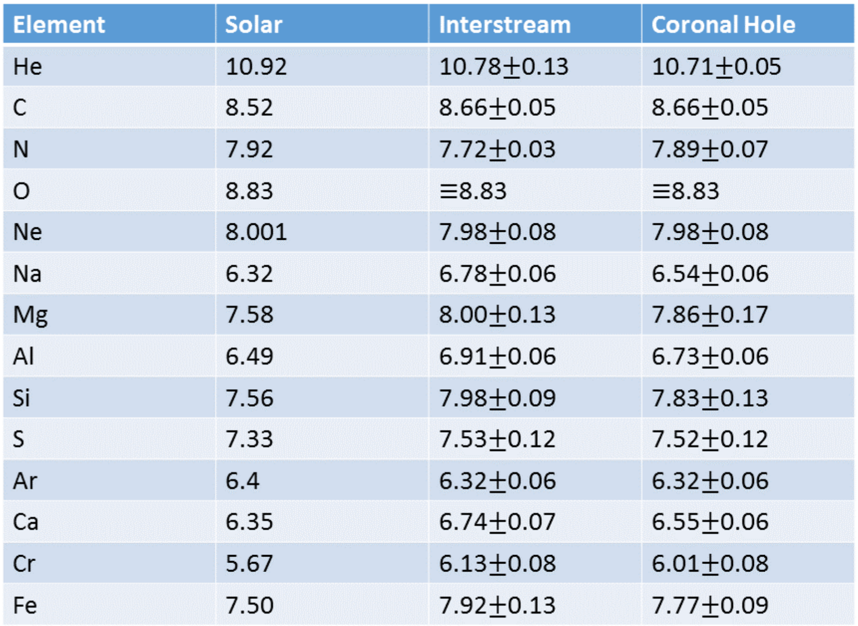

Element	Solar	Interstream	Coronal Hole
He	10.92	10.78±0.13	10.71±0.05
C	8.52	8.66±0.05	8.66±0.05
N	7.92	7.72±0.03	7.89±0.07
O	8.83	≡8.83	≡8.83
Ne	8.001	7.98±0.08	7.98±0.08
Na	6.32	6.78±0.06	6.54±0.06
Mg	7.58	8.00±0.13	7.86±0.17
Al	6.49	6.91±0.06	6.73±0.06
Si	7.56	7.98±0.09	7.83±0.13
S	7.33	7.53±0.12	7.52±0.12
Ar	6.4	6.32±0.06	6.32±0.06
Ca	6.35	6.74±0.07	6.55±0.06
Cr	5.67	6.13±0.08	6.01±0.08
Fe	7.50	7.92±0.13	7.77±0.09

Table 1.1: Solar elemental abundances and solar abundances. Values are giving relative to the hydrogen abundance in logarithmic (dex) scale, i.e. $A_{el}=\log_{10}(N_{el} / N_H) + 12.0$ *where* A_{el} *is the value shown in the table. For the case of solar values, the photospheric or meteoritic values of Grevesse and Sauval (1998) are used. "Interstream" solar wind refers to low speed wind thought to originate from the boundaries of closed-loop systems. Adapted from Bochsler (2007).*

1.1.3 Motivating science: Relating heavy ions to solar wind heating

As solar wind propagates through the heliosphere, it evolves through a variety of physical processes that include both collisions and interactions with the waves and turbulence present in the solar wind. Examining the kinetic properties of heavy ions in the solar wind, over their range of difference mass and charge values, allows for a quantitative test of numerous proposed candidate heating processes.

For example, quasi-linear wave particle interaction near ion-cyclotron resonance can strongly heat ions even beyond mass-proportional temperatures (Isenberg & Vasquez 2009) and will favor ions based on their respective gyrofrequencies. While the heating present in protons (H^+) and alpha particles (He^{2+}) in the solar wind has been shown to be consistent with the prediction of ion-cyclotron resonance, the same He^{2+} and proton data are also consistent with ion interaction with long wavelength kinetic Alfvén waves (Chandran et al. 2013). The observed kinetic signatures in the solar wind can also be explained as being due to intermittent MHD turbulence, such as small currents, current cores, current sheets and other structures (Osman et al. 2011; Greco et al. 2009).

Heavy ions in a solar wind parcel are continuously affected by these processes of dissipation and heating, but are also undergoing collisional relaxation and thermalization via the cumulative effect of infrequent small-angle Coulomb scattering (Spitzer 1967). This relaxation process tends to bring all ions in a plasma parcel towards thermal equilibrium, acting against any heating or temperature anisotropy that would be caused by mechanisms such as those listed above. The net effect of these heating and thermalization processes has been extensively studied with the alpha particle population in the solar wind.

Alpha particles in the fast, coronal-hole associated solar wind exhibit velocities that exceed those of the protons by up to an Alfvén speed (Neugebauer et al. 1996) and kinetic temperatures of alpha particles are between three to six times larger than proton temperatures (Marsch et al. 1982b; Kasper et al. 2008, Kasper et al. 2013). These non-thermal effects decrease with increasing heliospheric distance (Gershman et al. 2012), reaching values comparable to the values of the remote sensing observation of heavy ions in the corona (Landi 2007; Landi & Cranmer 2009). This evolution in non-thermal effects could suggest a collisional thermalization process acting on the solar wind He^{2+} that washes out large temperature differences generated closer to the Sun (Maruca et al. 2013).

The important role of these collisional processes in bringing the plasma toward thermal equilibrium was demonstrated in a detailed comparative analysis of alpha particles and protons (Kasper et al. 2008). Measurements of the alpha-to-proton temperature ratio by the Faraday Cup instruments on the Wind spacecraft at 1 AU were found to be very well organized by a collisional age parameter, $A_C = \nu \frac{R}{V_{SW}}$. In this expression, V_{SW} is the speed of the solar wind, R is the distance between the Sun and the observing spacecraft, and ν is the Coulomb collisional rate for He^{2+} and H^{+} energy exchange due to small angle Coulomb scattering. Note that $\nu = 1/\tau$, the Coulomb collisional time scale defined in

Kasper et al. (2008). This parameter, A_C, is the ratio of the propagation time of a solar wind parcel to 1 AU and the Coulomb collisional time scale for a given ion in that parcel, i.e., a measure of the number of collisional time scales elapsed for a solar wind plasma parcel during its travel to 1 AU. Organizing by this collisional age, it is shown that the temperature ratio of He^{2+} to H^{+} smoothly decays from values of 5-6 at low collisional age toward close to equal temperature at high collisional age.

The behavior of He^{2+} provides important constraints theories of solar wind heating. Similarly, an examination of the solar wind heavy ions is crucial to enable definitive discernment between the various proposed heating and dissipation models. In this regard there have been several studies of heavy ion kinetics in the solar wind, but none that fully considered the collisional thermalization effects on the heavy ion population.

An initial analysis of heavy ion kinetic temperatures was performed with the data from the Solar Wind Ion Composition Spectrometer (SWICS) onboard the Ulysses spacecraft (Gloeckler et al. 1992), which provided measurements over a range of 1-5.5 AU and all heliospheric latitudes. Using a comparison between data gathered near 1 AU and data from Ulysses at 5.4 AU, it was argued that the solar wind becomes decreasingly collisional with increasing radial distance so that equal thermal velocities among heavy ions should become more prevalent (von Steiger and Zurbuchen 2006). This was attributed to a relative increase of importance of wave-particle interactions as compared to Coulomb collisions as radial distance from the Sun increases. Heavy ions are expected to have equal thermal speeds under such a wave-particle interaction dominated regime (Marsch et al. 1982a). The heavy ion thermal velocities reported therein were not analyzed according to collisional age, making it difficult quantitatively to assess the importance of collisions in the measured solar wind plasma.

Such an investigation of the importance of collisions in measured solar wind parcels was employed in the study of the data from the CTOF sensor onboard SOHO (Hovestadt et al. 1995). This instrument was only able to provide a few months of data in 1995, before an irreversible hardware failure. The analysis of these data by Hefti et al. (1998) found that the majority of heavy ion measurements at 1 AU display mass-proportional temperatures. However, it was also found that equal temperatures among heavy ions and protons are observed when the expansion time scale of the solar wind parcel is much longer than the heavy ion to proton Coulomb collisional temperature equilibration time scale, i.e. high collisional age events. An important assumption in that work is that the Coulomb collisional thermalization with protons was the dominant thermalization term for heavy ions in the solar wind.

As discussed in Hefti et al. (1998), the expression for Coulomb thermalization rate is ordered by the $\frac{q^2}{m}$ ratio of the interacting ion species and also on their densities. Heavy ions in the solar wind have larger $\frac{q^2}{m}$ values than H^+, but substantially smaller densities, making it necessary to verify that the interaction of any given heavy ion species at 1 AU is not significantly affected by the interaction of that heavy ion with other heavy ion species. Detailed understanding the role of Coulomb collisions in heavy ion thermalization will allow the heavy ion kinetic measurements to be used to distinguish between the proposed theories of heating and dissipation for the solar wind.

1.1.4 Guiding science questions for heavy ion heating

As discussed above, heavy ions are ideally suited to differentiate between different proposed heating mechanisms in the solar wind. For the work of this thesis, we formed the issue of solar wind heating into two main guiding questions.

1-*How well are coronal heating signatures created in the heavy ion population of the solar wind preserved by the time they are observed at 1 AU?*

In order to quantify any heating signature that may remain from solar wind heating back at the corona, or to gauge any in-situ heating rate observed, we must know how well these heating signatures are preserved. If heavy ions experience a large amount of thermalization from Coulomb collisions there should not be any trace of preferential heating of heavy ions remaining at 1 AU.

2- *What does the heating of heavy ions relative to protons observed in the solar wind at 1 AU tell us about solar wind heating mechanisms?*

This question stems naturally from the first. Given that solar wind observations of heavy ions are not strongly thermalized, what signatures of heating remain? Comparisons of the relative temperatures of heavy ions to protons should show dependences on ion mass and charge that cannot be seen in the more abundant H^+ and He^{2+} ions of the solar wind. These observations can be directly compared to the predictions from leading theories on solar wind heating.

1.2 Mercury's Space Environment

The previous studies of the solar wind are very much concerned with the physical processes at work in the solar corona and in the solar wind in-situ as it propagates through the heliosphere. These important issues of heating and energization are not unique to the study of solar wind plasmas. We will move from the solar wind to the space environment of the planet Mercury where we enter a very different regime of plasma physics. The question remains similar however, what can be learned about the heating and energization processes relevant for plasmas at Mercury and in particular what can be learned by examining the heavy ion population.

The fact that the scale size of Mercury's magnetosphere is about eight times smaller than Earth's implies a non-adiabatic plasma environment for heavy ions that plays a large role in their possible energization. In addition to revealing the plasma dynamics present at Mercury, heavy ion observations also have important implications for planetary formation and surface process theories at Mercury. Observations of planetary ions like sulfur can be related back to the neutral composition to provide abundance measurements otherwise unobtainable. The small scale size of Mercury's magnetosphere also implies a relative small scale size for its bow shock and an interesting new regime of foreshock plasma to be explored.

1.2.1 Mercury's planetary magnetosphere

Mercury occupies a unique position in the solar system as the closest planet to the Sun, with its orbital distance ranging between 0.31 AU and 0.47 AU. As a result Mercury is embedded in a plasma with much different parameters than are usually observed at Earth. The solar wind and interplanetary environment are summarized in Table 1.1. Parameters like the solar wind density and photon flux vary as $1/R^2$ and can change by an order of magnitude between Earth and Mercury.

Planet	R [AU]	V_{sw} [km/s]	n_p [cm^{-3}]	B [nT]	T_p [10^4 K]	T_e [10^4 K]
Mercury	0.31	430	73	46	17	22
	0.47	430	32	21	13	19
Venus	0.72	430	14	10	10	17
Earth	1.00	430	7	6	8	15
Mars	1.52	430	3.0	3.3	6.1	13
(Scaling)	-	R^0	R^{-2}	$R^{-1}(2R^{-2}+2)^{1/2}$	$R^{-2/3}$	$R^{-1/3}$

Table 1.2: 'Typical' mean parameters at 1 AU, scaled to the orbits of other terrestrial planets using the approximate radial dependencies displayed in the last row. Two radial distances are included for Mercury, due to the eccentricity of its orbit. The least certain scalings are those for temperature, for details see original text. Adapted from Slavin and Holzer (1981).

The variation in radial distance is an indicator of Mercury's highly eccentric orbit. This implies that the parameter regime at Mercury is not only more extreme than that at Earth, but also more variable. This variation is apparent when one considers the $1/R^2$ scaling of photon flux and solar wind density between the periapsis and apoapsis of Mercury's orbit.

Despite being located in such an interesting parameter regime, it was thought for a long time that Mercury was a fairly uneventful planet in terms of solar wind-planetary interactions. This changed with the discovery of an intrinsic magnetic field during the Mariner 10 flybys of Mercury (Ness et al. 1974). The interaction of the solar wind with this intrinsic field implied the existence of a magnetosphere uniquely positioned in our solar system. This magnetosphere was investigated in much more detail with the MErcury Surface, Space ENvironment GEochemistry, and Ranging (MESSENGER) mission which orbited Mercury from 2011-2015 (Solomon et al. 2007). Instrumentation of MESSENGER relevant to our plasma studies will be described in more detail in the following sections.

The resulting magnetosphere is small. The scale length of Mercury's magnetosphere relative to the planetary radius is a factor of about eight smaller than Earth (Ogilvie et al. 1977). For reference, Mercury has a planetary radius (R_M) of 2440 km, less than half the radius of Earth (R_E = 6371 km). The small magnetosphere is a result of the weak magnetic moment of Mercury relative to the amplified solar wind parameters. Where the solar wind encounters the magnetic field of Mercury, a planetary bow shock forms on the dayside of the planet. This is where the solar wind transitions from super to sub-magnetosonic flow speeds. According to conservation of flux (in steady state conditions), the density of the solar wind increases by the same factor as the velocity decreases. Additionally, the Interplanetary Magnetic Field (IMF), the solar magnetic field that is embedded in the solar wind, experiences a rotation and the magnetic field magnitude is sharply enhanced. Consistent with the scaling between Earth and Mercury, the typical bow shock subsolar standoff distance ranges from 1.89-2.29 R_M with an average distance of 1.96 R_M (Winslow et al, 2013). The typical coordinate system used to describe Mercury's magnetosphere is the Mercury Solar Orbital (MSO) system, where the x-axis points toward the sun, the z-axis points northward, perpendicular to Mercury's orbital plane, and the y-axis completes the right hand system. A depiction of Mercury's magnetosphere can be seen in Table 1.2.

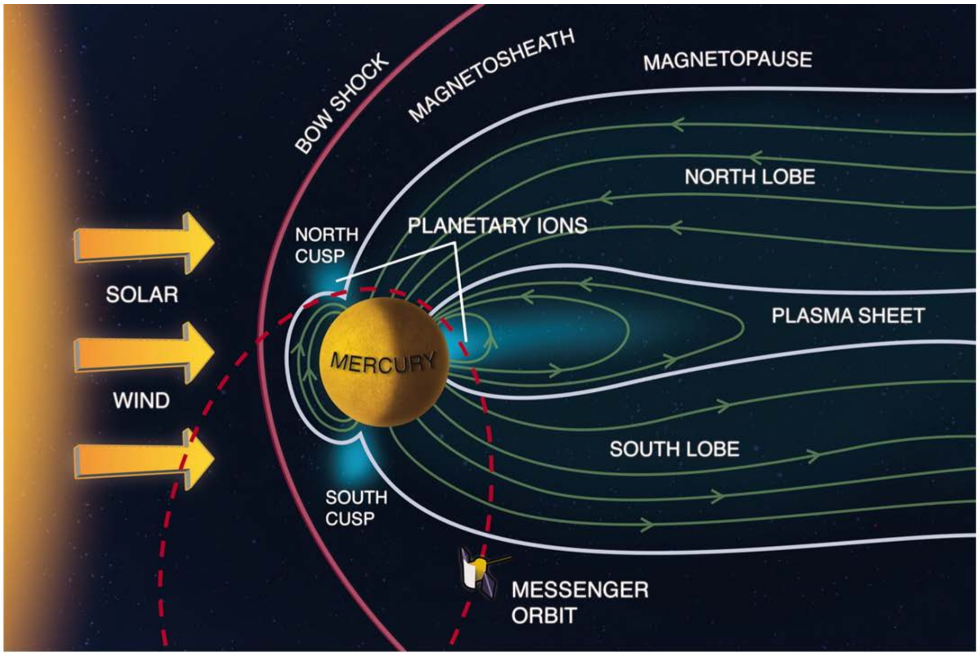

Figure 1.3: An artist's depiction of the different regions of Mercury's magnetosphere. The orbit of MESSENGER is overlaid on the schematic and is roughly to scale. As Mercury orbits the Sun, the orbit of MESSENGER will remained fixed in relative to an inertial coordinate frame and therefore will appear to precess relative to the Mercury-Sun line. Adapted from Zurbuchen et al. (2011).

The geometric scale of the magnetosphere is extremely important for the plasma dynamics therein. Planetary ions can have gyroradii that are comparable in size to the magnetosphere, this enables finite gyroradius effects which ultimately result in ions being lost to impact with the planetary surface or escape across the magnetopause (Delcourt et al. 2002, 2003). In simulations, it was found that non-adiabatic motion and centrifugal acceleration due to E x B drift path curvature could substantially energize ions like sodium, which is a prominent ion at Mercury. Non-adiabatic means that finite gyroradius effects are important, i.e. that the magnetic field at Mercury changes significantly over the spatial scale of an ion gyroradius. The fact that the scale size of Mercury's magnetosphere is small enough that finite gyroradius effects become important is a key deviation from the situation at Earth, where gyroradii are generally small relative to the magnetosphere's scale size. This scale size is also important for solar wind ions interacting with the planetary bow shock of Mercury. Mercury's foreshock presents an entirely new regime of shock acceleration physics that will be introduced following a discussion of heavy ions in the planetary magnetosphere.

1.2.2 Heavy Ion Environment inside Mercury's magnetosphere

The details of the magnetospheric environment are very important for the ions found at Mercury, but the heavy ions observed predominantly started out as neutrals on the surface or in the exosphere of Mercury. To better understand the source of heavy ions we briefly describe the surface and exospheric environment.

Mercury's atmosphere, actually a surface-bounded exosphere, is produced by a variety of mechanisms that act on the planet's surface. The makeup and dynamics present in the exosphere stem from the complex interactions between the solar wind and solar electromagnetic and energetic particle radiation, with Mercury's magnetosphere and the planet's surface. The knowledge of the species present in the exosphere has been steadily built up since the Mariner 10 mission to Mercury in 1970's which identified H, He, along with a tentative measurements of O, and upper limits of Ne, Ar, Xe, and C (Broadfoot et al. 1974, 1976). Later on, Earth ground based observations revealed prominent Na abundances (Potter and Morgan 1985), along with Ca, K, Al, and Fe (Bida et al. 2000; Killen et al. 2010). Most recently the MESSENGER spacecraft detected Mg in the exosphere, provided spatial maps of Na and Ca (McClintock et al. 2009) and made observations of Ca^+ ions present in the exosphere (Vervack et al. 2010).

The exosphere is populated by neutral atoms that are released from various physical processes on the surface. The proposed mechanisms for creation of these neutrals include photon stimulated desorption (PSD), electron stimulated desorption (ESD), thermal desorption, sputtering by impacting solar particles, and micro-meteoroid vaporization (e.g., Leblanc & Johnson 2003). The PSD process consists of solar photons impinging on the planet's surface, ionizing the surface lattice structure locally and causing repulsion of neutrals from the top layers of said surface (Johnson 1990). Thermal desorption also leads to mainly neutral rejection by means for thermal agitation of adsorbed material (Yakshinskiy et al. 2000). Solar particles (solar wind ions) penetrate Mercury's magnetosphere by traveling along the magnetic field lines at the cusps of the magnetosphere and as a result, these ions impact at high latitudes with keV/amu type energies (Johnson 1990). These solar particles eject mainly neutral particles from the upper layers of the planet's surface. Micro-meteoroid vaporization mixes the planet's surface and produces exospheric constituents by the vaporization of an impacting object and impacted surface (Killen and Ip 1999). Micro-meteoroid vaporization is thought to be an important contributor to the Ca exosphere seen at Mercury (Killen and Hahn 2015). Together these processes make up the observed exosphere at Mercury, although none of them appear to be dominant sources of the exosphere over the course of a Mercury year (Leblanc & Johnson 2010).

With these surface mechanisms producing Mercury's neutral exosphere, it is natural to probe the compositional connection between the surface and exosphere. A recent study of major surface abundances from the Gamma-Ray and Neutron Spectrometer (GRNS) onboard the MESSENGER spacecraft reports the surface presence of Si (24.6%), Ca (5.9%), Na (2.9%), S (2.3%), and Fe (1.9%), where the given percentages are by weight (Evans et al. 2012). Note that this list of detections is not a comprehensive list of the surface constituents at Mercury, and as such their relative abundances do not sum to unity (see Evans et al. 2012 for details). The exact connection between this surface composition and the observed exosphere is still a topic of active research. The relative abundance of Na in the exosphere and its presence on Mercury's surface has made it the focus of several such studies modeling surface process required to obtain the observed exosphere compositions (Leblanc & Johnson 2003; Sarantos 2009). These models have also begun to explore the relative abundances present in the exosphere and how known surface process would act on different surface constituents to influence these ratios (Leblanc & Doressoundiram 2011; Wurz et al. 2010).

1.2.3 Motivating Science: Quantifying heavy ions and neutrals

Understanding the exospheric distribution of neutrals is critical to pinning down the relation between surface processes and the observed exosphere. In addition to ground based observations, the Ultraviolet and Visible Spectrometer (UVVS) instrument on the MESSENGER spacecraft has been an important tool in observing exospheric neutrals at the planet (McClintock et al. 2009). The UVVS instrument has been very valuable in locating neutrals such as Na, K, and Ca (McClintock et al. 2009), but there are several important exospheric species not well observed by UVVS. Some reasons for this are that the "g-value" for the species is much lower than other exospheric constituents or is not in the spectral range of UVVS. The g-value is a measure of how well a species can be observed by UVVS based on an emission probability per atom (Killen et al. 2009). Examples of ions with these considerations are O, S or Si.

As we have already mentioned, S has been found to be a significant surface constituent on Mercury. The abundances of volatile elements such as sulfur relative to refractory elements such as Ca and Al have critical implications for theories of Mercury's formation from high temperature materials (Nittler et al. 2011). So in this regard, quantifying its spatial distribution in the exosphere is critical to our understandings of how the exosphere relates to the surface and its composition. Discrepancies between the surface abundance and exospheric abundance would reveal nature of the surface processes active in creating the neutral population in the exosphere. Understanding generated from these tasks would have a critical impact on the current understanding of the surface condition and dynamics at Mercury.

Given the g-value limitations for several interesting species with regard to UVVS it would be difficult to quantify their abundance in Mercury's exosphere. However, the fact that the neutrals present in the exosphere are subject to ionization via solar radiation offers another mode of observation. The Fast Imaging Plasma Spectrometer (FIPS) (Zurbuchen et al. 1998; Andrew et al. 2007) can observe heavy ions like S^+, O^+, or Si^+ present in the exosphere. If one accounts for differing ionization rates between different exospheric species then the observed ion abundance ratio is a good proxy for the neutral abundance ratio seen in Mercury's exosphere. Implicit in this assertion is the fact that the ions present in Mercury's exosphere experience analogous dynamics in the presence of Mercury's magnetosphere. This is a reasonable assertion as most of the ions we are interested in have a similar enough mass per charge that their gyroradius and any other magnetospheric interactions should not be drastically different.

As mentioned before, Na, Si, and S are present on the surface of the planet Mercury. In fact, they are present in comparable amounts; Si and S have a wt% of 24.6% and 2.3%, respectively, compared to Na at 2.9%. In terms of number density, this is about a 1 S: 2 Na ratio and a 7 Si: 1 Na ratio in abundance (Evans et al. 2012). Based on the aforementioned prevalence of Na in Mercury's exosphere it is reasonable to expect these heavy ion species to be present as well unless there are radically different surface processes between the two. Furthermore, Na^+ has already been observed by the FIPS instrument onboard MESSENGER in significant quantities (Raines et al. 2013). The FIPS instrument is a time-of-flight plasma spectrometer that can measure ions with energies in the range 0.05 to 13 keV/e and with mass per charge from 1 to 40 amu/e so the observation of these proposed ions is well within the FIPS measurement capability (Raines et al., 2011). More details on the FIPS instrument will follow in later sections.

1.2.4 Guiding Science Questions for heavy ions in Mercury's magnetosphere

1- What are the upper limits of previously unobserved heavy ions at the planet Mercury and what does that tell us about the magnetospheric dynamics, surface processes, and planetary formation?

The distribution of heavy ions, e.g. Si, S, Al, Mg, etc., in Mercury's space environment remains an outstanding issue from the MESSENGER mission. Based on surface abundances there should be a comparable amount of species like sulfur, silicon and sodium neutrals in the exosphere if they are desorbed from the surface at comparable rates. If we account for differences in ionization rate between these species, then their relative abundances will shed light the magnetospheric dynamics or surface liberation processes at Mercury.

1.2.5 Plasma environment outside Mercury's magnetosphere, the foreshock

The small scale size of Mercury's magnetosphere has important implications for more than just the plasma dynamics in its interior. The region directly upstream of Mercury's bow shock can play host to a variety of different plasma populations whose creation stems from the interaction of solar wind ions with the collisionless planetary bow shock. The terrestrial bow shock has been the primary focus for studies of the acceleration of ions at collisionless shock for more than half a century. This foreshock region, which is magnetically connected to the bow shock exhibits a large variety of waves and energized particles. The nature of the magnetic connections between the IMF and bow shock controls the spatial distribution of these populations. A rough sketch of the topology found in the terrestrial foreshock is shown in Figure 1.4.

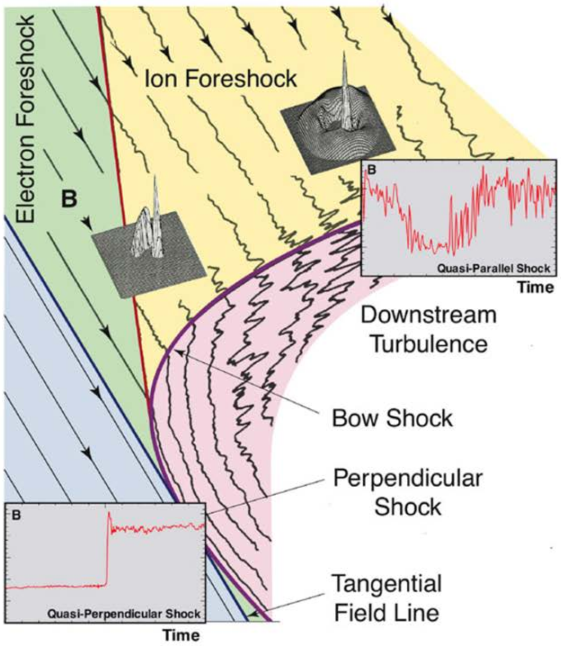

Figure 1.4: A schematic representation of the Earth's bow shock for a nominal interplanetary magnetic field direction. The inserted line plots show typical magnetic profiles for a bow shock transition for a quasi-perpendicular shock (lower left) and quasi-parallel shock (upper right). The inserted contours show examples of a 2D cut of the distribution function for each foreshock population along with a solar wind distribution (the narrow peak in each inset). Adapted from Burgess 2012.

In regions where the angle between the magnetic field and the bow shock normal (θ_{bn}) is greater than 45 degrees (referred to as quasi-perpendicular), collimated ion beams with energies of a few keV are seen to propagate in the sunward direction, along the IMF (Paschmann et al. 1980). This ion population is typically referred to as a Field Aligned Beam (FAB). Examples of the usual morphology for FAB distributions at quasi-perpendicular shocks are displayed as insets in Figure 1.4. Apart from their narrow pitch angle extent, FABs are distinguished by their temperature anisotropies (Paschmann et al. 1981), depletion of He2+ relative to the solar wind (Ipavich et al. 1988), and large variation in velocity and density with variation in θ_{bn} (Oka et al. 2005). The accepted acceleration mechanism for FABs is the Shock Drift Acceleration (SDA) mechanism (Burgess 1987). In this mechanism, FAB ions have multiple encounters with the shock and drift in along the convective electric field (in the frame of the shock). This mechanism is also consistent with earlier work where conservation of the magnetic moment, μ, during reflection at the shock in the deHoffman-Teller frame was used to explain FAB acceleration (Sonnerup 1969). The low relative abundance of alpha particles in FABs was also confirmed in hybrid simulation (Burgess 1989). A model for FAB acceleration involving the leakage of heated downstream plasma was proposed by Edmiston et al. 1982 and Tanaka et al. 1983, but has not equaled the success of the SDA theory at matching observations (Möbius et al. 2001, Kucharek et al. 2004, Oka et al. 2005).

The second foreshock population is the diffuse population, which is present where $\theta_{bn} < 45^o$ (the quasi-parallel foreshock). Diffuse ions are observed as a wide, largely isotropic shell-like distribution in velocity space that can extend well above 100 keV in energy (Paschmann et al. 1981). An example of this distribution and the structure of a quasi-parallel shock is shown in Figure 1.4. This population is further characterized by having a relative abundance of He^{2+} comparable to the upstream solar wind (Ipavich et al. 1984), in contrast to the depletion seen in FABs. The coexistence of low frequency waves with observations of diffuse populations was first demonstrated by Paschmann et al. 1979, and further analyzed by Hoppe et al. 1981. Another key observation is that the distributions of diffuse ion populations are well fit by an exponential in energy (Ipavich et al. 1979). More specifically, the spectra of ions with different charge states (H^+, He^{2+}, and C,N,O ions) are similar when organized by E/q. Most theories describing the creation of this population invoke some form of diffuse shock acceleration, i.e., first-order Fermi acceleration. There are several studies that attempt to measure a diffusion coefficient for the terrestrial foreshock to fit with this theory (e.g. Kis et al. 2004, Kronberg et al. 2009). However, the exact explanations of the exponential spectra within the frame work of diffusive shock acceleration is still debated. Three competing explanations are free escape (Ellison et al. 1990), time-dependence (Scholer et al. 1999) and cross field diffusion (Lee 1982, Wibberenze et al. 1985). The main difference between these theories lies in whether the Fermi acceleration process is limited by the spatial extent of the quasi-parallel foreshock region (extent upstream for free escape, or lateral extent for cross field diffusion) or governed by the amount of time the IMF remains connected to the region (time-dependent theories). At the time of this thesis work, a consensus on the dominant mode of diffusive shock acceleration that adequately explains the observations in the terrestrial foreshock has not been achieved.

1.2.6 Motivating Science: Mercury's Foreshock

These foreshock populations have been predominantly been studied at Earth, and thus over a limited range of ambient solar wind and bow shock conditions. The motivation to study foreshock populations at Mercury stems from the fact that its foreshock environment exists in such a different parameter space. This parameter space is roughly outlined in Table 1.3, where the values critical to planetary bow shocks are estimated.

Planet	R [AU]	P_{sw} [nPa]	M_s	M_A	β	Q	c/ω_{pi} [km]	Spiral Angle [deg]
Mercury	0.31	26	5.5	3.9	0.5	15	27	17
	0.47	11	6.1	5.7	0.9	32	40	25
Venus	0.72	5.0	6.6	7.9	1.4	62	61	36
Earth	1.00	2.5	7.2	9.4	1.7	88	86	45
Mars	1.52	1.1	7.9	11.1	2.0	120	130	57

Table 1.3: Basic parameters from Table 1.1 are used to compute plasma quantities relevant to planetary bow shocks for Mercury, Venus, Earth and Mars. Two radial distances are included for Mercury, due to the eccentricity of its orbit. The columns, from left to right are planet name, radial distance from Sun, dynamic pressure, sonic Mach number (ratio of solar wind bulk velocity and sound speed), Alfvénic Mach number (ratio of solar wind bulk velocity and Alfven speed), plasma beta (ratio of plasma pressure and magnetic pressure), dynamic pressure to magnetic pressure ratio, ion inertial length, and Parker spiral angle (angle between Earth-Sun line and Interplanetary Magnetic Field). See original text for further details, adapted from Slavin and Holzer 1981.

From our estimates so far we can see that Mercury's bow shock is about an order of magnitude smaller than Earth's, the sonic and Alfvénic Mach numbers are lower by a about a factor of 2, and the Parker spiral angle is significantly more radial as compared to the situation at Earth. This new parameter space raises the question of whether a foreshock at Mercury is at all similar to that seen at Earth. Preliminary analysis of MESSENGER magnetometer data has suggested that waves seen almost continuously in Earth's foreshock and associated with diffuse populations at Earth are only sporadically seen at Mercury (Le et al. 2013). It has been suggested that the absence of these waves implies that the small spatial scale of Mercury's bow shock limits the formation of a diffuse population at Mercury. Likewise with the small spatial size of Mercury's bow shock there is a question of whether the planar shock drift acceleration mechanism can act or if bow shock curvature effects become important. To date, the current analysis of Mercury's foreshock is lacking in substantial plasma measurements. Exploring whether the shock acceleration mechanisms as understood at Earth still apply in the Mercury foreshock is the primary motivation of this pursuit.

1.2.7 Guiding Science Questions for Mercury's Foreshock

1- How effective are shock energization processes at the bow shock of a small planetary magnetosphere?

There have been numerous observations of foreshock events upstream of Earth's bow shock, and even some at planets with larger bow shocks. However, there is a lack of observations at a bow shock of the small scale size seen at Mercury. Does the scale size of Mercury's bow shock limit the formation of foreshock populations? How does the smaller scale size, and different ambient solar wind conditions impact the observed foreshock environment?

1.3 Instrumentation

The results presented in this dissertation make abundant use of the plasma measurements from two main instruments, the Solar Wind Ion Composition Spectrometer (SWICS) and the Fast Imaging Plasma Spectrometer (FIPS). Here we give a brief overview of the operation of these two instruments.

1.3.1 SWICS

The work presented here makes extensive use the measurements of the Solar Wind Ion Composition Spectrometer (SWICS), which flew on both the Ulysses and Advanced Composition Explorer (ACE) spacecraft (Gloeckler et al. 1992; 1998). SWICS is a time-of-flight mass spectrometer capable of measuring the velocity distribution functions of over 50 charge states between the elements of He, C, N, O, Ne, Mg, Si, S, and Fe. The energy per charge range of SWICS extends from 0.11 keV/e to about 100 keV/e. A simplified sketch of the measurement process of SWICS is shown in Figure 1.5.

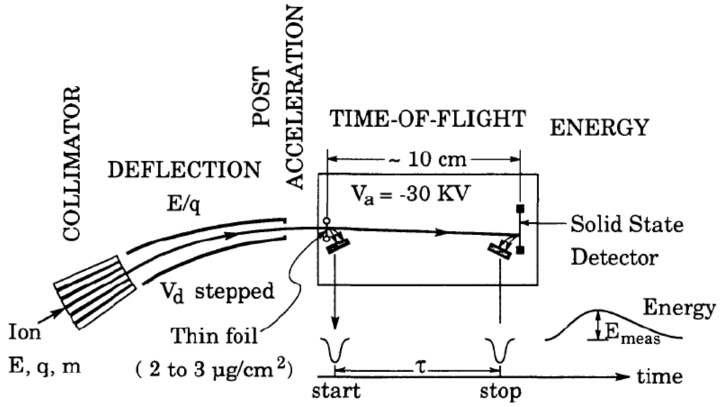

Figure 1.5: Schematic of the SWICS measurement method. Adapted from Gloeckler et al. 1992.

An incident ion has its trajectory bent by the electrostatic analyzer (ESA), essentially a pair of curved metal plates with a potential across them. At a given potential, only ions with a specific energy per charge (E/q) will have trajectories in this field that will allow them to pass through the entire ESA. The different E/q steps implemented by SWICS therefore allow filtering for ions of different E/q values. After passing through the ESA, an ion is accelerated through a potential drop of 25 kV, and then passes through a thin carbon foil which kicks off secondary electrons. These secondary electrons are responsible for triggering a start timer, and when the ion itself traverses the time-of-flight (TOF) section of the instrument and hits a solid state detector it triggers the emission of another set of secondary electrons the trigger a stop signal. In this way the flight time of the ion through the instrument can be measured. The ion's impact onto the solid state detector also allows for the total energy of the ion to be measured. With knowledge of an incident ion's E/q, total energy, and time of flight, it is then possible to calculate the mass, velocity, and charge state of that ion.

The SWICS instrument that flew with the ACE spacecraft is the one primarily used for the work presented in this dissertation. ACE was launched in February of 1998 and currently resides near the first Lagrangian (L1) point. At this location, ACE lies on the Earth-Sun line at close to 1 AU from the Sun and with a heliocentric orbit of the same period as Earth's. One of the ACE mission's objectives was to be an upstream solar wind monitor for Earth, providing early warning of conditions that could be hazardous to astronauts and space hardware near Earth. To these ends, ACE carries an array of plasma instruments (included SWICS, mentioned above) and a high resolution magnetometer.

1.3.2 FIPS

The primary instrument utilized in the work for studies of Mercury's space environment is the Fast Imaging Plasma Spectrometer (FIPS), which was designed at the University of Michigan. This instrument's stated purpose was to answer questions regarding the nature and origin of Mercury's magnetic field, radar-reflective materials at Mercury's poles, and sources and sinks of important volatile species on and near Mercury. To this end, FIPS surveyed positively charged ions encountered in-situ by the MESSENGER spacecraft (Andrews et al. 2007). The assembled flight instrument is shown in Figure 1.6.

Figure 1.6: Picture of the flight model of the Fast Imaging Plasma Spectrometer. Adapted from Andrews et al. (2007).

A more detailed cross-sectional diagram of FIPS is shown in Figure 1.7. FIPS is designed to measure ionized species within an energy-per-charge (E/q) range of 0.05 to 13 keV/e (Zurbuchen et al., 2008). The TOF measurements of FIPS allows for separation of ions with m/q between 1 and 40 amu/e. Ions are filtered by their E/q based on a deflection voltage applied to the sensor's electrostatic analyzer (ESA). The FIPS electrostatic deflection system enables an instantaneous ~1.4π steradian field of view (Zurbuchen et al. 1998). Depending on its scanning mode, FIPS scans through its entire E/q range every 60 seconds in "survey" mode and every 8 seconds in "burst" mode. The E/q range is covered in 60 logarithmically spaced steps (Andrews et al. 2007).

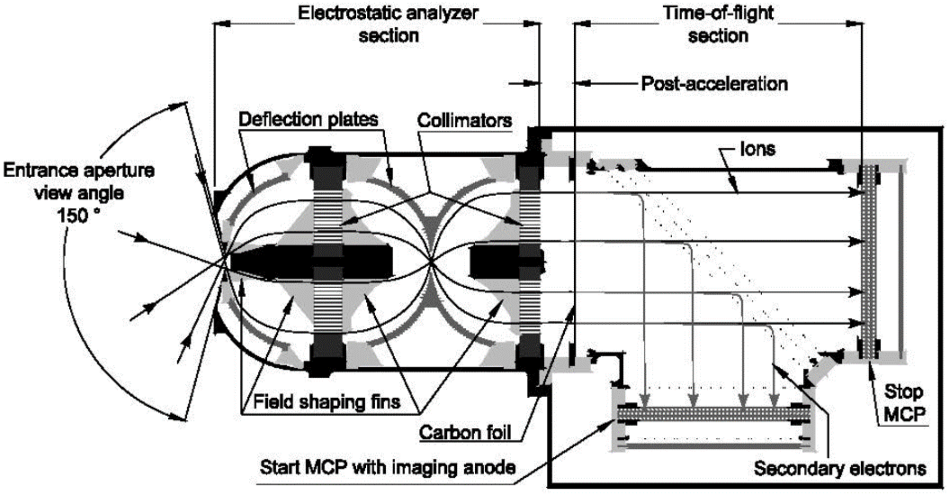

Figure 1.7: The FIPS sensor. Ions are guided through an electrostatic analyzer (ESA) that is optimized for ultraviolet light reduction, through a post-acceleration region, carbon foil, and into an electrostatic mirror Time-of-Flight (TOF) system. An ion passing through the carbon foil releases secondary electrons that trigger the start microchannel plate (MCP), opening a TOF window. When the ion impacts the stop MCP this TOF window is closed. Adapted from Andrews et al. (2007).

After passing through the ESA, the ion are post accelerated to gain sufficient energy to pass through a thin carbon foil. Upon impact with this foil, secondary electrons are ejected and guided via a mirror-harp assembly into a "start" micro-channel plate (MCP) detector. The MCP serves to amplify the impact of secondary electrons, through an electron cascade, into a measureable electrical signal. The ion optics of the ESA and TOF allow for a direct mapping from incident particle velocity vector direction to position on the start MCP (with an angular resolution of about 15 degrees). After this start signal is triggered, the incident ion (neutralized by the foil impact) travels through the TOF chamber and hits a "stop" MCP. With the distance through the TOF chamber known, as well as the time between the start and stop MCP signals, the velocity of the ion in the TOF chamber can be computed.

Using simulation data for the energy loss caused by the foil collision, and the incident energy of the measured ion, the mass-per-charge (m/q) of a given ion can be determined (Raines et al. 2013). This m/q value allows the FIPS instrument to distinguish between the different ions species observed in Mercury's magnetosphere. A forward model is utilized to facilitate identification of ion species in terms of the base measured instrument quantities, incident ion E/q and TOF. For a given ion species (or equivalently a given m/q) the expected TOF value can be computed based on the incident E/q value. This is then done over the range of E/q values measured by FIPS, and overplotted on a histogram of the number of measurements recorded at each E/q and TOF value. An example of this forward model and raw data is seen in Figure 1.8. The ions species of each measurement can be determined by where it lies relative to these modeled tracks.

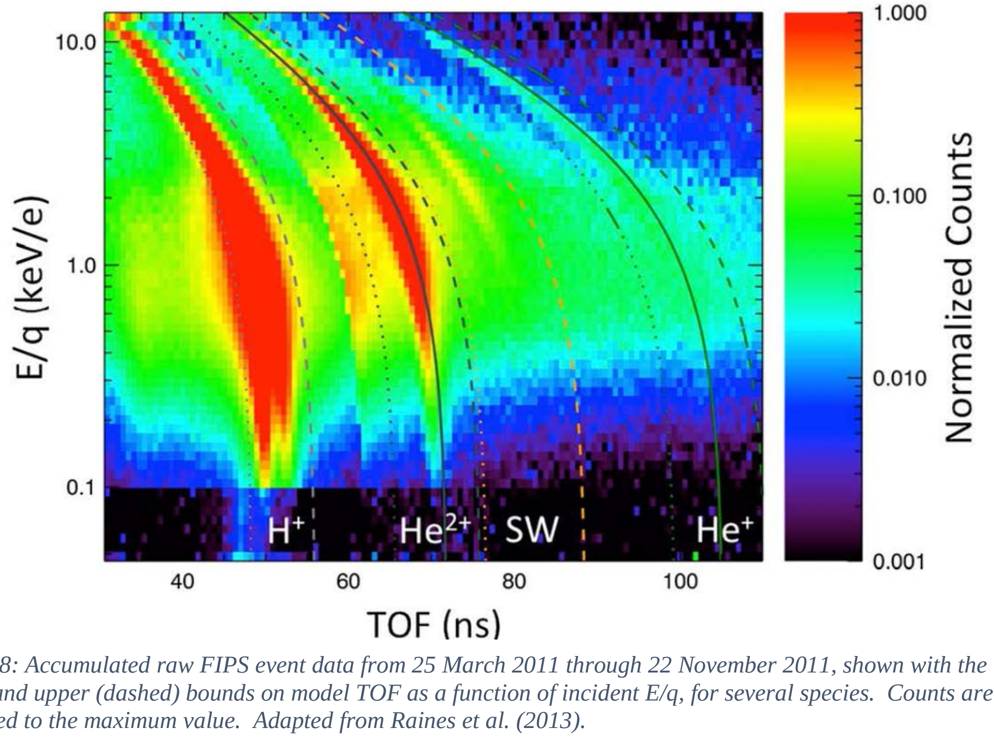

Figure 1.8: Accumulated raw FIPS event data from 25 March 2011 through 22 November 2011, shown with the lower (dotted) and upper (dashed) bounds on model TOF as a function of incident E/q, for several species. Counts are normalized to the maximum value. Adapted from Raines et al. (2013).

1.4 Chapter Overviews

In chapter 2 of this dissertation, we quantify the thermalization of heavy ions observed in the solar wind. We show that there exists a set of heavy ions that are collisionally young (initial heating profiles not erased by thermalization), and also that not all heavy ions show simple collisional relaxation with increasing collisional age. The collisionally young plasma is explored in more detail in chapter 3, where we compare the temperature ratios of solar wind heavy ions to protons. We focus on mass and charge dependencies of these relative temperatures and compare our findings to predictions of solar wind heating. We find that the collisionless heavy ions temperatures are not in agreement with predictions. In chapter 4 we detail the study of planetary heavy ions in Mercury's space environment and relate those measured ion abundances to the neutral exospheric abundances. The abundances can be used to constrain the various surface desorption processes proposed to contribute to Mercury's exosphere. Chapter 5 is dedicated to the identification and analysis of foreshock plasma population upstream of the Hermean bow shock. The energization mechanisms proposed in the terrestrial foreshock are investigated in the context of the plasma populations observed in this new parameter regime. Finally, in chapter 6 we summarize our findings, revisit the guiding science questions, and look at directions for future work.

Chapter 2 –Thermalization of Heavy Ions in the Solar Wind

The text in this chapter was published in Tracy, P.J., et al. (2015), *The Astrophys. J.*, **812**, 170. The abstract and introductory sections have been combined and edited for inclusion in this dissertation.

2.1 Introduction

Observations of velocity distribution functions from the ACE/SWICS heavy ion composition instrument are used to calculate ratios of kinetic temperature and Coulomb collisional interactions of an unprecedented fifty ion species in the solar wind. These ions cover a mass per charge range of 1-5.5 amu/e and were collected in the time range of 1998-2011. We report the first calculation of the Coulomb thermalization rate between the each of the heavy ion ($A > 4$ amu) species present in the solar wind along with protons (H^+) and alpha particles (He^{2+}). From these rates we find that protons are the dominant source of Coulomb collisional thermalization for heavy ions in the solar wind, and use this fact to calculate a collisional age for those heavy ion populations. The heavy ion thermal properties are well organized by this collisional age, but we find that the temperature of all heavy ions does not simply approach that of protons as Coulomb collisions become more important. We show that He^{2+} and C^{6+} follow a monotonic decay toward equal temperatures with protons with increasing collisional age, but O^{6+} shows a noted deviation from this monotonic decay. Furthermore, we show that the deviation from monotonic decay for O^{6+} occurs in solar wind of all origins, as determined by its Fe/O ratio. The observed differences in heavy ion temperature behavior points toward a local heating mechanism that favors ions depending on their charge and mass.

The guiding science question we aim to answer here is: *How well are initial heating signatures created in the heavy ion population of the solar wind preserved by the time they are observed at 1 AU?* The answer to this question requires the careful consideration of thermalization sources that may wash out nonthermal features present in the solar wind heavy ion populations. The existence of mass-proportional temperatures in the fastest solar wind (von Steiger and Zurbuchen 2006) imply that such nonthermal features exist, certainly, but we cannot know if the observed nonthermal features at 1 AU are representative of the nonthermal features that existed earlier in a solar wind parcel's evolution. The calculation of the collisionality of the solar wind at 1 AU will shed some light on the degree to which these initial features are mitigated.

In section 2.2, we will first investigate the collisional rates between all species in the solar wind to identify the most important collisional rates leading to thermalization of any given ion species. We describe the correct formalism for this analysis, applicable to the solar wind ionic charge states of ions ranging in mass from H to Fe. The observations and analysis methodology used in this work is introduced in section 2.3. Last a detailed discussion is provided in section 2.4, quantifying the observed thermalization for three specific ion species, followed by concluding remarks in section 2.5.

2.2 Coulomb collisional rates of solar wind ions

2.2.1 Collisional Rate Calculation

To investigate the relevant collisional interactions, a Coulomb thermalization rate, $\nu_{th,ij}^{\epsilon}$, analogous to the inverse of the collisional time scale used in Kasper et al. (2008), was calculated for each ion coupling pair, of solar wind we observe. We defined an interaction between ion i and ion j such that ion i is the test particle, interacting with a field of particles of ion species j. However, it is important to note that although we use the language of "test particle" we do not mean to imply that we used a cold beam formulation with test particles that had zero temperature. The formulation used involves the interaction of two thermal Maxwellian distributions and is discussed below. In any case, we choose to keep the distinction between test particle and field particle as $\nu_{th,ij}^{\epsilon} \neq \nu_{th,ji}^{\epsilon}$ in general. The thermalization rate is computed using the formalization found in Hernandez and Marsch (1985),

$$\nu_{th,ij}^{\epsilon} = \frac{1}{3\pi\epsilon_0^2} \frac{q_i^2 q_j^2 \, ln\Lambda_{ij} n_j}{m_i m_j \left(v_{th,i}^2 + v_{th,j}^2\right)^{\frac{3}{2}}} \frac{\phi(x)}{x}, \tag{2.1}$$

where all units are in SI and all common variables have their usual meanings. The term $\ln \Lambda_{ij}$ is the Coulomb logarithm and for an interaction between ion species i and j, with mass number, A, and charge number, Z, is defined as

$$ln\Lambda_{ij} = 29.9 - ln\left(\frac{Z_i Z_j \left(A_i + A_j\right)}{A_i T_j + A_j T_i} \left(\frac{n_i Z_i^2}{T_i} + \frac{n_j Z_j^2}{T_j}\right)^{\frac{1}{2}} \right), \tag{2.2}$$

where all variables are in SI, except the temperature, T_i and T_j, which are in eV. We define x as the normalized differential streaming between ion i and ion j,

$$x = \frac{\left|\boldsymbol{U}_i - \boldsymbol{U}_j\right|}{\left(v_{th,i}^2 + v_{th,j}^2\right)^{\frac{1}{2}}}, \tag{2.3}$$

and $\phi(x)$ is the standard error function

$$\phi(x) = \frac{2}{\pi^{\frac{1}{2}}} \int_0^x e^{-z^2} dz. \tag{2.4}$$

The thermal velocity is the most probable thermal speed (assuming a Maxwellian distribution),

$$v_{th,i}^2 = \frac{2 k_B T_i}{m_i}. \tag{2.5}$$

The error function term is a correction for how differential streaming decreases the thermalization rate between two ion species. As explained in the next section, we will use two hour time resolution data which means that we cannot well resolve the differential streaming between heavy ions in the solar wind. As an approximation for this effect, we assume a value of $x = 0.5$ as $v_{th} \approx c_A$ (the Alfvén speed) when the plasma beta is close to unity ($\beta \approx 1$) in the solar wind parcel. This value of $x = 0.5$ is only applied for interactions of non-protons with protons (as, for example, O^{6+} with H^+); on the other hand for interactions between ions of the same species (O^{6+} with O^{6+} or H^+ with H^+) we assume $x = 0$. This is in accordance with the findings of Berger et al. (2011), which found that most heavy ions stream at about 0.5 times the Alfvén speed relative to the protons.

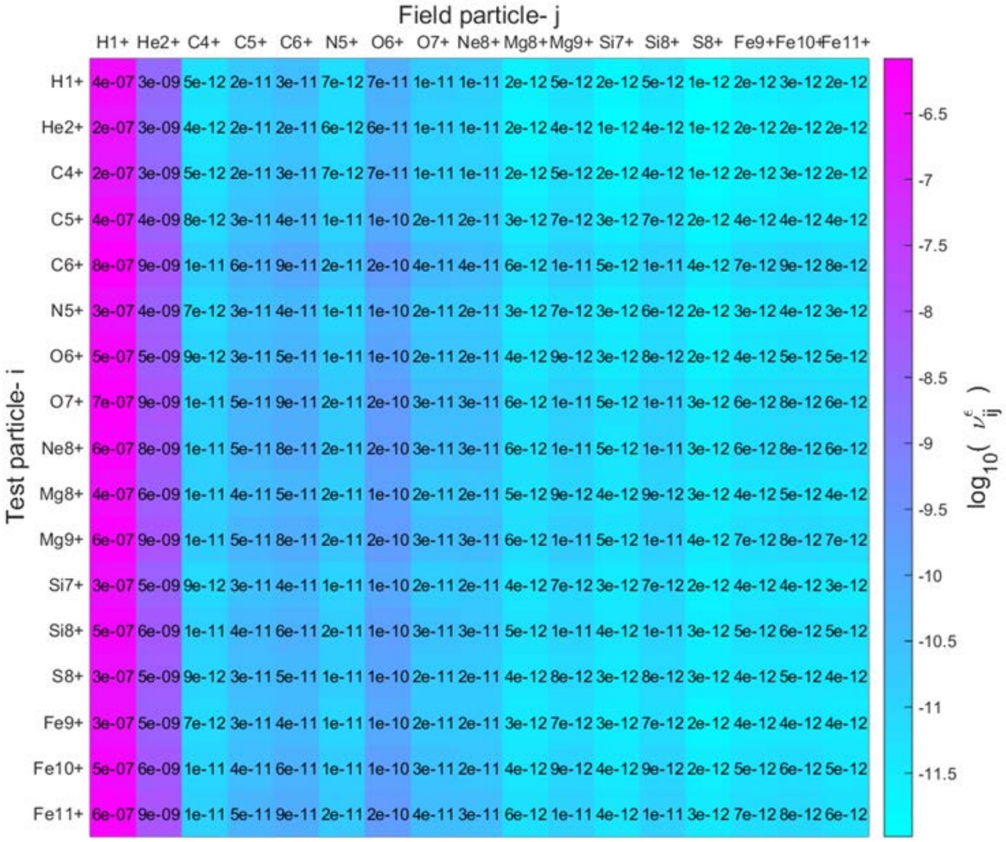

	H1+	He2+	C4+	C5+	C6+	N5+	O6+	O7+	Ne8+	Mg8+	Mg9+	Si7+	Si8+	S8+	Fe9+	Fe10+	Fe11+
H1+	4e-07	3e-09	5e-12	2e-11	3e-11	7e-12	7e-11	1e-11	1e-11	2e-12	5e-12	2e-12	5e-12	1e-12	2e-12	3e-12	2e-12
He2+	2e-07	3e-09	4e-12	2e-11	2e-11	6e-12	6e-11	1e-11	1e-11	2e-12	4e-12	1e-12	4e-12	1e-12	2e-12	2e-12	2e-12
C4+	2e-07	3e-09	5e-12	2e-11	3e-11	7e-12	7e-11	1e-11	1e-11	2e-12	5e-12	2e-12	4e-12	1e-12	2e-12	3e-12	2e-12
C5+	4e-07	4e-09	8e-12	3e-11	4e-11	1e-11	1e-10	2e-11	2e-11	3e-12	7e-12	3e-12	7e-12	2e-12	4e-12	4e-12	4e-12
C6+	8e-07	9e-09	1e-11	6e-11	9e-11	2e-11	2e-10	4e-11	4e-11	6e-12	1e-11	5e-12	1e-11	4e-12	7e-12	9e-12	8e-12
N5+	3e-07	4e-09	7e-12	3e-11	4e-11	1e-11	1e-10	2e-11	2e-11	3e-12	7e-12	3e-12	6e-12	2e-12	3e-12	4e-12	3e-12
O6+	5e-07	5e-09	9e-12	3e-11	5e-11	1e-11	1e-10	2e-11	2e-11	4e-12	9e-12	3e-12	8e-12	2e-12	4e-12	5e-12	5e-12
O7+	7e-07	9e-09	1e-11	5e-11	9e-11	2e-11	2e-10	3e-11	3e-11	6e-12	1e-11	5e-12	1e-11	3e-12	6e-12	8e-12	6e-12
Ne8+	6e-07	8e-09	1e-11	5e-11	8e-11	2e-11	2e-10	3e-11	3e-11	6e-12	1e-11	5e-12	1e-11	3e-12	6e-12	8e-12	6e-12
Mg8+	4e-07	6e-09	1e-11	4e-11	5e-11	2e-11	1e-10	2e-11	2e-11	5e-12	9e-12	4e-12	9e-12	3e-12	4e-12	5e-12	4e-12
Mg9+	6e-07	9e-09	1e-11	5e-11	8e-11	2e-11	2e-10	3e-11	3e-11	6e-12	1e-11	5e-12	1e-11	4e-12	7e-12	8e-12	7e-12
Si7+	3e-07	5e-09	9e-12	3e-11	4e-11	1e-11	1e-10	2e-11	2e-11	4e-12	7e-12	3e-12	7e-12	2e-12	4e-12	4e-12	3e-12
Si8+	5e-07	6e-09	1e-11	4e-11	6e-11	2e-11	1e-10	3e-11	3e-11	5e-12	1e-11	4e-12	1e-11	3e-12	5e-12	6e-12	5e-12
S8+	3e-07	5e-09	9e-12	3e-11	5e-11	1e-11	1e-10	2e-11	2e-11	4e-12	8e-12	3e-12	8e-12	3e-12	4e-12	5e-12	4e-12
Fe9+	3e-07	5e-09	7e-12	3e-11	4e-11	1e-11	1e-10	2e-11	2e-11	3e-12	7e-12	3e-12	7e-12	2e-12	4e-12	4e-12	4e-12
Fe10+	5e-07	6e-09	1e-11	4e-11	6e-11	1e-11	1e-10	3e-11	2e-11	4e-12	9e-12	4e-12	9e-12	2e-12	5e-12	6e-12	5e-12
Fe11+	6e-07	9e-09	1e-11	5e-11	9e-11	2e-11	2e-10	4e-11	3e-11	6e-12	1e-11	4e-12	1e-11	3e-12	7e-12	8e-12	6e-12

Figure 2.1: The median value of the collisional rate for thermalization between every possible ion interaction pair for selected ions in the solar wind. The test particle of each collision is shown by the row of a given entry, and the field particle of the collision is shown by the column. The value in each box is the collision rate (1/sec) and each box is shaded by the logarithm (base 10) of its value.

By setting $x = 0.5$, we are also not accounting for the variation in differential streaming in the solar wind parcels that we measure. When we set the differential streaming of heavy ions in this manner, varying our choice of x will only affect the collisional rates that involve protons (Figure 2.1). Varying the value of x by 0.5 will cause the heavy-to-proton thermalization rate to vary by factors of 20%, according to equation (1), which we will show is small compared to the difference between the ion to proton interaction and the next largest interaction, ion to He^{2+}.

Using this methodology we compute the thermalization rate, $\nu_{th,ij}^{\epsilon}$, between all ion interaction pairs measured by Solar Wind Ion Composition Spectrometer (SWICS) onboard the Advanced Composition Explorer (ACE) spacecraft (Gloeckler et al. 1998). The details of this instrument will be elaborated on in the next section. The average thermalization rate from 1998-2011 for a representative sample of heavy ions is shown in Figure 2.1. Examining this table, we see that the important field particle for each heavy ion species is indeed H^{+}. We find that $He2^{2+}$ is the second most important field particle with an average thermalization rate about 2 orders of magnitude lower than that of protons. This confirms that the effect of high proton density dominates the collisional rate expression, and the interaction of heavy ions with other heavy ions is indeed negligible. The table of thermalization rates was also calculated after sorting the solar wind into two groups with velocities above and below 450 km/s. The rates were in general lower in the high velocity solar wind, but the relative values among ion interaction pairs were roughly constant.

Based on this analysis, we define the collisional age for each heavy ion in the same way as Kasper et al. (2008), which is solely based on the thermalization rate of the heavy ion with protons.

$$A_C = \nu_{th,ip}^{\epsilon}\left(\frac{R}{V_{SW}}\right), \tag{2.6}$$

where $\nu_{th,ip}^{\epsilon}$ is the thermalization rate of heavy ion i with protons and $\frac{R}{V_{SW}}$ is the estimated travel time to 1 AU for the observed parcel of solar wind plasma, based on the measured speed at 1 AU. More realistic calculations of the collisional age would include treatments of the evolution of temperature, differential flow, and bulk speed with distance from the Sun, but this simple form is sufficient for this first examination of minor ion thermalization.

2.2.2 SWICS Analysis

Nearly 14 years of heavy ion measurements (1998-2011) from the Solar Wind Ion Composition Spectrometer (SWICS) onboard the Advanced Composition Explorer (ACE) spacecraft were used in this analysis (Gloeckler et al. 1998). Taken at 2 hour time resolution for 77 ion species, the solar wind ions range in mass-per-charge ratios (m/q) of 1-5.5 amu/e and in collisional parameters (m/q^2) from about 0.3 to 1 amu/e^2 during typical solar wind conditions. We utilized the reprocessed SWICS data set (version 4.06), in which the observed counts of each of the ions species detectable by SWICS were determined with a maximum likelihood methodology described in Shearer et al. (2014). Simple moments of this count distribution were used to recover each species' density, bulk speed, and thermal speed. The proton parameters were gathered from two different sources, the first being the H/He channel of the SWICS instrument. The second source was the Solar Wind Electron, Proton, and Alpha Monitor (SWEPAM) also onboard the ACE spacecraft (McComas et al. 1998), which was downloaded from the ACE Science Center Website (Garrard et al. 1998). SWICS H/He channel data is acquired in the same time cadence as the main channel of the SWICS instrument, and is cross-calibrated to the ACE/SWEPAM and Wind/SWE (Oglivie et al. 1995) datasets. The H/He channel and SWEPAM measurements, which have 12 minute and 64 second resolution, respectively, were then averaged over 2-hour periods to match the sampling time steps of the SWICS instrument.

For our time period of analysis, we required that a given heavy ion species have at least 30 observed counts in a given 2-hour time period, and these counts had to be spread over at least 3 of the 58 energy-per-charge (E/q) bins of the SWICS instrument. When SWEPAM data was utilized, we required that SWEPAM had reported valid density, bulk velocity, and temperature for protons. The same requirement is made of the SWICS H/He channel data. In addition to these other requirements we also enforced that the time period not fall within one of the ICME times given by the Richardson and Cane ICME list (Richardson and Cane 2010). Removing the ICMEs from the data set has very little effect on the observed trends, but is done for completeness.

The 30 counts and 3 E/q bin requirement was chosen somewhat arbitrarily by observing the nature of the measured distribution functions of SWICS. To justify these selections, we computed our results for several selection criteria, for example requiring 100 total counts and 3 E/q bins with at least 10 counts. Changing these criteria has the largest effect on the lower abundance ions analyzed, such as C6+, but does not appreciably change our reported results. For heavy ions such as He^{2+}, C^{6+}, and O^{6+}, the chosen requirements result in about 36000 valid 2-hour data events in the time period from 1998-2011 when using the SWEPAM proton data. Due to the limitations of the SWEPAM instrument, particularly noticeable at low solar wind velocities, it is the SWEPAM valid data requirements that limit the number of valid data intervals. When the SWICS H/He channel is used to acquire proton data, we recover about 50,000 valid 2-hour event periods between 1998-2011. Due to the greater number of valid events, we choose to utilize the SWICS H/He channel in the data we report in this study.

2.3 Thermalization of Heavy Ions in the Solar Wind

2.3.1 Thermalization as a function of Collisional Age

For each of the two hour data events observed by SWICS, we now compute the collisional age, A_C, and the ratio of thermal velocities between heavy ions and protons, $v_{th,i}/v_{th,H^+}$. With these two parameters we perform a 2-dimensional histogram and show the frequency of events at each collisional age in a similar manner as Kasper et al. (2008). Note that all the histogram bins in each column have been normalized to the total number of events in that column, and that the color is proportional to that normalized value. These histograms are shown for ion species, He^{2+}, C^{6+}, and O^{6+}, in Figure 2.2, Figure 2.3, and Figure 2.4, respectively. These ions are representative of the behavior observed in the 77 ions observed with ACE/SWICS. He^{2+} and C^{6+} have the same m/q ratio with C^{6+} having a $\frac{q^2}{m}$ value three times larger than He^{2+}. Including O^{6+} illustrates an ion with a m/q ratio different than the others and a $\frac{q^2}{m}$ value intermediate to the previous two. Typically, fast and low-density solar wind corresponds to low A_C values and slower, high density wind tends to high A_C values. Fully thermalized ions would lie on the solid purple horizontal line ($T_i = T_p$) and ions with equal thermal speeds would lie on the dashed purple line ($v_{th,i} = v_{th,p}$). A magenta line is overlaid to trace the median value of the thermal velocity ratio in each collisional age bin.

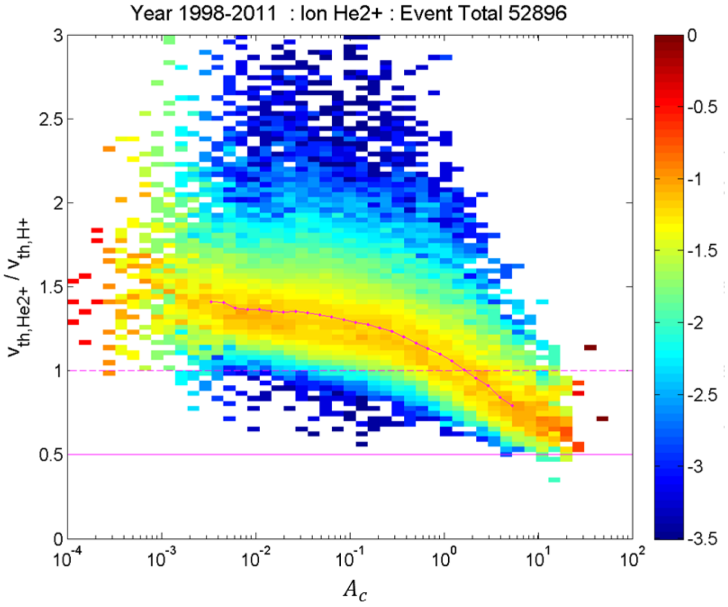

Figure 2.2: A two dimensional histogram of the collisional age A_C, and $v_{th,He^{2+}}/v_{th,\,H^+}$ .This is an accumulation of every ACE/SWICS valid 2 hour data interval from 1998-2011 of ACE/SWICS data. The color of each bin represents the logarithm (base 10) of the number of events falling in that bin normalized by the total number of events with the same collisional age. The magenta line overlaid represents the median thermal velocity ratio value at each collisional age.

In Figure 2.2 the thermal velocity ratio of He^{2+} relative to protons $\left(v_{th,He^{2+}}/v_{th,H^+}\right)$ is shown as a function of collisional age. There is a decreasing trend in thermal velocity ratio with increasing collisional age, as expected. However there are two differences between what we have observed and results by Kasper et al. (2008). First, the plot does not cover the entire collisional age range seen in Kasper et al. (2008). The beginning of an exponential decay toward an equal temperature value is seen, as observed by Kasper, but that state is never fully reached at high A_C values. Second, our thermal velocity ratios are somewhat elevated as compared to Kasper et al. (2008). This is especially visible in the low collisional age measurement, where Kasper et al. (2008) showed the thermal velocity ratio to peak at around 1.2. The SWICS observations show thermal velocity ratios that peak around 1.5 for the same regime of low collisionality.

The differences observed between our data and that of Kasper et al. (2008) may be explained by the differences in measurement methodologies used. The energy resolution of SWICS is about 6% and the energy steps are separated from each other by 7 or 15% (7% for the lower energy steps and 15% for the higher) to cover the full energy range of the solar wind heavy ion distribution during all conditions (Gloeckler et al. 1998). For solar wind bulk velocities of 300-400 km/s, roughly corresponding to the highest collisional age wind, the spacing between the bin centers for the measurement of He^{2+} is about 10-15 km/s. This value can be comparable to the expected He^{2+} thermal speed, making the recovery of thermal velocity difficult because there are just too few bins to create a valid second moment (Shearer et al. 2014). This process, along with our requirement that at least three energy per charge bins possess measured counts, will act to systematically eliminate low thermal speeds or high collisional age events from the ACE/SWICS dataset.

The longer accumulation period for data collection with ACE/SWICS relative to the 96 second cadence of the measurements in Kasper et al. (2008) will also affect the reported ion kinetics. The slower cadence of the SWICS instrument will cause the more extreme, short time duration, solar wind events to be averaged with adjacent time periods in the two hour accumulation. This two hour binning of the ACE/SWICS instrument is necessary for low density time periods, however, particularly if the measured plasma distribution has a large thermal width. In that scenario, the density observed in each velocity interval measured by SWICS can be quite low and the two hour accumulation is necessary for sufficient signal to noise ratios. This trait allows SWICS superb background suppression (von Steiger and Zurbuchen 2011), and means SWICS is better suited to observe hot low density heavy ion populations than a simple flux measurement as a function of energy. A similar systematic difference at large temperatures was also found in the inner heliosphere by Gershman et al. (2012).

Figure 2.3 shows the non-thermal behavior of C^{6+} in the same format as Figure 2.2. The thermal velocity ratio between C^{6+} and protons is again monotonically decreasing with increasing collisional age. This plot is qualitatively very similar to that for He^{2+}. One will notice that the higher q^2/m value of C^{6+} compared to He^{2+} causes the calculated collisional age range observed to extend to higher values. Thus there is slightly more decay toward equal temperatures for C^{6+}, although the equal temperature point itself is again not quite obtained in the most collisional events.

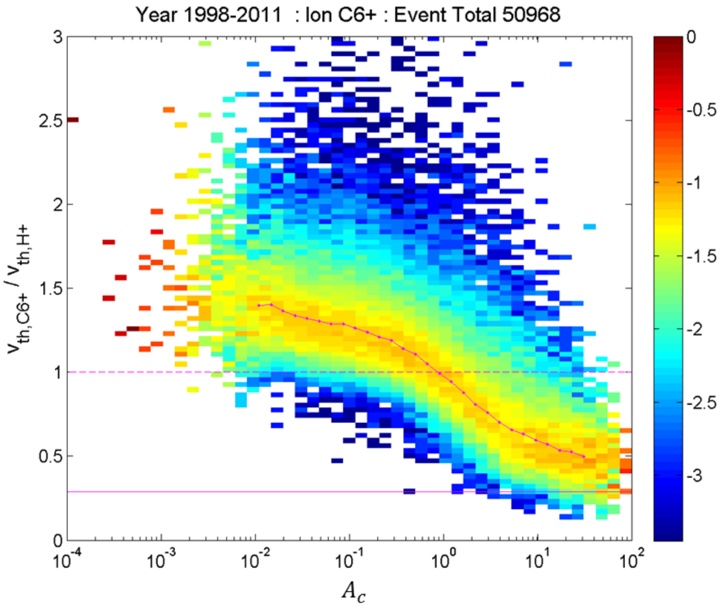

Figure 2.3: A two dimensional histogram of the collisional age A_C, and $v_{th,C^{6+}}/v_{th,H^+}$ .This is an accumulation of every ACE/SWICS valid 2 hour data interval from 1998-2011 of ACE/SWICS data. The color of each bin represents the logarithm (base 10) of the number of events falling in that bin normalized by the total number of events with the same collisional age. The magenta line overlaid represents the median thermal velocity ratio value at each collisional age.

We show an analogous plot for O^{6+} in Figure 2.4. Here the most interesting feature is the noted deviation from simple exponential decay for collisional ages less than 0.1. This feature in the organization of data by collisional age is not observed to any extent in the results of Kasper et al. (2008). We also note again that the thermal velocity ratios observed at low collisional ages are above the equal thermal velocity line and therefore well above the equal temperature line (which corresponds to a thermal velocity ratio of 0.25 for O^{6+}).

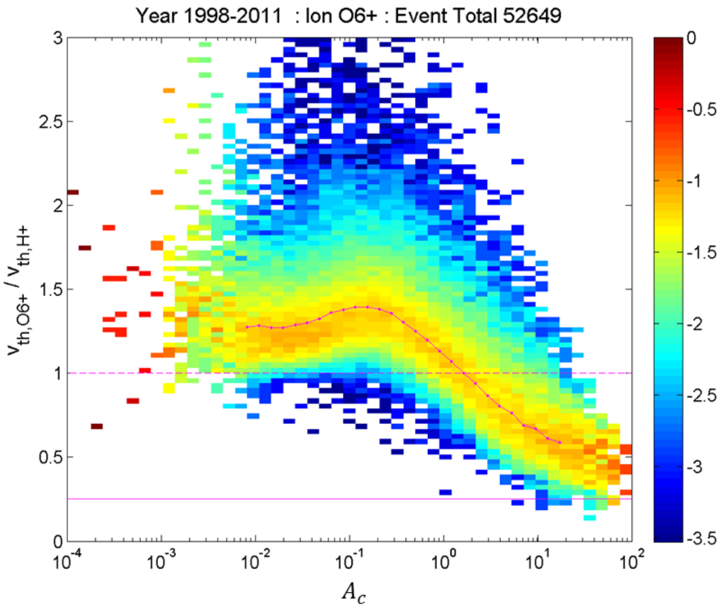

Figure 2.4: A two dimensional histogram of the collisional age A_C*, and* $v_{th,O^{6+}} / v_{th,\,H^+}$ *.This is an accumulation of every ACE/SWICS valid 2 hour data interval from 1998-2011 of ACE/SWICS data. The color of each bin represents the logarithm (base 10) of the number of events falling in that bin normalized by the total number of events with the same collisional age. The magenta line overlaid represents the median thermal velocity ratio value at each collisional age.*

The fact that we do not see simple exponential decay of the thermal velocity ratio for higher collisional ages for O^{6+} implies there is another process at work in determining the observed ion temperatures in the solar wind. We see that He^{2+} and C^{6+}, which have the same mass per charge ratio, show a monotonic decay toward equal temperature with increasing collisional age. The fact that O^{6+} has a mass per charge higher than He^{2+} and C^{6+} and shows very different behavior in its $v_{th,O^{6+}}/v_{th,H^+}$ dependence on A_C is particularly interesting. This suggests that, in additional to Coulomb thermalization, some process that depends on an ion’s mass and charge characteristics is responsible for determining that ion’s thermal evolution.

2.3.2 Dependence on IMF Direction

To enable an accurate interpretation of these results one has to understand the observational characteristics of the SWICS instrument. First and foremost, SWICS observed only the radial projection of a nominally 3D distribution function of the solar wind plasma. Thus, if we consider the solar wind as a Bi-Maxwellian distribution, with different temperatures perpendicular and parallel to the magnetic field, SWICS will measure a different projection of that distribution depending on the angle the Interplanetary Magnetic Field (IMF) makes with the Sun-Earth line. This is illustrated for He^{2+} (Figure 2.5a), C^{6+} (Figure 2.5b), and O^{6+} (Figure 2.5c) using the same histogram binning as Figure 2.2, but now with each bin colored by the median value of IMF angle for all events that fell in that bin. A minimum of 30 valid 2 hour periods was required in each displayed colored bin. This shows the bias toward observing more perpendicular IMF angles at higher A_c values, which roughly corresponds with slower solar wind bulk velocities. We have also overlaid additional traces of the median value of thermal velocity ratio at each collisional age, for quasi-radial and quasi-perpendicular filters of IMF angle. These filters represent substantial decreases in the total number of valid events, but serve to illustrate how the measured thermal velocity ratio depends on the IMF angle. A slightly higher thermal velocity ratio between the ions is seen for events with a perpendicular IMF configuration, but there is not a strong discrepancy observed between the perpendicular and radial IMF orientations.

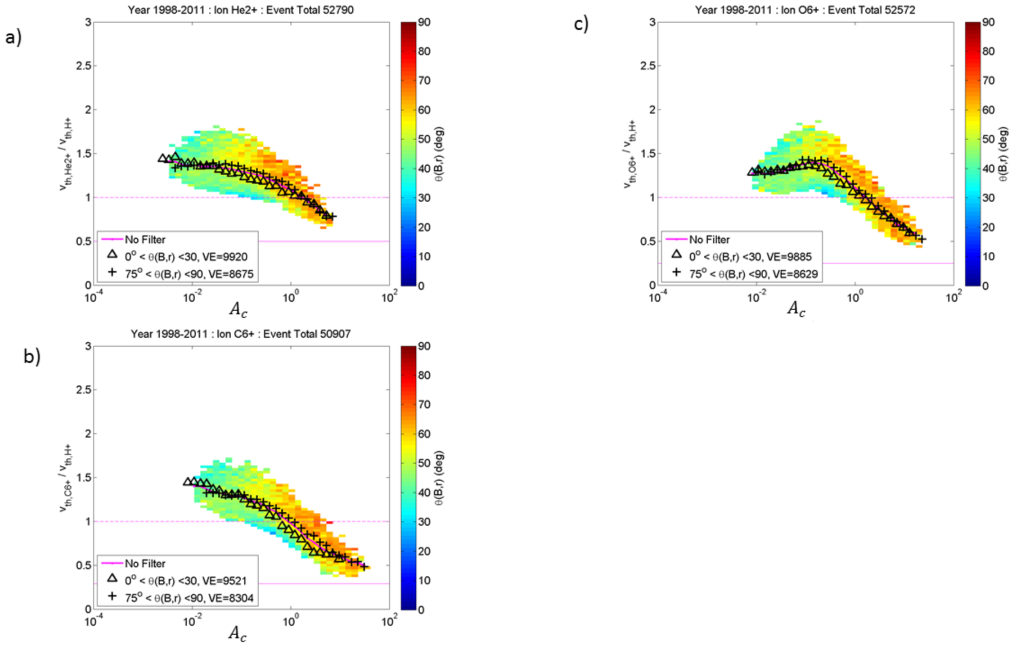

Figure 2.5: This figure depicts the same binning by collisional age and thermal velocity ratio as Figure 2. The color scale represents the angle of the IMF relative to the Sun-Earth line. The magenta overlaid line is the same curve as in

Figure 2-4, representing the median thermal velocity ratio at each collisional age. The black triangles and crosses represents the median thermal velocity ratio when $\theta(B,r)$ is less than 30 degrees or $\theta(B,r)$ is more than 75 degrees, respectively. The number of valid 2 hour events (VE) in each IMF orientation median trace is indicated in the plot legend. Only bins that had at least 30 events are shaded, and the median lines are only plotted over the range of collisional age that have shaded bins.

The thermal velocity ratio for C^{6+} and O^{6+} also show a modest deviation from the radial orientation starting at collisional ages of about 0.1. For both heavy ions we see the thermal velocity ratio for the radial orientation fall slightly below the median value line (magenta) computed without an IMF directional filter. The observation of this slight discrepancy between perpendicular and radial orientations is at least consistent with the idea that the perpendicular temperature may be preferentially heated over the parallel temperature in our observations. As A_c increases above about 10, we see the perpendicular IMF and radial IMF orientation events begin to converge to the same thermal velocity ratio values.

The main result of Figure 2.5 is that the deviation from decay toward equal temperatures as A_c increases is slightly more prominent in times when SWICS measures the temperature component perpendicular to the magnetic field. It is unclear whether this observation of slightly higher thermal velocity ratios in time of perpendicular IMF is enough to be considered significant. If significant, this suggests that the process acting on the solar wind plasma does so preferentially in the perpendicular direction. This fact is at least consistent with wave-particle interaction models for heating solar wind plasma (Isenberg and Vasquez 2007; Cranmer and van Ballegooijen 2003). We also observe a difference in the thermal velocity ratio for the He^{2+} and C^{6+} species under perpendicular IMF conditions, suggesting a signature of perpendicular heating in those populations as well.

2.3.3 Dependence on Solar Wind Type

When analyzing the solar wind population at 1 AU over a large time range, we must investigate how the thermal velocity ratio behaves for different solar wind types. Do the trends of thermal velocity ratio with collisional age appear in solar wind parcels from different source regions? To allow for insight in that regard we present another histogram of our 14 year data set by Fe/O abundance ratio of each event. It has been shown that the Fe/O ratio is related to the FIP effect in the source region of a given solar wind parcel, with the slow solar wind showing a greater enhancement in low FIP elements than fast solar wind (von Steiger et al. 2000). We use the Fe/O ratio to act as rough proxy for the source region of the observed solar wind parcel. The lowest values of Fe/O ratio shown in Figure 2.6 correspond to coronal hole associated solar wind and the highest values should be tied to solar wind emanated from reconnection of quiet closed loops (Fisk et al. 1999).

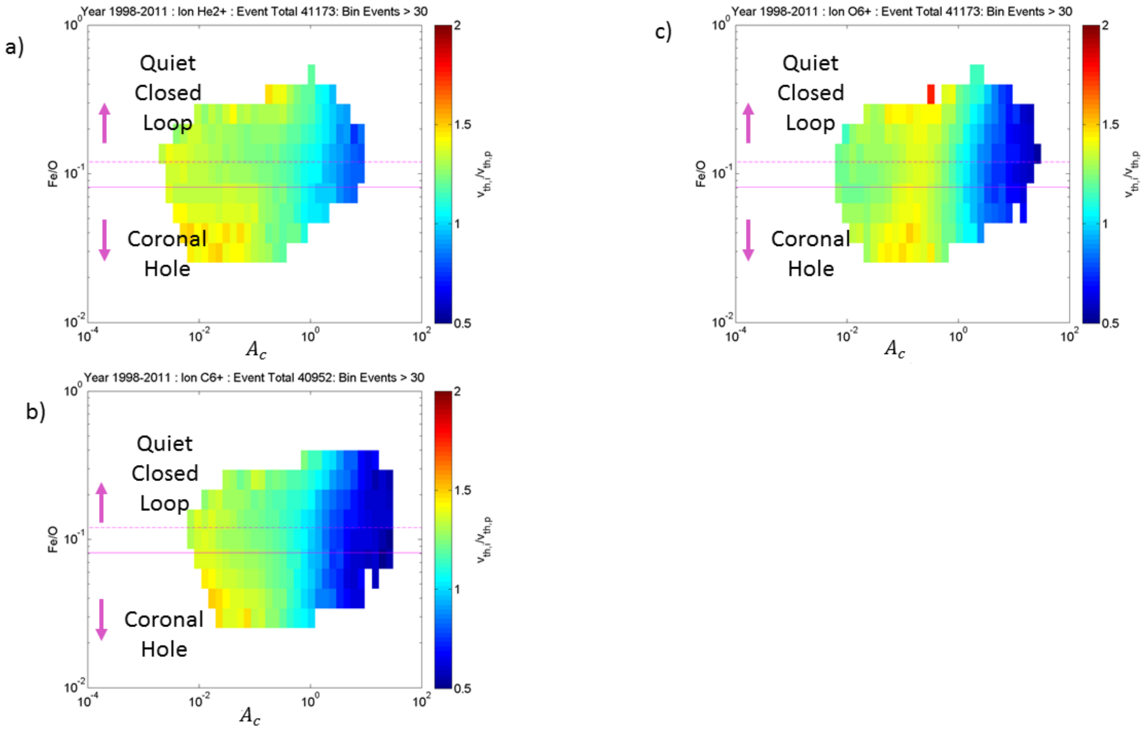

Figure 2.6: Shown in this figure is a two dimensional histogram for each heavy ion of interest over all events that had valid Fe, O, and H data from 1998-2011. We histogram the Fe/O density ratio against the collisional age computed for each 2 hour event observed by SWICS. Each bin is shaded by the median value of the thermal velocity ratio of all the events in that bin. Only bins with at least 30 events are shaded. In a) we show the resultant histogram for He2+, in b) for C6+, and c) for O6+.

We present a histogram by collisional age and Fe/O ratio for He^{2+} in Figure 2.6a. The more stringent requirement of valid Fe and O values existing in each time period reduces the total number of valid events included by about 20%. In each bin of Fe/O and A_c we have shaded by the median value of the thermal velocity ratio for each event that lies in that bin range. For reference, we have overlaid magenta lines for typical values of the Fe/O ratio for coronal hole (fast) wind and quiet closed loop (slow) wind, taken from von

Steiger et al. (2000). Solar wind parcels with Fe/O > 0.12 lie above the dashed magenta line and are predominantly associated with origin quiet close loops. Solar wind with Fe/O < 0.081 lies below the solid magenta line and are predominantly associated with a coronal hole source. In Figure 2.6a, we see that the thermal velocity ratio of He^{2+} to H^+ is elevated at low values of collisional age and Fe/O ratios below about 0.04. On the other hand, at higher values of A_c and higher Fe/O ratio we see the thermal velocity ratios moving closer to unity or mass-proportional temperatures. We do not see a strong deviation from a decaying thermal velocity ratio with increasing A_c at any value of Fe/O ratio.

If we look at the same histogram for C^{6+} in Figure 2.6b, we observe trends very similar to those for He^{2+}. We see a monotonic decay from high thermal velocity ratios to low with increasing collisional age in all bands of Fe/O ratio. Furthermore, when we examine Figure 2.6c for O^{6+}, we find that the deviation from exponential decay noted in Figure 2.4 is present at all values of Fe/O. The values of the thermal velocity ratio are highest for lower Fe/O ratio events, but the systematic deviation from monotonic decay with increasing A_c appears at all Fe/O ratios. This suggests that this phenomenon is a feature present in the O^{6+} temperatures in all observed solar wind, irrespective of its coronal source.

2.4 Discussion

The most important findings in this work are: 1) Heavy ions are predominantly thermalized by protons which dominate by over two orders of magnitude during solar wind conditions, 2) Heavy ion temperatures relative to H^+ are well organized by collisional age, but some heavy ions (O^{6+}) do not show a monotonic decay with increasing collisional age indicating heliospheric heating, and 3) the collisional age behavior of any given heavy ion seems to be similar for solar wind parcels of all Fe/O values, irrespective of their coronal source.

By computing the Coulomb collisional coupling for each ion in the solar wind, we have verified that interactions with protons are the dominant source of thermalization for any given ion. This allowed us to define a simple two-species collisional age parameter in equation (6) and organize the SWICS measurements of ion thermal velocities in the solar wind accordingly. The thermal velocities of all heavy ions presented were well organized by their respective collisional ages. We find that He^{2+} and C^{6+}, which have the same m/q value, both display a monotonic decay in their thermal velocity ratio with protons at high collisional ages. What is intriguing is that O^{6+} does not display the same monotonic behavior with collisional age. Instead we see a noted deviation from decay at a collisional age of around 0.1, as shown in Figure 2.4.

The behavior of O^{6+} was not observed in at least two other reports of ion thermalization in the solar wind at 1 AU. The work of Kasper et al. (2008) shows the monotonic thermalization of He^{2+} only, which we have also shown does not display the deviation for monotonic decay seen for O^{6+}. The second report comes from Hefti et al. (1998), which did report on the temperature ratio of O^{6+} and H^+ ($T_{O^{6+}}/T_{H+}$) as a function of what is essentially collisional age. In that work they find that $T_{O^{6+}}/T_{H+}$ follows a smooth trend of monotonic decay toward equal temperatures in high collisional age solar wind. The data used in that work only spanned 100 days during a solar minimum, so there is a question of whether the trend we see in the SWICS data is the result of temporal changes in the solar wind. However, we have observed our deviation from simple decay in histograms of data over smaller time ranges (hundreds of days). The ordering of the kinetic measurements we report for ACE/SWICS have not been observed before for heavy ions in the solar wind.

With the observation of this deviation from monotonic decay in thermal velocity ratio for our O^{6+} measurement, we then ask if such an effect is due a superposition of solar wind from different source regions, such as fast and slow wind, streamer belt plasma, or transient material that was not removed by our filtering of periods with coronal mass ejections. The Fe/O ratio of a solar wind parcel is used as a proxy for its source region, with lower Fe/O corresponding to coronal hole associated wind, and higher Fe/O to wind from closed coronal loops which exhibit a FIP effect. We see in Figure 2.6c that the increase in the thermal velocity ratio between collisional ages of 10^{-2} to 10^{-1} is present in solar wind populations with a wide range of Fe/O ratios. This suggests that this effect is present in all types of solar wind, and is not solely due to a difference in source. That in turn implies that the mechanism is not a lower coronal one and instead affects the O^{6+} ions in the solar wind plasma parcel somewhere along its journey through the heliosphere to 1 AU.

We also comment on the general behavior of the thermal velocities that SWICS reports at low collisional ages. In particular, we note again that our reported $v_{th,He^{2+}}/v_{th,H^{+}}$ value is elevated compared to the findings of Kasper et al. (2008). Where a thermal velocity ratio of about 1.22 was common at low collisional age in Kasper et al. (2008), we observe values around 1.5. We have already discussed that the SWICS instrument may be better suited to measure hot tenuous plasma, such as that found in this collisional age range. In addition to that we note that the reported values are not entirely unreasonable in light of observations of the temperature ratio by the Fast Imaging Plasma Spectrometer (FIPS) instrument onboard the MErcury Surface, Space, ENvironment, GEochemistry, and Ranging (MESSENGER) spacecraft, which orbited the planet Mercury from March 2011 to April 2015 (Solomon et al. 2001). The FIPS instrument (Andrews et al. 2007) observed thermal velocity ratios of He^{2+} to H^{+} around 1.66 at a radial distance of about 0.3 to 0.5 AU (Gershman et al. 2012). Thus our observed thermal velocity ratios are within the bounds of previously observed values. Under the influence of Coulomb collisional thermalization alone, the temperature ratios between heavy ions and protons should decrease toward unity with increasing radial distance from the Sun.

2.5 Conclusions

We have presented the first comprehensive analysis of the effect of Coulomb collisions on thermalizing the heavy ions present in the solar wind. The Coulomb collisional thermalization rate between every heavy ion measured in the solar wind is calculated, and we find the interaction with protons is the dominant source of thermalization for heavy ions. After computing the collisional age of measured heavy ion populations from this interaction we investigated how a given heavy ion’s temperature ratio with protons depends on its collisional age. We find that the thermal velocity ratio of He^{2+} and C^{6+} to protons shows decay toward equal temperatures with increasing collisional age over the parameter range we observe. When the same analysis is performed for O^{6+} however, we find that there is a noted deviation from simple decay with increasing collisional age that has not been observed before. We suggest that this increase in $v_{th,O^{6+}}/v_{th,H^+}$ is slightly preferential to the component perpendicular to the magnetic field and occurs for all solar wind types. This implies the presence of a heating mechanism, in addition to Coulomb thermalization, which depends on an ion's mass and charge characteristics, and acts on the heavy ions in a given solar wind parcel, regardless of the source region for that parcel.

These results have important consequences for our understanding of ion heating in the solar corona and solar wind, as the thermalizing heavy ions are an additional energy source for the protons within the expanding solar wind. We have shown that protons are the dominant source of thermalization for heavy ions, and that heavy ions usually have temperatures greater than that of the protons. Thus, the Coulomb relaxation process will always act to increase the temperature of protons as they expand away from the Sun. Prior work has used the observed radial temperature profile of solar wind protons to solve for the level of local proton heating due to turbulent dissipation under the assumption that the only other process changing the proton temperature is the cooling effect of adiabatic expansion (Breech et al., 2009; Cranmer et al., 2009). Although we expect the proton heating from Coulomb thermalization to be relatively small, these studies should be updated to include this effect.

If a local process, such as turbulent dissipation, was the only mechanism creating unequal temperatures, then at most we would expect to see a trend between ion temperature ratios and the local dissipation and Coulomb collision rates. Instead we find that temperature ratios are well ordered by an approximation for the total elapsed collisional age of the plasma since it left the corona. Kasper et al. (2013) argued that the strong dependence of helium to hydrogen temperature ratios on collisional age suggests that a significant fraction of non-thermal ion heating occurred close to the Sun. The observed heavy ion to proton temperature ratios reported in this study, along with their dependence on collisional age for each species, further suggest that a significant, possible majority fraction, of non-thermal heating occurs closer to the Sun and not locally in the solar wind.

The departure of O^{6+} from a simple exponential curve suggests that there is more to this picture for some species. These results help explain high temperature ratios observed by MESSENGER and Helios, but are also valuable predictions of the conditions in the inner heliosphere that will be observed by the upcoming Solar Orbiter and Solar Probe Plus missions.

Chapter 3 -Constraining Solar Wind Heating Processes by kinetic properties of heavy ions

The text in this chapter was published in Tracy, P.J., et al. (2016), Phys. Rev. Lett., **116**, 255101. The abstract and introductory sections have been combined and edited for inclusion in this dissertation.

3.1 Introduction

We analyze the heavy ion components (A > 4 amu) in collisionally young solar wind plasma and show that there is a clear, stable dependence of temperature on mass, probably reflecting the conditions in the solar corona. We consider both linear and power law forms for the dependence and find that a simple linear fit of the form $T_i / T_p = (1.35 \pm .02) m_i / m_p$ describes the observations twice as well as the equivalent best fit power law of the form $T_i / T_p = (m_i / m_p)^{1.07 \pm .01}$. Most importantly we find that current model predictions based on turbulent transport and kinetic dissipation are in agreement with observed non-thermal heating in intermediate collisional age plasma for $m/q < 3.5$, but are not in quantitative or qualitative agreement with the lowest collisional age results. These dependencies provide new constraints on the physics of ion heating in multi-species plasmas, along with predictions to be tested by the upcoming Solar Probe Plus and Solar Orbiter missions to the near-Sun environment.

The primary question we aim to address here is: *What does the heating of heavy ions relative to protons, observed in the solar wind at 1 AU, tell us about solar wind heating mechanisms?* We consider multiple theories for solar wind heating and attempt to isolate signatures of heating that remain in the solar wind observed at 1 AU. This depends heavily on our calculations of the collisionality of the plasma observed at 1 AU. The alteration of the relative heavy ion temperatures by Coulomb collisional thermalization must be accounted for to accurately assess proposed heating theories. In section 3.2 the pertinent theories of solar wind heating are reviewed and put into the context of this work. A description of the analysis technique utilized is discussed in section 3.3, followed by a discussion of the results in section 3.4. Finally, the conclusions of the work and the broader implications of our findings are discussed in section 3.5.

3.2 Theories of solar wind heating

The solar corona has a temperature that far exceeds that of the photosphere and results in the acceleration of the coronal plasma into the supersonic and super-Alfvénic solar wind (Kuperus et al. 1981; Parker 1958). The physical processes responsible for this heating and acceleration have been the subject of experimental and theoretical study for more than half a century. Many proposed mechanisms require interactions between fluctuations and particles on short kinetic scales comparable to the gyroradii of the constituent species of the plasma. This is a particularly challenging plasma regime to observe and to model because it occurs at scales where fluid approximations break down and kinetic descriptions of the plasma are needed.

Several of the most promising theories that seek to explain ion heating in the corona and solar wind use the dissipation of fluctuations via wave-particle interactions on kinetic scales such as ion-cyclotron resonance (Isenberg & Vasquez 2009; Cranmer & van Ballegooijen 2012), stochastic heating by long wavelength kinetic Alfvén waves (Chandran et al. 2013), or the interaction of particles with localized structures such as current sheets or topological null-points emerging through turbulence (Osman et al. 2011; Osman et al. 2012; Greco et al. 2009). Theories that preferentially act on different species are motivated by the observed non-thermal nature of the near-corona (< several solar radii) from spectroscopy (Landi & Cranmer 2009), and the fact that temperatures of observed ion species and electrons are different when directly observed in interplanetary space by instruments on spacecraft (Newbury et al. 1998).

Multiple models have been reported to be qualitatively and even quantitatively consistent with in situ measurements of protons (H^+) and alpha particles (He^{2+}), which constitute over 99.9% of the particle density of the solar wind (Chandran et al. 2013; Kasper et al. 2013). Furthermore, alpha particles account for 20% or more of the internal energy in these measurements (McKenzie et al. 1995), causing them to have an important effect on the dispersion relations relevant for wave-particle interactions and complicating their use in evaluation of heating theories (Isenberg 1984). Heavy ions ($A > 4$ amu) can further constrain the physical mechanisms. With number densities several orders of magnitude lower than alpha particles, they are an excellent approximation to test particles, responding to wave-particle interactions throughout the inner heliosphere without causing significant changes to the expansion and acceleration of the solar wind itself (von Steiger & Zurbuchen 2006).

Extensive studies have demonstrated that the occurrence of non-thermal kinetic effects in the solar wind is strongly limited by the cumulative effects of Coulomb collisions occurring as the wind travels from the corona to interplanetary space (Kasper et al. 2013; Kasper et al. 2008, Maruca et al. 2013, Hefti et al. 1998, Tracy et al. 2015). The net effect of these heating and thermalization processes has been extensively studied with the alpha particle population in the solar wind (Kasper et al. 2008), and Coulomb collisional relaxation has recently been shown to also be important for the heavy ion populations (Tracy et al. 2015). By examining the temperature ratios of heavy ions relative to protons, organized by the collisional thermalization of the plasma, we can reveal several important features of the heavy ion heating present in the solar wind, and provide crucial constraints on the proposed heating theories in the solar wind. This is critical because the Coulomb collision frequency is a function of the charge and mass of the ions involved, and different levels of collisional relaxation could be misinterpreted as evidence of a particular charge or mass ordering of ion temperatures. Previous studies of heavy ion kinetics have not explicitly accounted for the effects of collisional thermalization in reports of trends in ion temperatures (von Steiger & Zurbuchen 2006).

Our methodology is to search for evidence that an asymptotic ordering of ion temperatures by mass and charge characteristics is achieved when we examine solar wind with decreasing levels of Coulomb thermalization. The initial relative temperature state between solar wind ion species is reflected in these plasma parcels with the lowest collisional thermalization (Kasper et al. 2013). Assuming negligible heating during their subsequent propagation to 1 AU and equal relative cooling due to similar adiabatic expansion effects, these parcels preserve the initial temperature ratios of the solar wind, created in some critical radial distance from the Sun. There has been observational evidence that all solar wind converges to a single non-thermal state after collisional effects are removed (Maruca et al. 2013), supporting the assertion that most preferential ion heating occurs near the Sun, followed by expansion and collisional relaxation.

3.3 Analysis technique

We use the techniques described in Tracy et al. (2015) to examine the kinetic behavior of heavy ions in the solar wind and relate it to the collisional age (Kasper et al. 2008) of each two-hour measurement interval of solar wind plasma made by ACE/SWICS at 1 AU. The second moment of the reduced velocity distribution function measured by the ACE/SWICS main and H/He channels (Tracy et al. 2015;Shearer et al. 2014) is used to estimate the thermal velocity of the heavy ions and protons, respectively. This work extends that analysis to the 11 most abundant heavy ions in the solar wind, which we select from over 70 different measured ions, chosen for the high signal to noise of the measured distribution functions. We require that at least 100 particles are measured for a given ion charge state within a two hour interval before we calculate our moments, preventing the inclusion of scarcer solar wind ions in this study. In total, about 50,000 two hour intervals collected by ACE between 1998-2011 form the basis of this study. A critical aspect of this analysis is the use of a statistical inversion procedure to account for the fact that these particle populations do not have sufficient count rates to warrant Gaussian errors and because most of the ion peaks partially overlap with other species. Previously published results (von Steiger et al. 2000; Wimmer-Schweingruber 1998) are based on simplifying assumptions that are not generally justifiable for this analysis (Shearer et al. 2014). One must also note that the calculation of the second moment used in this work is a moment of the entire distribution, which will include suprathermal tails and other features. Filtering these tails out of the moments can result in thermal velocities up to 10-15% smaller than the full moment method, in some cases.

3.4 Ordering of heavy ion temperatures by mass and charge

In Figure 3.1 we show the median value of $v_{th,i}/v_{th,p}$, the ratio of the most probable thermal speed of each species to the proton thermal speed, as a function of collisional age A_C. The specifics of A_C are defined in (Kasper et al. 2008) and involve calculating the timescale for Coulomb thermalization between each species and protons compared to the time it takes for the solar wind to reach 1 AU, assuming constant speed and collision frequencies. It is an approximation, but has been shown to order the data well (Kasper et al. 2008; Tracy et al. 2015). Note that A_C must be calculated separately for each of the heavy ion species analyzed. Each heavy ion curve is only shown over the extent in A_C where it had at least 100 valid measurements at each A_C bin (Tracy et al. 2015). For most points shown in this figure far more than 100 points are included in the calculations.

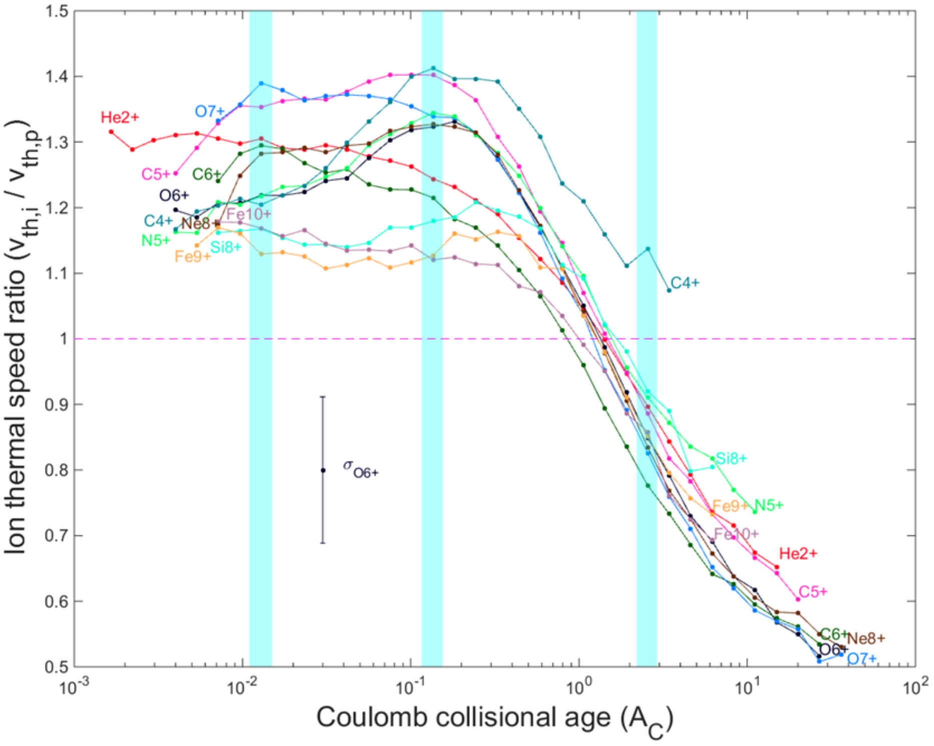

Figure 3.1: The median value of ion thermal speed ratio $v_{th,i}/v_{th,p}$ as a function of collisional age, A_C, for several heavy ions measured in the solar wind. The median absolute deviation is shown as errorbars for O6+ and is representative of the variability of the data for the other ions. Subintervals over specified collisional age ranges used in subsequent analysis are highlighted in blue.

The typical median absolute deviation (MAD) is shown for O^{6+} ($\sigma_{O^{6+}}$). This value can be fairly large relative to the separation between the ion curves, and is representative of the MAD seen for other ion species. A large variety of physical processes apart from collisional relaxation, governed by factors like differential streaming or plasma beta (Chandran et al. 2013; Kasper et al. 2013), drive the observed variability in the solar wind. With the current data set we cannot accurately filter for these other processes whose contributions result in a MAD that is an overestimate of the actual measurement uncertainty. Note that the uncertainty in the median value $\left(\frac{\sigma_{O^{6+}}}{\sqrt{N}}\right)$ is small relative to the separation between ion curves, with the uncertainty bars being less than the width of the points shown on each curve. The physically relevant measurement uncertainty is somewhere between these extremes. The clear overall trend in the observations is the highly unequal and elevated heavy ion thermal velocities at low A_C, gradually decaying towards thermal equilibrium with protons as A_C increases.

It is interesting that some heavy ions do not show a simple monotonic exponential decay toward equal temperature with protons as collisional age increases as would be expected from simple Coulomb relaxation. In particular, for heavy ions with m/q around 3 amu/e, e.g. O^{6+}, we see a distinct enhancement to higher thermal velocity ratios around $A_C = 0.1$ before the eventual decay toward thermal equilibrium. This figure verifies that heavy ion temperatures in the solar wind are strongly affected by Coulomb collisional thermalization, even if that alone cannot explain the trend of $v_{th,i}/v_{th,p}$ with A_C for all heavy ions.

Figure 3.2 is presented in the same format as Figure 1, except we show the temperature ratio, T_i/T_p, of heavy ions to protons. At the lowest collisional ages heavy ions are far from thermal equilibrium, and Coulomb collisional thermalization has a large effect on decreasing these temperature ratios toward unity. Note that there are very few measurements of unity values for T_i/T_p in the SWICS data set. This appears to be in contrast to other data sets at 1 AU (Kasper et al. 2008), which observe a significant number of events with alphas and protons at equal temperatures. It is possible that

SWICS cannot resolve equal temperatures due to its energy resolution Tracy et al. 2015), or differences in how temperatures are calculated, since prior studies have shown that differences in algorithms can lead to errors in temperature (Kasper et al. 2006). In any case, this is an issue at high collisional age (high A_C) and does not affect the primary conclusions of this work, which is behavior at small A_C. However, the mean values of the ratios at large A_C are useful indicators of the approximate error of these temperature ratio measurements if they indeed should be approaching unity.

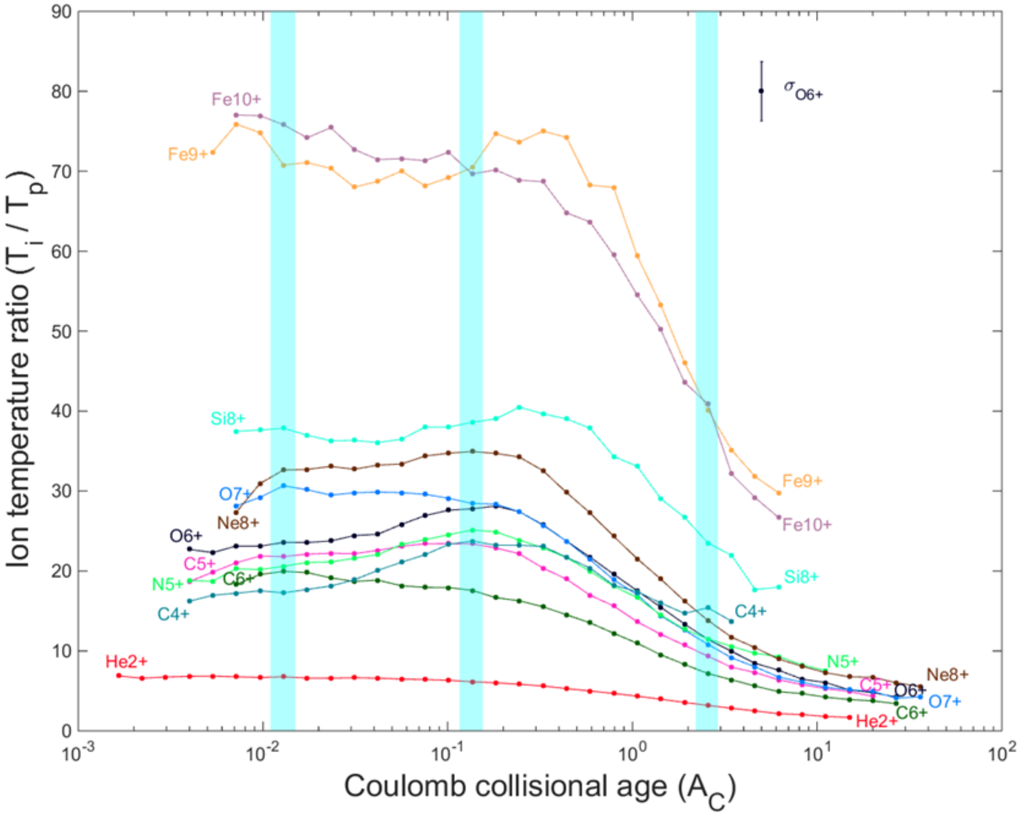

Figure 3.2: The median value of T_i/T_p as a function of collisional age, A_C, for several heavy ions measured in the solar wind. The median absolute deviation is shown as errorbars for O^{6+} and is representative of the variability of that data for the other ions. Subintervals are highlighted as in Figure 3.1.

As Coulomb thermalization has such a large effect on the observed heavy ion kinetics, we must look at Figure 3.1 and Figure 3.2 at different values of A_C to understand the evolution of trends in heavy ion temperatures. Three intervals of A_C are highlighted in blue in the previous figures and are examined in Figure 3.3. In Figure 3.3a we display the median value of the temperature ratio between heavy ions and protons at several values of A_C, ordered by the mass of the heavy ion. The specific A_C ranges are indicated in the legend, and the black line is a reference curve for strictly mass proportional temperatures. For both the lowest and the intermediate collisional age ranges a strong organization of the heavy ion temperatures by their mass is clear.

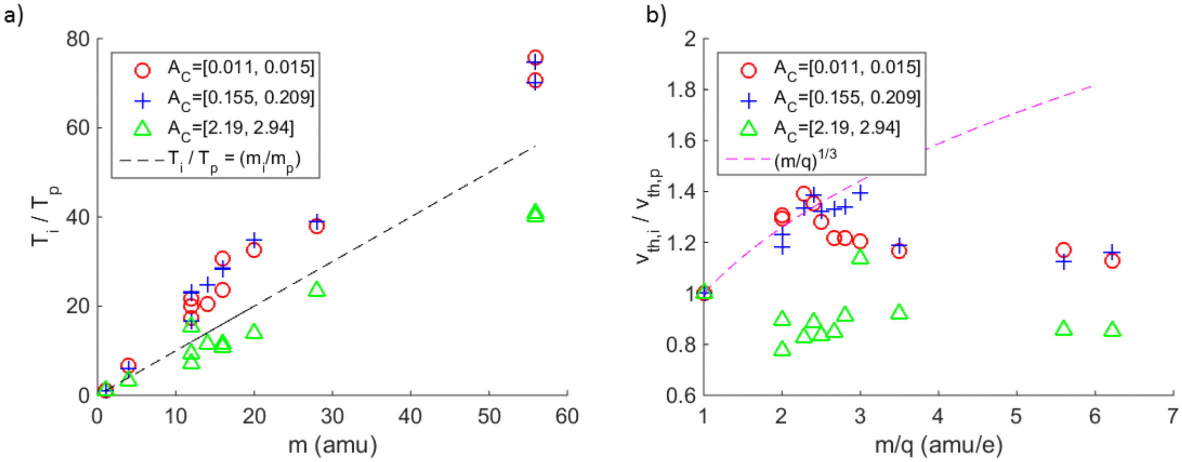

Figure 3.3: In a) the ratio T_i/T_p is plotted vs the mass of heavy ions, for plasma with collisional age ranges indicated in the plot legend. In b), the ratio $v_{th,i}/v_{th,p}$ is plotted against the mass per charge ratio of ion i, for the same collisional age ranges as in a). The ions included are He^{2+}, $O^{6\text{-}7+}$, $C^{4\text{-}6+}$, N^{5+}, Ne^{8+}, Si^{8+}, and $Fe^{9\text{-}10+}$. The MAD values for the data points shown are the same as those in Figure 3.1 and Figure 3.2 for $v_{th,i}/v_{th,p}$ and T_i/T_p, respectively.

Examining the same collisional age ranges, we look at the thermal velocity ratio between the heavy ions and protons in Figure 3.3b. The thermal velocity ratio effectively divides out the mass dependence shown in Figure 3.3a, revealing additional orderings in the observed plasma heating. The thermal velocity ratio vs *m/*q value of the heavy ions appears to show an inverse relation at the lowest A_C, but a positive correlation for a subset of the intermediate A_C group. This is particularly interesting as most wave heating theories predict that this ratio should increase with increasing *m/*q values. We have plotted one such prediction from Chandran et al. (2013) for how the thermal velocity ratio scales with *m/q* to show the discrepancy. The lowest A_C range does not well match the prediction, but the intermediate A_C range agrees well for $m/q < 3.5$. The fact that the data points of the intermediate A_C group lie below the predicted curve for m/q<3.5 is likely a result of the marginal relaxation implied by their collisional age. However, if one were to just focus on the He^{2+} (m/q=2) measurements it would appear that both the low A_C and intermediate A_C ranges agree with the predicted curve. It must be noted that this prediction is only valid for low beta plasmas, and we have not filtered our data to meet this requirement, as we don't know what the value of plasma beta was in the outer corona where these temperature ratios presumably were set.

The importance of looking at low collisional age plasmas is made apparent in Figure 3.3, where we see a significant alteration of the trends present from Figure 3.3a and Figure 3.3b for the highest collisional age shown (triangles). The mass proportionality in Figure 3.3a is much diminished and the thermal velocity organization in Figure 3.3b has completely disappeared for the high A_C range. In Figure 3.4 we present the recovered parameters for a linear fit to the T_i/T_p vs m curve at each collisional age in our data set (three of which are displayed in Figure 3a). In Figure 3.4, we see that in the lowest collisional age wind, the proportionality factor between temperature ratio and mass ratio is about 1.35±.02. We also performed a power law fit (not shown), which yields an exponent of 1.07±.01 at the lowest collisional age values.

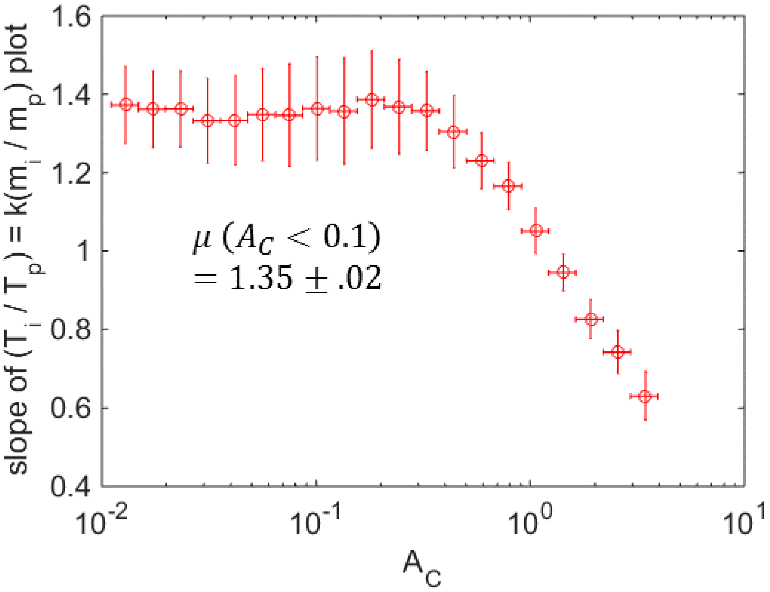

Figure 3.4: The slope of the linear fit to the T_i/T_p vs m curves at all collisional ages is shown, along with the 95% confidence interval of the recovered slope as a vertical error bar, and the histogram bin width over A_C as the horizontal error bar. The uncertainty weighted average and uncertainty in that average for all collisional age bins less than 0.1 is also inset on the figure.

Both the linear and power law fit suggest that the temperature dependence on mass in collisionless solar wind has a proportionality factor greater than unity. By visual inspection we cannot readily distinguish whether linear or power-law models better describe our data, but we can compare the reduced χ^2 values for the two models. The reduced χ^2 values for the lower collisional age range vary from 0.4-0.6 for the linear fit and from 0.9 to 1.2 for the power law fit, indicating that the linear fit does twice as well reproducing the temperatures than the power law. As we have conservatively overestimated the error with the MAD, we expect the reduced χ^2 values for a model consistent with observations to be below unity. The coefficient of determination, R^2, of the fits also shows that the linear fit is superior at low collisional ages, but that both fits show a decreasing R^2 value with increasing collisional age. This shows that for either of the fits to the ion temperatures, the fit works best at low collisional ages.

3.5 Implications for astrophysical plasmas

The thermal properties of heavy ions in the solar wind, comprehensively presented in this paper for the first time as functions of Coulomb collisional age, mass, and mass per charge, provide important constraints on heating theories of coronal and solar wind plasma. The linear dependence of heavy ion temperatures on mass shows a distinct asymptote to 1.35±.02 in the absence of significant Coulomb collisions. This asymptotic value has not been reported before and we propose it is indicative of the typical coronaI mass dependence of ion temperatures, and is not necessarily produced by local heating in the solar wind in interplanetary space. The slope of the linear dependence is gradually decreased in more collisional solar wind. We suggest that prior studies of the ordering of ion temperatures in the solar wind that did not account for Coulomb relaxation were reporting a mix of the effects of non-thermal heating and Coulomb collisions. Not all heavy ions undergo a simple monotonic and exponential decay toward equal temperatures with increasing A_C (e.g. O^{6+}, N^{5+}, C^{4+}). This deviation may be a valuable signature of additional heating occurring between the corona and interplanetary space, or reflect the presence of two solar wind populations with different asymptotic values at low A_C.

Of equal interest is that we show for the first time the ordering of heavy ion thermal velocity ratios by *m/q*, accounting for collisional effects. We find that heavy ion thermal velocities do not increase with *m/q* in low A_C wind, in disagreement with several heating theories for the solar wind. The ion cyclotron resonance (Kasper et al. 2013) and stochastic heating by low frequency turbulence (Chandran et al. 2013) should both have a larger impact on ions with larger *m/q* values. However, for intermediate A_C, which coincides with the deviation from simple exponential decay in Figure 3.1-Figure 3.2, the heavy ion thermal velocities agree fairly well with their predicted *m/q* dependence for $m/q<3.5$ (Chandran et al. 2013). It is intriguing that the highest m/q ions show no trend with m/q for any collisional age. It is crucial to note that if one were to just look at the He^{2+} ($m/q=2$) population relative to the protons in Figure 3.3b, it would appear that the heating of He^{2+} is in rough agreement with the *m/q* dependence predicted by Chandran et al. (2013) for both the low and intermediate A_C ranges. This emphasizes the need to examine heavy ions, which can act as test particles in the solar wind and may reveal different aspects of the heating mechanisms present.

Solar Probe Plus, a spacecraft that will traverse from 1 AU to 9.86 solar radii from the Sun will be able to directly observe the evolution of the solar wind as it propagates to 1 AU. Solar Probe will measure the non-thermal properties of a limited set of ions during the entire orbit (Kasper et al. 2015), perhaps comparable to the data reported by Gershman et al. (2012). The upcoming Solar Orbiter mission will carry an instrument allowing independent mass and charge measurements of heavy ions as presented here, but it will not venture nearly as close to the Sun, ranging 0.29-1.4 AU. Combining heavy ion plasma measurements at 1 AU with these upcoming missions should allow significant progress in understanding heavy ion thermalization and plasma heating in the solar wind.

The results discussed here also have important consequences for the understanding of other astrophysical plasmas (Safi-Harb et al. 2000; Romero et al. 2010). Many remote diagnostics of the thermal state of energetic plasma such as supernovae remnants and accretion disks rely on x-ray spectroscopy of trace ions such as oxygen and iron. As we have demonstrated, in the absence of strong Coulomb collisions on the dynamical scale of the shock or accretion flow, these trace ions may have significantly different plasma properties than the protons, which carry the momentum and most of the energy of the plasma. It is instructive to note for our Sun that –despite having a metallicity of approximately 2% (von Steiger & Zurbuchen 2016) – heavy ions carry approximately 4% of the internal energy and 3% of the momentum of the solar wind to be added to 20% of energy and momentum for alphas. In the near-solar environment, if observations such as Kohl et al. (1998) are correct, these numbers might be as high as 14% of the internal energy and 4% of momentum for the heavy ions.

Chapter 4 – Identification of New Ions in Mercury's Space Environment

4.1 Introduction

The focus of this investigation is the characterization of new ion species at Mercury using the Fast Imaging Plasma Spectrometer. Abundances of these ions have important implications for surface desorption processes active at Mercury. These processes determine the connection between the surface abundances observed at Mercury and the abundances in the exosphere. Many of these species do not have emission lines in the MESSENGER UVVS spectral range, and therefore FIPS measurements present the only way to update current upper limits.

The guiding science question we aim to answer here is: *Can we identify new components of Mercury's exosphere by measuring the ionized populations therein?* The answer to this question requires a careful analysis in the measurement space of the FIPS instrument. In section 4.2 a reliable model to predict what measurements of these scarce ions will look like in the context of the FIPS instrument is created. In section 4.3 a statistically robust way to separate contributions from different ion species that overlap in the FIPS measurement space is created and characterized. Finally, in section 4.4 a summary of the initial recovery of new heavy ions species in Mercury's exosphere is presented.

4.2 Ion Recovery Methodology

4.2.1 Forward modeling

The identification of ion species with the FIPS instrument stems from the base measurements of the Energy per Charge (E/q) and Time-of-Flight (TOF) of incident ions. A given ion species will occupy a specific region of this E/q and TOF parameter space, which is referred to as that ion's track. Creating a forward model to predict where a given ion will fall in this E/q vs. TOF space requires a detailed model for energy straggling through the FIPS carbon foil and the ion motion through the instrument's TOF section. To model the carbon foil energy straggling we make use of the TRansport of Ions in Matter (TRIM) software (Ziegler et al. 2010). A basic kinematics based model of a species motion through the TOF section of the FIPS instrument is also developed. For more extensive details regarding these models the reader is referred to Appendix 2.3. Of particular importance in this forward modeling is an estimate for the TOF characteristics of prominent noise (or dark count) sources for the FIPS instrument. A detailed discussion of the selection of a representative noise TOF model can also be found in Appendix 2.3. The net result of these forward models is a prediction (at every E/q step) for the TOF distribution of every ion species observed by FIPS.

4.2.2 Data Accumulation

The E/q and TOF data collected by the FIPS instrument can be analyzed by making use of these predicted TOF distributions. For the ion identification investigation pursued in this work, we will make use of two relatively large data accumulations from the FIPS flight mission. This allows our models to be applied to a statistically significant set of measurements and enables the separation of the ion counts observed into their most probable ion sources. The first measurement period occurred near the end of the MESSENGER mission, and corresponds to a time when the post acceleration voltage (PAHV) was set to -13 kV, its highest setting of the mission. This larger PAHV should reduce the effects of energy straggling as the ions encounter the carbon foil and create greater separation between ion tracks in the E/q vs TOF measurement space. The time range of the first period is 12-Mar-2015 02:00:00 to 30-Apr-2015 17:30:00, and will be referred to as the "-13 kV period". The second period is more representative of the state of the FIPS instrument throughout its nominal mission, with the PAHV set to -10.5 kV.

A time period as close as possible to the -13 kV period was chosen to minimize time dependent behaviors of the instrument between the two intervals. This "-10.5 kV period" ranges from 1-Jan-2015 00:00:00 to 23-Feb-2015 23:59:59. For both time periods, only intervals when MESSENGER was inside the magnetopause were included.

4.2.3 Maximum Likelihood Count Assignment

With the data accumulations defined, the predicted TOF distributions can be used to separate the FIPS E/q and TOF measurements into their most likely ion sources. The basis of the separation model we use is the Maximum Likelihood Count Assignment (MLCA) scheme as implemented in Shearer et al. (2014). In that work the counts attributable to each species measured by the ACE/SWICS instrument were recovered according to the probability distributions of each ion in the measurement space of the instrument. The only difference between the recovery method in that work was that the probability distributions were two dimensional as SWICS measures the total energy and TOF of incident ions at each E/q step, whereas FIPS only measured the TOF of each ion at each E/q step.

The end product of the MLCA scheme is a unique estimate of the number of counts attributable to each ion's probability distribution function in TOF space, at each E/q step of FIPS. An iterative scheme can be used to determine this unique solution. In this study we will separate the contributions of 13 prominent ion species in Mercury's space environment to the E/q versus TOF measurements recorded by FIPS. These ion species are H^+, He^+, He^{2+}, O^+, Ne^+, Na^+, Mg^+, Al^+, Si^+, S^+, Ar^+, Ca^+, and K^+.

Let $\boldsymbol{c}$ be a column vector of the number of counts attributable to each species, s, for a given energy per charge step, i. Thus there is one column vector of the counts for each ion species recovered at each E/q step. The following recursive relation yields a sequence of vectors, $\boldsymbol{c}^{(k)}$, that converge to the Poisson maximum likelihood estimate for $\boldsymbol{c}$ at a given E/q step.

$$c_s^{(k+1)} = \sum_{b=1}^{n_{bin}} P_{bs} c_s^{(k)} M_b / \left(\boldsymbol{P}\boldsymbol{c}^{(k)}\right)_b \tag{4.1}$$

In this expression, b, is the index over the n_{bin} TOF bins, s is the index over species, and k indicates the current iteration of the recursive scheme. P_{bs} is a 1024 x 13 matrix (1024 TOF bins by 13 ion species) with the probability mass distribution of each ion in each column. There is a different P_{bs} matrix for each E/q step. The observed TOF distribution is given by $M_b$where, again, each E/q step will have a different M_b. In this formulation it is important that each column of P_{bs} is normalized to sum to one. A more efficient, but more complex to implement, technique that utilizes interior point methods from convex optimization theory is also discussed in Shearer et al. (2014). For the analysis utilized in this work, the recursive scheme is used and convergence is defined as when the sum of the squared deviations of $\boldsymbol{c}^{(k)}$ between consecutive iterations differs by less than 10^{-5}.

An example of this MLCA recovery scheme applied to an inflight measurement of the FIPS instrument for the -13 kV period can be seen in Figure 4.1. Here the raw TOF distribution (black circles) is broken up into the most likely contributions from ions and noise sources of the FIPS instrument. The ptail, FE, and HE legend entries correspond to proton tail, Field Emission and Harp Emission noise distributions, respectively. These distributions are chosen to represent the contribution of noise sources to the observed TOF distributions, based on the work of Gershman et al. (2013a) and Gilbert et al. (2014). The remaining legend entries are the recovered contributions of each ions species to the observed TOF distribution.

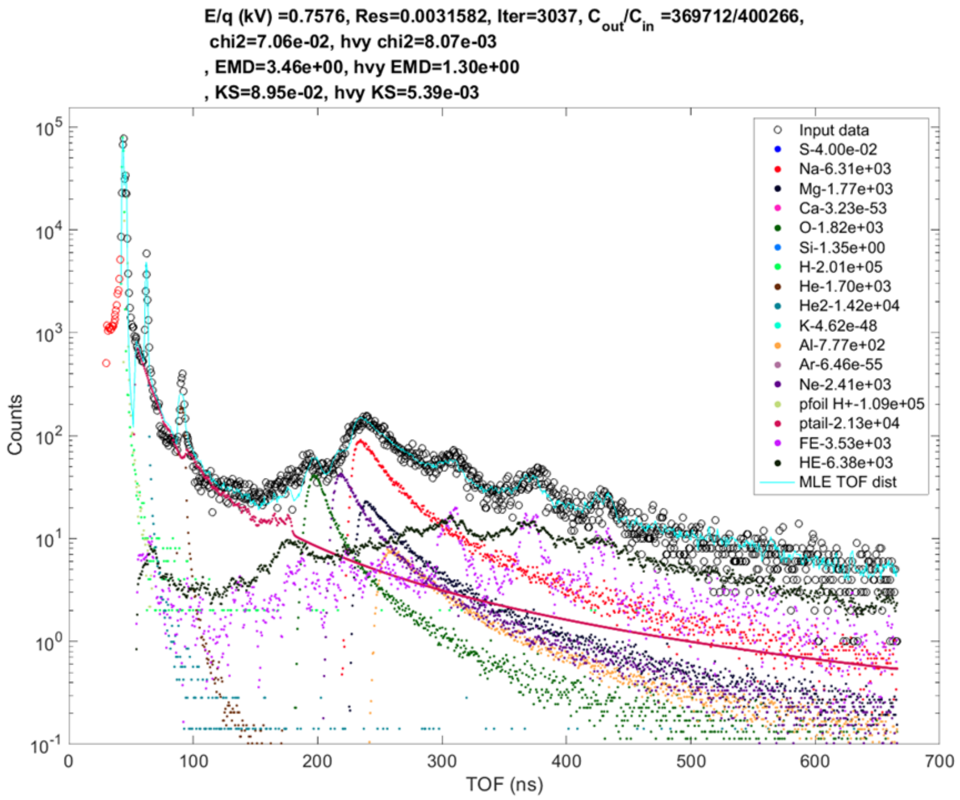

Figure 4.1 Example of the MLE recovery from a real in flight TOF distribution collected by FIPS. The measured TOF distribution (black circles) corresponds to an incident E/q of 0.7576 kV, and a PAHV of -13 kV. The red circles indicate points in the measured TOF distribution that were not assigned to any ion (no valid probability distributions in those TOF bins). The legend entries of ptail, FE, HE indicate noise distributions input into the MLCA model. All other colored dots in legend are ions recovered via the MLCA scheme. The cyan line indicates the sum of all the recovered distributions, for comparison with the measured TOF distribution.

One potentially misleading feature of Figure 4.1 is that a TOF distribution of the recovered ion species is shown. From (4.1), it is clear that the TOF dimension is summed over during the recovery process, making it impossible to recover TOF resolved ions. The displayed distributions result from simply scaling the probability distribution of an ion species by the number of recovered counts. This is valid in the high count limit, but for sufficiently low counts, the actual TOF distribution will be some random sampling of the displayed distribution.

4.3 Measurement of planetary ions with FIPS

The MLCA method described in the previous section can be used to recover previously unquantified ions from the FIPS E/q vs. TOF measurement space. This represents a substantial improvement in the ion identification capabilities of the FIPS instrument. The ions that benefit most from this treatment are those whose tracks were overlapped and could not be simply separated by a bounding curve in the E/q vs TOF space. This recovery is performed for both the -10.5 kV and -13 kV PAHV periods, whose time intervals were discussed in Section 4.2. Within these periods, only times when the MESSENGER spacecraft was within the magnetopause of the Hermean magnetosphere were included.

Utilizing the MLCA method on these time intervals results in a recovery of a count distribution versus E/q for each ion species included in the MLCA framework. These count distributions are used to calculate the observed phase space density (PSD) using the methods described in Appendix 2.1. With these PSD distributions recovered for each ion, the density can then be computed, with limitations dependent on the ion distribution (Gershman et al. 2013b). The recovered PSD distributions for the -10.5 kV and -13 kV PAHV periods are shown in Figure 4.2 and Figure 4.3, respectively.

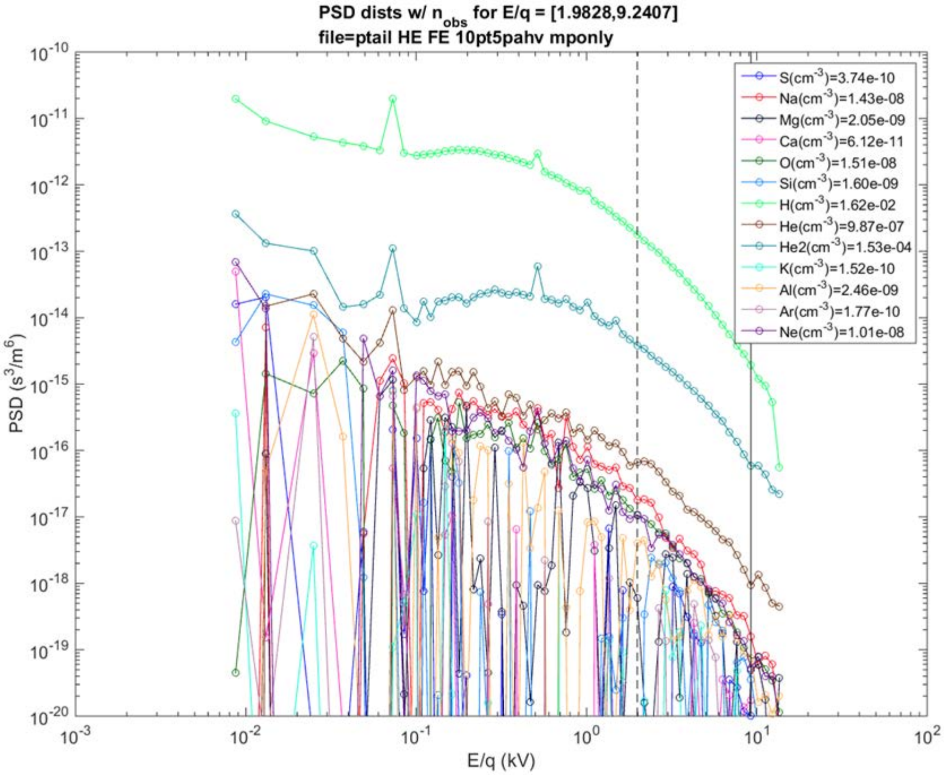

Figure 4.2 The recovered phase space density (PSD) distributions for the ion species input to the MLE algorithm for the -10.5 kV PAHV time period. The E/q region which seems to show the cleanest recovered profiles is indicated by two vertical black lines from about 2 kV to 9.2 kV (dashed is start and solid is end of region). The reported n_obs values for each ion in the plot legend are computed only over this range of E/q.

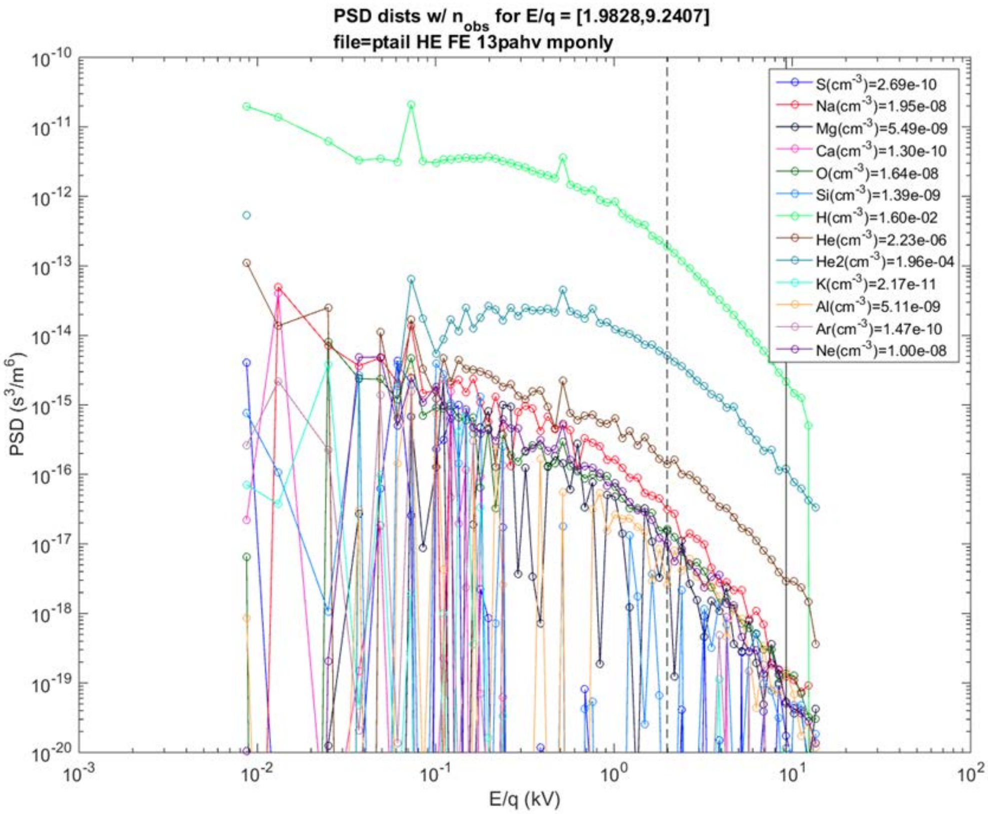

Figure 4.3 The recovered phase space density (PSD) distributions for the ion species input to the MLE algorithm for the -13 kV PAHV time period. The E/q region which seems to show the cleanest recovered profiles is indicated by two vertical black lines from about 2 kV to 9.2 kV (dashed is start and solid is end of region). The reported n_obs values for each ion in the plot legend are computed only over this range of E/q.

The most prominently recovered species in Figure 4.2 are H^+, He^{2+}, He^+, Na^+, and O^+, and these have been studied in previous works as well (e.g. Raines et al. 2013). The species included in our model that have not been reliably observed by FIPS before are Ne, Al, Mg, S, Si, Ar, K, and Ca. Based on the recovered distributions functions in Figure 4.2, it appears that some ions like Si, Al, or Mg have a partially recovered PSD distribution. From about 2 kV to 9 kV, these distributions behave quite consistently with the other distribution functions. Examining the distribution functions in Figure 4.3, we also see that Al, and maybe Mg are satisfactorily recovered in the range above about 2 kV. There is also some evidence of a recovered Si distribution in that same E/q range, but not as well captured as that of Al.

The improved recovery of ion species above 2 kV is likely due to the separation between the HE and FE TOF distributions and the TOF distribution of the ions of interest. At E/q steps below about 1-2 kV, the ion tracks for species such as Al, Mg, Si are intermingled with the TOF region where the noise signatures are most prominent. At higher E/q steps, the TOF distributions for these ions move to lower TOF values, while the TOF distributions for the noise signatures remain unchanged. As the TOF distributions for the noise signatures are the least well determined, they are the most difficult to separate from the signatures of other ion species using the MLCA scheme. Thus the farther removed an ion's track is from the predicted noise distributions, the more reliable its recovery. For more details on the E/q and TOF behavior of the modeled ion and noise tracks the reader is referred to Appendix 2.5.

Since a reasonable distribution for some ions is only recovered in the E/q range of 2-9 kV, the calculation of density for each ion species is also limited to that range in E/q. The intercomparison of these densities requires a large assumption that the PSD vs E/q distribution of all ions is similar. If this is not true then comparing these partial densities among different ion species is not a useful tool for specifying relative abundances.

With these assumptions we can compile the observed densities for each ion over the range of energies 2-9 kV. The observed density we compute is defined in (4.2) and is similar to the method of Raines et al. (2013) or Gershman et al. (2013b), except we are using different limits on the lower and upper velocity range of integration.

$$n_{obs} = \int_{v_{min}}^{v_{max}} f_{obs}(v) v^2 dv \tag{4.2}$$

Here f_{obs} is the observed distribution function integrated over the FIPS FOV as specified in Gershman et al. (2013b). With this expression we compute the observed density corresponding to the specific range of energies where we expect the noise source to have less influence. The results of this calculation are shown in Figure 4.4a, along with estimates of the uncertainty from Poisson counting statistics. For completeness the resultant densities from the integration over the full E/q range (about 0.1 to 10 kV) used in prior FIPS studies are included as well in Figure 4.4b (see Gershman et al. 2013b).

The densities recovered for the -10.5 kV period are quite similar to those for the -13 kV period and are not included.

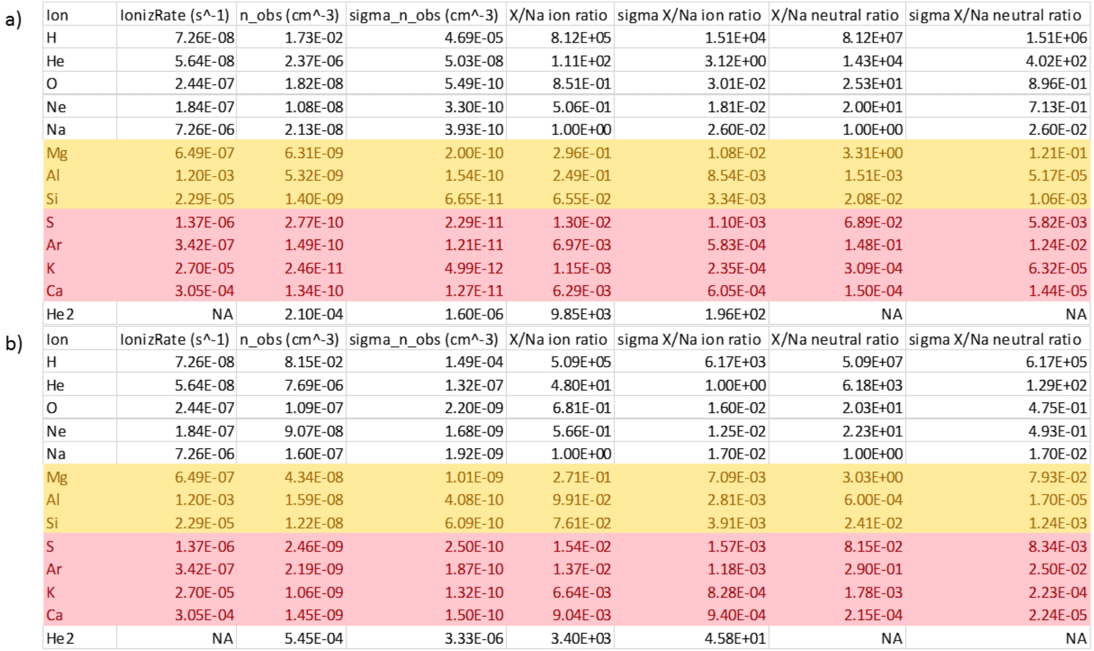

a)

Ion	IonizRate (s^-1)	n_obs (cm^-3)	sigma_n_obs (cm^-3)	X/Na ion ratio	sigma X/Na ion ratio	X/Na neutral ratio	sigma X/Na neutral ratio
H	7.26E-08	1.73E-02	4.69E-05	8.12E+05	1.51E+04	8.12E+07	1.51E+06
He	5.64E-08	2.37E-06	5.03E-08	1.11E+02	3.12E+00	1.43E+04	4.02E+02
O	2.44E-07	1.82E-08	5.49E-10	8.51E-01	3.01E-02	2.53E+01	8.96E-01
Ne	1.84E-07	1.08E-08	3.30E-10	5.06E-01	1.81E-02	2.00E+01	7.13E-01
Na	7.26E-06	2.13E-08	3.93E-10	1.00E+00	2.60E-02	1.00E+00	2.60E-02
Mg	6.49E-07	6.31E-09	2.00E-10	2.96E-01	1.08E-02	3.31E+00	1.21E-01
Al	1.20E-03	5.32E-09	1.54E-10	2.49E-01	8.54E-03	1.51E-03	5.17E-05
Si	2.29E-05	1.40E-09	6.65E-11	6.55E-02	3.34E-03	2.08E-02	1.06E-03
S	1.37E-06	2.77E-10	2.29E-11	1.30E-02	1.10E-03	6.89E-02	5.82E-03
Ar	3.42E-07	1.49E-10	1.21E-11	6.97E-03	5.83E-04	1.48E-01	1.24E-02
K	2.70E-05	2.46E-11	4.99E-12	1.15E-03	2.35E-04	3.09E-04	6.32E-05
Ca	3.05E-04	1.34E-10	1.27E-11	6.29E-03	6.05E-04	1.50E-04	1.44E-05
He2	NA	2.10E-04	1.60E-06	9.85E+03	1.96E+02	NA	NA

b)

Ion	IonizRate (s^-1)	n_obs (cm^-3)	sigma_n_obs (cm^-3)	X/Na ion ratio	sigma X/Na ion ratio	X/Na neutral ratio	sigma X/Na neutral ratio
H	7.26E-08	8.15E-02	1.49E-04	5.09E+05	6.17E+03	5.09E+07	6.17E+05
He	5.64E-08	7.69E-06	1.32E-07	4.80E+01	1.00E+00	6.18E+03	1.29E+02
O	2.44E-07	1.09E-07	2.20E-09	6.81E-01	1.60E-02	2.03E+01	4.75E-01
Ne	1.84E-07	9.07E-08	1.68E-09	5.66E-01	1.25E-02	2.23E+01	4.93E-01
Na	7.26E-06	1.60E-07	1.92E-09	1.00E+00	1.70E-02	1.00E+00	1.70E-02
Mg	6.49E-07	4.34E-08	1.01E-09	2.71E-01	7.09E-03	3.03E+00	7.93E-02
Al	1.20E-03	1.59E-08	4.08E-10	9.91E-02	2.81E-03	6.00E-04	1.70E-05
Si	2.29E-05	1.22E-08	6.09E-10	7.61E-02	3.91E-03	2.41E-02	1.24E-03
S	1.37E-06	2.46E-09	2.50E-10	1.54E-02	1.57E-03	8.15E-02	8.34E-03
Ar	3.42E-07	2.19E-09	1.87E-10	1.37E-02	1.18E-03	2.90E-01	2.50E-02
K	2.70E-05	1.06E-09	1.32E-10	6.64E-03	8.28E-04	1.78E-03	2.23E-04
Ca	3.05E-04	1.45E-09	1.50E-10	9.04E-03	9.40E-04	2.15E-04	2.24E-05
He2	NA	5.45E-04	3.33E-06	3.40E+03	4.58E+01	NA	NA

Figure 4.4 A summary table of the recovered ion densities to the -13 kV PAHV period. Recovered values for the E/q range of 2 kV – 9 kV and the E/q range of 0.1 kV to 9 kV are shown in a) and b) respectively. The format for both a) and b) are identical. The Ion name is indicated in column one, the photoionization rate for the ion is indicated in column two (from Huebner and Mukherjee 2015), the observed density in column three, the uncertainty in observed density (from Poisson counting statistics) in column four, the observed ion density ratio to sodium in column five, the uncertainty in this ratio in column six, the estimated neutral density ratio in column seven, and the uncertainty in the neutral ratio in eight. Value for ions whose recovered distribution functions are deemed untrustworthy are shaded in red, those whose distribution functions are intermediate in yellow, and those whose distribution functions are acceptable (over some range of E/q) are not shaded.

In addition to this ion density, the neutral abundances of the exosphere are also of interest. Therefore the estimated ionization rates of each species (Huebner and Mukherjee 2015) are used to compute an approximate neutral abundance of each species relative to Na. This calculation assumes that the observed ions are primarily created via photoionization, which may not be true for all constituents, especially those entering the magnetosphere as part of the solar wind (H^+ and He^{2+}). These neutral abundance ratios can be used to determine the relative efficacy of different desorption processes on Mercury's surface.

A rough comparison with surface abundance and column abundance estimates from Killen et al. (2007) reveals that our recovered He abundance is much higher than predicted. Furthermore, the recovered O neutral abundance is about 10 times higher than expected. However, our estimate for the Si/Na neutral ratio is only about a factor of three smaller than the predicted surface or column abundances. The value for Al/Na we recover is about an order of magnitude less than predicted in Killen et al. (2007). The recovered value for Ne/Na is within the range of variance of predictions. Recall that the values we report here are average densities over the portion of the orbital path of MESSENGER that lies within the planetary magnetosphere (see Figure 1.3 or Raines et al. 2013 for orbit details). Thus comparing to surface or column abundances exactly is not appropriate.

Moreover, our assumptions relating the observed neutral and ionized populations may require modification. Some surface desorption processes (e.g. ESD) can result in an ion being released from the surface. If not all the ions of a given species observed with FIPS are produced by photoionization, our current assumption would overestimate the neutral content for that species. The content for a given exospheric species could also be overestimated if the TOF signature of a species not included in the MLCA model is present in the FIPS data. For example, if a molecular species (i.e. H_2O, CH_4, etc…) passes through the carbon foil the current forward model would misassign counts from those species to one of the monoatomic species available to the MLCA scheme. To a lesser extent if the isotopes of the monoatomic species considered in our model are not representative of the isotopic makeup of species at Mercury, a similar misassignment could occur. Each of the processes outlined above could contribute to the misestimation of species' abundances in Mercury's exosphere and should be investigated moving forward.

With such future refinements in mind, we emphasize that these are the first reported measurements of the abundance for many of these ions by FIPS at Mercury. Such a measurement that would not be possible without the use of the statistical model employed here. These measurements of the neutral and ionized components of Mercury's exosphere are invaluable for constraining models of Mercury's exosphere and the surface desorption processes that contribute to it.

4.4 Summary and Conclusions

We have developed a robust statistical method to identify new ion signatures in the E/q vs TOF space of the FIPS instrument. This method is validated over a large time interval of FIPS data spanning several months, and average abundance ratios are recovered over this period. The most reliably recovered new ion appears to be Al, which we find to have an ion abundance ratio of about 25% relative to Na for energies above 2 keV. Assuming ion production primarily via photoionization for both species, this corresponds to a neutral abundance ratio of about 0.15% for Al/Na. With the uncertainties associated with the description of the noise sources in the data, the recovered values for these ions can be considered upper limits. In this light, upper limits are recovered for Ne, Mg, Al, Si, S, Ar, K, and Ca relative to Na.

This is the first time upper limits have been reported for these species using the FIPS instrument. These measurements offer important constraints to exospheric models and provide precedents for the neutral and ion instruments onboard the upcoming BepiColombo mission, scheduled to arrive at Mercury in late 2024 (Saito et al. 2010). Comparison of exospheric neutral ratios to surface abundances at Mercury is critical in quantifying the dominant desorption mechanisms at the planet’s surface.

4.4.1 Future Work

There is still much more that can be accomplished with this powerful new tool for FIPS analysis. The first step would be to improve the spatial resolution of the ion recoveries. This requires finding the balance between having a statistically significant number of counts to resolve overlapping ion peaks, while still dividing the magnetosphere into reasonably sized regions for analysis. A first attempt at this division might divide the magnetosphere into dayside, cusp, plasma sheet, and plasma lobe regions and look for significant differences in the ion recovery. Further attempts could focus on the different magnetospheric local time regions sampled by the MESSENGER orbit as Mercury orbits about the Sun. The abundances recovered from these techniques could further be compared to the measured surface composition at Mercury (Evans et al. 2012, Nittler et al. 2011). Enhancements in species relative to the surface compositional ratio would suggest preferential desorption and may further elucidate the dominant surface weathering processes.

Future refinement to the model itself is also possible. One example of this is to make use of the model for the total noise quantity in a measurement period predicted by Gershman et al. (2013a). Currently the MLCA method can assign any amount of counts to the noise distributions at its disposal. If a modification could allow the total amount of counts assigned to noise to be somehow fixed it may improve the separation of noise from real data. The better constrained the noise distribution the better real ions can be recovered via MLCA. Difficulties involved with current noise model implementation are detailed in Appendix 2.5.

Another refinement to the recovery method is to further explore the signatures of molecular species in the measurement space of FIPS. As discussed prior, this entails an examination of potential misassignment of different molecular species to the monoatomic species assumed in the current MLCA scheme. Similar investigations into whether the appropriate isotopic signatures are included in the forward model are also possible. Specific to the recovery of neutral species is a further investigation into whether all ions observed in the Mercury's exosphere are due to photoionization of a neutral population.

Furthermore, the MLCA recovery lacks an uncertainty estimate beyond the simple Poisson uncertainty. The sensitivity of the ion recovery to perturbations in the observed TOF distribution could be quantified through Monte Carlo simulations. This would yield a better quantification of the significance of the recovered ion abundances. Last, if laboratory measurements yield significant differences in the input TOF probability distributions used by the MLCA model this could significantly change the results of the recovery. There are some aspects of the TRIM model compared to flight data (Appendix 2.2) that suggest the energy losses from TRIM do not fully capture the losses seen in actual inflight observations. In particular there remains little verification of TRIM's validity for the heavier ions observed with FIPS.

Chapter 5 – Mercury's Foreshock Plasma Environment

5.1 Introduction

Observations of the foreshock populations at Mercury are presented for the first time utilizing measurements from the Fast Imaging Plasma Spectrometer (FIPS). The magnetosphere and foreshock system at Mercury exists in a unique parameter space, due to the planet's relatively weak magnetic dipole and the proximity of its orbit to the Sun. Foreshock populations have thus far been predominantly studied at the terrestrial foreshock, and therefore over a limited range of ambient solar wind and bow shock conditions. Mercury's small magnetosphere (about an order of magnitude smaller than Earth's), low Alfven Mach number shock, and more radial IMF are all factors that should dramatically influence the character of the foreshock.

The guiding science question is: *How effective are shock energization processes at the bow shock of a small planetary magnetosphere?* Are there dramatic differences in how the mechanisms postulated at Earth manifest themselves in this new regime? A detailed analysis of the foreshock populations present at Mercury is performed to answer this question. This involves the development of tools and methods to enable the analysis of these new populations given the capabilities of the FIPS instrument, discussed in Section 5.2. The nature of the decay of diffuse plasma populations with distance from the quasi-parallel bow shock is then investigated and quantified in Section 5.3. Finally, several energization mechanisms for observed plasma populations are investigated in Section 5.4. One result suggests that the observed energies of the FAB populations can be explained by Shock Drift Acceleration. For the diffuse populations, estimates of the IMF-bow shock connection times and the Fermi acceleration time scale suggest that a connection time limited diffusive shock acceleration is responsible for the behavior of the observed diffuse energy distributions.

5.2 Identification of Foreshock Populations

The identification of foreshock plasma populations at Mercury is made possible by the measurements of the Fast Imaging Plasma Spectrometer (FIPS). FIPS measured the mass per charge (m/q) and energy per charge (E/q) of incident ions with time of flight (TOF) mass spectrometry. A more in depth description of the FIPS instrument can be found in Section 1.3.2. Especially pertinent for the measurements in this work was the field of view of the FIPS instrument. The electrostatic analyzer of FIPS had an instantaneous field of view of about 1.4π sr and recorded the arrival direction of incident ions with an angular resolution of about 15 degrees. However, due to FIPS position on MESSENGER, its FOV was partially obstructed by the sunshade and other parts of the spacecraft. Accounting for these obstructions, the FOV of FIPS was approximately 1.15π sr (Gershman et al. 2013b). Understanding the viewing geometry of FIPS is essential in the proper identification of foreshock populations.

For the data presented here, FIPS was operating with 60 logarithmically spaced E/q steps with an integration time of 50 ms at each step and a total scanning time of about 10 seconds. Depending on the time range, the steps were either spaced from 100 eV/e to 13.7 keV/e, 46eV/e to 13.7 keV/e, or 8.5 eV/e to 13.7 keV/e as the lower E/q bound of the instrument was lowered first in March 2012, and then again in August of 2014. Unlike the work performed in previous chapters, this analysis will primarily focus on proton data measured by FIPS. Although FIPS has the ability to observe heavy ions, the small number that were observed in the foreshock region at Mercury did not permit a detailed analysis. Unless otherwise mentioned, all following analysis pertains entirely to proton measurements. For more details on FIPS operation and its capabilities see Andrews et al. (2007).

5.2.1 Field-Aligned Beams

The identification of FABs makes extensive use of the incident ion direction abilities of FIPS. In particular, the direction and angular distribution are critical in the identification of a given foreshock population. We begin with an example of a FAB population that occurred on 2012-09-19 at about 14:30:00. The multi-paneled time series of relevant FIPS and MAG measurements for this period is shown in Figure 5.1. An observation of a FAB population, indicated by vertical lines, occurred between 14:15:00 – 15:00:00 just upstream of a quasi-perpendicular bow shock. The quasi-perpendicular nature of the shock is revealed by the sharp increase in |B| as the bow shock is crossed and MESSENGER enters the magnetosheath at 15:03:00.

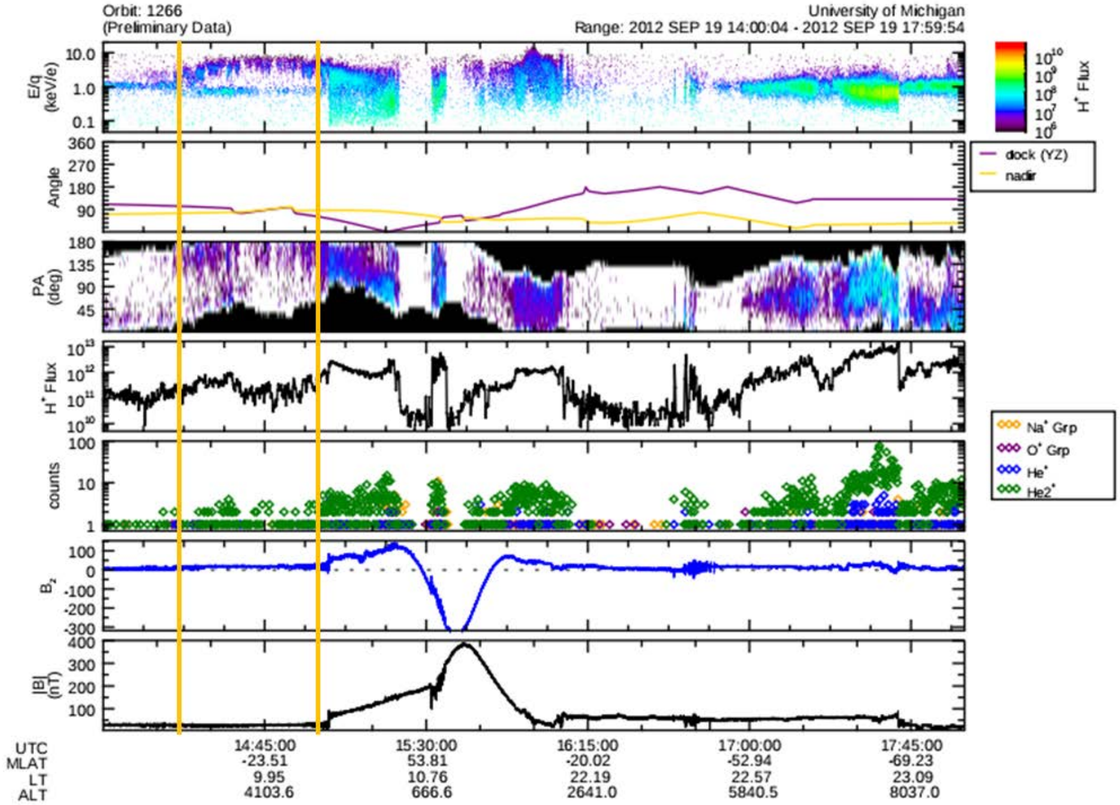

Figure 5.1: Energy spectrogram (top panel), Clock angle, i.e., the angle between the MSO y-axis and the FIPS boresight vector, projected into the x plane (second panel), Pitch Angle distribution (third panel), Integrated Proton Flux (fourth panel), Heavy Ion Counts (fifth panel), Z-Component of the Magnetic Field (normal to the Ecliptic in MSO Coordinates, sixth panel), Magnetic Field Magnitude (bottom panel), all as a time series of data measured over a single orbit of the MESSENGER spacecraft. The high energy particles roughly between 14:20 and 15:00 (vertical lines) are the observed FAB plasma population.

In the E/q spectrogram, two populations are clearly seen during the FAB event period, one at low E/q and one at higher E/q values. Noting that the lower E/q population is consistent with solar wind energies allows us to identify the higher E/q population as a FAB, but without the directional capabilities of FIPS it would be very difficult to verify this. In Figure 5.2a, the angular distribution (top panel) and energy-resolved pitch angle distribution (bottom panel) of the plasma measured by FIPS with E/q between 0.3 and 1 keV/e are plotted. In the top panel, the center of the Mollweide projection corresponds to plasma with an antisunward vector direction, plasma with a duskward velocity vector would fall on the “Dusk” label, and so on. Solar wind observed by FIPS should be abberated due to Mercury’s orbital motion about the Sun and indeed we see that the portion of the solar wind visible by FIPS was abberated in the duskward direction around the heat shield of the MESSENGER spacecraft (Gershman et al. 2012). The important point in Figure 5.2a is simply that the observed plasma has an antisunward velocity.

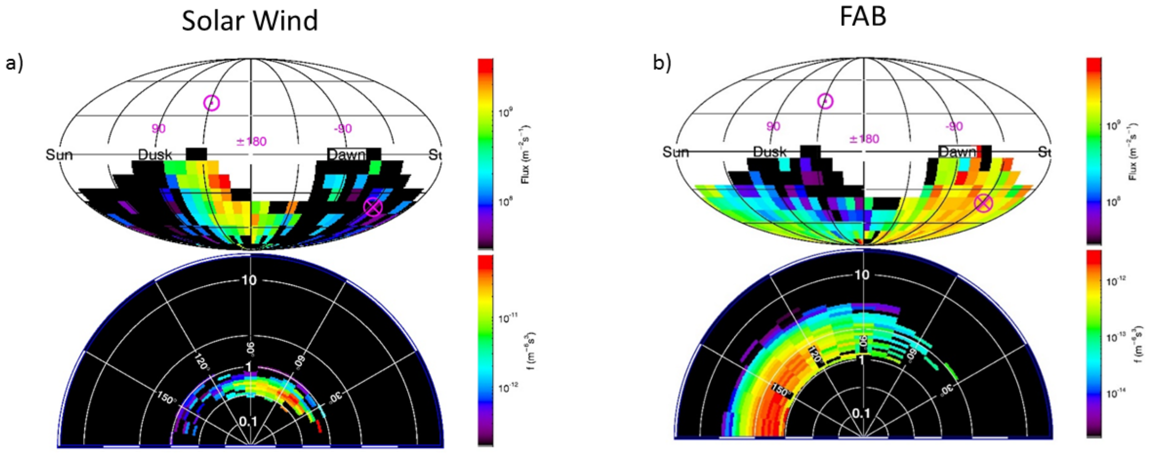

Figure 5.2: In a) the angular flux map (top) and energy-resolved pitch angle distribution (bottom) of the solar wind is shown over the time period Sept 19th, 2012, 14:25:00-15:00:00. The solar wind corresponds to an energy range of 0.3-1 keV (roughly 239-437 km/s). Also shown on the figure is the average vector magnetic field direction, the magenta circle with a dot is the +B direction, while the magenta circle with the X is the -B direction. In b) the same plots are shown for the Field-Aligned Beam population over the same time range. The FAB corresponds to an energy range of 1-5 keV (437-978 km/s).

In Figure 5.2b, we see an angular flux map and an energy resolved pitch angle distribution in the same format as Figure 5.2a, but for the higher E/q range of the FAB event, 1-5 keV/e. It is clear to see in the top panel that the observed ion flux was closely aligned with the anti-parallel magnetic field direction, and had a velocity vector that is below the ecliptic plane and between the dawnward and sunward directions. The bottom panel shows that plasma measured during this event had a pitch angle distribution that peaks between 150 and 180 degrees, and doesn’t extend much beyond 90 degrees. These observations of a beam of plasma roughly aligned with the magnetic field clearly match the characteristics for FABs observed at Earth.

The last step in the identification of this FAB is to quantify the moments of the observed distribution. As this FAB was a supersonic distribution, the techniques developed in Gershman et al. (2012) for solar wind observations by FIPS are directly applicable to the recovery of the moments. The only difference between the analysis in that work and the present analysis is that the core of the FAB distribution lies within the FOV of the FIPS instrument whereas the core of the supersonic solar wind distribution was obscured by the MESSENGER spacecraft's heat shield. With the core of the distribution in the FOV (Figure 5.2b), an accurate density for the FAB can be recovered.

The measured count distribution and phase space distribution for the FAB event are shown in Figure 5.3. In Figure 5.3, the top panel shows the count distribution for the solar wind which is shaded in green while that for the FAB is shaded in blue. Two peaks, clearly separated in velocity space, are observed. In the bottom panel, this count distribution is then converted to phase space density (Gershman et al. 2013b), where it is more clear that the FAB population had a much lower density than the typical ambient solar wind at Mercury (Slavin and Holzer 1981). For reference, the phase space density corresponding to a single observed count at each velocity bin of FIPS is shown with the dashed line. For the solar wind population, only the bulk velocity and thermal velocity can be reliably recovered (Gershman et al. 2012) and those recovered values are shown in the figure title. The recovered density, bulk velocity, and thermal velocity for the FAB event are also shown in the title.

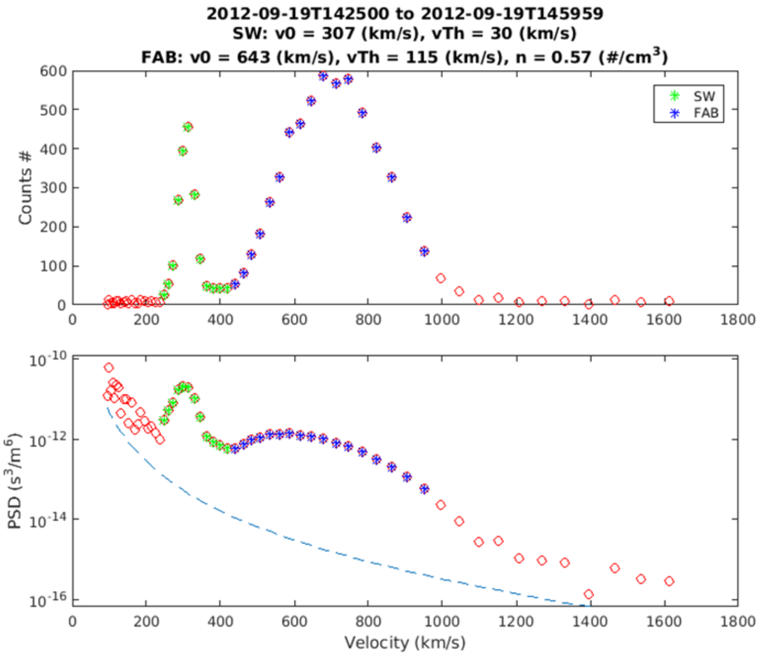

Figure 5.3: Top panel: Measured count distribution of protons. Green points indicate the lower energy solar wind filter, and blue points the higher energy FAB population. Bottom panel: the calculated phase space density distribution, with the same color scheme. The dashed line represents the "one-count" line in phase space. The recovered plasma parameters for the solar wind and FAB population are shown in the plot title.

The recovery scheme shown here is then implemented for the 15 best FAB populations identified so far with FIPS measurements. A summary of the recovered density, temperature and bulk velocity for these FAB populations is displayed in Figure 5.4.

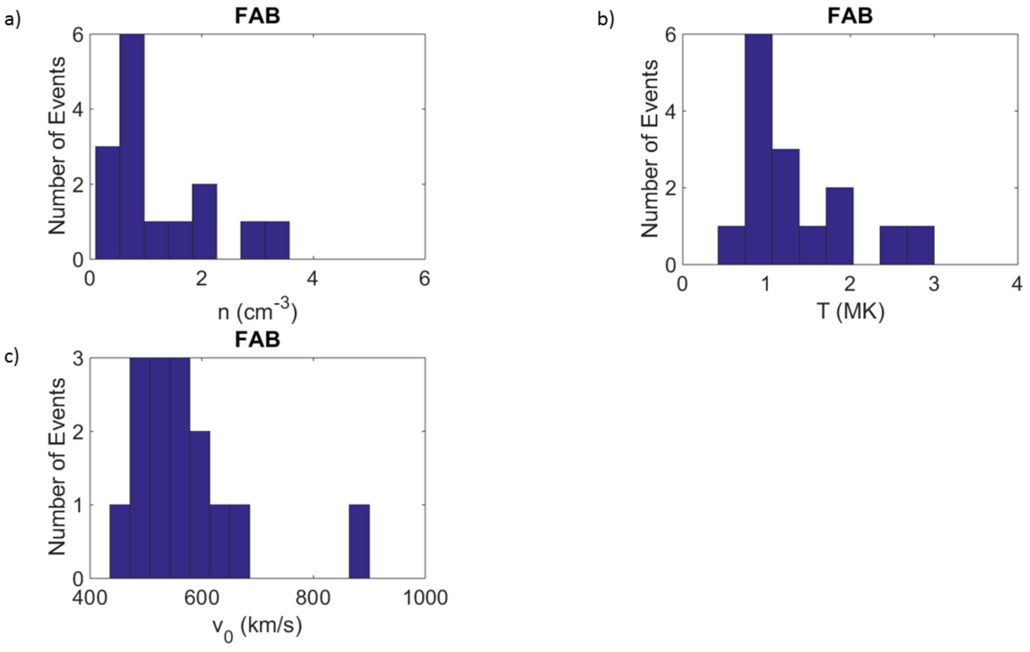

Figure 5.4: Summary histograms of the density (a) and temperature (b) and (c) bulk velocity for the 15 best FAB events observed by FIPS in Mercury's foreshock.

5.2.2 Diffuse Events

The accurate identification of diffuse foreshock populations also requires the full directional capabilities of the FIPS instrument. To illustrate the process, which has a large degree of overlap with the FAB identification process, we show the details of the identification of the diffuse event which occurred on Aug. 27th, 2013 from 07:10:00 to 08:20:00. In Figure 5.5 a detailed time series of the diffuse event is shown. The time duration of the diffuse event is indicated by the vertical bars. It is less obvious that two distinct populations are observed upstream of the bow shock than was the case for the FAB population. In this case the solar wind was seen as a horizontal stripe just below 1 keV/e, and the diffuse population extends from 1 keV/e up to about 10 keV/e. Examination of the outbound bow shock crossing indicates that a diffuse population was observed there as well.

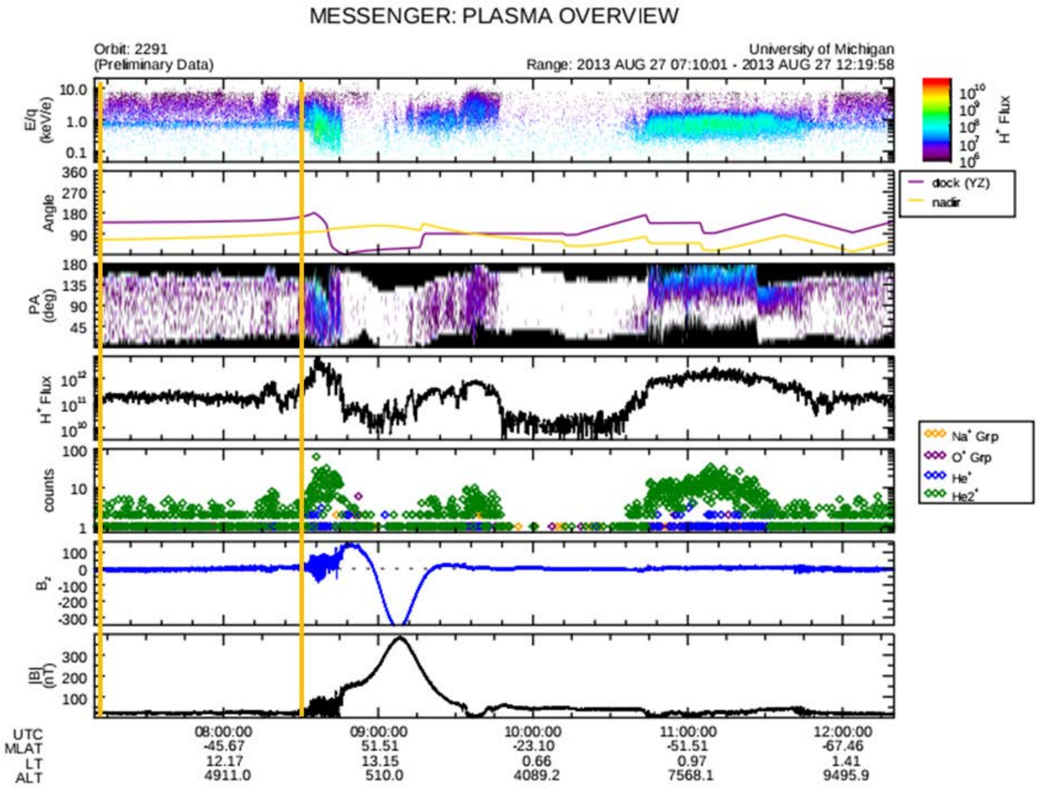

Figure 5.5: Energy spectrogram (top panel), Clock angle, i.e. the angle between the MSO y-direction and the FIPS boresight vector, projected into the x-plane (second panel), Pitch Angle distribution (third panel), Integrated Proton Flux (fourth panel), Heavy Ion Counts (fifth panel), Z-Component of the Magnetic Field (normal to the Ecliptic in MSO Coordinates, sixth panel), Magnetic Field Magnitude (bottom panel), all as a time series of data measured over a single orbit of the MESSENGER spacecraft. The high energy particles roughly between 07:20 and 08:30 (vertical lines) are the observed diffuse plasma population.

Just as for the FAB, confirmation of the diffuse population's existence relies on the angular distribution measurements of FIPS. In Figure 5.6 we show the angular flux maps and energy resolved pitch angle distributions for the event time period, as in Figure 5.2. The E/q range corresponding to the solar wind (0.2 – 0.8 keV/e) is shown in Figure 5.6a.

Again, one can see the portion of the duskward abberated solar wind distribution that made it past the heat shield and was observed by FIPS. There is also a small amount of a more isotropic distribution observed, which will be seen to be the lower E/q range of the diffuse population. In Figure 5.6b, the E/q range of 0.8-13 keV/e is shown, and it is clear that the observed distribution was almost isotropic in the regions of velocity space observable by FIPS. Examination of the bottom panel of Figure 5.6b, also shows a nearly uniform pitch angle distribution, with the highest and lowest pitch angles not observable by FIPS. The observed isotropy in these diffuse events makes them easy to distinguish from solar wind and matches the observations made in the Earth's foreshock.

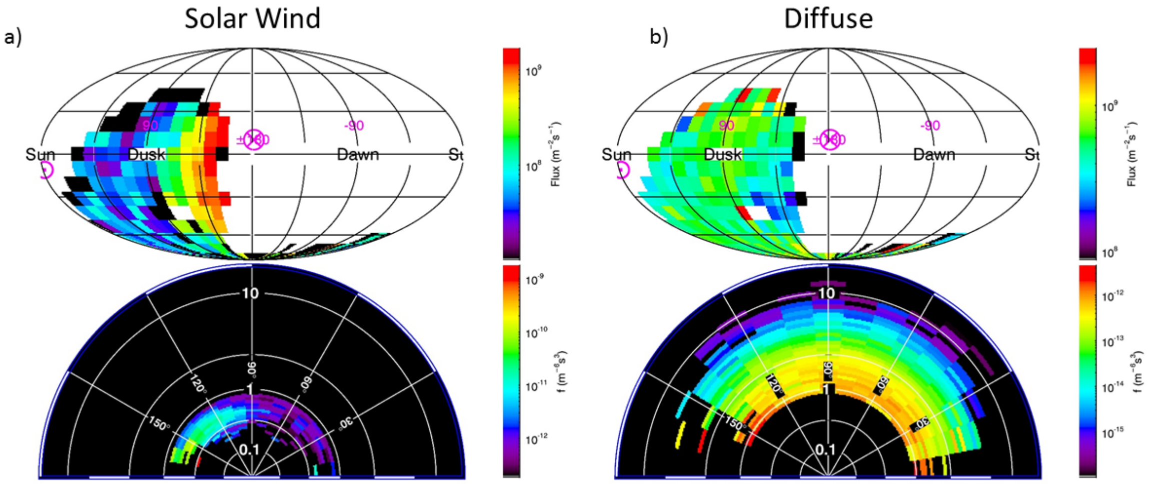

Figure 5.6: In a) the angular flux map (top) and energy-resolved pitch angle distribution (bottom) of the solar wind is shown over the time period Aug.27th, 2013, 07:10:01-08:19:57. The solar wind corresponds to an energy range of 0.2-0.8 keV (roughly 200-390 km/s). Also shown on the figure is the average vector magnetic field direction, the magenta circle with a dot is the +B direction, while the magenta circle with the X is the -B direction. In b) the same plots are shown for the diffuse population over the same time range. The diffuse corresponds to an energy range of 0.8-13 keV (roughly 390-1500 km/s).

The last step in identifying diffuse populations is examination of the count and phase space distributions. In Figure 5.7 we show these distributions, and separate the solar wind (green) and the diffuse populations (blue). The top and bottom panels are presented in the same format as Figure 5.3, although there are clear differences between the diffuse and FAB populations. The diffuse population does not show up as a distinct peak in the phase space distribution, instead manifesting as a high velocity tail to the Maxwellian solar wind distribution. The recovery of the bulk plasma parameters for the diffuse populations can be achieved by using assumptions similar to those in Gershman et al. (2013b). In that work they assumed an isotropic Maxwellian distribution for observations of magnetosheath plasma, with an assumption of low Mach number, to evaluate the bulk parameters of the observed plasma. We will also assume isotropy, based on the isotropy of the angular observations by FIPS. In the recovery method of Gershman et al. (2013b) they assume the Maxwellian plasma distribution isn't well observed below some lower velocity bound. That assumption is a complicated for the case of diffuse population observations. There is some evidence at Earth (Paschmann et al. 1981) that there is not any substantial amount of the population at these low velocities, but the lack of observations could also be dependent on the distance of the observation from the bow shock (Scholer et al. 1985). Lower velocity diffuse ions would have less ability to diffuse upstream, and therefore may not be observed at large distances from the bow shock.

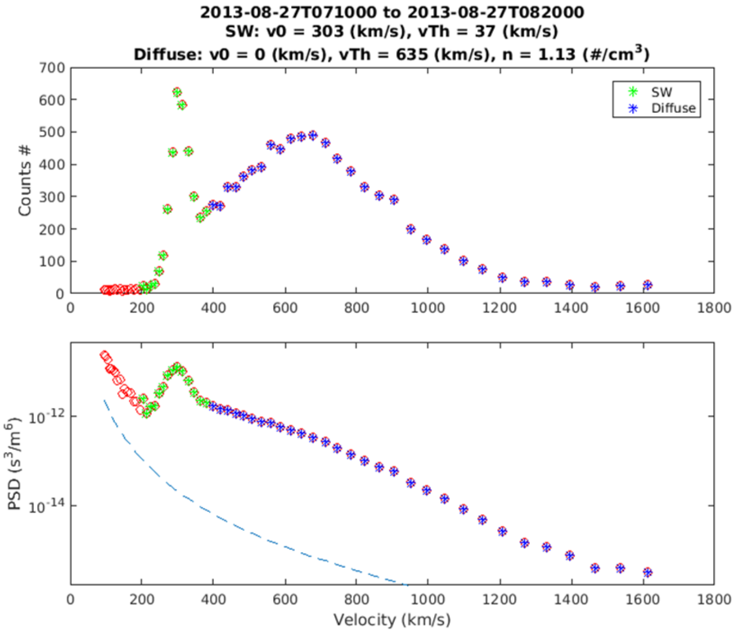

Figure 5.7: a) Measured count distribution of protons. Green points indicate the lower energy solar wind filter, and blue points the higher energy diffuse population. In b) we should the calculated phase space density distribution, with the same color scheme. The dashed line represents the "one-count" line in phase space. The recovered plasma parameters for the solar wind and diffuse population are shown in the plot title.

In our calculations of the plasma moment for diffuse populations we assume that the portion of the diffuse population that is below our lower E/q cut (see Figure 5.7) has a negligible phase space density. This is consistent with some observations at Earth, and also convenient as the solar wind obscures the lower velocity distribution for many of our observed diffuse events. This assumption means that we may be underestimating the density and overestimating the thermal velocity of our observed diffuse distributions. With the assumption of a low Mach number (or a thermal velocity much greater than the bulk velocity) we essentially assume that the bulk velocity of our diffuse population is zero and therefore isn't recoverable with this scheme. The recovered plasma parameters for the solar wind and diffuse populations in our example diffuse event are shown in the plot title of Figure 5.7. The techniques applied in this section are then applied to about 24 of the better quality diffuse events observed in Mercury's foreshock. The summary histograms of the recovered density and temperatures from these diffuse populations are shown in Figure 5.8. There were several hundred total diffuse events identified over the 4000 orbits MESSENGER had through the foreshock.

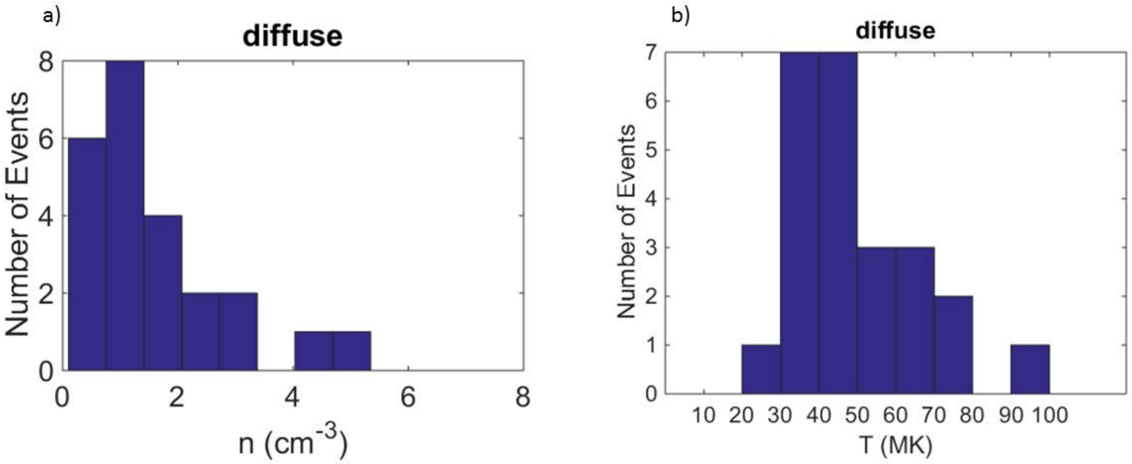

Figure 5.8: Summary histograms of the density (a) and temperature (b) for the 24 best diffuse events observed by FIPS in Mercury's foreshock.

5.2.3 Characterization of Populations

With our identification of FAB populations and diffuse populations in the foreshock at Mercury we aim to highlight the spatial distribution, compositional signatures, and wave signatures associated with the events. This is the first time these events have been observed at Mercury and therefore any differences in the general appearance of the foreshock region between Mercury and Earth are especially valuable.

At Earth, the foreshock is typically drawn with a fairly clearly organized boundary between regions where FABs are likely to be observed and regions where diffuse populations are likely to be observed. With the typical IMF orientation the diffuse populations tend to appear on the dawn side of the bow shock and the FAB on the dusk. Some recent work with Cluster has focused on observations where both populations were observed at the same time (Kis et al. 2007). Our first analysis was to see how our events in Mercury's foreshock are organized. This is shown in Figure 5.9a, where the average local time and magnetic latitude of the MESSENGER spacecraft during each event observation is scatter plotted. The magnetic latitude is more appropriate for describing the bow shock as it accounts for the northward offset of Mercury's dipole field (Anderson et al. 2011). It is clear to see that the diffuse and FAB populations are not well organized by local time or magnetic latitude, but there is a slight preference to observe these events on the dawn side of the planet. The magnetic latitude range covered by MESSENGER outside the bow shock is also illustrated in this plot. Outside the bow shock the MESSENGER spacecraft was almost exclusively below the ecliptic plane (see Figure 1.3 or Raines et al. 2013), further complicating the foreshock geometry.

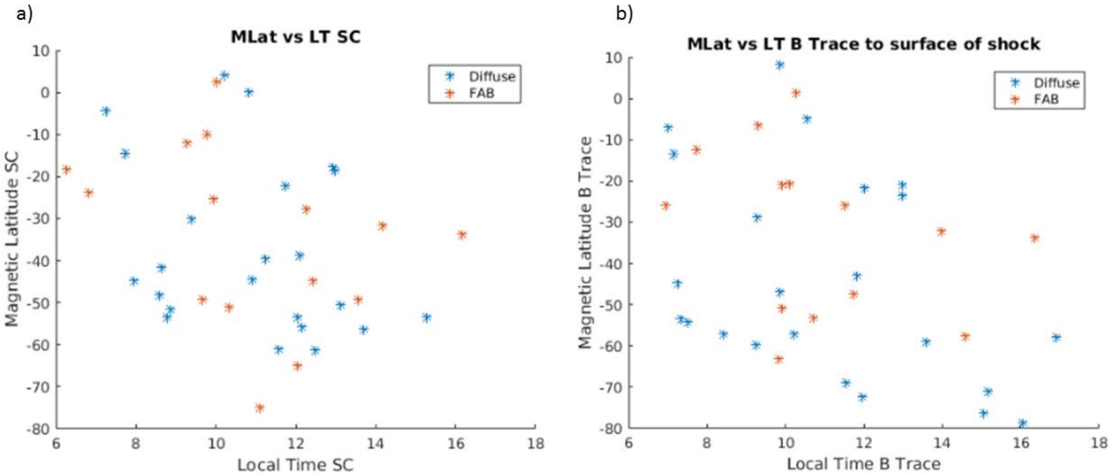

Figure 5.9: In a) the magnetic latitude and local time of the MESSENGER spacecraft for each of the foreshock events observed. The orange stars indicate the observation of a FAB population, while the blue indicate a diffuse population. In b) the observed population is traced back along the average IMF direction to the first intersection point with a model of Mercury's bow shock. The magnetic latitude and local time of this intersection point is then shown in the same manner as in a).

For completeness, we also show the positions on the bow shock surface where we have traced the origin of the events observed by the spacecraft. This tracing relies on the analytic bow shock model described in Winslow et al. (2013). We used the eccentricity and offset parameters directly from that work, but we allowed the focal parameter to vary which essentially adjusts the scale size of the bow shock surface. The bow shock was then scaled to coincide with the closest bow shock crossing to the event. For each diffuse event, we then traced back from the spacecraft to the bow shock surface in the direction of the average measured magnetic field vector at the spacecraft. For FAB events, which have a significant bulk velocity, we accounted for the vector velocity of the FAB in the MSO coordinate frame and traced along that vector from the spacecraft to the bow shock surface. A rough sketch of the tracing from the spacecraft to the bow shock surface is shown in Figure 5.10, and the full details can be found in Appendix 2. The results of these tracings are shown in Figure 5.9b, and we see no significant differences between these traced locations and the previous plot of spacecraft location for each event.

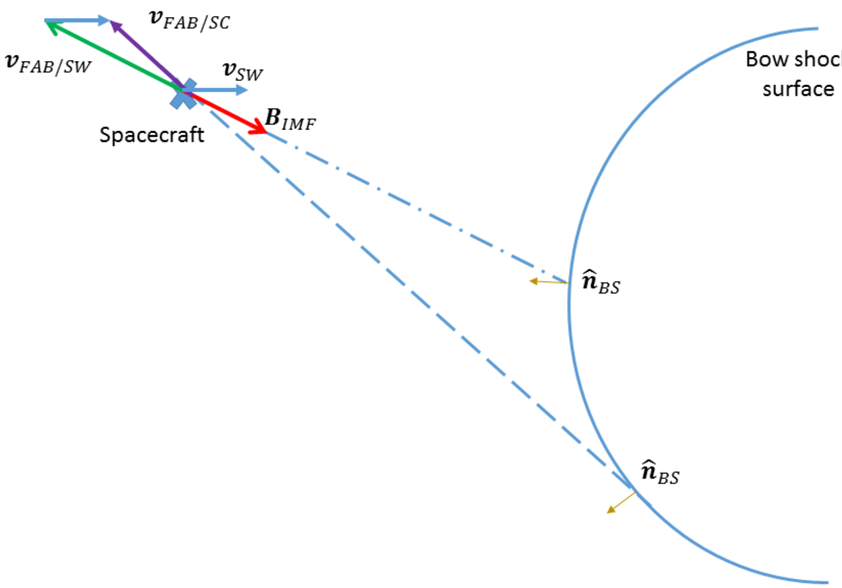

Figure 5.10: Sketch of the tracing scheme for a FAB population in the Hermean foreshock. Traces along both the IMF direction and the FAB propagation direction relative to the spacecraft (shown as an X) are indicated. At the point these traces intersect the bow shock surface, normals to the surface are depicted.

The large scatter in upstream locations at which both FAB and diffuse events can be observed speaks to the temporal and spatial variability of the IMF, the solar wind, and the bow shock at Mercury. It is also likely that the smaller scale size of the bow shock allows these populations to intermix more readily along their upstream trajectories. However, we still expect the populations to be roughly organized by the relevant shock type at their origin, i.e. whether they have their source at a quasi-perpendicular or quasi-parallel bow shock. To this end, we use our traced bow shock locations and computed the normal vector to our analytic shock model. The IMF at the bow shock is assumed to be the same as that observed by the spacecraft during the measured event. The angle between our calculated normal and the measured IMF vector defines θ_{bn}, which in turn determines the drift trajectory of ions at the shock (Gosling et al. 1982). In Figure 5.11 the calculated θ_{bn} angle for each of our foreshock events is histogrammed in bins of 5 degrees. It is clear to see that our FAB events are preferentially observed in the range $30^o < \theta_{bn} < 70^o$, and diffuse events in the range $\theta_{bn} < 40^o$. These ranges are within 10 degrees of the ranges observed at Earth for the respective foreshock populations. The limitations of a single spacecraft require the assumptions of a constant IMF between the spacecraft and the bow shock, and a constant bow shock which will naturally cause some uncertainty in our estimates of θ_{bn}.

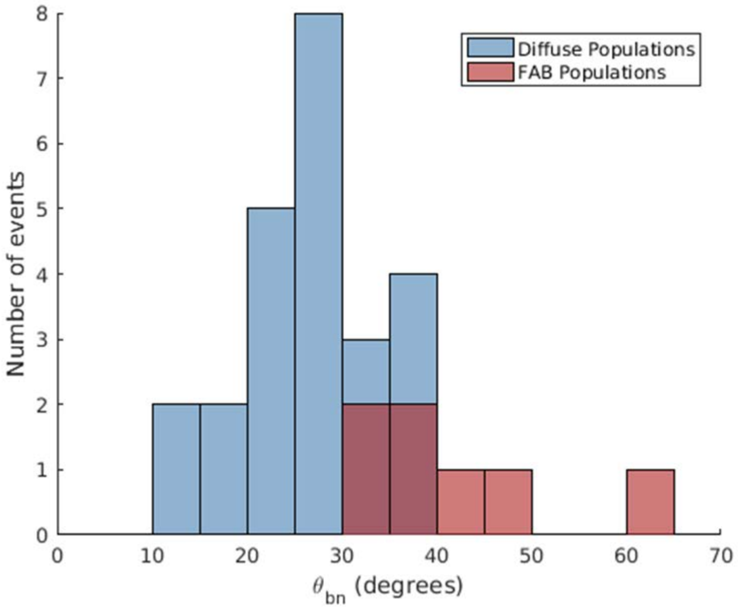

Figure 5.11: A histogram of the recovered angle between the bow shock normal and the IMF B field at the location the modeled foreshock population trajectory intersects the modeled bow shock. For diffuse populations this is a trace back from the spacecraft along the local field line, and for FAB this account for the relative velocity of the FAB along the field line and SW velocity.

An important distinction between FAB and diffuse populations observed in Earth's foreshock is the wave signatures associated with each. In the Earth's foreshock there is generally no association with waves different from the background wave activity and the FABs close to the upstream ion foreshock boundary. However, as the FAB distributions widen and scatter in pitch angle, there have been observations of waves in the magnetic field with a frequency close to 1 Hz (spacecraft frame). As one continues deeper into the terrestrial foreshock (toward the quasi-parallel shock) the presence of .03 Hz (or 30-sec) waves is seen, and the high frequency components fade away (Hoppe et al. 1981).

In our observations of FAB plasma we found no consistent correlation of wave activity of a given frequency. This may have been caused by a lack of pitch angle scattering in the

FABs that were most easily observed. In general FAB populations that show some degree of scattering are not well identified in our study as they have features intermediate to those for the FAB and diffuse populations and are therefore difficult to identify within FIPs FOV. However, our observations of diffuse populations have a clear correlation with the presence of the 0.1 Hz or 10-sec waves reported at Mercury (Le et al. 2013). A particularly good example of this correlation is seen in Figure 5.12. Here it is clear that the presence of the sinusoidal wave activity in the y and z component of the magnetic vector corresponded with a time when we observed a diffuse distribution of plasma in the E/q spectrogram. Angular flux maps confirm the approximate isotropy of the plasma observations and a wavelet analysis shows that the peak of the power spectrum is at a period of about 8 seconds (see Figure 5.13). The important feature is that the amplitude of the 10-sec waves vanishes when the diffuse plasma population is no longer observed by FIPS, but returns when FIPS again observes the diffuse population.

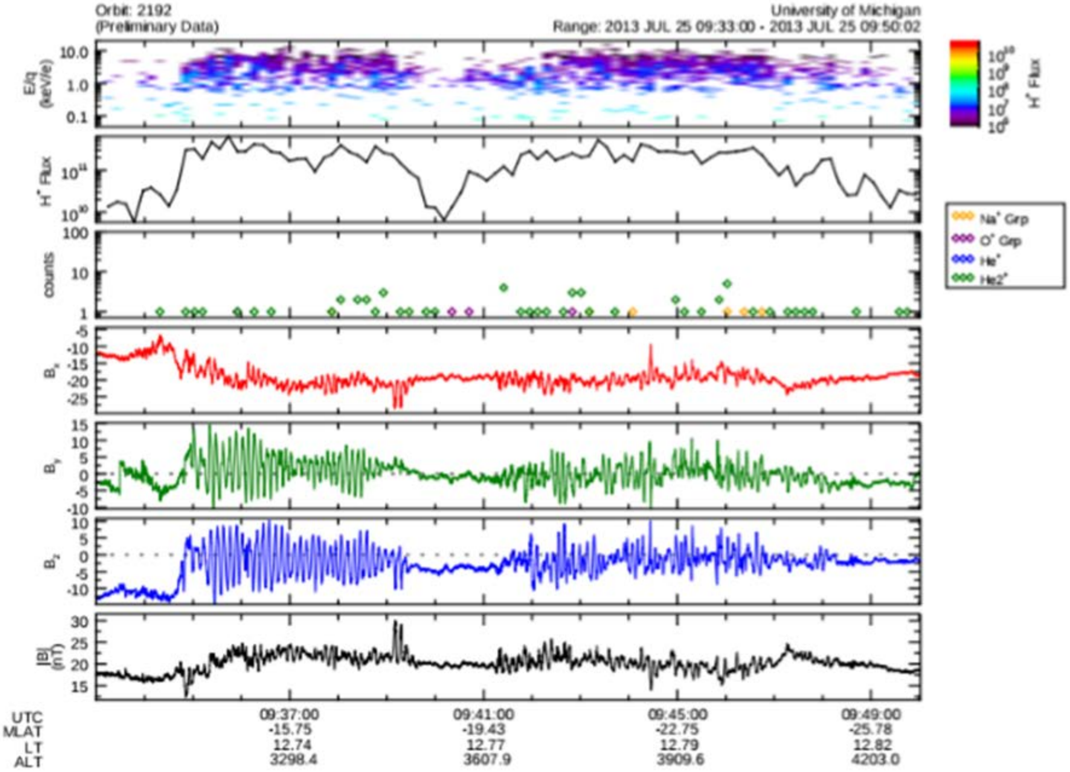

Figure 5.12: Time series of data from observation of diffuse event. Panel 1 is an E/q spectrogram of FIPS plasma measurements. Panel 2 is the integrated proton flux at each time step. Panel 3 is the number of heavy ion counts observed. Panel 4-7 are the MSO x,y,z components and magnitude of the measured magnetic field, respectively.

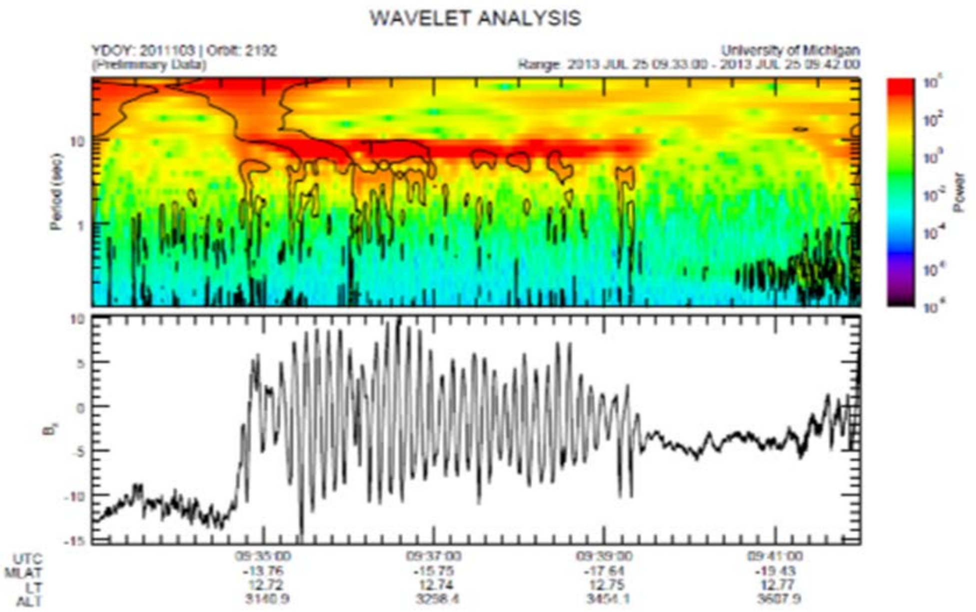

Figure 5.13: Wavelet analysis for the time interval 25-Jul-2013 09:33:00 to 25-Jul-2013 09:42:00. The z-component of the magnetic field (bottom panel) is used as an input to the wavelet analysis algorithm. The resultant time resolved power spectral density plot is shown in the top panel.

This time period is in fact very similar to the event reported in Sundberg et al. (2013), where they document the presence of 10-sec pulsations from the foreshock to the inner magnetosphere. They also show plasma measurements of that event period, but do not perform any analysis of the plasma properties. We have shown in this work that FIPS is capable of providing estimates of the plasma density and temperature for these time periods. While the diffuse events are the most prevalent foreshock observation made by FIPS, due to their isotropy, our initial survey yielded only several hundred diffuse periods in the 4000 or so orbits of the MESSENGER mission. This may corroborate the reports of diffuse event being sporadic at Mercury as stated by Le et al. (2013), but MESSENGER orbit could also just have been outside the spatial region of the foreshock where diffuse event occurs. The wave event just presented shows how localized the observations of a diffuse foreshock plasma can be at Mercury, most of MESSENGER's time upstream of the bow shock could just simply have been outside the diffuse plasma environment.

5.3 Calculation of Diffusion Coefficient

Diffusive foreshock populations have been measured extensively in the quasi-parallel regime of the terrestrial bow shock. A critical symptom of the diffusive acceleration process thought to accelerate these populations is the spatial decay in the population density away from the bow shock. Comparisons of the spatial profile of the phase space density of these diffuse populations can be used to estimate the diffusion coefficient parallel to the magnetic field for this diffusive process.

The essential components used in this analysis for measurements in the terrestrial foreshock are outlined in Kis et al. (2004) and Kronberg et al. (2009). A spatially resolved phase space density distribution must be obtained at variable distances from the bow shock in the quasi-parallel region of the foreshock. With the measurement of these PSD distributions assembled, one must look at how the PSD at a given energy varies with distance from the bow shock. For a given energy, the PSD will fall off exponentially with increasing distance from the bow shock, i.e.,

$$f(E) \sim \exp\left(-\frac{x}{\frac{\kappa(E)}{V_{SW}}}\right) \tag{5.1}$$

, where f is the PSD, x is the distance from the bow shock along the IMF, $\kappa(E)$ is the diffusion coefficient which is a function of energy, and V_{SW} is the solar wind bulk velocity. Thus if one simply plots the measured phase space density at a given energy against the distance from the bow shock, the e-folding value of this plot will be directly related to the diffusion coefficient.

For our analysis this diffusion coefficient will be estimated in two different ways, with the difference depending on how the PSD profile vs. distance from the bow shock is estimated. In the first method we will look at three diffuse events that have relatively long time duration, all on the order of 1-2 hours. The three events chosen for this analysis are 1) 2011-11-18T23:00:00 to 2011-11-19T00:00:00, 2) 2012-02-27T10:42:00 to 2012-02-27T12:24:00, and 3) 2012-05-26T16:00:00 to 2012-05-26T17:24:00 (all times in UTC). During these time periods the spacecraft was traveling at a speed of roughly 3 km/s, and at distances ranging from 1800 km to 13,000 km from the bow shock (along the IMF direction). These events were then broken into 6 minute time intervals and the proton PSD and mean distance from the bow shock is computed for each of these intervals. The variation of the measured PSD with distance from the bow shock was analyzed for each E/q bin corresponding to the diffuse population. An example of this analysis is shown for two E/q bins in Figure 5.14. In this case we show the E/q steps corresponding to proton velocities of 710 km/s and 1050 km/s. The three different long diffuse event periods are shown in three different colors with errorbars corresponding to uncertainty in the distance from the bow shock and counting uncertainty in the recovered PSD values.

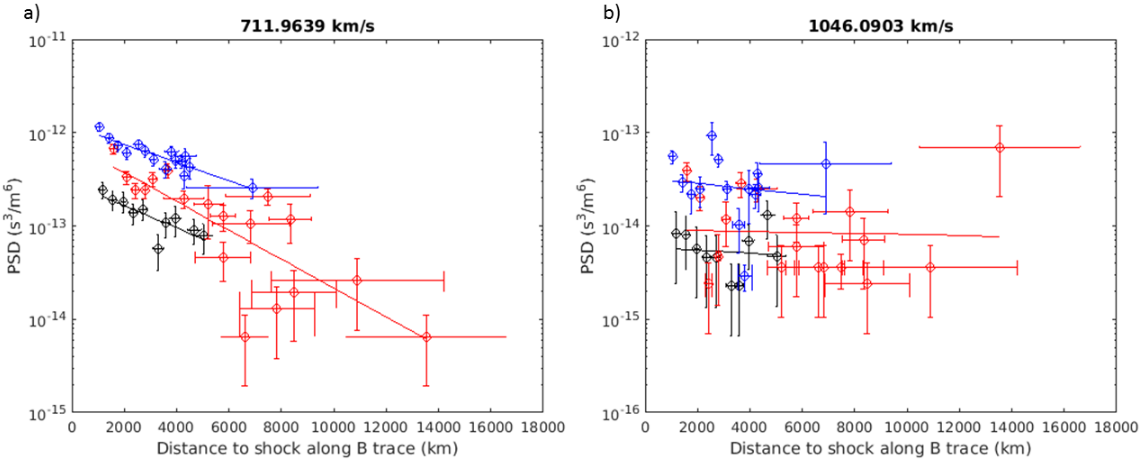

Figure 5.14: The observed phase space density in a single velocity interval as a function of distance from the bow shock. This phase space density is measured for three different diffuse events, as indicated by the different colored data points. In a) the measured phase space densities for the velocity bin centered on 710 km/s are shown. In b) the measure phase space densities for the velocity bin centered on 1050 km/s are shown. In both cases the linear fits to the decay of measured phase space density with increasing distance from the shock are shown.

When presented in a format with a logarithmic y-axis, the e-folding distance at these E/q steps can be read off as the inverse of the slope of a linear fit to the measurements for each event. In Figure 5.14, this best fit line is overplotted on the data points. With the average solar wind velocity calculated for each long event, using the methods of Gershman et al. (2012) described earlier, the diffusion coefficient can be estimated with (5.1). The results of this calculation for a subrange of the E/q bins analyzed is shown in

Figure 5.15. The uncertainties shown in this figure are propagated uncertainties in PSD and bow shock distance as shown in Figure 5.14. We have limited the velocity range of our diffusion coefficient recovery to E/q bins that have several 10s of counts and where significant decay in the PSD was observed. For the higher energies steps, as shown in Figure 5.14b, the scatter in the PSD vs bow shock distance due to variability in the magnetic field and counting statistics is large relative to the decay trend we hope to recover. Furthermore at the higher energies the e-folding distance of the density decay can become comparable to the maximum distance that MESSENGER travels away from the bow shock. Observing less than one e-fold in the density of the diffuse population complicates the recovery of the e-folding value.

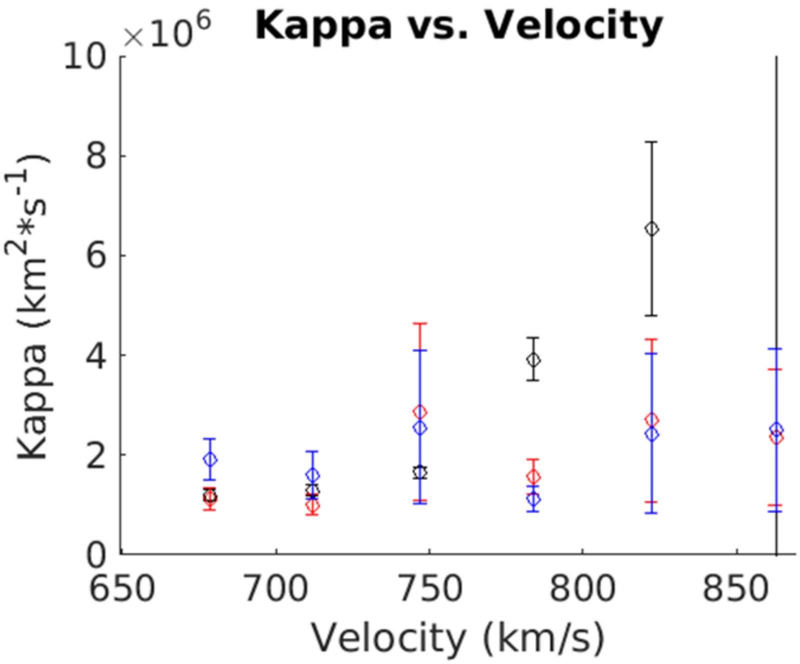

Figure 5.15: Estimate of the diffusion coefficient based on the rate of decay of the PSD in several velocity bins. The diffusion coefficient is calculated for each of three diffuse events, but only for velocity bins where a clear decrease of the PSD with increasing distance from the bow shock was observed.

The recovered diffusion coefficients in the range of velocities we sampled are around 1-2E6 km^2/s in the velocity range of 700-800 km/s. This is as high as can be reliably recovered before uncertainties dominate the slope recovery.

As a way to confirm the diffusion coefficients recovered in this first method we also present the recovery of the diffusion coefficient based on about 130 diffuse events. The majority of these events are shorter in duration than the three diffuse events discussed previously. As such we use the entire time period of each event to calculate the average PSD and average distance from the bow shock for each event. Although this method has less temporal resolution and a greater variability in the ambient solar wind conditions between events, it allows us to average over a larger number of observations, lessening the effect of statistical outliers and counting statistics.

Just as for the three diffuse event scenario, we construct a PSD vs. bow shock distance plot for each E/q step of FIPS that corresponds to a diffuse population (see Figure 5.7 for typical diffuse population distribution). Each data point on these plots now corresponds to a single diffuse event observed, instead of multiple time subsets of the same diffuse event. The slopes of these plots are again used to compute the diffusion coefficient at each energy. We have to assume an average solar wind velocity for the 130 diffuse events to estimate the diffusion coefficient, and this is estimated at about 350 km/s from the diffuse events that have valid solar wind measurements. The recovered diffusion coefficients are shown in Figure 5.16.

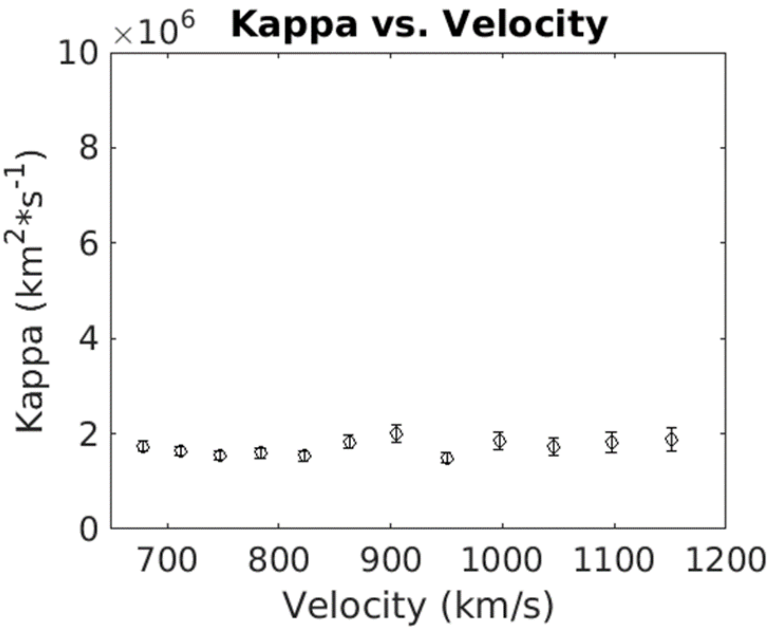

Figure 5.16: Calculated diffusion coefficients as a function of observed velocity bin in diffuse events observed upstream of the bow shock. This is a compilation of about 120 diffuse events. Details of the diffusive coefficient calculation can be found in the text.

We see that the diffusion coefficient estimated from this method is about 2E6 km^2/s, which is very similar to the value derived from the three diffuse event method. It is curious that the recovered diffusion coefficient is constant over the velocity range we have analyzed, but again this has to do with the sources of variability in the measurement dominating over the actual decay in density of the plasma. To get a feel for how our diffusion coefficients and their energy dependence compare with those made in the terrestrial foreshock we examine the work by Kronberg et al. (2009). The key figure from that work is shown in Figure 5.17, where the diffusion coefficient from protons (and helium) has been estimated over a range of energies.

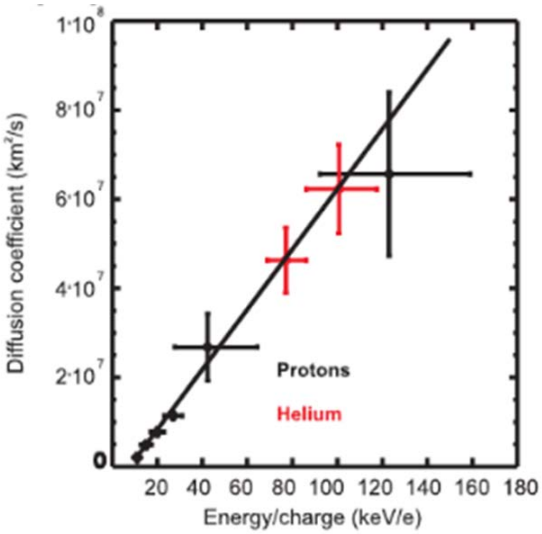

Figure 5.17: Adapted from Kronberg et al. 2009. The diffusion coefficient versus energy per charge; black points are for protons and red for helium. The first four points at low energy ranges are obtained using the CIS instrument on Cluster, for comparison. The straight line is a linear fit for the CIS and RAPID data points.

The energy range corresponding to our FIPS measurements is at the lowest energy end of the measurements displayed in Figure 5.17. However, we see that our value of about 2E6 km^2/s is quite similar to the values recovered around 10 keV/e in the terrestrial foreshock. As far as the energy dependence of the diffusion coefficient in the terrestrial bow shock, we estimate the slope of the linear relation between the diffusion coefficient and particle energy is about 7E5 (km^2/s)/ (keV/e). Thus over the range of energies that we have evaluated diffusion coefficients over (about 3-6 keV/e), if the diffusion coefficient had the same E/q dependence as at Earth, we would expect the diffusion coefficient to vary by about $\left(7E5\frac{\frac{km^2}{s}}{keV/e} * 3\frac{keV}{e}\right) \approx 2E6\frac{km^2}{s}$over our measurement range. However, if the diffusion coefficient varied by this much the e-folding length for the diffuse populations at the higher energy range of our measurements would be about $L(E) = \frac{\kappa(E)}{V_{SW}} \approx 10{,}000\ km$, which is comparable to MESSENGER's max distance from the bow shock (see Figure 5.14). We would expect to have difficulty recovering the true e-folding values of the higher energy portion of the diffuse population if they are much larger than the distance that MESSENGER traverses away from the bow shock. The main reason for this is that variations in the ambient solar wind conditions and errors in the tracing to the bow shock are much larger relative to the density decay we are trying to measure for these higher energy cases. Thus we must confine ourselves to report a single diffusion coefficient for the E/q range of about 3-6 keV/e of $\kappa = 2E6\frac{km^2}{s}$, and note it is consistent with measurements at Earth. Future missions to Mercury by the BepiColumbo spacecraft should carry instruments such as the HEP-ion instrument on the Mercury Magnetospheric Orbiter (Saito et al. 2010) that will measure plasma ions from 30 keV to 1.5 MeV and will be ideally suited to further explore the energy dependence of the diffusion coefficient in the Hermean foreshock.

5.4 Energization of Foreshock Particles at Mercury

5.4.1 FAB Energization

In this section the observed energies of the FAB populations are examined. We are interested in whether or not the Shock Drift Acceleration (SDA) mechanism (Burgess 1987) that has been employed in the terrestrial foreshock can also explain the energies seen at Mercury. First, the ranges of energies of the FABs at Mercury, in the frame of the solar wind are examined. Next, the observed energies of the FAB population are compared with predictions from a simplified form of SDA. Last, we demonstrate with a simple calculation whether the drift path lengths required to energize an ion via SDA are reasonable relative to the scale size of the Hermean foreshock.

Utilizing the methods of Gershman et al. (2012) for supersonic distributions we calculate the velocities, thermal widths and densities for a study of 10 FAB events. A histogram of the ratio of the bulk velocity of the FAB relative to the solar wind velocity is presented in Figure 5.18. The solar wind frame is the frame moving with the solar wind such that the bulk velocity of the solar wind is zero. Note that the velocity of the FAB in this solar wind frame will be larger than in the frame of Mercury as FABs are generally directed sunward and the solar wind antisunward. The velocity of the FAB in the solar wind frame can be more relevant for some applications (two stream instabilities, wave growth). The ratio of the FAB and solar wind velocities in the frame of Mercury (MSO) are shown in (a) and in (b) the velocity of the FAB in the solar wind frame is compared to the solar wind velocity in Mercury’s frame.

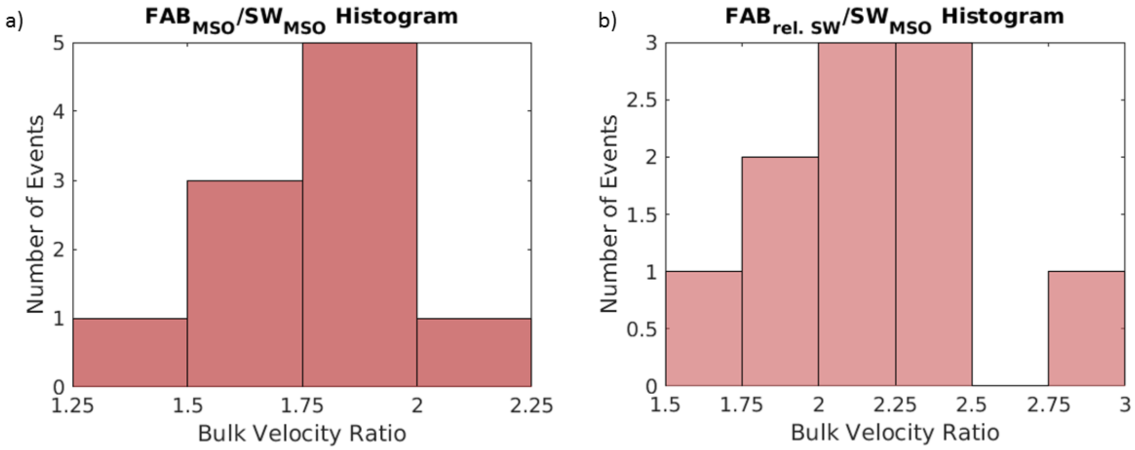

Figure 5.18: The ratio between the bulk velocity of FAB events and the observed solar wind. In a) the ratio of these velocities in the frame of Mercury (MSO) is presented. In b) the ratio of the FAB velocity in the solar wind frame relative to the solar wind velocity in the MSO frame is presented.

In the frame of the solar wind the observed FAB populations had velocities anywhere from 1.5 to 3 times the solar wind velocity. We also note that for these events, the thermal width of the FAB populations was higher than in the solar wind, with the FAB thermal width usually 1.2-2.9 times the solar wind thermal width. It is clear that FABs represent populations with greater kinetic and thermal energy as compared to the solar wind.

The first attempt at comparing the observed FAB energies to theory uses a simple reflection model based on the conservation of the first adiabatic invariant (the magnetic moment of the ions). This formulation was used in Paschmann et al. (1980) to analyze FAB populations at Earth and show they are in good agreement with predictions by this theory. In that model, the energy gained during reflection is a function of the angles between the IMF, the solar wind velocity, and the local shock normal. Using the methods described previously to derive the FAB moments and trace to the bow to find the local shock normal we can estimate the energy gain for our FAB populations. The formulation for the energy gain of a FAB, in the spacecraft frame, is given by

$$\frac{E_r}{E_i} = 1 + 2(1+\delta)\frac{\cos^2\phi - cos\phi cos\theta cos\psi}{\cos^2\theta} \tag{5.2}$$

, where ϕ is the angle of the solar wind velocity relative to the shock normal, θ is the angle of the IMF relative to the shock normal, and ψ is the angle between the IMF and the solar wind velocity. The factor δ is an empirical factor for the degree of conservation of the magnetic moment. If the magnetic moment is conserved δ will be equal to unity, if it is less than unity then a fraction of the bulk energy of the incident solar wind is converted into thermal energy of the reflected beam.

In Figure 5.19 the results of this calculation are shown. The blue points represent the predicted energy ratios where the angles required for (5.2) are calculated by simply tracing the local IMF back to the model bow shock surface. This is not completely accurate as the FAB only moves along the IMF in the solar wind frame so aberration should be accounted for to trace the FAB population back to its true source on the bow shock. The orange points represent the predicted energy ratios where the angles for (5.2) are calculated by accounting for the aberration of the FAB population away from the IMF direction on its way from the shock to the spacecraft. However, the traced location on the bow shock for this method is more susceptible to temporal variation in the solar wind and bow shock as the intersection of traces with the quasi-perpendicular region of the shock (where FABs typically originate) are much more oblique. Therefore a small change in the bow shock size or solar wind velocity can dramatically affect the region on the bow shock surface that is recovered from the trace. This is reflected in the greater scatter of the orange points. The value of δ that results in the best fit to the observed data for each case is indicated in the plot legend. The basic take away is that the predictions from conservation of magnetic moment and the observed energy ratios for the FABs at the Hermean foreshock do not show great agreement.

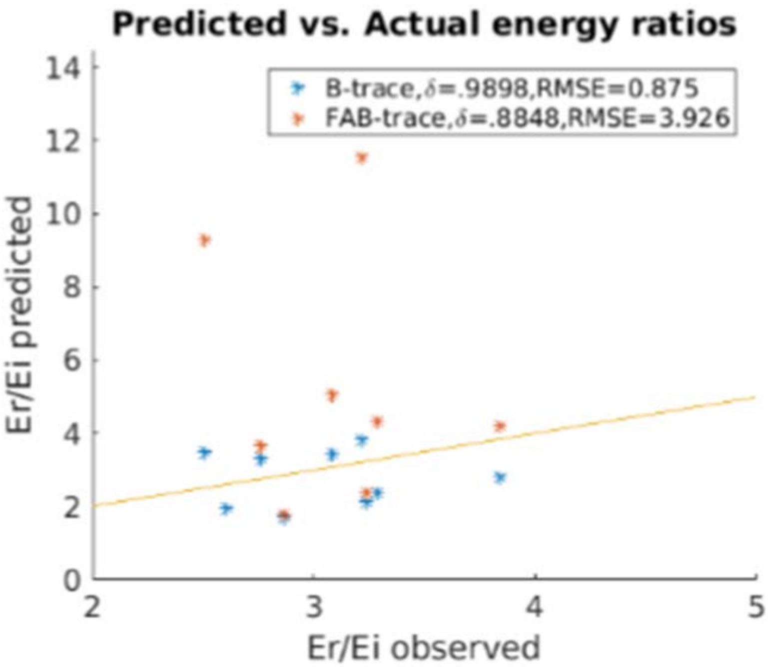

Figure 5.19: Comparison of the observed and predicted energies of FAB populations (E_r) relative to the energy of the incident solar wind population (E_i). The predicted energy ratio derived from a trace along the local IMF to the model bow shock surface are shown in blue. The predicted energy ratio derived from a trace back along the calculated FAB velocity vector is shown in orange. The yellow-orange line delineates where the points would fall if the predicted energy ratio was equal to the observed. The legend indicates the value of δ that yield the best fit of the observed data points and the Root Mean Squared Error (RMSE) associated with the fit.

As the previous effort to model the expected FAB energies at Mercury was not satisfactory we adopted a simpler approach to see if the SDA mechanism could reasonably explain the energies we observe in our FAB populations. This involved an estimation of the drift length along the shock surface during the SDA process. The energy gained during SDA is essentially due to ions drifting through a potential drop caused by the convective electric field of the solar wind (Sonnerup 1969; Burgess 1987). Furthermore, the drift direction for ions undergoing SDA at the bow shock is roughly the gradient curvature drift direction due to the large gradient in B that is the bow shock. For the 10 FAB events from above (those shown in Figure 5.18), we performed a calculation based on the expression for work done by the convective electric field, $\Delta E = q * \Delta x *$

$(\boldsymbol{E}_{IMF} \cdot \widehat{\boldsymbol{x}}_{\mathrm{GC}})$. In this formulation, ΔE is the difference in energy of the FAB and the incident solar wind, q is the charge of a proton, Δx is the parameter of interest, i.e., the drift length required to accelerate protons to a given energy. This distance, Δx, is the travel distance required in the direction of gradient curvature drift (Gombosi 1998), $\widehat{\boldsymbol{x}}_{\mathrm{GC}} = \widehat{\boldsymbol{b}}_{IMF} \times \frac{\boldsymbol{\nabla B}}{|\boldsymbol{\nabla B}|} \approx \widehat{\boldsymbol{b}}_{IMF} \times -\widehat{\boldsymbol{n}}_{BS}$, as the largest gradient in B is in the normal direction to the bow shock. Finally, $\boldsymbol{E}_{IMF}$ represents the solar wind convective electric field, and is given by $\boldsymbol{E}_{IMF} = -\boldsymbol{V}_{SW} \times \boldsymbol{B}_{IMF}$ (Gombosi 1998).

For the FAB events utilized, all measurements were taken in the center of each event time interval. The inward shock normal was found at the point on the modeled shock surface corresponding to the trace toward the planet along the calculated vector velocity direction of the FAB. For these events, the mean drift length required was 0.13 R_M, with a spread from .04 R_M to .36 R_M. Recalling that the flank distance for our model of the bow shock is 3.35 R_M (Winslow et al. 2013), we can safely say that the distances required for SDA are much smaller than the scale size of the shock. These results suggest that the effects of curvature of the shock surface are small for considerations of SDA occurring at Mercury's bow shock. It is worth noting that the energy ratios in FABs observed at Mercury are smaller than those observed at Earth. Ratios between solar wind and FAB kinetic energies range from 2-4 in our sample of FABs, whereas observations at Earth can range from 2-20 (Paschmann et al. 1980). This may suggest that there are some aspects of the small scale size of Mercury's bow shock may limit the energization possible for FABs.

5.4.2 Diffuse Energization

In the studies of Earth's bow shock the process of diffusive acceleration is ubiquitously invoked to explain the existence of the diffuse population. This process typically involves a form of Fermi acceleration, which in the most general sense involves ions interacting with moving magnetic irregularities (Fermi 1949; 1954). In the case of the bow shock this manifests itself as some fraction of the upstream ion population being reflected between the bow shock and magnetic irregularities or scattering centers that are convected from the quasi-parallel foreshock toward the bow shock. As these ions undergo multiple encounters with the bow shock some fraction of the population will undergo a stochastic increase in energy as seen in the frame of the bow shock.

While this mechanism is well accepted in general at Earth's bow shock, the particulars of connecting the proposed mechanisms to the exact distributions seen in the diffuse population remains a subject of debate. At energies above 20 keV/e, the diffuse populations (of multiple ion species) at Earth appear to show an exponential spectra with an e-folding value of around 15-25 keV/e (Ipavich et al. 1979). Three competing explanations for the observed spectra of diffuse ions are the free escape mechanism, a time dependent mechanism, and those that rely on cross-field diffusion. For further details on these competing theories the reader is referred to the recent review paper by Burgess et al. (2012). The diffuse populations at Mercury exist in a much different parameter regime than those observed at Earth. Therefore observations of the energization of diffuse populations at Mercury offers valuable insight into the nature of the diffusive shock acceleration process in general.

In line with the observations of Ipavich et al. 1979, the diffuse populations are investigated in terms of an exponential fit with respect to E/q. An example of this fit is shown in Figure 5.20, where is can be seen that the observed diffuse population is well described by an exponential fit. The "slope" value that is reported refers to the slope in a log y vs x type fitting, and therefore is actually the exponent, m, in a fit of the form $y = exp(-mx)$. A summary of the exponential fits for the all 124 diffuse events selected in the previous study of the diffusion coefficient are shown, superposed with the selected "Best" diffuse events in terms of counting statistics and clearness of signatures described in Section 5.2 is shown in Figure 5.21

.

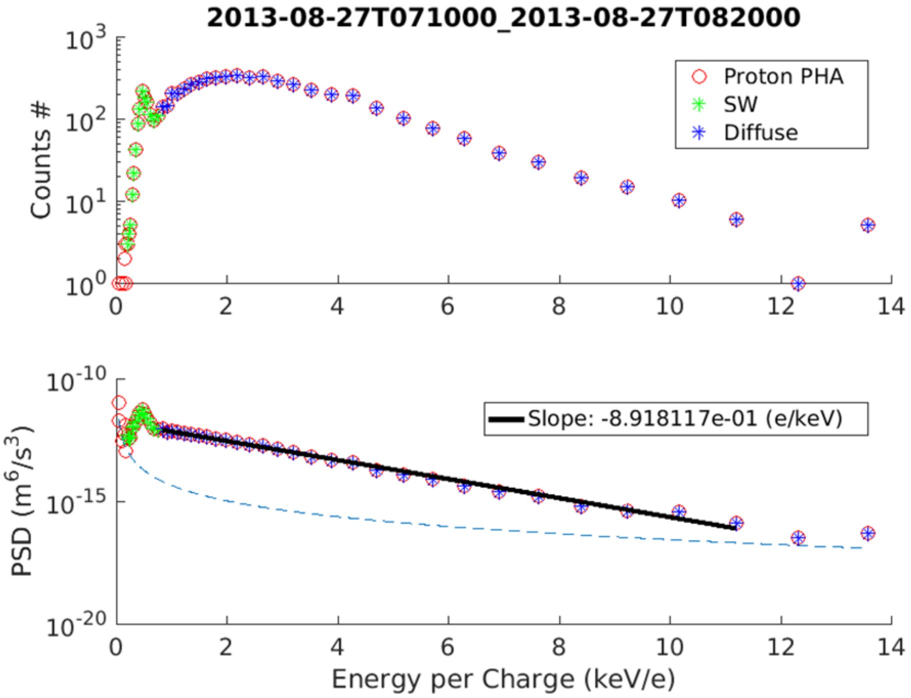

Figure 5.20: Count distribution (top panel) and PSD distribution (bottom panel) versus E/q for a diffuse event observed by FIPS. The bottom panel displays an exponential fit to the high energy tail of the diffuse population. The slope of the fit is shown in the plot legend. The portion of the distribution that is identified as solar wind is shaded in green, and the portion identified as diffuse is shaded in blue. The dashed line in the bottom panel represents the "one-count" line in phase space.

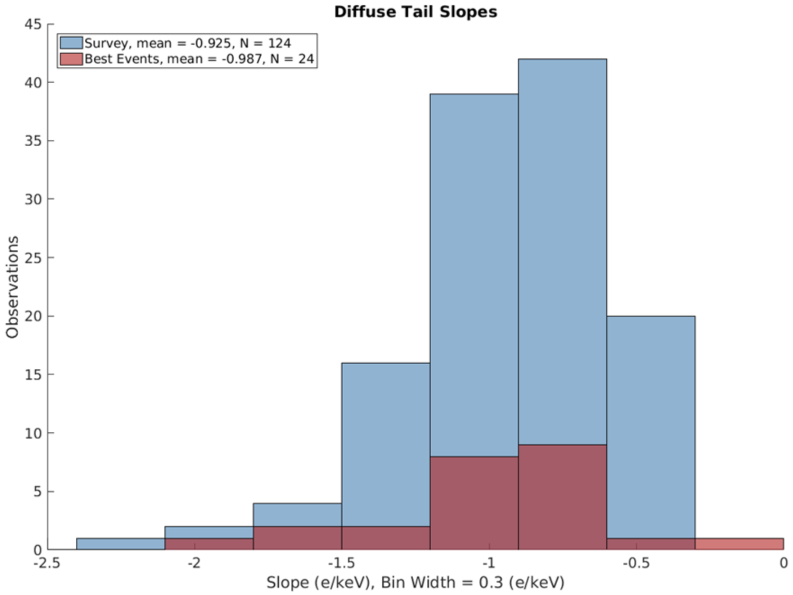

*Figure 5.21: Summary histogram of the fits to the diffuse populations PSD distribution. The portion of the PSD distribution corresponding to the diffuse population (excluding the solar wind) is fit with an exponential function and the coefficient ,m, of the fit ,exp(-m*x), in that exponential fit is histogrammed in the figure. A separate histogram for the best 24 diffuse events (red) and for all 124 diffuse events (blue) identified are included.*

The recovered e-folding values for these exponential fits are equal to the inverse of the recovered slope values. Thus we recovered e-folding values between about 0.67 and 2 keV/e for most diffuse events. The most common e-folding value recovered is about 1 keV/e.

This e-folding value is quite a bit lower than would be expected in some theories of diffuse shock acceleration in the foreshock. In particular the self-consistent theory for the excitation of hydromagnetic waves and the acceleration of ions in the foreshock presented by Lee (1982) offers a prediction for what this e-folding value should be in the steady state quasi-parallel foreshock. In that work the e-folding value is given by

$$E_C = \left(\frac{1}{4}\right) 3^{\frac{1}{2}} a V_u \xi_1^{-1} q_p |B| \tag{5.3}$$

, where a is the lateral distance to unconnected field lines, assumed to be the characteristic dimension of the nose of the bow shock. V_u is the upstream solar wind velocity, ξ_1 is the first zero of the standard Bessel function (=2.4048), q_p is the ion charge, and $|B|$ is the magnitude of the magnetic field. At Earth, assuming a bow shock standoff distance of 10 R_E (R_E=6400 km), solar wind velocity of 400 km/s, and magnetic field strength of 5 nT, Lee 1982 estimated $E_C = 23\ keV$, which is in rough agreement with observations at Earth. Repeating that calculation for parameters suited to Mercury, a bow shock standoff distance of 2 R_M (R_M=2440 km), solar wind velocity of 400 km/s, and magnetic field strength of 35 nT the estimate value of e-folding value is $E_C = 12\ keV$. The predicted evolution of the diffuse distribution transitions from a complicated power law expression at energies below the e-folding energy to a simple exponential decay according to $f \sim \exp\left(-\frac{E}{E_C}\right)$ at higher energies (see Lee 1982 for details). Thus the formulation of Lee 1982 doesn't predict that we should see an exponential decay profile at the energies observed by FIPS, as we are well below the predicted e-folding energy.

Since (essentially) all of the FIPS observations are below this predicted e-folding value it is prudent reinvestigate the distributions with respect to possible power law fits. One of the better examples of such a fit is shown in Figure 5.22. The main point is that we do not find any diffuse spectra that are cleanly fit by a single power law expression over the range of energies of the diffuse event. In the example shown we see that different portions of the distribution can be fit by different power law expressions. However we also saw in Figure 5.20, that this same time period was nicely fit by a single exponential function. Thus we must grapple with the ambiguity of whether a portion of our diffuse population is better fit by the power law or exponential over a small range of E/q. Discriminating between a power law and exponential fit over less than an order of magnitude in the independent variable is often a difficult task so we will entertain two options and discuss their implication with theories in the literature.

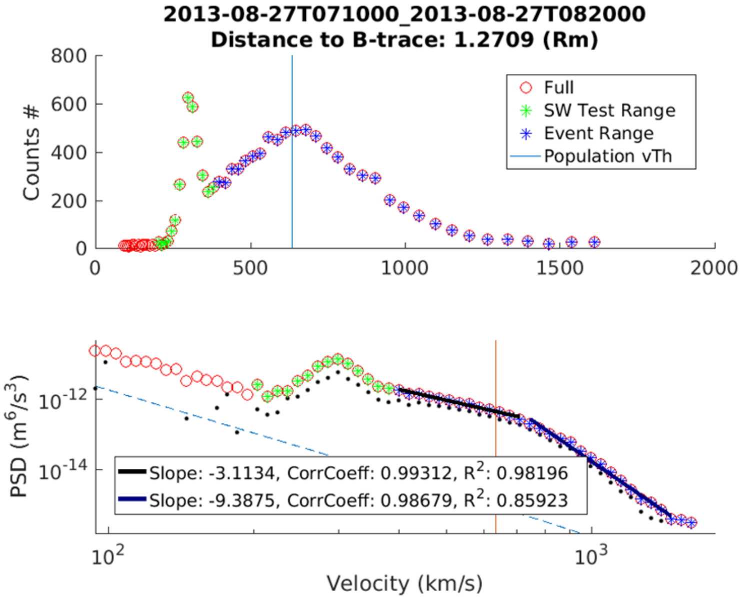

Figure 5.22: Count distribution (top panel) and PSD distribution (bottom panel) versus E/q for a diffuse event observed by FIPS. The bottom panel displays several power laws fit to the high energy tail of the diffuse population. The slope of the fit is shown in the plot legend, along with the correlation coefficient and the R^2 *value. The black dots in the bottom panel represent a subset of the data is plotted in red circles, namely protons that had TOF measurements reported, but they are not relevant in this discussion.*

In option 1 we interpret the fit in Figure 5.22 as a power law fit in the range of 400-700 km/s and the beginning of an exponential rollover from 700 km/s onward. This would imply that the prediction of Lee 1982 is inaccurate and the rollover occurs at around 3 keV instead of 12 keV. We must also note that the majority of the power law fitting attempts are not as well organized as this case and the simple exponential fit is generally more justifiable across the hundreds of diffuse events surveyed. Further analysis of the whether the steady state distribution form of Lee 1982 is justifiable for Mercury's foreshock is required to verify this option. The easiest route for this analysis would be to look at a range of measurements that extend significantly beyond FIPS energy range.

In option 2 we explore whether the consistency of the observed distributions with an exponential fit could indicate that finite connection times are the dominant factor in determining the observed diffuse PSD distribution. Finite connection time effects occur when the time it takes an IMF field line to sweep over the bow shock is small compared to the time scale required for ions to undergo multiple encounters with the bow shock (Fermi time scale). This finite connection time effectively limits the energy gains that can be made by the diffuse population.

Using a formulation similar to that in Lee & Skadron (1985) we estimate the connection times for the IMF geometries and solar wind conditions experienced in our survey of diffuse events. The time, τ_{cxn} it takes an IMF field line to sweep across a scale length comparable to Mercury's bow shock is given by

$$\tau_{cxn} = \frac{L}{V_{SW}|sin\theta_{BV}|} \tag{5.4}$$

, where L is the scale length of the magnetosphere (assumed to be the flank distance of the bow shock, 3.35 R_M), V_{SW} is the solar wind velocity, and θ_{BV} is the angle between the solar wind velocity and the IMF direction. A histogram of the connection times calculated for the diffuse events with valid solar wind measurements is shown in Figure 5.23. We can see that the mode connection time is around 10 seconds, but some diffuse events can have connection times up to around 100 seconds.

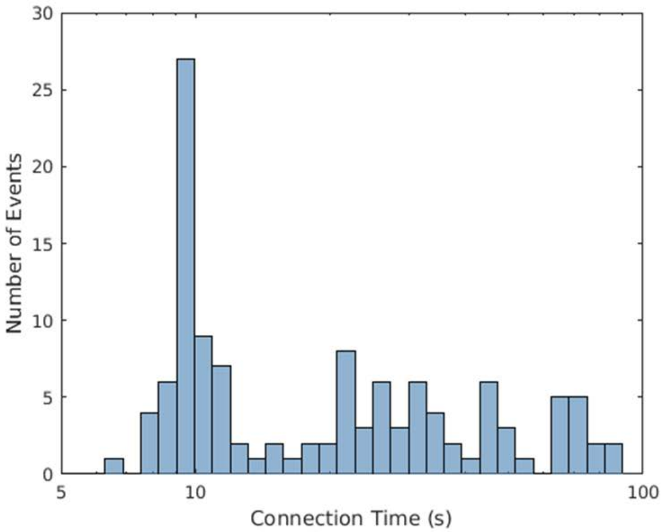

Figure 5.23: Histogram of the calculated connection times based on the observed IMF and solar wind conditions for each diffuse event observed during the survey.

This connection time can be compared to the Fermi acceleration time, which can be estimated from our measurements of the diffusion coefficient and the solar wind velocity. Using the methods of Kronberg et al. (2009) and Forman (1981) we estimate the Fermi acceleration time as $\tau_{Fermi} = \frac{4\kappa}{V_{SW}^2} \approx 65\ sec$ for our diffusion coefficient of around 2E6 km^2/s, for energies around 3 keV, and for a mean solar wind velocity of about 350 km/s for our diffuse survey. If the energy dependence of the diffusion coefficient across the FIPS energy range is the same as observed in the terrestrial foreshock (Kronberg et al. 2009) then the Fermi acceleration time would vary from about 65 sec at around 3 keV to about 230 sec at 10 keV. A reference for the solar wind velocities for this large survey of diffuse events is shown in Figure 5.24. It appears that relative to the mean solar wind distribution, the solar wind velocities during diffuse events are almost 40 km/s slower. This implies that diffuse events have longer connection times than those for typical solar wind conditions at Mercury.

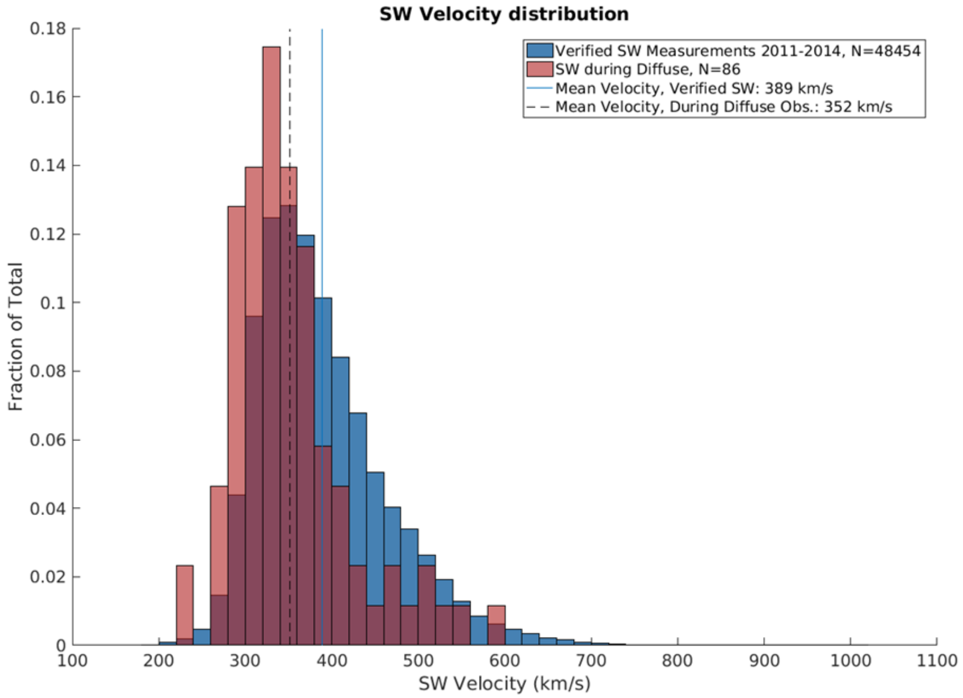

Figure 5.24: Summary normalized histogram of the calculated solar wind velocity for the years of 2011-2014 from valid FIPS measurements upstream of Mercury's bow shock. Overlaid on this plot is the normalized distribution of solar velocities measured during diffuse events. The mean values of these distributions are shown with vertical lines and indicated in the plot legend.

From our calculations of characteristic times it seems clear that the average connection time is less than the Fermi acceleration time scale. This supports the idea that the observed diffusive distributions are limited by a finite connection time rather than by the lateral escape due to diffusion as would be the case for the steady state solution of Lee 1982. The connection time limited PSD distribution should also be exponential in nature, at least in the high energy asymptote. The characteristic e-folding value for this exponential can be estimated from the work of Smith and Lee (1986) or Forman and Drury (1983). In these formulations, the PSD distribution, for energies much greater than the injection energy, is given by

$$f(p) \propto \sqrt{\kappa(p)}\ \exp\left(-\frac{9\,\kappa(p)}{(\Delta V)^2 t)}\right) \tag{5.5}$$

, where f is the PSD distribution, κ is the momentum dependent diffusion coefficient, ΔV is the velocity change across the shock, and t is the connection time. If we transform this distribution to be in terms of energy it takes the following form

$$f_E(E) = f_p\big(p(E)\big)\frac{dp(E)}{dE} \tag{5.6}$$

, where the subscript "E" indicates the functional form in terms of energy and "p" in terms of momentum. If we assume that the diffusion coefficient is linearly dependent on energy as seen in at Earth (Kronberg et al. 2009), such that $\kappa(E) = \kappa_0\left(\frac{E}{E_0}\right)$, then we can simplify this expression to

$$f_E(E) \propto \exp\left(-\frac{9\kappa_0\left(\frac{E}{E_0}\right)}{(\Delta V)^2 t}\right). \tag{5.7}$$

This final expression then has a clean exponential dependence on energy with an e-folding value, E_C, of

$$E_C = \frac{E_0(\Delta V)^2 t}{9\kappa_0}. \tag{5.8}$$

From our measurement of the diffusion coefficient we estimate $\kappa_0 = 1 - 2E6\ \ km^2/s$ at an energy of $E_0 \approx 3.3\ keV$ (from the range of values in Figure 5.15), a connection time of about 10 sec, and a velocity change across the shock of about 245 km/s which corresponds to a solution for a hydrodynamic shock with M=4 and upstream solar wind velocity of 350 km/s. The choice of Mach number was selected to be in rough agreement with the parameters presented in Slavin and Holzer (1981). This yields an e-folding energy of 0.1 to 0.2 keV. In the extreme case of connection times closer to 100 sec this would result in e-folding energies of around 1 keV, but we observe the majority of our diffuse events connection times in the range of 10 sec. These estimates are therefore significantly lower than the observed e-folding values in our diffuse populations. We must keep in mind that this approximation for the finite connection distribution is strictly only valid for energies much greater than the injection energy, which is presumably not smaller than the solar wind energy ($\sim 1\ keV$).

Our findings indicate there is compelling evidence that the diffuse populations at Mercury are due to connection time limited diffusive shock acceleration. This stems from basic estimates showing that the connection times are not large compared to the Fermi acceleration time scale. Furthermore, our observed exponential distributions have an exponential scaling is smaller than what is predicted by Lee 1982. This connection time limited acceleration has been used to explain diffuse populations at Jupiter (Smith and Lee 1986) that also displayed a lower than expected density at the higher energy portion of the distribution. However, our rough estimates for the expected e-folding value of the exponential distribution resulting from finite connection times are insufficient to explain our observations. Further research is required to see if a more satisfactory description of the connection time limited diffuse acceleration for energies close to the injection energy can be obtained. Last, we cannot completely rule out the steady state solution of Lee 1982, due to the ambiguity in fitting a power law vs. exponential spectrum over the limited energy range of our measurements. It is possible that a modification of the work of Lee 1982, such as the escape condition of the diffuse ions, could explain our observations. To fit observations, this would require that the scale size distance to the escape boundary be about an order of magnitude smaller than the standoff distance of Mercury's bow shock. All in all, these measurements of PSD profiles of diffuse populations at Mercury should provide interesting new constraints to the proposed mechanisms for diffusive shock acceleration.

5.5 Conclusions

The focus of this chapter was the first comprehensive application of the plasma measurements of the FIPS instrument to Mercury's foreshock environment. The FAB and diffuse plasma populations are successfully identified and quantified using the full directional capabilities of the FIPS instrument. We find on the order of several hundred diffuse events over the mission lifetime of MESSENGER, but only several 10s of FAB events. This may be due to the directional limitations of FIPS and the small velocity space angular extent of the FAB populations. The organization of the foreshock populations by θ_{bn} is confirmed, with FAB populations observed for $\theta_{bn} = [30^o, 70^o]$ and diffuse for $\theta_{bn} = [10^o, 40^o]$. Furthermore, the coexistence of 10-sec period waves with diffuse plasma populations is demonstrated.

For the diffuse observations a detailed analysis of the spatial decay of density with distance from the bow shock was performed. This allowed for an estimation of the diffusion coefficient in Mercury's quasi-perpendicular foreshock over a limited range of energies. The value of the diffusion coefficient was found to be consistent with the low energy range of observations in Earth's foreshock.

Last, an analysis of the energization processes that create these foreshock populations was performed. It was found that for FAB populations the framework of the SDA mechanism is a reasonable one based on the required length scales to produce the observed FAB energies. The typical FAB required about 0.13 R_M of drift length along the potential drop of the solar wind convective electric field to reach the observed energies. This is relatively small compared to the scale size of the bow shock ($\sim 3.35\ R_M$ at the flank), justifying the planar shock assumptions of SDA.

For the diffuse populations, the analysis focused on the specific mechanisms of diffusive shock acceleration that could create the observed diffuse distributions. This involved the quantification of the decay of the diffuse populations as a function of energy. Several theories including a steady state self-consistent diffuse shock acceleration and finite-connection time limited acceleration were explored and none were found to fully explain the observations. However, a study of the typical IMF connection times to the quasi-parallel bow shock and the estimated Fermi acceleration times suggest that the energization of the diffuse populations should be limited by connection time.

These first measurements of the foreshock plasma populations at Mercury provide constraints for current theories of particle acceleration in the foreshock. They also set an important precedent for comparison with future measurements of Mercury's foreshock. In particular the BepiColombo will arrive at Mercury in 2024 and consist of two spacecraft: the Mercury Planetary Orbiter (MPO) and the Mercury Magnetospheric

Orbiter (MMO). On the MMO spacecraft the High-energy ion sensor (HEP-ion) instrument will sample energies from 30-1500 keV mission (Saito et al. 2010). In particular, this energy range will enable more comprehensive analysis of the diffusion coefficients and the observed diffuse PSD distributions as discussed in this chapter. In general the broader range of energies will enable further investigation and understanding of shock acceleration mechanisms via the unique Hermean foreshock parameter regime.

Chapter 6 –Summary and Conclusions

6.1 Returning to the Guiding Science Questions

Several guiding questions relating to the heating and origins of plasma in the heliosphere are considered in this work. The signature of solar wind heating mechanisms revealed by heavy ions, the recovery of the ion and neutral composition of Mercury's exosphere, and the discovery of a foreshock plasma population at Mercury are the primary topics explored in pursuit of these questions. We revisit these questions below with short summaries of the new perspective provided by this research.

6.1.1 How well are coronal heating signatures created in the heavy ion population of the solar wind preserved by the time they are observed at 1 AU?

The heavy ion population in the solar wind is predominantly thermalized via Coulomb collisional interactions with solar wind protons. Organizing the thermal velocity ratio of heavy ions to protons by this collisional interaction with a "collisional age" parameter quantifies the degree of preservation of initial heating signatures. It is also discovered that not all heavy ions simply approach thermal equilibrium with proton as Coulomb collisions become more important. This behavior in heavy ion temperature could suggest a local heating mechanism that favors certain ions depending on their charge and mass.

6.1.2 What does the heating of heavy ions relative to protons observed in the solar wind at 1 AU tell us about solar wind heating mechanisms?

The heavy ions components in collisionally young solar wind, where the initial heating profiles should be best preserved, are analyzed and reveal a clear stable dependence on mass. We find that current model predictions based on turbulent transport and kinetic dissipation are in agreement with observed non-thermal heating in intermediate collisional age plasma for $m/q < 3.5$ amu/e, but are not in quantitative or qualitative agreement with the lowest collisional age results. It is crucial to note that these trends could not have been seen if only the He^{2+} population had been analyzed. This further demonstrates the usefulness of heavy ions as tracers to understand heating processes in the solar wind. These dependencies provide new constraints on the physics of ion heating in multi-species plasmas, along with predictions to be tested by the upcoming Solar Probe Plus and Solar Orbiter missions to the near-Sun environment.

6.1.3 What are the upper limits of previously unobserved heavy ions at the planet Mercury and what does that tell us about the magnetospheric dynamics, surface processes and planetary formation?

A detailed forward model and a robust statistical method were created to identify new ion signatures measurement space of the FIPS instrument. The initial validation of this method is performed over two large time intervals of FIPS measurements spanning several months, and average abundance ratios are recovered over this period. New heavy ions species recovered include Al, Ne, Si, and Mg, along with tentative recoveries of S, Ar, K, and Ca. Assuming ion production primarily via photoionization for these species, the neutral abundance ratio relative to Na is also recovered. For the best recovered new ion, Al, these yields an ion abundance ratio of 25% relative to Na, and a neutral ratio of about 0.15%.

This is the first time upper limits have been reported for the ion and neutral abundance for these species using the FIPS instrument. It is difficult to compare these recovered abundances, which are averaged over MESSENGER's entire orbital path within the magnetopause, to the predictions and measurements of the neutral surface and column abundances for Mercury's exosphere. The comparison of exospheric neutral ratios to surface abundances at Mercury is critical in constraining the dominant desorption mechanism at the planet's surface.

6.1.4 How effective are shock energization processes at the bow shock of a small planetary magnetosphere?

The efficacy of shock energization processes at the Hermean bow shock is carried out with the first identification of foreshock plasma populations with the FIPS instrument. With the development of many new tools and methods to enable this analysis, many aspects of the diffuse and FAB foreshock populations at Mercury were illuminated. One example is the quantification of the decay of diffuse plasma populations with distance from the quasi-parallel bow shock. The energization processes for the observed FAB and diffuse populations are also explored, per the guiding science question. One result suggests that the observed FAB energies can be explained by Shock Drift Acceleration, which is not limited by the small spatial size of Mercury's bow shock. For diffuse populations it is shown through estimates of the IMF-bow shock connection times and the Fermi acceleration time scale that a connection time limited diffusive shock acceleration is likely responsible for the behavior of the observed diffuse energy distributions.

6.2 Future Work

The investigations into the connection between heavy ion signatures and plasma heating phenomena in the solar wind and planetary magnetospheres have paved the way for future investigations. These new endeavors will not only focus on refining the work we have presented, but also on applying the concepts we have outlined to new (or even revisited) explorations within the heliosphere.

6.2.1 Heating signatures from heavy ions in other regions of the heliosphere

The heating signature discovered solar wind heavy ions measurements with the ACE/SWICS is only the tip of the iceberg in uncovering the dominant heating mechanisms in the solar wind. Future work should focus on primarily on missions that observe the solar wind at varying radial distances. One prominent mission scheduled to do so will be Solar Probe Plus, a spacecraft that will traverse from 1 AU to 9.86 solar radii from the Sun (Kasper et al. 2015). Solar Probe Plus will be able to directly observe the evolution of a limited set of ions in the solar wind as it propagates to 1 AU, perhaps comparable to measurements of the solar wind by MESSENGER. The upcoming Solar Orbiter mission will carry an instrument allowing independent mass and charge measurements of heavy ions as present in the ACE/SWICS work, but will not venture as close to the Sun, ranging 0.29-1.4 AU. The study of heavy ions in the solar wind does not have to be limited to future missions however. The Ulysses spacecraft traversed from 1-5 AU and carried an ion spectrometer almost identical to that onboard ACE/SWICS (von Steiger et al. 2000). A study of the collisional processes in the solar wind involving both the Solar Probe Plus and Ulysses data would allow for characterization of heavy ion kinetics in the solar wind over a broad range of solar distances, which would provide crucial constraints to many theories of solar wind heating.

6.2.2 Spatial and temporal refinement of heavy ion identification at Mercury

The work performed in this thesis is intended to serve as a stepping stone for future heavy ion analysis at Mercury. There is still more that can be accomplished with this powerful new tool for FIPS analysis. From a validation perspective, continuing work on laboratory measurements to corroborate the TRIM simulations used in the MLCA model could prove quite useful. There are some aspects of the TRIM model comparison with flight data that suggest energy losses from TRIM do not fully capture the losses seen in the flight version of the instrument.

From an analysis perspective, the next step would be to try and improve the spatial resolution of the ion recoveries. This would require finding the balance between having a statistically significant number of counts to resolve overlapping ion peaks, while still dividing the magnetosphere into reasonably sized regions for analysis. A first attempt at this division might divide the magnetosphere into dayside, cusp, plasma sheet, and plasma lobe region and look for significant differences in the ion recovery. This spatial resolution would aid in comparison to predictions and measurements of the neutral populations in Mercury's exosphere. Further attempts could focus on the different magnetospheric local time regions sampled by the MESSENGER orbit as Mercury orbits about the Sun. A deeper understanding of how the abundances of our recovered species vary spatially and temporally will allow for more direct connections between the variations in abundance and the changes in surface processes driving the exospheric compositional makeup.

6.2.3 Extended energy range and heavy ion investigation in foreshock

The work presented here showcased the first measurements of the foreshock plasma populations at Mercury and provides valuable constraints for current theories of particle acceleration in the foreshock. This work also sets an important precedent for comparison with future measurements of Mercury's foreshock. In particular the BepiColombo will arrive at Mercury in 2024 and consist of two spacecraft: the Mercury Planetary Orbiter (MPO) and the Mercury Magnetospheric Orbiter (MMO). On the MMO spacecraft the High-energy ion sensor (HEP-ion) instrument will sample energies from 30-1500 keV mission (Saito et al. 2010). As the FIPS instrument measured up to 10 keV ions, this energy range will enable more comprehensive analysis of the diffusion coefficients and the observed diffuse PSD distributions as discussed in Chapter 5.

Another important pursuit is to identify heavy ions in the foreshock region and compare their E/q distributions to those observed in the proton population. The near identical e-folding values across ion species in the diffuse populations of Earth's foreshock are an important constraint to proposed theories of shock acceleration and would be just as valuable in the Hermean foreshock. In general, the broader range of energies and ion species will enable further investigation and understanding of shock acceleration mechanisms via the unique Hermean foreshock parameter regime.

Appendix 1

SWICS Instrument Analysis

A1.1 How SWICS observes the solar wind

A1.1.1 Geometric viewing model

What follows is a brief description of a geometric model to describe how SWICS would observe a given distribution function in the solar wind. It is interesting as it does not make use of the typical “duty cycle” used with ACE/SWICS or Ulysses/SWICS to account for the fraction of the solar wind that is observable by the instrument. Instead it simply performs an accumulation of an input distribution function, in a RTN type coordinate frame, over a rotation of the spacecraft.

We start with an expression for the number of counts expected at each E/q step, i, in which counts are accumulated for a full spacecraft (S/C) rotation.

$$N_i = g \int_{t=0}^{t_{step}} \left[\iiint_{\Gamma(t)} f(\boldsymbol{v}')v' d^3\boldsymbol{v}' \right] \tag{A1.1}$$

In this equation, N_i is the number of counts measured, g is the geometric factor of the instrument (0.0185 cm^2 for SWICS), t_{step} is the step time or time to complete one spin (12 sec), $\Gamma(t)$ is the region of velocity space observed as a function of time, $f(\boldsymbol{v}')$, is the ambient distribution function, v' is the velocity, and $d^3\boldsymbol{v}'$ is a differential element of velocity space.

We convert from accumulating the number of counts over one time step to over one spin of the spacecraft, knowing the relation between angular position of the instrument aperture and the rotation rate is $\phi = \omega t$, where $\omega = \frac{2\pi}{12\ sec}$.

$$N_i = \frac{g}{\omega}\int_{\phi_{spin}=0}^{2\pi}\left[\iiint_{\Gamma(\phi_{spin})} f(\boldsymbol{v}')v'd^3\boldsymbol{v}'\right]d\phi_{spin} \tag{A1.2}$$

Now, we essentially have to evaluate this integral over one spin of the space craft. This will involve rotation from the RTN frame where the distribution function is specified (usually the solar wind distribution) to the sensor frame where we know the viewing geometry. This order of operation requires a bit of care, so we will adapt a more specific notation about what coordinate system we are referring to and describe the relation between the RTN or GSE frame and the sensor frame. We use RTN and GSE interchangeably in what follows to represent the frame the distribution function is specified in.

We start with the integration over GSE coordinates, as seen below.

$$N_i = \frac{g}{\omega}\int_{\phi_{spin}=0}^{2\pi}\left[\iiint_{\Gamma(\phi_{spin})} \left[f\left(v_{x,GSE}, v_{y,GSE}, v_{z,GSE}\right)v\right]\ dv_{x,GSE}\ dv_{y,GSE}\ dv_{z,GSE}\right]d\phi_{spin} \quad \text{(A1.3}$$

However, because we cannot easily express the region of phase space that is observed by SWICS in the GSE frame, we perform a change of variables to the frame of the sensor. This will transform the velocity components and change the form of the distribution function accordingly. This new integral can be expressed as,

$$N_i = \frac{g}{\omega}\int_{\phi_{spin}=0}^{2\pi}\left[\iiint_{\Gamma(\phi_{spin})}\left[h\left(v_{x,sensor}, v_{y,sensor}, v_{z,sensor}; \phi_{spin}\right)v\right]\ \left[d^3\boldsymbol{v}^*\right]\right]d\phi_{spin} \tag{A1.4}$$

, where

$$d^3\boldsymbol{v}^* = |J| dv_{x,sensor}\ dv_{y,sensor}\ dv_{z,sensor}. \tag{A1.5}$$

Note that, for a rotation, the determinant of the Jacobian, J, of the transformation equals one.

Now, in the final step, we will convert to spherical coordinates in this sensor frame to more easily implement the bound of the region observed by SWICS.

$$N_i = \frac{g}{\omega}\int_{\phi_{spin}=0}^{2\pi}\left[\int_{v=v_{i^-}}^{v_{i^+}}\int_{\theta=\theta_0}^{\theta_1}\int_{\phi_0}^{\phi_1} l\left(v,\theta,\phi;\phi_{spin}\right)v\ (v^2 sin\theta d\phi d\theta dv)\right]d\phi_{spin} \tag{A1.6}$$

In the previous expression, $l(v,\theta,\phi;\phi_{spin})$ is the form of the distribution function in this frame, note that it depends on the current value of ϕ_{spin}.

This last expression could then be evaluated numerically using the following recipe (at each E/q step, i.

1) Input v, θ, ϕ values in the sensor frame
2) Convert these to $\boldsymbol{v}$ in the GSE frame (frame rotation, more on this later)
3) Evaluate f($\boldsymbol{v}_{GSE}$**)** to find phase space density at a given location in the sensor frame, this gives $l(v,\theta,\phi;\phi_{spin})$

4) Repeat this calculation over a grid of v, θ, ϕ values, specified in the sensor frame (and evaluated in the GSE frame as described above). This grid of v, θ, ϕ values is then repeated for a set of ϕ_{spin} values ranging from [0, 2π]. This numerical integration will yield the expected counts at E/q step i, for one 12 minute sample cycle (12 second steps, 60 steps)

The bounds of the integral are then easily evaluated in the sensor frame and so the grid of v, θ, ϕ will then lie within these bounds. These bounds are as follows

The portion of phase space corresponding to the look direction of the SWICS instrument in the instrument frame (spherical coordinates) is

$[\theta_0, \theta_1] = [55^o, 59^o]$

$[\phi_o, \phi_1] = [0^o, 69^o]$

$[v_{i^-}, v_{i^+}] = depends\ on\ bounds\ of\ ith \frac{E}{q} step$

Therefore, the region of velocity space observed by SWICS is given by

$[\theta_0, \theta_1] = [\pi - 55^o, \pi - \ 59^o]$

$[\phi_o, \phi_1] = [\pi + 0^o, \pi + 69^o]$

$[v_{i^-}, v_{i^+}] = same\ as\ above$

as the look direction is the negative of the unit vector of the velocity vector it can observe.

With this method, one would essentially just have to specify a distribution function in GSE coordinates and then evaluate the integral given in (A1.6).

One of the more complicated aspects of this method is the rotations between the sensor frame and the GSE frame as the ACE spacecraft spins about its spin axis (roughly pointing toward the Sun). We will describe those in more detail now.

In Figure A1.1 we show the relation between the spin axis of the spacecraft and the solid angle that is observed by the SWICS instrument. The coordinate system here is that of the sensor frame and thus this coordinate frame is "fixed" on the SWICS instrument. The angle bounds discussed above are applicable in this coordinate frame and describe the solid angle region shown. We will now apply an Euler angle sequence to rotate from this sensor frame to the GSE frame where we can evaluate the specified distribution function.

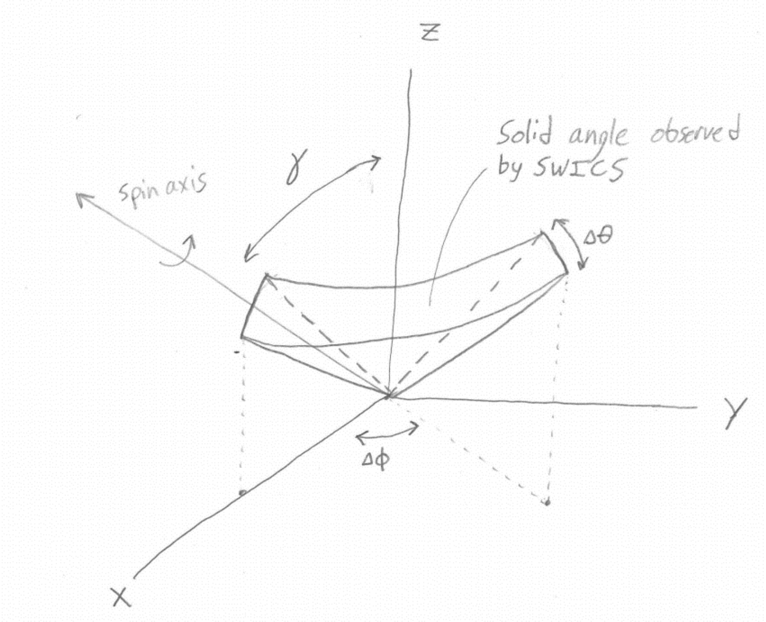

Figure A1.1: A sketch of the relationship between the solid angle in velocity space observed by SWICS and the rotation axis of the ACE spacecraft relative to this solid angle.

The advantage of an Euler sequence is we can break up the rotation into three simpler ones. Be sure to keep in mind that since SWICS rotates about the spacecraft spin axis, the exact mapping between the SWICS frame and the GSE frame has to depend on what phase about the spin axis SWICS is currently at. We specify this with ϕ_{spin}, and it will be more rigorously defined shortly.

The Euler sequence is shown schematically in

$$\begin{pmatrix} \mathrm{x} \\ \mathrm{y} \\ \mathrm{z} \end{pmatrix}_3 = (\mathrm{Q}_3\mathrm{Q}_2\mathrm{Q}_1)\begin{pmatrix} \mathrm{x} \\ \mathrm{y} \\ \mathrm{z} \end{pmatrix}_0 \tag{A1.10}$$

, where the rotation matrices are as defined above.

Figure A1.2, and we describe it in more detail in the text. The first rotation in the sequence rotates from the SWICS frame to a frame where the z-axis aligns with the space craft rotation axis. We number the frames starting with 0 for the SWICS frame and ending with 3, which will coincide with the GSE frame. That angle between the z0 and z1 axis is always $\gamma = 57^o$, so the first rotation matrix (which we will call Q1) is,

$$\begin{pmatrix} x \\ y \\ z \end{pmatrix}_1 = \begin{pmatrix} cos\gamma & 0 & -sin\gamma \\ 0 & 1 & 0 \\ sin\gamma & 0 & cos\gamma \end{pmatrix} \begin{pmatrix} x \\ y \\ z \end{pmatrix}_0 \tag{A1.7}$$

, which describes rotation about the y0 axis. The second rotation (Q2) will align the coordinate system with the current phase of the spin about the space craft spin axis. Since the spin axis now aligns with z1, this is simply rotation about z1 by the angle ϕ_{spin},

$$\begin{pmatrix} x \\ y \\ z \end{pmatrix}_2 = \begin{pmatrix} cos\phi_{spin} & sin\phi_{spin} & 0 \\ -sin\phi_{spin} & cos\phi_{spin} & 0 \\ 0 & 0 & 1 \end{pmatrix} \begin{pmatrix} x \\ y \\ z \end{pmatrix}_1 \tag{A1.8}$$

, where we now see that ϕ_{spin} is properly defined as the angle between x1 and x2. The final rotation (Q3) is simply for convenience to align with the GSE frame, it makes it so that the x-direction in GSE coordinate is in the direction of z2 (rotation axis of the spacecraft).

$$\begin{pmatrix} x \\ y \\ z \end{pmatrix}_3 = \begin{pmatrix} \cos\left(-\frac{\pi}{2}\right) & 0 & -\sin\left(-\frac{\pi}{2}\right) \\ 0 & 1 & 0 \\ \sin\left(-\frac{\pi}{2}\right) & 0 & \cos\left(-\frac{\pi}{2}\right) \end{pmatrix} \begin{pmatrix} x \\ y \\ z \end{pmatrix}_2 \tag{A1.9}$$

Now, we have defined our Euler sequence, such that that complete rotation between the SWICS frame and the GSE frame is given by,

$$\begin{pmatrix}x\\y\\z\end{pmatrix}_3 = (Q_3Q_2Q_1)\begin{pmatrix}x\\y\\z\end{pmatrix}_0 \tag{A1.10}$$

, where the rotation matrices are as defined above.

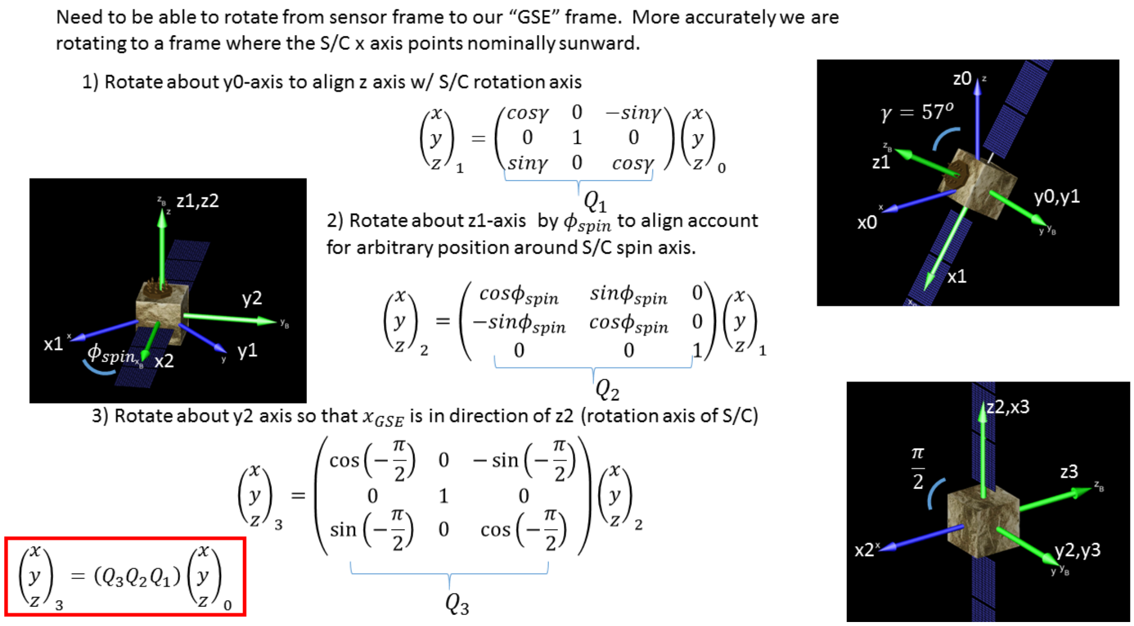

Need to be able to rotate from sensor frame to our “GSE” frame. More accurately we are rotating to a frame where the S/C x axis points nominally sunward.

1) Rotate about y0-axis to align z axis w/ S/C rotation axis

$$\begin{pmatrix}x\\y\\z\end{pmatrix}_1 = \underbrace{\begin{pmatrix}cos\gamma & 0 & -sin\gamma\\ 0 & 1 & 0\\ sin\gamma & 0 & cos\gamma\end{pmatrix}}_{Q_1}\begin{pmatrix}x\\y\\z\end{pmatrix}_0$$

2) Rotate about z1-axis by ϕ_{spin} to align account for arbitrary position around S/C spin axis.

$$\begin{pmatrix}x\\y\\z\end{pmatrix}_2 = \underbrace{\begin{pmatrix}cos\phi_{spin} & sin\phi_{spin} & 0\\ -sin\phi_{spin} & cos\phi_{spin} & 0\\ 0 & 0 & 1\end{pmatrix}}_{Q_2}\begin{pmatrix}x\\y\\z\end{pmatrix}_1$$

3) Rotate about y2 axis so that x_{GSE} is in direction of z2 (rotation axis of S/C)

$$\begin{pmatrix}x\\y\\z\end{pmatrix}_3 = \underbrace{\begin{pmatrix}\cos\left(-\frac{\pi}{2}\right) & 0 & -\sin\left(-\frac{\pi}{2}\right)\\ 0 & 1 & 0\\ \sin\left(-\frac{\pi}{2}\right) & 0 & \cos\left(-\frac{\pi}{2}\right)\end{pmatrix}}_{Q_3}\begin{pmatrix}x\\y\\z\end{pmatrix}_2$$

$$\boxed{\begin{pmatrix}x\\y\\z\end{pmatrix}_3 = (Q_3Q_2Q_1)\begin{pmatrix}x\\y\\z\end{pmatrix}_0}$$

Figure A1.2: A flow chart describing the Euler angle sequence employed to rotate between the SWICS frame and the GSE frame.

A1.1.2 SWICS solar wind recovery

With the machinery to evaluate how SWICS observed a distribution function specified in GSE coordinates, we now perform a few diagnostic checks on the SWICS instrument’s abilities. We will specify a drifting Gaussian in GSE coordinates, given by,

$$f(\boldsymbol{v}) = n(2\pi v_{th}^2)^{-\frac{3}{2}} \exp\left(-\frac{(\boldsymbol{v}-\boldsymbol{v}_0)^2}{2v_{th}^2}\right) \tag{A1.11}$$

, where all variables have their usually meaning. In line with previous SWICS work, we will test out a range of bulk and thermal velocities, but we will report the parameter range in terms of the Mach angle, $\Delta\Psi$, and the aspect angle, α. These are found to be most relevant to how SWICS observes a solar wind distribution and are described in von Steiger et al. (2000). The Mach angle is a proxy for the Mach number of the solar wind distribution and is given by,

$$\Delta\Psi = \mathrm{atan}\left(\frac{v_{th}}{v_0}\right) \tag{A1.12}$$

, where v_{th} is the thermal velocity of the Gaussian, and v_0 is the bulk velocity (in the anti-sunward direction). The aspect angle is the angle between the spacecraft rotation axis and the bulk velocity direction of the specified distribution (usually the solar wind). The aspect angle is then given by

$$\alpha = \mathrm{acos}(\hat{\mathrm{v}}_0 \cdot \hat{z}_1) \tag{A1.13}$$

, where $\hat{\mathrm{v}}_0$ is a unit vector in the direction of the solar wind bulk velocity, and $\hat{z}_1$ is a unit vector in the direction of the spacecraft rotation axis. The Mach angle and aspect angle aim to capture how wide the specified distribution appears in the angular space of SWICS, and where the center of the distribution falls relative to SWICS viewing angle, respectively.

For the first check, we evaluate the effect of SWICS rotation and limited observed solid angle on the observations of the solar wind. For a solar wind of about 450 km/s we look at each E/q step of our SWICS model and calculate how many counts SWICS would observe with its actual solid angle, and also with a full 4π steradian field of view. The results of this test can be seen in Figure A1.3. We are most interested in any variation of this count ratio across E/q steps, as that could skew the observed distribution function.

The fact that the ratio is less than unity is of less concern as that will simply scale the amplitude of the observed distribution function and won't affect the recovery of parameters like bulk and thermal velocity. The count ratio would be important for recovery of solar wind density, but that is not the focus of this analysis. There is some variation across E/q channels, but it is on the order of only a few percent.

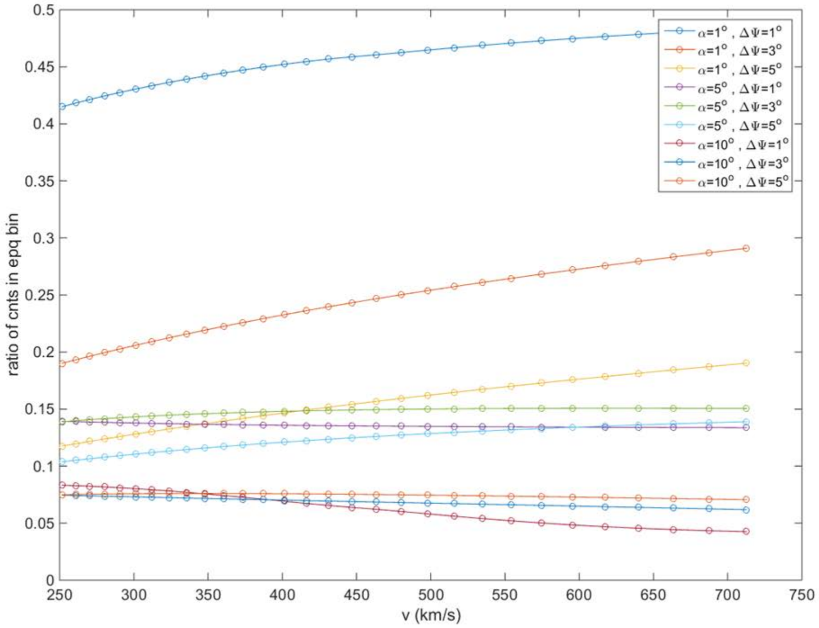

Figure A1.3: The ratio of measured counts for the SWICS instrument and an ideal 4π steradian instrument, computed for the first 30 E/q steps of the instrument.

To verify that the distribution functions observed by SWICS should not be skewed in velocity, we also show the measured distribution functions for a Gaussian solar wind input. We present a range of Mach and aspect angles in Figure A1.4. These different input parameter cases are labeled in the figure, and one should note that the variation in aspect angle has no effect on the observations of the 4π FOV instrument as all solar wind bulk velocities would have the same symmetry with respect to its FOV. In contrast, for the actual SWICS FOV, changes in aspect angle affect what portion of the distribution function lies within the FOV and as a result, the number of counts observed.

To summarize, we see that the 4π and SWICS FOVs for the same Mach angle are essentially the same within a scaling factor. We do not see any obvious signs of skewness caused the viewing geometry of the SWICS instrument.

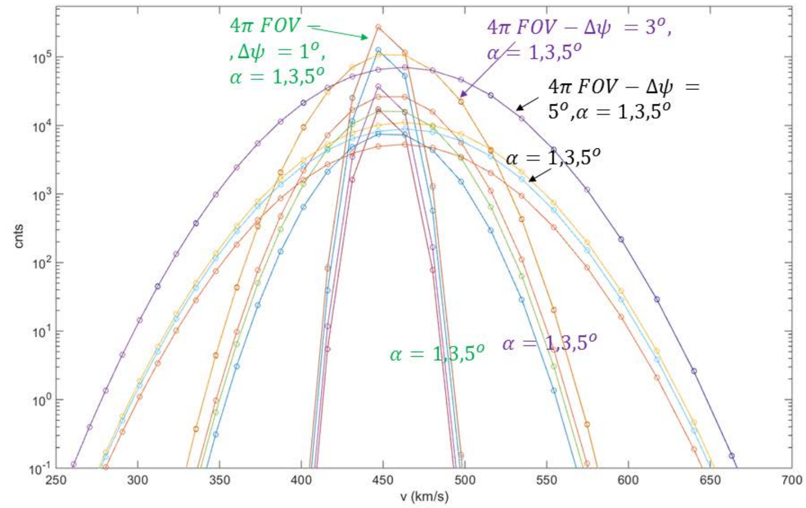

Figure A1.4: SWICS FOV versus a 4π FOV instrument observation of a Gaussian distribution function. All 3 of the 4π FOV curves for a given Mach angle lie on top of each other (as expected).

Another important difference between SWICS and an "ideal" instrument is the nature of the E/q bins employed by the instrument. The solid angle of SWICS determined the angular extent of velocity space that is observable, but the E/q binning determines the "radial" extent of observations in velocity space. In the case of SWICS, the E/q bins have noticeable gaps between E/q bins. Just to make the point that this can matter, we again present in

Figure A1.5 the ratio of observed counts at the first 30 E/q steps for two versions of our model of the SWICS instrument. We have assumed a 4π steradian FOV in both cases, but in the first case we take the exact E/q stepping (with gaps), of the instrument and in the second we expand the E/q steps so that there are no gaps. We see that the ratio of observed counts between these two cases can be very non-uniform, depending on the Mach angle of the observed distribution. We will investigate further into the effects of the E/q stepping of SWICS in the next section of the appendix.

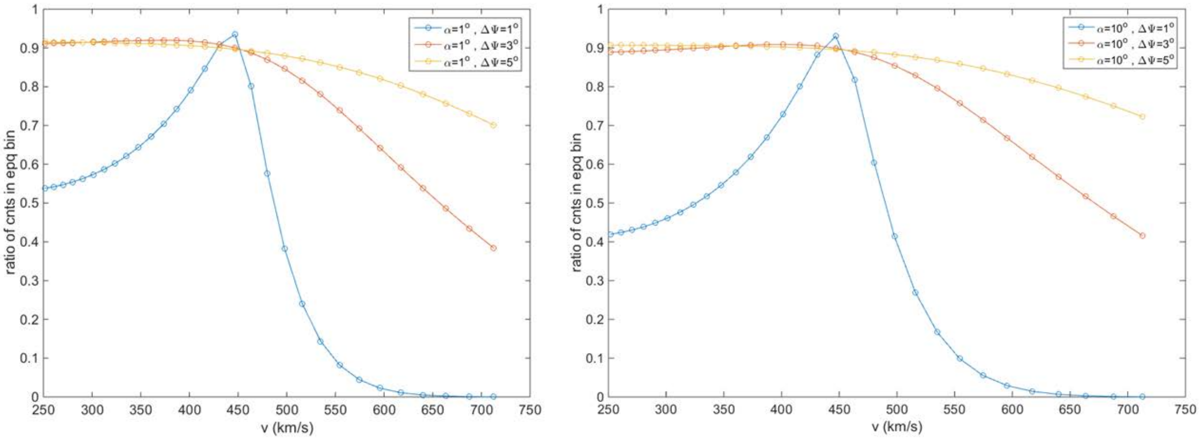

Figure A1.5: Comparison of the ratio of counts observed at 30 E/q steps of an ideal 4π instrument with the E/q stepping of SWICS, and an ideal 4π instrument with no gaps between its E/q steps.

The main focus of this first geometric model was how the angular viewing limitations of SWICS could affect the recovered plasma moments. We believe this is captured nicely in Figure A1.6, where we show the ratio between the recovered plasma parameters and the parameters of the input Gaussian distribution function. We see that the variation in the Mach angle is the most important factor in the recovery of both the bulk velocity and thermal velocity. However, the most important feature is that the parameter recovery is essentially the same for both the SWICS FOV and the ideal 4π FOV. This makes the point that it is not the viewing effects of SWICS that contribute to any bias in the recovery of solar wind bulk and thermal velocities.

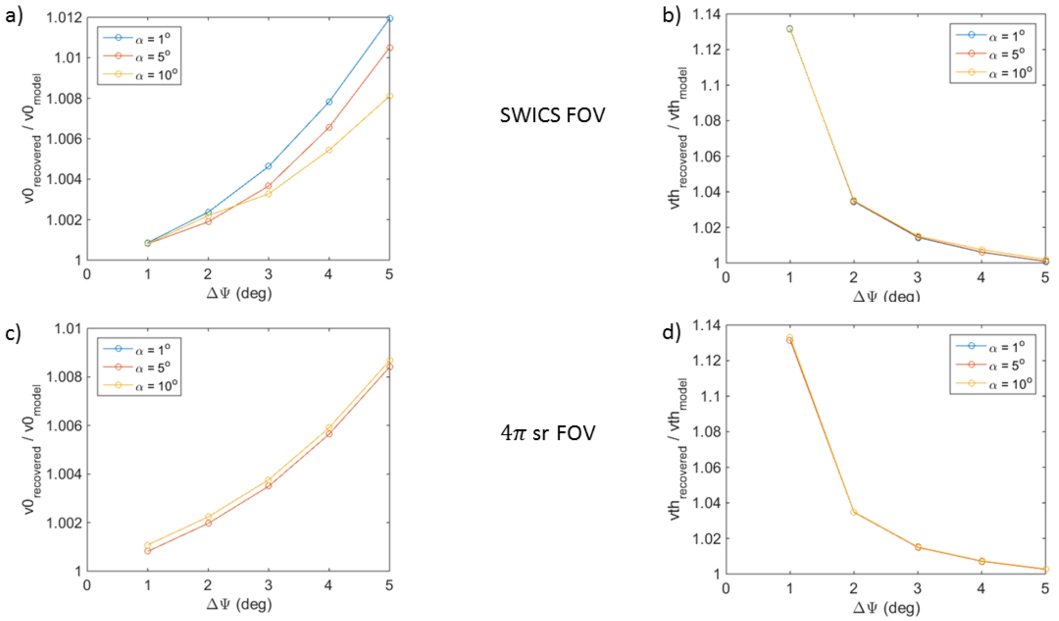

Figure A1.6: Comparison of the recovered bulk and thermal velocities to those of the input distribution function. In panels a), and b), we show the ratio of recovered and input bulk and thermal velocities, respectively, assuming the actual SWICS FOV constraints. In c) and d) we show that same plots, but assuming an ideal 4π steradian FOV.

As an additional caveat, we also verified that if there was a kappa distribution observed in the solar wind (Lividiotis and McComas 2013), that SWICS would be able to observe it distinct from a Gaussian. In Figure A1.7 we compare the count distribution recovered from input Gaussian and kappa distributions. It is clear to see that these distributions would clearly show up differently in the observed count distributions of the SWICS instrument.

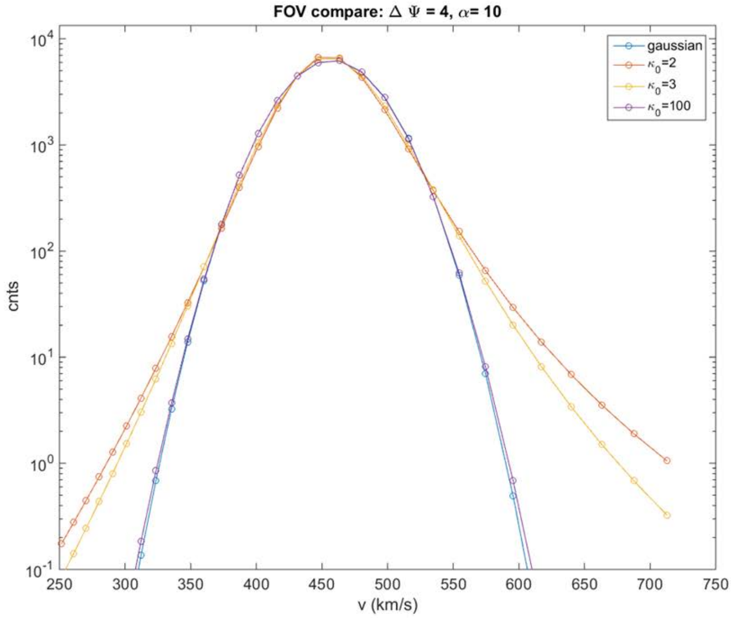

Figure A1.7: Comparison of the recovered count distribution for one Gaussian and several kappa input distribution functions.

The final conclusion of this section is that the viewing geometry of SWICS has a negligible effect on the recovery of solar wind bulk and thermal velocities. We must pursue other effects, such as E/q discretization, to explain discrepancies in recovered parameters.

A1.2 Discrepancies between SWICS and SWE

In the course of analyzing the thermal velocities of heavy ions for the work in Chapters 2 and 3, there was an extensive analysis that endeavored to track down discrepancies between the thermal velocities reported by ACE/SWICS and those reported by Wind/SWE. While a completely satisfactory explanation was never found, there were a number of promising ideas suggested and tested. We include a list of these attempts to assist in future pursuits (if they should occur) of the thermal velocities of ACE/SWICS.

The plot that very nicely summarizes the issue is that of Figure A1.8, where we show a summary of the comparison between SWE and SWICS measurements of the thermal velocity of alpha particles (He^{2+}) in the solar wind. We have selected all time periods where SWE and SWICS had valid data, and we have averaged the 92 sec SWE data set into the 2 hour resolution of the SWICS instrument. In panel a), we show the histogram of the measured He^{2+} thermal velocities for the two instruments. The two curves that are most important are the red curve and the light blue curve. The red curve is the SWE measurements and the light blue is the most recent reported value for SWICS, following the analysis by Shearer et al. (2014). It is clear from this plot that there are significantly more low thermal velocity He^{2+} measurements made by SWE than by SWICS.

In panel b) of Figure A1.8, we see that ratio of the thermal velocity of He^{2+} and H^+ histogrammed. Here it is obvious that SWE reports many more measurements of solar wind where the protons and alphas are at the same temperature (thermal velocity ratio equal 0.5). SWICS simply doesn't have these same measurements. Remember that these histograms are over exactly that same time periods when both SWE and SWICS were in orbits about the L1 point of the Earth-Sun system. It is therefore very unlikely that SWE

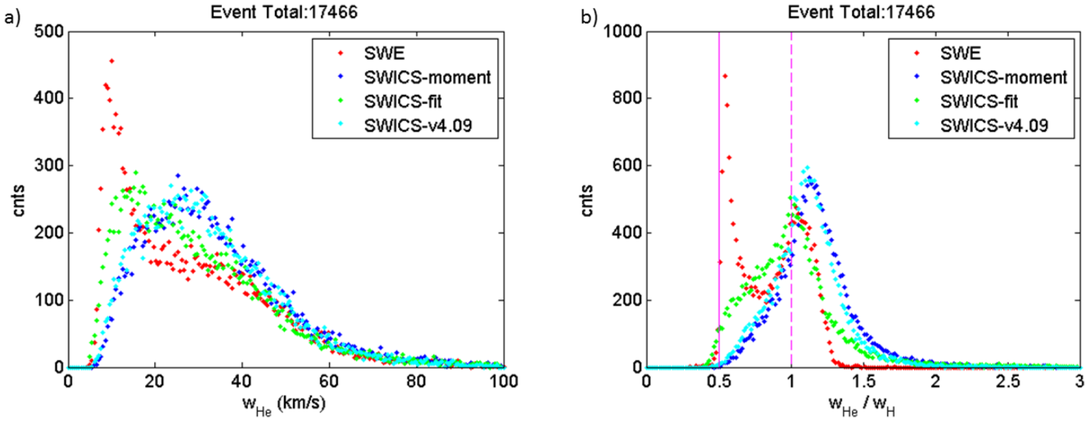

and SWICS were observing substantially different ambient solar wind populations. The question then remains, why do the two instruments measure thermal velocity differently?

Figure A1.8: In a) we show a histogram of the all the time periods where both SWICS and SWE had valid measurements of He2+ and H+ thermal velocities in the solar wind. The red curve represent the thermal velocity reported in the 92 sec data available on CDAWeb, which has been re-averaged into SWICS 2 hour resolution. The blue curve is the 2nd moment of the recovered phase space distribution as measured by SWICS. The green curve is the result of attempt to fit the SWICS distributions instead of taking moments. And last the light blue curve is histogram of the final version of the thermal velocities after the work of Shearer et al. 2014. In b) we show exactly the same curves, except now instead of histogramming the He2+ thermal velocity for the time periods, we histogram the thermal velocity ratio between He2+ and H+.

We expand upon what we have shown in the previous figure with a more detailed comparison of the thermal velocities measured by the two instruments. We again take all two-hour time periods where both SWE and SWICS had valid measurements He^{2+} thermal velocity in the solar wind and histogram them by the SWE reported values of bulk and thermal velocity. Then, in each bin of this histogram we compute what the average ratio between the SWE and SWICS thermal velocity is and shade the bin accordingly. The result of this weighted histogram is shown in Figure A1.9. In this format, we see that SWE reported a higher thermal velocity than SWICS for periods of high SWE thermal velocity (reddish and yellow region). This gradually transitions to SWE reporting lower thermal velocity than SWICS for low thermal velocity and high bulk velocity events (dark blue region). If SWICS and SWE recovered exactly the same thermal velocity values, this histogram would appear as solid green (with the chosen color table). Notice that the overall disagreement between SWICS and SWE can be as bad as 50% in some regions!

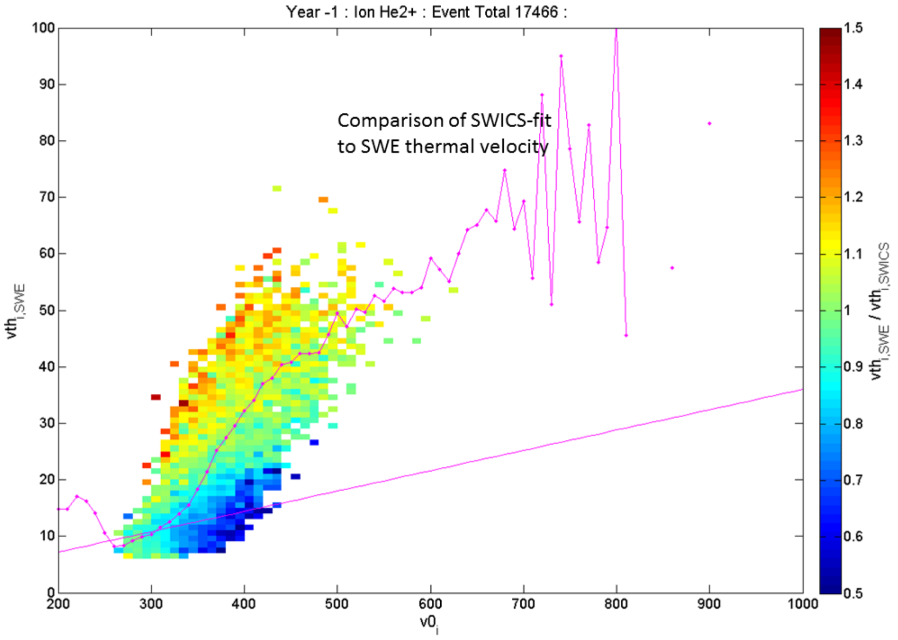

Figure A1.9: A weighted histogram of the SWICS and SWE He2+ thermal velocities. All events where both SWICS and SWE had valid measurements of He2+ thermal velocities are histogrammed according to the SWE reported bulk and thermal velocities of He2+. Then each bin of that histogram is shaded by the average SWE/SWICS thermal velocity ratio of the events in that bin.

It is clear that there is a discrepancy between the SWICS and SWE measurements, and our tactic was to try out likely sources of this discrepancy. The sources considered in this work are 1) Differences stemming from the fact that SWE uses fits to recover its thermal velocities and SWICS uses moments 2) The effects of kappa distributions increasing the apparent thermal width of the distribution 3) Time resolution differences between SWICS and SWE (a time variable Gaussian distribution measured over 92 sec by SWE and 2 hours by SWICS could appear differently), and 4) The effects of the E/q discretization and binning used by ACE/SWICS.

An example of our investigation into fits versus moments can be seen in Figure A1.10. In panel a) we show a summation of all events that fell into the bin defined by SWE thermal velocity [10,11] km/s and SWE bulk velocity [370,380] km/s. The summation of the count distributions for each event can be seen in red, and the summation of the modeled fits to these count distributions can be seen in blue. For this model we allowed for a kappa distribution in the fit, as described by Livadiotis and McComas (2013). What we are trying to discern from this model is if there is a way that the SWE distribution could be described as perhaps just a fit to the thermal width of the core of the kappa distribution, as a way to explain the smaller SWE velocities.

The SWE count distribution is estimated by assuming a Gaussian shape for the reported bulk and thermal velocities from the SWE data set. We sum together Gaussians for both the 2 hour averaged SWE data for each event (green circles) and also for the summation of raw 92 second SWE data within each 2 hour event period.

The SWE distribution being a fit to just the core of the SWICS distribution seems fairly plausible in panel b), but recall from Figure A1.9 that SWE and SWICS actually show good agreement at that point. In panel a), where there is large disagreement between SWICS and SWE it is hard to imagine that SWE could be a fit to the core of the measured SWICS count distribution. There is a significant difference between the distribution implied by the reported SWE thermal velocities, and the distribution observed by SWICS. Without the actual SWE distributions (which we have not obtained) we can’t investigate much further into comparing the raw distributions.

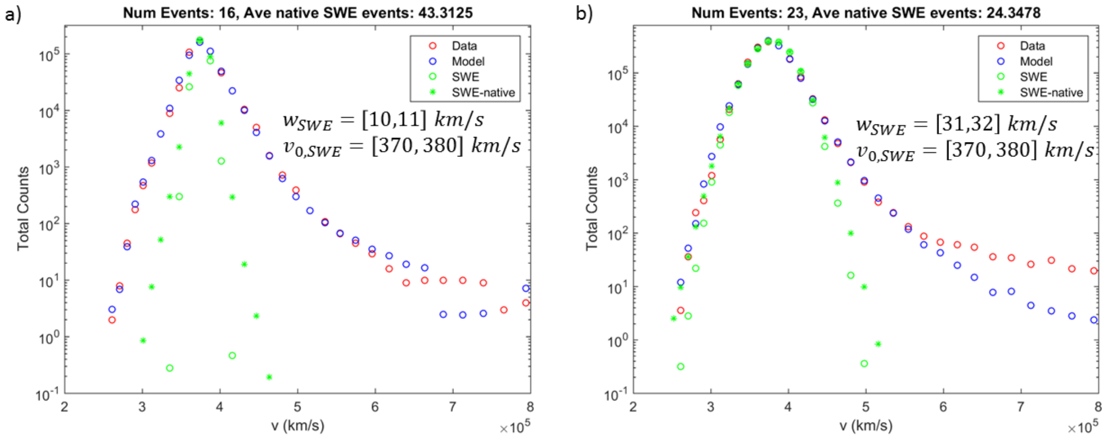

Figure A1.10: This figure is based on individual bins of Figure A1.9, that is, all events from a given bin are summed together and their distributions are compared. In red the sum of the count distributions for all SWICS events in that bin is shown, in blue the sum of all model fits to the SWICS data, in green circles the sum of a Gaussian distribution for all 2 hour averaged SWE events based on the reported SWE thermal and bulk velocities, in green stars the sum of Gaussian distributions for each 92 sec SWE event in each bin, based on reported SWE parameters. The criteria of SWE bulk and thermal velocities for choosing events that go into this plot is shown in the text inset into the plot.

We further the investigation of issue one and two by addressing the efficacy of fitting kappa distributions to our observed distributions in SWICS data. We initially tried to fit a sort of truncated Gaussian distribution to the core of our distributions, but soon realized that there was no justifiable way to decide where the "core" region ended. We would just get systematically different recovered thermal velocity values depending on where we arbitrarily defined the "core" to end. Tails appear to be an almost ubiquitous feature in the He^{2+} count distributions. Thus we were lead to the fitting of kappa distributions, where we referred to the work of Livadiotis and McComas (2013) for the proper definition of the thermal velocity of a kappa distribution. After a lot of time investment to get the kappa fitting scheme to work, we found that, when using the proper definition of thermal velocity, the recovered thermal velocities were very similar to those found in the moment scheme. We found some slight improvement in the lowest thermal velocity regime of SWICS measurements, but no major improvement in the values relative to those reported by SWE. These findings are summarized in Figure A1.11, where we see that the ratio between SWICS and SWE thermal velocities is essentially the same when using either the moment based calculation or the kappa fitting.

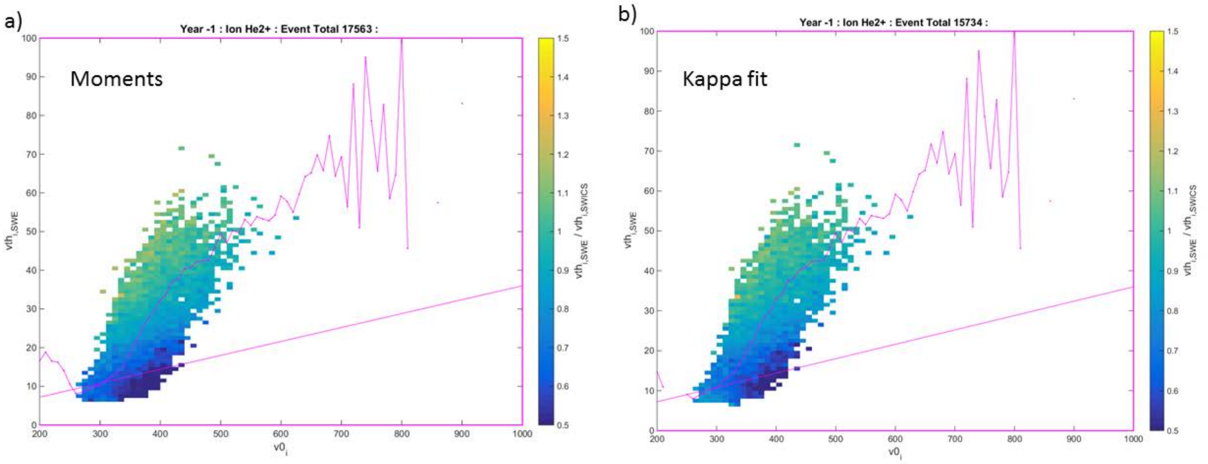

Figure A1.11: Summary of results of kappa fitting presented in the same format as Figure A1.8. In panel a) we repeat the information shown in Figure A1.8, just with a different color scale. In panel b), we shade the histogram bins like in panel a), but instead of the SWICS thermal velocity from moments, we shade by the recovered thermal velocity from the kappa fitting scheme.

Based on results so far we have concluded that we cannot explain the discrepancy by either differences in fitting or by modeling for kappa distributions in our data. Thus we move on to testing the time resolution considerations. To investigate this we calculated the standard deviation of the 92 second SWE observation over the 2 hour intervals that they are averaged into. We then histogram these standard deviation values against the reported SWE thermal velocity for that 2 hour event period. In this way we can look for trends in variability with measured thermal velocity. These histograms are presented in Figure A1.12. We can see that a there is an average standard deviation of about 4 km/s in the bulk velocity over the 2 hour measurement resolution of SWICS. This is fairly constant for events of all thermal velocities. The standard deviation of the SWE 92 sec thermal velocities is about 2-3 km/s when averaged into the SWICS time resolution. The question is whether these fluctuations can significantly affect the reported parameters of SWICS relative to SWE. The answer as we found it is that the standard deviation in the bulk velocity has to be comparable to the measured thermal velocity in order to significantly increase the recovered thermal velocity. However, we will incorporate the effect of a fluctuating solar wind in our final hypothesis test.

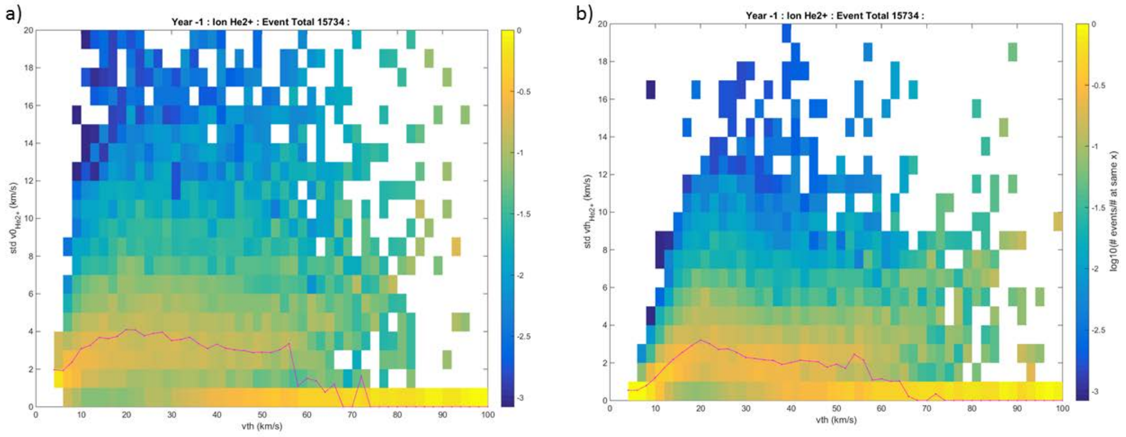

Figure A1.12: Here we present histograms of the standard deviations of the 92 second SWE plasma parameters over the 2 hour intervals that they are averaged into. The standard deviation of the 92 sec SWE bulk velocity values and the average of the 92 sec SWE thermal velocity value for each 2 hour SWICS time interval are histogrammed in panel a). In panel b) the standard deviation of the 92 sec SWE thermal velocity values and the average of the 92 sec SWE thermal velocity values for each 2 hour SWICS time interval are histogrammed.

The final effect to test, and the most promising, is the effect of the bin spacing and separation of the SWICS instrument. Our preliminary tests shows that discretization could have a large effect on the recovered thermal velocity values, particularly at low thermal velocities. The first model used a 1D integration of a Gaussian distribution over the E/q bins of the SWICS instrument. This took into account the actual widths of the bins in velocity space and also the gaps between the bins. After accumulating counts in theses bins, the moment was then computed in the same way as for the actual reported SWICS thermal velocities. We were confident in using a 1D model approach as our geometric model of the SWICS instrument (section A1.1) showed that viewing geometry had a very small effect in biasing SWICS plasma parameter recovery.

The primary factor in determining the severity of this discretization effect is the width of the distribution function relative to the spacing between the E/q bins of SWICS in velocity space. As you might expect, when the E/q bin spacing is on the order of the thermal velocity of the distribution function, you run into problems. We describe the width of the distribution function using the Mach angle, as discussed earlier. We input a Gaussian solar wind distribution and then integrate over the modeled SWICS E/q bins to accumulate counts and then take a moment of the counts in those bins to recover bulk and thermal velocity. The thermal velocity is the value focused on here. We find that as we vary the input solar wind bulk velocity, and the different parts of the distribution fall into the gaps between the E/q bins, the recovered thermal velocity can vary wildly for low Mach angle solar wind distributions. An example of this variability is shown in Figure A1.13. For Mach angles above about 1 degree, it doesn't matter where the bulk velocity of the solar wind falls relative to the SWICS bins, but below about 1 degree, the recovered thermal velocity varies wildly depending on the exact position of the solar wind distribution relative to the gaps between the SWICS E/q bins. This all stems naturally from our argument about the width of the solar wind distribution being on the order of the bin spacing. The main take away is that discretization effects can be important for low Mach angle solar wind.

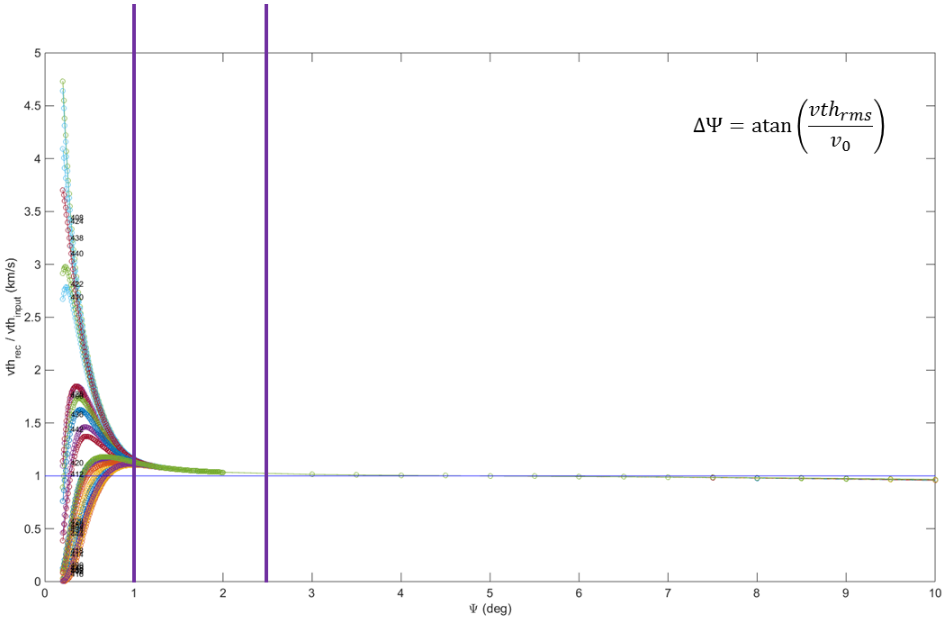

Figure A1.13: Here we show the results of a 1D model for SWICS observations of the solar wind using the actual E/q widths and spacing of the SWICS instrument. We input a solar wind distribution function, specified by a bulk and thermal velocity, and then compared the recovered thermal velocity to the input thermal velocity. This is done over a range of solar wind Mach angles and bulk velocities. Each curve represents a different bulk velocity, and the x-position of the data point on each curve corresponds to the Mach angle of that input condition. The y-axis shows the ratio for the recovered to input thermal velocity value.

In the last portion of this discussion, we effectively combine all the theories we have tested to see if together they can explain the observed discrepancy between the SWICS recovered thermal velocity and the SWE thermal velocities. We reiterate the discrepancy in terms of the Mach angle in Figure A1.14. The main panel we will focus on is panel a). This nicely summarizes the thermal velocity ratio between SWICS and SWE as a function of Mach angle. The low Mach angle correspond to times when the solar wind was “narrow” in its distribution, relative to the fixed spacing of the SWICS E/q bins. We see that the lower the Mach angle the larger the value of the SWICS recovered thermal velocity is relative to SWE.

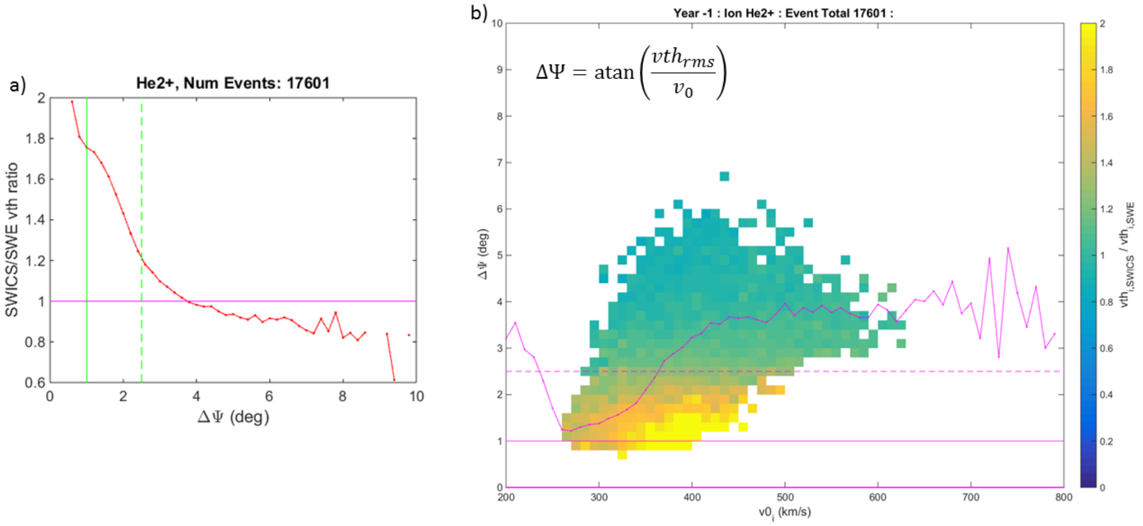

Figure A1.14: In panel a) we show the median value of the SWICS/SWE thermal velocity ratio in each Mach angle bin of a histogram over the Mach angle calculate from the SWE bulk and thermal velocities for the all 2 hour event period where SWICS and SWE both had valid solar wind measurements. Vertical lines are placed at Mach angles of 1 and 2.5 degree for reference. In panel b) we show a 2D histogram over the Mach angle and bulk velocity of all 2 hour event periods where SWICS and SWE both had valid solar wind measurements. Each bin is then shaded according to the average SWICS/SWE thermal velocity ratio in that bin. Horizontal lines at Mach angle of 1 and 2.5 degrees are included for reference.

We will attempt to reproduce this behavior with a 1D model of how SWICS would observe a solar wind distribution. To include all effects we can muster, we will input a 1D kappa distribution with a prescribed thermal velocity, bulk velocity, and $\kappa_0 = 4$ (see Livadiotis and McComas 2013 for details on κ_0). We also "smear" this input distribution by summing together distributions with a Gaussian distributed bulk velocity value, in line with the calculated standard deviation observed in the SWE 92 sec data of about 4 km/s. This resultant distribution is then integrated only over the extent of the E/q bins of SWICS, accounting for the gaps and spacing of the bins. The recovered count totals in each bin are then used to compute a moment and calculate the recovered thermal velocity the SWICS instrument should observe. The ratio of the recovered and input thermal velocity is then recorded, and plotted against the Mach angle of the input solar wind condition. This plot is shown in Figure A1.15, and curves of the same color correspond to a set of Mach angles that have the same solar wind bulk velocity. This plot has a lot of qualitatively correct features. We see the ratio of SWICS/SWE thermal velocities dip below unity at high Mach angle and we also see the SWICS/SWE ratio asymptotically increase as you get to the lowest Mach angles. However, if you just examine the portion of the plot between the green vertical lines, positioned at Mach angles of 1 and 2.5 degree, you will see that the predicted thermal velocity ratios from our model are still well below what is observed in the data. Further tweaking of the kappa distribution and the fluctuation of the bulk velocity (within reasonable values) still does not reproduce the observations.

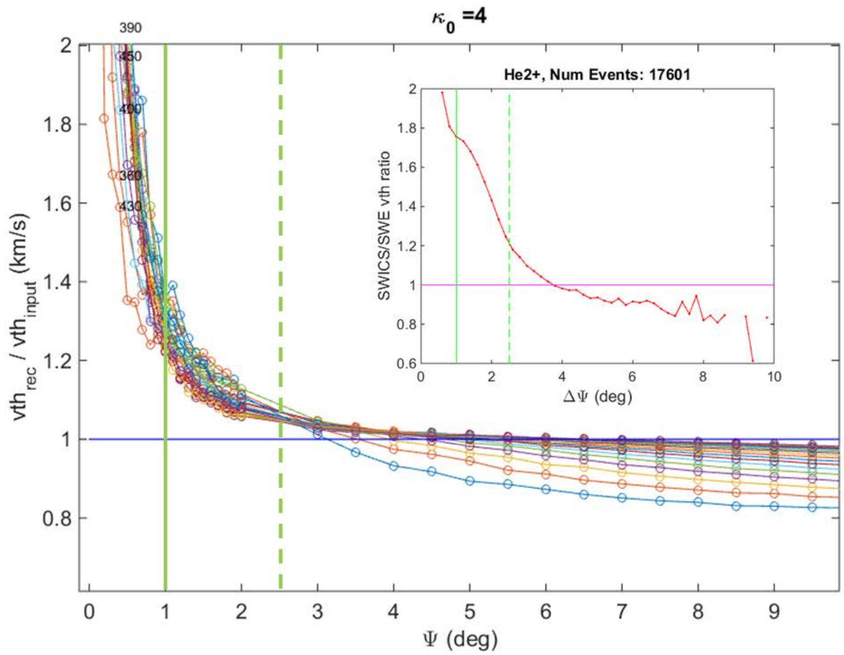

Figure A1.15: We present the results of a comprehensive 1D model of SWICS thermal velocity recoveries. The Mach angle of the incident solar wind distribution is shown on the x-axis, and the ratio between the recovered and input thermal velocity is shown on the y-axis. Curves of similar color correspond to a series of input condition Mach angles that all had the same bulk velocity. The observed disagreement between SWICS and SWE is inset on the plot, a reproduction of Figure A1.14a. Vertical lines are shown at Mach angle of 1 degree and 2.5 degree for reference and comparison with Figure A1.14a.

Thus, we have investigating several promising candidates to explain the observed SWICS/SWE thermal velocity ratio discrepancy, but there is likely another factor that has eluded us so far. Ideally we would like to be able to fully explain why SWICS and SWE measurements differ so we can have confidence in the thermal velocity values that we make use of in our scientific endeavors. The most promising and direct path to solve this issue is to acquire the base SWE distributions and compare them directly to those of SWICS.

A1.3 Statistical uncertainties in plasma moments

A1.3.1 Moment Expressions

The purpose of this appendix is to extend the results of Section 5.4 in Paul Shearer's ACE/SWICS document, located on aneris at /home/shearerp/axlv2_v4/report/aswx_report.pdf.

From section 5.3 of the aswx_report.pdf, we have that the total density from one count distribution is given by the differential density contributions at each E/q step of the count distribution, n_i.

$$n = \sum_i n_i \tag{A1.14}$$

This differential density distribution is then used to calculate all moments,

$$\langle v^k \rangle = \frac{\sum_i \ v_i^k n_i}{n} \tag{A1.15}$$

, where bulk and thermal velocity are calculated as

$$v_0 = \langle v \rangle \tag{A1.16}$$

$$v_{th} = \sqrt{\langle v^2 \rangle - \langle v \rangle^2} \tag{A1.17}$$

We can apply filtering to these results which slightly changes the expressions

$$n = \sum_{i \in I_f} n_i \tag{A1.18}$$

$$\langle v^k \rangle = \frac{\sum_{i \in I_f} v_i^k n_i}{n} \tag{A1.19}$$

, where I_f is the subset of E/q steps in the velocity filter.

A1.3.2 Relating Counts to Density

The Poisson error propagation is based on the number of counts in each E/q step propagated through the moment expression

$$n_i = c_i / K_i \tag{A1.20}$$

$$K_i = \Delta t v_i g D \left(\frac{\gamma}{\rho_i} \right) \eta_i \tag{A1.21}$$

You can see from (A1.20) and (A1.21) that the differential density is just the number of counts at a given step, c_i, times a step dependent constant factor. We will briefly describe the terms in (A1.21), for more details see Paul’s aswx_report.pdf.

Time for each step in a scan

$$\Delta t = 12\ sec \tag{A1.22}$$

Velocity at each step, i, is v_i. Calculated from E/q of that step, and mass/charge values of specific ion.

Geometric factor

In Paul's handout, he gives this as geometric factor

$$g = 0.181\ cm^2 \tag{A1.23}$$

, but in talking with Jim Raines, I think this is the actual value…

$$g = 0.0185\ cm^2 \tag{A1.24}$$

D is the duty cycle value, see Paul's handout for calculation of this.

E/q step relative width, $\Delta\left(\frac{E}{q}\right) = \left(\frac{E}{q}\right)\gamma$

$$\gamma = 0.064 \tag{A1.25}$$

Step-dependent growth factor

$$\begin{gathered} \rho_i = 0.0744\ for\ i \le 46, \\ \rho_i = 0.1544\ for\ i \ge 47 \end{gathered} \tag{A1.26}$$

Percent bandpass coverage (see appendix B.2 of Paul's report)

$$\delta_i = \frac{\frac{1}{4}\left(\left(1+\frac{\gamma}{2}\right)^2 - \left(1-\frac{\gamma}{2}\right)^2\right)}{\frac{1}{3}\left(\left(1+\frac{\rho_i}{2}\right)^{\frac{3}{2}} - \left(1-\frac{\rho_{i-1}}{2}\right)^{\frac{3}{2}}\right)} \approx \frac{\gamma}{\frac{1}{2}(\rho_{i-1}+\rho_i)} \tag{A1.27}$$

,where $\rho_0 = \rho_1$is defined for convenience.

And finally**, $\boldsymbol{\eta_i}$ is the detection efficiency** at a given E/q step. This is different for each ion, but is available in a table.

A1.3.3 Poisson Uncertainty from Counts

The Poisson uncertainty in the counts is calculated as in (65) of Paul Shearer's technical document. To account for times when every energy per charge step has zero counts, Paul uses the expression

$$\Delta c_i^2 = \max\left(\frac{1}{N_f}, c_i\right) \tag{A1.28}$$

, to calculate the counting uncertainty at each energy per charge step. The standard Poisson error for each step is $\Delta c_i^2 = c_i$, but that underestimated the uncertainty for times when $c_i = 0$. The new formula will yield a total uncertainty of one count for a species for a time step where no counts were observed at any energy per charge step.

Given the counting statistical error, Δc_i, the associated error Δn_i in the differential density is

$$\Delta n_i = \Delta c_i / K_i \tag{A1.29}$$

The error in the total density Δn is obtained by propagating the error in each step based the on the expression for density given in (A1.14)

$$\Delta f = \sum_i \left[\left(\frac{\partial \mathrm{f}}{\partial \mathrm{n_i}}\, \Delta n_i\right)^2\right] \tag{A1.30}$$

For density we have $f = \sum_i \; n_i$, which then has error of,

$$(\Delta n)^2 = \sum_i (\Delta n_i)^2 \tag{A1.31}$$

For bulk velocity, we have $f = \langle v \rangle$

$$(\Delta v_0)^2 = \sum_j \left[\left(\frac{\partial \mathrm{f}}{\partial \mathrm{n_j}}\ \Delta n_j\right)^2\right] \tag{A1.32}$$

$$(\Delta v_0)^2 = \sum_j \left[\left(\frac{\partial}{\partial n_j}\left(\frac{\sum_i\ v_i n_i}{\sum_i\ n_i}\right)\Delta n_j\right)^2\right] \tag{A1.33}$$

Using the quotient rule of differentiation

$$(\Delta v_0)^2 = \sum_j \left[\left(\frac{\left(\sum_i\ n_i\right)v_j - \left(\sum_i\ v_i n_i\right)}{\left(\sum_i\ n_i\right)^2}\ \Delta n_j\right)^2\right] \tag{A1.34}$$

$$(\Delta v_0)^2 = \left(\frac{1}{(\Sigma n_i)^4}\right)\sum_j \left[\left(\left(\left(\sum_i n_i\right) v_j - \left(\sum v_i n_i\right)\right)\Delta n_j\right)^2\right] \tag{A1.35}$$

For thermal velocity, we have $f = \sqrt{\langle v^2\rangle - \langle v\rangle^2}$

$$(\Delta v_{th})^2 = \sum_j \left[\left(\frac{\partial \mathrm{f}}{\partial \mathrm{n_j}}\ \Delta n_j\right)^2\right] \tag{A1.36}$$

$$(\Delta v_{th})^2 = \sum_j \left[\left(\frac{\partial}{\partial n_j}\left(\frac{\sum_i\ v_i^2 n_i}{\sum_i\ n_i} - \left(\frac{\sum_i\ v_i n_i}{\sum_i\ n_i}\right)^2\right)^{\frac{1}{2}}\Delta n_i\right)^2\right] \tag{A1.37}$$

Using the chain rule (for terms under the square root)

$$
\begin{aligned}
(\Delta v_{th})^2 = \sum_j \Bigg[\Bigg(\left(\frac{1}{2}\right) \Bigg(\frac{\sum_i v_i^2 n_i}{\sum_i n_i} & \\
- \left(\frac{\sum_i v_i n_i}{\sum_i n_i} \right)^2 \Bigg)^{-\frac{1}{2}} \Bigg(\frac{\left(\sum_i n_i\right) v_j^2 - \left(\sum_i v_i^2 n_i\right)}{\left(\sum_i n_i\right)^2} & \\
- 2 \left(\frac{\sum_i v_i n_i}{\sum_i n_i} \right) \left(\frac{\left(\sum_i n_i\right) v_j - \left(\sum_i v_i n_i\right)}{\left(\sum_i n_i\right)^2} \right) \Bigg) \Delta n_i \Bigg)^2 \Bigg] &
\end{aligned}
\tag{A1.38}
$$

To allow for filtering over the E/q steps to include in these expression as shown in (A1.18-A1.19), one simply changes the summation range over the indices to be the filtered range of indices. Change for the summation over “i” and over “j”.

Note: After inspection we found that the vth moment errors were unrealistically large due to the condition of (A1.28). This led to a large contribution to the uncertainty from the E/q bins at high velocity that had no counts. Thus we removed the conditions and let bins with zero counts have an uncertainty of zero.

A rough time series of the Poisson uncertainties calculated for He^{2+} and O^{6+} can be seen in Figure A1.16 and Figure A1.17, respectively. Notice that the uncertainties in bulk velocity are the smallest, followed by uncertainties in density and thermal velocity. He2+ generally has more observed counts that O^{6+}, which naturally leads to smaller counting uncertainties for He^{2+}. Statistical uncertainties in the thermal velocity of O^{6+} can be quite high at times, as seen in the third panel of Figure A1.17.

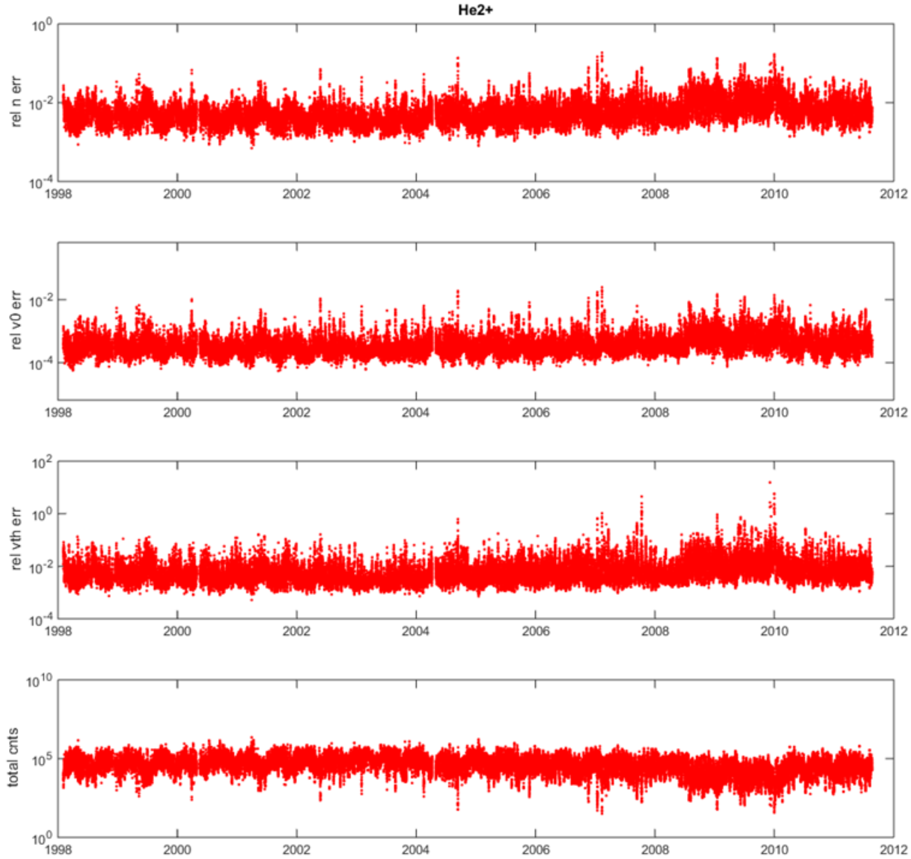

Figure A1.16: A time series of the relative error in density, bulk velocity, and thermal velocity for He2+ (panel 1,2,3). This error used here is only the statistical error propagated from Poisson counting statistics. The last panel is the total number of counts at each time step.

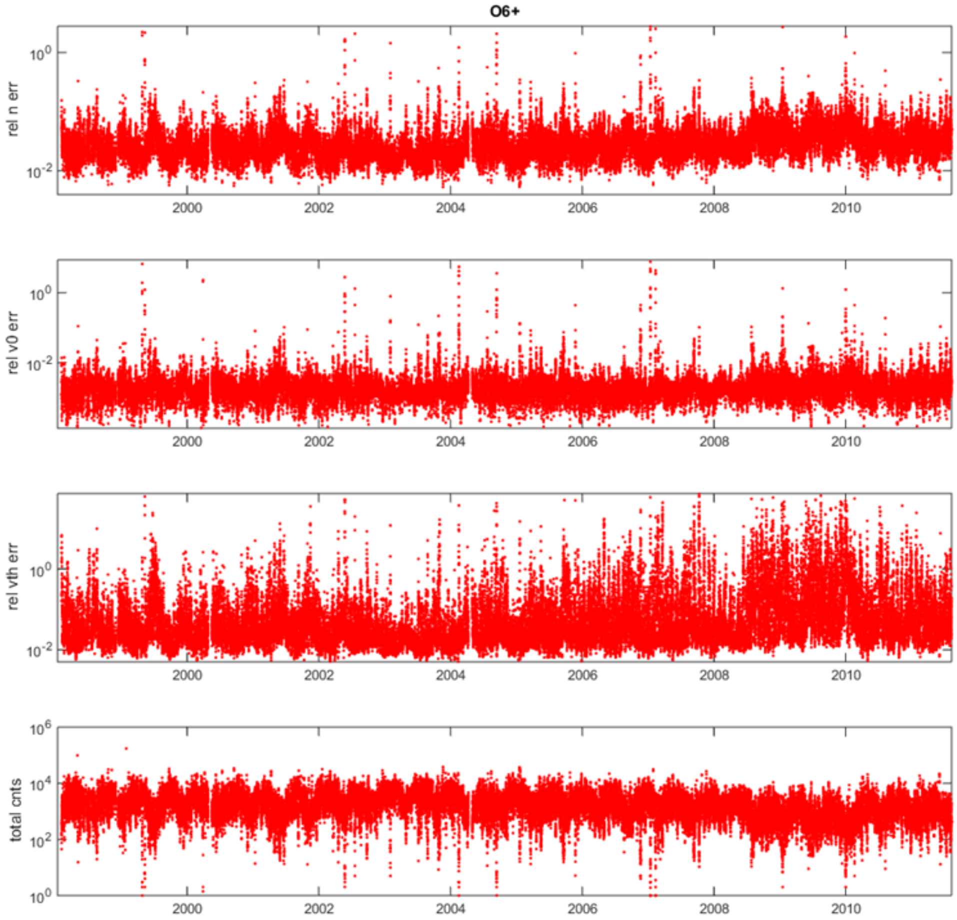

Figure A1.17: A time series of the relative error in density, bulk velocity, and thermal velocity for O6+ (panel 1,2,3). This error used here is only the statistical error propagated from Poisson counting statistics. The last panel is the total number of counts at each time step.

Appendix 2

FIPS Instrument Analysis

A2.1 FIPS counts to PSD derivation and related calculations

A2.1.1 Relating counts to PSD

Our first goal is to relate the number of counts that FIPS would observe to the phase space density of the plasma that is being observed. We are observing properties of the ambient plasma by passing it through an electric field in the FIPS instrument. Therefore it is worth mentioning that for an ideal instrument, the Louiville theorem guarantees that the phase space density measured by the instrument is the same as the incident phase space density in this situation.

We know that the total number of counts in a phase space element of dimension d^3xd^3v is given by

$$dN = f(\boldsymbol{x}, \boldsymbol{v})d^3xd^3v \tag{A2.1}$$

Thus the total number of particles (counts) in a volume of finite extent is obtained by integrating over the volume

$$N = \int_{\boldsymbol{x}} \int_{\boldsymbol{v}} f(\boldsymbol{x}, \boldsymbol{v})d^3vd^3x \tag{A2.2}$$

However, we want to know something slightly different for our instrument though, namely, the number of particles that would pass through into our instrument aperture in a time Δt.

It is instructive to consider the situation where a population of particles is incident on a flat plate. If the incident population were just a (spatially uniform) beam of particles with velocity $\vec{\boldsymbol{v}}_{\boldsymbol{0}}$ (directed toward the plate) and density n_0, then the number of particles that would pass through the plate in a time Δt is given by (we define the normal and velocity vector such that the dot product is positive, so we avoid any minus sign troubles)

$$N = \int_{\boldsymbol{v}} \int_{\boldsymbol{x}} f(\boldsymbol{x}, \boldsymbol{v}) d^3x d^3v \tag{A2.3}$$

$$N = \int_{\boldsymbol{v}} \int_{x} \int_{y} \int_{t} f(x, v) \left((\vec{\boldsymbol{v}} \cdot \hat{\boldsymbol{n}}\, dxdy) dt \right) d^3v \tag{A2.4}$$

Note that the infinitesimal volume element we are integrating depends on the velocity of the incident particle. A particle with a larger velocity normal to the plate can travel a farther distance in a time Δt and pass through the plate. We have defined the z axis to be normal to the plate in this case and $\hat{\boldsymbol{n}}$ is the normal to the plate (x and y are in the plane of the plate). Now, if we put in a delta function to represent the beam of particles with density g_0 and velocity $\vec{\boldsymbol{v}}_{\boldsymbol{0}}$**,** we will get the usual expression for flux through a surface.

$$N = \int_{\boldsymbol{v}} \int_{x} \int_{y} \int_{t} g_0 \delta(\vec{\boldsymbol{v}} - \overrightarrow{\boldsymbol{v_0}}) \left((\vec{\boldsymbol{v}} \cdot \hat{\boldsymbol{n}}\, dxdy) dt \right) d^3v \tag{A2.5}$$

$$N = g_0 (\vec{\boldsymbol{v}}_{\boldsymbol{0}} \cdot \hat{\boldsymbol{n}}) A \Delta t \tag{A2.6}$$

Where integrating over x and y produced the area of the plate, A. Note that if we divide out the density, n_0 what remains in this expression effectively defines a spatial region of particles with velocity $\vec{\boldsymbol{v}}_{\boldsymbol{0}}$**,** that will pass through a plate of area, A, in a time, Δt. One of the spatial dimensions becomes an integral over time (the vdt term) and so we are implicitly assuming in this integral that all quantities in the integral are constant with respect to time (at least over the short interval FIPS accumulates counts over). Thus when we integrate over time, the dt simply becomes a Δt for a finite time step.

The geometry of the FIPS instrument is a little more involved than the flat plate, so we will define new terms in analogy with the flat plate example that better represent the scenario for FIPS. Due to the design of the aperture and collimator, every incident direction that FIPS observes, $\widehat{\boldsymbol{v}}$, the infinitesimal area that the particle passes through is effectively normal to the incident direction for all incident directions. However, in principle, the magnitude of the area could vary between different incident directions. Thus we will reform our earlier expression for the volume element as

$$N = \int_{\boldsymbol{v}} \int_{\boldsymbol{x}} f(\boldsymbol{x},\boldsymbol{v}) \; \left((v\widehat{\boldsymbol{v}} \cdot \widehat{\boldsymbol{n}} dA) \mathrm{d}t \right) d^3 v \tag{A2.7}$$

$$N = \int_{\boldsymbol{v}} \int_{\boldsymbol{x}} f(\boldsymbol{x},\boldsymbol{v}) \; \left(dA(\widehat{\boldsymbol{v}}) \, v \mathrm{d}t \right) d^3 v \tag{A2.8}$$

Where we have introduced $dA(\widehat{\boldsymbol{v}}) = \widehat{\boldsymbol{v}} \cdot \widehat{\boldsymbol{n}}(\widehat{\boldsymbol{v}}) dA(\widehat{\boldsymbol{v}})$, the differential cross section area that a particle coming from direction $\hat{v}$ will see as it passes into the instrument. For the flat plate we would have, $dA(\widehat{\boldsymbol{v}}) = dxdy \; (\widehat{\boldsymbol{v}} \cdot \widehat{\boldsymbol{n}})$**,** where the dot product can vary for different incident directions. With the term $dA(\widehat{\boldsymbol{v}})$ we can apply our flat plate concepts to a larger range of geometric conditions, namely that of FIPS. An example of another geometry where this formulation may be useful is a cup-like aperature (as shown in Figure 1). Where the angle between the surface normal and incident velocity will not vary in the $\cos(\theta)$ fashion as it does for a flat plate.

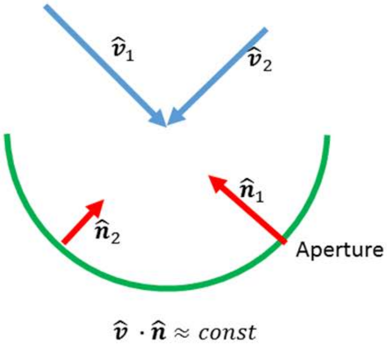

Figure A2.1: Sketch of a cup-like geometry. If the cup has small spatial extent, then the angle between the aperture normal and the incident particle velocity will be approximately constant (at about 0 degrees in this case) for every incident direction.

If we assume that $f(\boldsymbol{x}, \boldsymbol{v})$, is spatially uniform over the small aperture of FIPS (a reasonable assumption) and also constant over the time period of integration (the time period FIPS observes the particles) we can carry out the spatial integral as follows.

$$N = \int_{\boldsymbol{v}} \int_{\boldsymbol{x}} f(\boldsymbol{x}, \boldsymbol{v}) \; (dA(\hat{\boldsymbol{v}}) \, v\mathrm{d}t) \, d^3v \tag{A2.9}$$

$$N = \int_{\boldsymbol{v}} f(\boldsymbol{v}) v \left[\int_{\boldsymbol{x}} dA(\hat{\boldsymbol{v}}) dt \right] d^3v \tag{A2.10}$$

$$N = \int_{\boldsymbol{v}} f(\boldsymbol{v}) v \Delta t A(\hat{\boldsymbol{v}}) \, d^3v \tag{A2.11}$$

Where, we say that the differential cross sectional area for a given incident direction, $dA(\hat{\boldsymbol{v}})$, when integrated over the spatial extent of the FIPS aperture, gives the total cross sectional area for the incident direction, $A(\hat{\boldsymbol{v}})$.

$$N = \Delta t \int_{\boldsymbol{v}} f(\boldsymbol{v}) v A(\hat{\boldsymbol{v}}) \, d^3v \tag{A2.12}$$

If we now express the velocity space in spherical coordinates with the z-direction in the direction of the boresight of FIPS, we get

$$N = \Delta t \int_{v} \int_{\theta} \int_{\phi} f(v,\phi,\theta) v\, A(\theta,\phi)\, (dv)(v d\theta)\, (v sin\theta d\phi) \tag{A2.13}$$

Where $A(\hat{\boldsymbol{v}}) = A(\theta,\phi)$ in spherical coordinates. For a flat plate, the bounds of this integration would look like, the following. Note we are only integrating over velocity direction heading toward the plate!

$$N = \Delta t \int_{v} \int_{\theta=0}^{\pi/2} \int_{\phi=0}^{2\pi} f(v,\phi,\theta) A(\theta,\phi) v^3\, sin\theta\, dv\, d\theta\, d\phi \tag{A2.14}$$

Note that the bounds of the integral correspond to the flat plate geometry. For FIPS these bounds are not so well defined and we generally deal with solid angle in a discrete sense or else integrate over FIPS whole field of view with some assumption of isotropy. So in general

$$N = \Delta t \int_{v} \int_{\theta} \int_{\phi} f(v,\phi,\theta) A(\theta,\phi) v^3\, sin\theta\, dv\, d\theta\, d\phi \tag{A2.15}$$

We have now defined how to calculate the total number of counts observed by our instrument for an arbitrary phase space distribution. However, what we usually want to do is actually the reverse. That is, calculate the observed phase space distribution based on the total number of observed counts.

A2.1.2 Calculating observed phase space density from observed counts

FIPS has the ability to resolve incident particle energy per charge and also the direction that the particle came from. With these measurements we can reconstruct the three dimensional phase space distribution that FIPS observed at any one point in space (in-situ instrument). Each particle that FIPS observes is registered in one of its MCP pixels, where each pixel corresponds to a particular particle incident direction. Just as the MCP pixels discretize the direction space that incident particles can arrive, the energy steps of the FIPS instrument discretize the incident velocity that incoming particles can have. FIPS steps through various energy steps during each scan and at each energy step only particles with velocities (or more specifically E/q's) in a specific range can pass into the instrument ESA and be counted.

Let us examine the relation between counts observed by each pixel and the portion of the phase space distribution observed by that pixel. We left off the in the previous section with the following expression for the relation between counts and phase space.

$$N = \Delta t \int_v \int_\theta \int_\phi f(v, \phi, \theta) A(\theta, \phi) v^3 \, sin\theta \, dv \, d\theta \, d\phi \tag{A2.16}$$

Now, let's consider the number of counts observed by one pixel during one E/q step. This means we want the number of counts observed in an interval of $[v_1, v_2], [\theta_1, \theta_2], and\ [\phi_1, \phi_2]$. The E/q step defines the bounds v_1 and v_2 that v may lie between, and the MCP pixel and its mapping to incident particle direction defines the angular bounds, $\theta_1, \theta_2, \phi_1, \phi_2$, of the region of velocity space being observed. For FIPS it is valid to assume that $A(\theta, \phi) = A_{eff} = const$ within the angular range of a single MCP pixel. With these bounds we have,

$$N(v_1, v_2, \theta_1, \theta_2, \phi_1, \phi_2) = A_{eff} \Delta t \int_{v=v_1}^{v_2} \int_{\theta=\theta_1}^{\theta_2} \int_{\phi=\phi_1}^{\phi_2} f(v, \phi, \theta) v^3 \, sin\theta \, dv \, d\theta \, d\phi \tag{A2.17}$$

So this is the expression for the number of counts in our discrete interval. However, we don't know any information about how the phase space distribution varies within the interval (that is below our measurement resolution). Thus, we assume that the phase space information that we will retrieve is more accurately represented by the average of the actual ambient phase space distribution over the discrete interval we measured. We will also assume that every particle we measured came in with a velocity corresponding to the central value of the current E/q step (v_c) and a direction corresponding to the center of the current directional interval observed (θ_c, ϕ_c). We have no way of knowing the actual velocity and direction of the particles observed in a given bin to any better accuracy than this assumption. Let us consider what this implies about the phase space density that we recover.

Note that this implies that a notational equivalent for A_{eff} is $A(\theta_c, \phi_c)$ which is a constant over the range of an MCP pixel.

Recall the following from calculus, the definition of the average of a function over an interval, [a,b] is

$$g_{ave}(a,b) = \frac{1}{b-a}\int_{x=a}^{b} g(x)dx \tag{A2.18}$$

For our 3D spherical geometry in velocity space, this average will take the following form.

$$g_{ave}(v_1, v_2, \phi_1, \phi_2, \theta_1, \theta_2) \\ = \frac{1}{\int_{\phi=\phi_1}^{\phi_2}\int_{\theta=\theta_1}^{\theta_2}\int_{v=v_1}^{v_2} 1\, v^2 sin\theta dv d\theta d\phi} \int_{v=v_1}^{v_2}\int_{\theta=\theta_1}^{\theta_2}\int_{\phi=\phi_1}^{\phi_2} g(v,\phi,\theta)\, v^2\, sin\theta\, dv\, d\theta\, d\phi \tag{A2.19}$$

And if the volume we are integrating over is small, we can approximate the volume by

$$\int_{\phi=\phi_1}^{\phi_2}\int_{\theta=\theta_1}^{\theta_2}\int_{v=v_1}^{v_2} 1\, v^2 sin\theta dv d\theta d\phi \approx\ (\Delta v)\ (v_c sin\theta_c \Delta\phi)\ (v_c \Delta\theta) \tag{A2.20}$$

, where $\Delta v = (v_2 - v_1), \Delta\theta = (\theta_2 - \theta_1), \Delta\phi = (\phi_2 - \phi_1)$. We have used the subscript c to denote the value at the bin center (center of region we are integrating over). This is just the definition of a spherical volume element, note that each term in parenthesis on the right hand side of the above equation has units of velocity (no steradians). Each of the factors out in front of the integral (eqn 19) in the definition of the volume (the denominator) have units of$(\frac{m}{s})$, with NO radians or steradians! Remember that it is the multiplication of the angular widths by the appropriate factor of v that converts radians (or steradians) into regular velocity units. That is, just like multiplying a radius by the angle spanning a circular arc, in radians, gives the arc length of that circular arc, multiplying solid angle by r^2 gives the corresponding area on a sphere (the sphere exists in velocity space in this case).

For our case the function that we would be averaging over our velocity space volume is

$$g(v, \theta, \phi) = f(v, \theta, \phi)v \tag{A2.21}$$

So what we will get is an average value of this term over our interval. Thus,

$$\begin{aligned} &< f(v_1, v_2, \phi_1, \phi_2, \theta_1, \theta_2)v > \\ &= \frac{1}{(\Delta v)\ (v_c sin\theta_c \Delta\phi)\ (v_c \Delta\theta)} \int_{v=v_1}^{v_2}\int_{\theta=\theta_1}^{\theta_2}\int_{\phi=\phi_1}^{\phi_2} f(v, \phi, \theta)v\ v^2 sin\theta\ dv\ d\theta\ d\phi \end{aligned} \tag{A2.22}$$

Or, specifying the interval by the values at the center of the interval

$$\begin{aligned} &< f(v_c, \theta_c, \phi_c)v > \\ &= \frac{1}{(\Delta v)\ (v_c sin\theta_c \Delta\phi)\ (v_c \Delta\theta)} \int_{v=v_1}^{v_2}\int_{\theta=\theta_1}^{\theta_2}\int_{\phi=\phi_1}^{\phi_2} f(v, \phi, \theta)v\ v^2 sin\theta\ dv\ d\theta\ d\phi \end{aligned} \tag{A2.23}$$

Where we have used the <> notation to indicate the average of the quantity. Putting this definition into our expression for the number of counts observed over our interval gives,

$$N(v_1, v_2, \theta_1, \theta_2 , \phi_1, \phi_2) \\ = A_{eff} \Delta t \; (\Delta v) \; (v_c sin\theta_c \Delta\phi) \; (v_c \Delta\theta) \; \langle f(v_c, \theta_c, \phi_c) v \rangle \tag{A2.24}$$

Now, by definition the value $\langle f(v_c, \theta_c, \phi_c) v \rangle$ is constant over the interval we integrated over. It also makes good sense that the average value of this "flux-like" quantity is what we recovered as the FIPS instrument by its very nature measures flux. So, to get to phase space density, we make one more assumption. We calculate the value of $f(v_c, \theta_c, \phi_c)$ at the center of our interval that corresponds to the average value $\langle f(v_c, \theta_c, \phi_c) v \rangle$ over that interval (we assume that $f(v_c, \theta_c, \phi_c) v_c = \langle f(v, \theta_c, \phi_c) v \rangle$). Thus we take

$$f_{recovered}(v_c, \theta_c, \phi_c) = \frac{< f(v_c, \theta_c, \phi_c) v >}{v_c} \approx f(v_c, \theta_c, \phi_c) \tag{A2.25}$$

Note that we have not directly approximated the phase space density. We have only calculated a value of f that is consistent with the measured average flux at the center of each velocity interval. If we would have used the velocity at the edges of the bin, we would have calculated a different phase space density value. In general, we should assume that this value of derived phase space density corresponds only to a single velocity, v_c, if we are not assuming that f is constant over each interval. With our definition that the average flux $< fv >$ is constant over the interval, we will actually have that the recovered phase space density will vary as $1/v$ over the interval. This is a subtle point in our assumptions for the recovery of phase space density, the fact that we have only recovered a point value corresponding to a phase space density at the bin center that is consistent with the measured average flux over the interval.

But, there is a case where the recovered value of f makes physical sense. If we assume that the velocity interval is small enough then we can assume (to zeroth order) that $f =$

$const$ over the entire velocity interval. This would then imply that the quantity fv would vary linearly across the interval. If this is the case, then the average value of fv over the interval, $< fv >$ is equivalent to the value of fv at the center of the interval (Mean Value Theorem). Thus if $f = const$ over the interval in question, we have

$$f_{recovered}(v_c, \theta_c, \phi_c) = \frac{< f(v_c, \theta_c, \phi_c)v >}{v_c} = \frac{f(v_c, \theta_c, \phi_c)v_c}{v_c} = f(v_c, \theta_c, \phi_c) \quad \text{(A2.26)}$$

So, if the assumption of $f = const$ over the interval is valid then the phase space density we recover will actually directly correspond to the ambient phase space measured by FIPS.

With this final assumption, we can now relate the recovered phase space density at the center of an interval with the number of counts observed in that interval.

$$N(v_c, \theta_c, \phi_c) = A_{eff}\Delta t\ (\Delta v)(v_c sin\theta_c \Delta\phi)(v_c\Delta\theta)\ f(v_c, \theta_c, \phi_c)\ v_c \quad \text{(A2.27)}$$

Where $\Delta v = (v_2 - v_1), \Delta\theta = (\theta_2 - \theta_1), \Delta\phi = (\phi_2 - \phi_1)$. Note again that each of the first three terms in parentheses have units of velocity, a steradian is removed with the appropriate multiplication by v_c. These are precisely in line with the definition of a spherical volume element.

This is the expression we have been working toward, but we can express it a little more conveniently. In practice we do not specify the width of the velocity interval with a width in velocity, but instead with a width in E/q. We will assume that Δv is sufficiently small that we can use differential notation/operations and relate dv to $d(\frac{E}{q})$. Thus we have,

$$\frac{E}{q} = \frac{1}{2}\frac{m}{q}v^2 \tag{A2.28}$$

$$d\left(\frac{E}{q}\right) = \frac{m}{q}\ v\ dv \tag{A2.29}$$

$$dv = \frac{d\left(\frac{E}{q}\right)}{\frac{m}{q}\ v} \tag{A2.30}$$

$$= \frac{\frac{1}{2}v * d\left(\frac{E}{q}\right)}{\frac{1}{2}v * \frac{m}{q}\ v} \tag{A2.31}$$

$$= \frac{\frac{1}{2}\ v\ d\left(\frac{E}{q}\right)}{\frac{1}{2}\frac{m}{q}\ v^2} \tag{A2.32}$$

$$= \frac{1}{2}\ v \frac{d\left(\frac{E}{q}\right)}{\frac{E}{q}} \tag{A2.33}$$

$$dv = \frac{1}{2}\ v\ \delta \tag{A2.34}$$

This expression for the velocity width is actually a first order approximation of the actual bin width (valid for small δ).

Where we define δ to be the relative width in energy per charge of each velocity interval, which is approximately a constant for the FIPS instrument. Note that the v in the above expression will be assumed to be equal to v_c for a given velocity bin. Thus the number of measured counts from our interval centered on v_c, θ_c, ϕ_c is

$$N(v_c, \theta_c, \phi_c) = \frac{1}{2} A_{eff} \Delta t \ (sin\theta_c \Delta\phi \ \Delta\theta) \ \delta \ v_c^4 \ f_{ave}(v_c, \theta_c, \phi_c) \qquad \text{(A2.35)}$$

For the specifics of the FIPS instrument, the A_{eff} term is generally considered constant for all incident direction (all MCP pixels). It also convenient to note that for the design of FIPS, the $sin\theta_c \ \Delta\phi \ \Delta\theta$, solid angle term for each pixel that observes counts is approximately the same. Thus each pixel in the FIPS instrument corresponds to about the same solid angle of observation. In (35) you should note that the quantity $A_{eff}\epsilon(\sin(\theta_c) \ \Delta\phi\Delta\theta)$ generally varies by less than 30% across all incident direction (MCP pixels). One last thing to note is that generally the solid angle term and the A_{eff} term are combined into the geometric factor for the instrument.

When we consider the observing efficiency, ϵ, of the instrument in this case, we can account for the pixel dependent efficiency and the energy dependent ones as we know the incident direction and therefore the pixel that a given count landed on. This gives

$$\frac{N(v_c, \theta_c, \phi_c)}{\epsilon(v_c, \theta_c, \phi_c)} = \frac{1}{2} A_{eff} \Delta t \ (sin\theta_c \Delta\phi \ \Delta\theta) \ \delta \ v_c^4 \ f_{ave}(v_c, \theta_c, \phi_c) \qquad \text{(A2.36)}$$

Where $N(v_c, \theta_c, \phi_c)$ is the actual observed counts in a given interval and $\frac{N(v_c,\theta_c,\phi_c)}{\epsilon(v_c,\theta_c,\phi_c)}$ is the number of counts incident on the instrument in a given interval. This correction to get actual incident counts is also where any dead time limitations in instrument sampling rate should be taken into account. From this expression we recover the value of phase space density *at the center* (see above assumptions) of each measured interval.

A2.1.3 Estimating phase space information from rates (instead of PHAs)

This scenario is particularly relevant when working with proton data. It is often the case that we have a lot of observed protons, but did not have the telemetry to include the 3D data with those protons. Thus we know the E/q for the protons, but not the arrival direction information. This means we cannot recover full 3D phase space distribution information. However, it is often useful to recover the speed distribution of the observed particles.

This method is almost identical to the derivation we completed for each MCP pixel (above). The difference is that we are now considering the entire FIPS FOV as one effective pixel in this new case (as we do not know which pixel each particle was actually detected by). Thus, the solid angle of this effective pixel will be $sin\theta_c \Delta\phi \Delta\theta = \Delta\Omega_{\text{full FOV}}$, where $\Delta\Omega_{\text{full FOV}}$ is the full field of view of the FIPS instrument (about 1.15π sr). The values of $\epsilon(v_c, \theta_c, \phi_c)$ also have to be modified to be for the entire field of view. This means that the effective efficiency must be a representative average of all the MCP pixel efficiencies, $\epsilon'(v_c)$.

$$\frac{N(v_c)}{\epsilon'(v_c)} = \frac{1}{2}\, A_{eff}\, \Delta t\, \Delta\Omega_{\text{full FOV}}\, \delta\, \mathrm{v}_\mathrm{c}^4\, f_{ave}(v_c) \tag{A2.37}$$

A2.1.4 Computing differential flux for each incident direction (MCP pixel)

The total flux passing through one pixel of the FIPS instrument is given by

$$\Phi_{flux,pixel} = \int_{\phi=\phi_1}^{\phi_2} \int_{\theta=\theta_1}^{\theta_2} \int_{v=0}^{\infty} v\, f(\vec{v})(dv)(vd\theta)(vsin\theta d\phi) \tag{A2.38}$$

Where we are integrating over the entire velocity range of the FIPS instrument. The total flux passing through one pixel will have units of #/(m^2 * sec). The definition of differential flux that we are interested in is the differential flux *per energy step per solid angle*. To achieve this quantity we will manipulate the above equation into a form where we can read off differential flux, $\frac{dJ}{dE}$.

We have no information about any variation within a pixel, since it is below the resolution of the instrument. Therefore we have to assume that phase space density is uniform over the solid angle of the individual pixel we are computing the flux over (or equivalently, assume that we have obtained the average phase space density over that discrete interval as shown in the counts to phase space density calculation shown above). Thus f doesn't vary with θ, ϕ within a given pixel, and we can pull $f(v, \theta_c, \phi_c)$ out of the angular integrals.

$$\Phi_{flux,pixel} = \left[\int_{\phi=\phi_1}^{\phi_2} \int_{\theta=\theta_1}^{\theta_2} sin\theta d\phi d\theta\right] * \int_{v=0}^{\infty} f(v, \theta_c, \phi_c) v^3 dv \tag{A2.39}$$

$$= \Delta\Omega_{\text{pixel}} * \int_{v=0}^{\infty} f(v, \theta_c, \phi_c) v^3 dv \tag{A2.40}$$

Where $\Delta\Omega_{\text{pixel}}$ is the solid angle of the pixel we are integrating over. Next we will use the relation between energy and velocity to change the integration variable of the velocity integral.

$$E = \frac{1}{2} m v^2 \tag{A2.41}$$

$$dE = mv\, dv \tag{A2.42}$$

So that we can rewrite the integral as (dropping the θ_c, ϕ_c dependence of f for simplicity)

$$\Phi_{flux,pixel} = \Delta\Omega * \int_v f(v)v^3 dv \tag{A2.43}$$

$$= \Delta\Omega * \int_E f(v)v^3 \left(\frac{dE}{mv}\right) \tag{A2.44}$$

$$= \Delta\Omega * \int_E f(v)\frac{v^2}{m} dE \tag{A2.45}$$

Thus, we can see that the remaining integrand has units (in SI) of flux per solid angle per energy (as the left hand side of the equation must have units of flux, $\frac{\#}{m^2 s}$).

$$\left[f(v) * \frac{v^2}{m}\right] = \frac{1}{m^2 * s * sr * J} \tag{A2.46}$$

$$= \frac{s}{m^4 * kg * sr} \tag{A2.47}$$

The steradians in this formulation are technically not necessary in the denominator. This is another case where $r * \theta[rad] = s\ [meters]$, but you wouldn't really express the radius as having units of [m/rad].

Thus, the integrand is the differential flux term that we have been going for so that we can write

$$\frac{dJ}{dE} = \frac{v^2}{m} f(v) \tag{A2.48}$$

And in terms of the discretized quantities we derived earlier, the average differential flux over an given solid angle, and velocity range (remember, differential flux has a value at every velocity step in a given angular range i.e. a value at every energy per charge step in a given pixel of FIPS).

$$\left(\frac{dJ}{dE}\right)_{ave,i} = \frac{v_{c,i}^2}{m} f_{ave}(v_{c,i}, \theta_c, \phi_c) \tag{A2.49}$$

The question of how the steradian units filter through the calculation is a common source of confusion. So we will work with the calculation in the context of the above work we have done going from counts to PSD, and try to make sense of the appropriate units for differential flux.

The total flux passing through the aperture from a single incident direction is given by

$$\Phi_{flux}(\theta_c, \phi_c) \tag{A2.50}$$

$$= \int_{\phi=\phi_1}^{\phi_2} \int_{\theta=\theta_1}^{\theta_2} \int_{v=0}^{\infty} v\, f(\vec{v})(dv)(vd\theta)(vsin\theta d\phi)$$

$$= \int_{\phi=\phi_1}^{\phi_2} \int_{\theta=\theta_1}^{\theta_2} \int_{v=0}^{\infty} v\, f(v, \phi, \theta)(dv)(vd\theta)(vsin\theta d\phi) \tag{A2.51}$$

$$= \int_{\phi=\phi_1}^{\phi_2} \int_{\theta=\theta_1}^{\theta_2} \int_{v=0}^{\infty} f(v, \phi, \theta)v^3 dv\; sin\theta d\phi d\theta \tag{A2.52}$$

The integral over the velocity dimension can be broken up (approximately, as there are gaps between velocity intervals) into integrals over each velocity bins range for k E/q bins. $v_{L,i}$and $v_{U,i}$ are the upper and lower velocity bounds of the bins, respectively.

$$= \sum_{i=1}^{k} \int_{\phi=\phi_1}^{\phi_2} \int_{\theta=\theta_1}^{\theta_2} \int_{v=v_{L,i}}^{v_{U,i}} f(v,\phi,\theta) v^3 dv\ sin\theta d\theta d\phi \tag{A2.53}$$

We can now use the same averaging definition we used above in (23), for a "differential" spherical volume element

$$< f(v_c,\theta_c,\phi_c)v > \tag{A2.54}$$

$$= \frac{1}{(\Delta v)\ (v_c sin\theta_c \Delta\phi)\ (v_c \Delta\theta)} \int_{v=v_1}^{v_2} \int_{\theta=\theta_1}^{\theta_2} \int_{\phi=\phi_1}^{\phi_2} f(v,\phi,\theta) v\ v^2 sin\theta\ dv\ d\theta\ d\phi$$

To rewrite (52) as

$$= \sum_{i=1}^{k} \Delta v_i \left(v_{c,i} sin\theta_c \Delta\phi\right)\left(v_{c,i}\Delta\theta\ \right)\langle f(v_c,\theta_c,\phi_c)v\rangle_i \tag{A2.55}$$

And using our assumptions for the velocity width of the interval and the constancy of f over each velocity interval we can write

$$= \sum_{i=1}^{k} \frac{1}{2} \delta v_{c,i} \left(v_{c,i} sin\theta_c \Delta\phi\right)\left(v_{c,i}\Delta\theta\ \right) f\left(v_{c,i},\theta_c,\phi_c\right) v_{c,i} \tag{A2.56}$$

$$= \sum_{i=1}^{k} \frac{1}{2} \delta v_{c,i}^4\ sin\theta_c \Delta\phi\Delta\theta f\left(v_{c,i},\theta_c,\phi_c\right) \tag{A2.57}$$

And now using our relation between counts and phase space we can express this in terms of counts (35)

$$\frac{N(v_c,\theta_c,\phi_c)}{\epsilon(v_c,\theta_c,\phi_c)} = \frac{1}{2} A_{eff} \Delta t\ (sin\theta_c \Delta\phi\ \Delta\theta)\ \delta\ v_c^4\ f_{ave}(v_c,\theta_c,\phi_c) \tag{A2.58}$$

So that,

$$\Phi_{flux}(\theta_c,\phi_c) = \sum_{i=1}^{k} \frac{N(v_{c,i},\theta_c,\phi_c)}{\epsilon(v_{c,i},\theta_c,\phi_c)A_{eff}\Delta t} \tag{A2.59}$$

Or, to get in terms of energy, multiply top and bottom by ΔE_i.

$$\Phi_{flux}(\theta_c,\phi_c) = \sum_{i=1}^{k} \frac{N(v_{c,i},\theta_c,\phi_c)}{\epsilon(v_{c,i},\theta_c,\phi_c)A_{eff}\Delta t} * \frac{\Delta E_i}{\Delta E_i} \tag{A2.60}$$

By definition, $\delta * E_i = \Delta E_i$

$$= \sum_{i=1}^{k} \frac{N(v_{c,i},\theta_c,\phi_c)}{\epsilon(v_{c,i},\theta_c,\phi_c)A_{eff}\Delta t\ (\delta * E_i)} \Delta E_i \tag{A2.61}$$

So, to be consistent with the differential flux definition in (47) we need to pull out a solid angle term

$$\begin{aligned} &\Phi_{flux}(\theta_c,\phi_c) \\ &= \Delta\Omega_{pixel} \sum_{i=1}^{k} \left[\frac{N(v_{c,i},\theta_c,\phi_c)}{\epsilon(v_{c,i},\theta_c,\phi_c)A_{eff}\Delta t\ (\delta * E_i)\Delta\Omega_{pixel}} \right] \Delta E_i \end{aligned} \tag{A2.62}$$

So that now the bracketed term is the differential flux at each energy (or energy per charge) step. And this will be consistent with the integral definition presented in (44), so if we discretized (44) in the same fashion as we have in the previous few expressions we would have

$$\Phi_{flux}(\theta_c,\phi_c) = \Delta\Omega_{pixel} \sum_{i=1}^{k} \left[f(v_{c,i},\theta_c,\phi_c) \frac{v_{c,i}^2}{m} \right] \Delta E_i \tag{A2.63}$$

We now explore the relation between reporting a quantity as “per steradian” and the directional intensity that is used in radiative transfer texts (Watts/(m^2 * sr)). We note that we are computing this flux for a single incident direction (MCP pixel), and so the solid angle term $\Delta\Omega_{\text{pixel}} = \sin(\theta_c)\,\Delta\theta\Delta\phi$ is a constant at every velocity step.

Now since we have the flux for a single incident direction, we will appeal to the following definition of intensity (the per steradian flux quantity from radiative transfer) from G.W. Petty – “A First Course in Atmospheric Radiation”

$$I(\widehat{\Omega}) = \frac{\delta F}{\delta \Omega} \tag{A2.64}$$

You take the flux observed from a particular direction of “small enough” solid angle and divide by the observing solid angle. Typically the maximum arc subtending the observation solid angle is about 5 deg or less. This is exactly what we have with these MCP pixel flux measurement, the flux observed in a particular direction of “small” solid angle. So, our definition of a per steradian quantity will have the same implication, that this is the flux per solid angle in a given look direction. Thus our flux is

$$I(\theta_c, \phi_c) = \frac{< nv >_{\theta_c,\phi_c}}{(\Delta\Omega_{pixel})} = \sum_{i=1}^{k} \left[f(v_{c,i}, \theta_c, \phi_c) \frac{v_{c,i}^2}{m} \right] \Delta E_i \tag{A2.65}$$

Now, notice that the quantity inside the summation is the discretized version of the integrand in (44), and we can see clearly how the steradian unit has played out and the implications. The differential flux is the term in brackets (an array of values, at each energy step of the instrument), and the flux is the evaluation of that integral.

Note that we have ended up with a Reimann sum type expression for the velocity integral in (60). If you actually wanted to evaluate the flux (and not just see the differential flux relation) you would want to evaluate the integral in (38) using a trapezoidal type rule. This will better account for the fact that there are gaps between the velocity bins in the measurements, but the actual phase distribution will have some value in these gaps and interpolating over these gaps with the trapezoidal rule is the most reasonable thing to do.

And if we wanted to compute the total flux through the FIPS instrument from the PHAs, we would perform this process for each MCP pixel.

$$\Phi_{whole\ FOV} = \int_{\phi} \int_{\theta} \int_{v=0}^{\infty} v\, f(\vec{v})(dv)(vd\theta)(vsin\theta d\phi) \tag{A2.66}$$

$$\Phi_{whole\ FOV} = \int_{\phi} \int_{\theta} \int_{v=0}^{\infty} v^3\, f(v, \theta_c, \phi_c) dv\ sin\theta d\phi d\theta \tag{A2.67}$$

And we are integrating over each MCP pixel, so break integrand up into angular range of each MCP pixel, say there are l pixels, and we use the same upper and lower bound notation as before

$$\Phi_{whole\ FOV} = \sum_{j=1}^{l} \int_{\theta=\theta_{L,j}}^{\theta_{U.j}} \int_{\phi=\phi_{L,j}}^{\phi_{R,j}} \int_{v=0}^{\infty} v^3\, f(v, \theta_c, \phi_c) dv\ sin\theta d\phi d\theta \tag{A2.68}$$

Now, we are assuming that f does not vary within a given pixel, j. So we can integrate out the solid angle portion. There are also no “gaps” between the pixels in solid angle space.

$$\Phi_{whole\ FOV} = \sum_{j=1}^{l} \left[\Delta\Omega_j \int_{v=0}^{\infty} v^3\, f\left(v, \theta_{c,j}, \phi_{c,j}\right) dv \right] \tag{A2.69}$$

Where we left the integral over velocity as a trapezoidal scheme which is better to use than using the Reimann sums as we showed in the calculation for a single pixel.

But, if we want to get back to the expression for differential flux over the whole field of view, in the manner we derived for each pixel, we need to express the above in terms of Reimann sums and we would end up with

$$\Phi_{whole\ FOV} = \sum_{j=1}^{l}\left[\Delta\Omega_{pixel,j}\sum_{i=1}^{k}\left[\frac{N(v_{c,i},\theta_{c,j},\phi_{c,j})}{\epsilon(v_{c,i},\theta_{c,j},\phi_{c,j})A_{eff}\Delta t\ (\delta * E_i)\Delta\Omega_{pixel,j}}\right]\Delta E_i\right] \tag{A2.70}$$

We will cancel out the solid angle in each pixel and change the order of summation to yield

$$\Phi_{whole\ FOV} = \sum_{i=1}^{k}\left[\sum_{j=1}^{l}\left[\frac{N(v_{c,i},\theta_{c,j},\phi_{c,j})}{\epsilon(v_{c,i},\theta_{c,j},\phi_{c,j})A_{eff}\Delta t\ (\delta * E_i)}\right]\right]\Delta E_i \tag{A2.71}$$

Now we will choose to multiply and divide by the solid angle of the entire instrument to match up with the definition of differential flux we had in (44), giving

$$\Phi_{whole\ FOV} = \Delta\Omega_{whole\ FOV}\sum_{i=1}^{k}\left[\left(\sum_{j=1}^{l}\left[\frac{N(v_{c,i},\theta_{c,j},\phi_{c,j})}{\epsilon(v_{c,i},\theta_{c,j},\phi_{c,j})A_{eff}\Delta t\ (\delta * E_i)\Delta\Omega_{whole\ FOV}}\right]\right)\right]\Delta E_i \tag{A2.72}$$

Where the term in parentheses is the differential flux for the whole FOV of the FIPS instrument

We can again try to define an “intensity” type value by divided by the solid angle we observed this flux over, but now we are dividing by a “large” solid angle and so the definition we used above, $I(\widehat{\Omega}) = \frac{\delta F}{\delta \Omega}$, is no longer valid (our solid angle is not a small “differential quantity”). So, now what the “intensity” really corresponds to is not a directional quantity, $I(\widehat{\Omega})$, but more of an average intensity over the field of view. Now technically, the intensity for each pixel is also this same type of average, but it is over a "small" field of view and can therefore also be interpreted as a directional intensity.

$$I(\Delta\Omega_{whole\ FOV}) = \frac{\Phi_{whole\ FOV}}{(\Delta\Omega_{whole\ FOV})} \tag{A2.73}$$

$$I(\Delta\Omega_{whole\ FOV}) = \sum_{i=1}^{k}\left[\left(\sum_{j=1}^{l}\left[\frac{N(v_{c,i},\theta_{c,j},\phi_{c,j})}{\epsilon(v_{c,i},\theta_{c,j},\phi_{c,j})A_{eff}\Delta t\ (\delta * E_i)\Delta\Omega_{whole\ FOV}}\right]\right)\right]\Delta E_i \tag{A2.74}$$

Or, in terms of phase space density again

$$I(\Delta\Omega_{whole\ FOV}) = \sum_{i=1}^{k}\left[\left(\left(\frac{1}{\Delta\Omega_{whole\ FOV}}\right)\sum_{j=1}^{l}\left[f_{pixel}(v_c,\theta_{c,j}\ ,\phi_{c,j})\left(\frac{\mathrm{v}_{\mathrm{c,i}}^2}{\mathrm{m}}\right)\Delta\Omega_j\right]\right)\right]\Delta E_i \tag{A2.75}$$

Again, the term in the larger parentheses is the differential flux in each E/q step.

This is now the average flux over the solid angle observed, it no longer has "directional" meaning.

A2.1.5 Comparing phase space density calculations from PHAs vs. from rates

We need to remember our definition of the "average" phase space we recover to compare the phase space recovered from the two different methods. When we calculate from the PHAs we recover the average phase space density for each MCP pixel. When we calculate from the rates, we recover the average phase space density for the whole instrument field of view. Let us indicate the average phase space density for each pixel as $f_{ave}(\theta_c, \phi_c, v_c)$ where the arguments have the same meaning as in previous derivations. We will indicate the average phase space density over the whole instrument as $f_{ave}(v_c, whole\ FOV)$ where the θ_c, ϕ_c are not needed as we are talking about the average over the entire instrument FOV.

To relate phase space density calculated from rates to that from PHAs, we have to compare the phase space density calculated from rates and PHAs by integrating over the entire velocity space, as we know the total density must be equal as calculated from these two definitions. So the integral over velocity space observed by FIPS is the following.

$$\int_v \int_\theta \int_\phi f_{ave}(v_c, whole\ FOV) v^2 sin\theta d\theta d\phi dv \\ = \int_v \int_\theta \int_\phi f_{ave}(v_c, \theta_c, \phi_c)\ v^2 sin\theta d\theta d\phi dv \tag{A2.76}$$

We can get rid of the velocity integral as we know we are integrating over the same velocity range in both cases, so the integrands must be equal for the equality to hold.

$$\int_v v^2 \left[\int_\theta \int_\phi f_{ave}(v_c, whole\ FOV) sin\theta d\theta d\phi\right] dv \\ = \int_v v^2 \left[\int_\theta \int_\phi f_{ave}(v_c, \theta_c, \phi_c)\ sin\theta d\theta d\phi\right] dv \tag{A2.77}$$

Is simplified to,

$$\int_\theta \int_\phi f_{ave}(v_c, whole\ FOV) sin\theta d\theta d\phi \\ = \int_\theta \int_\phi f_{ave}(v_c, \theta_c, \phi_c)\ sin\theta d\theta d\phi \tag{A2.78}$$

Since the value of phase space density if constant over any one pixel on the right hand side, this integration turns into a summation over the k pixels of the FIPS instrument. For the left hand side, the phase space density term is constant over the entire field of view by definition of the average.

$$f_{ave}(v_c, whole\ FOV)\Delta\Omega_{whole\ FOV} = \sum_{j=1}^{l}\left[f_{ave}\left(v_c, \theta_{c,j}\ , \phi_{c,j}\right)\Delta\Omega_j\right] \tag{A2.79}$$

We can now equate these two averages over the entire instrument so that

$$f_{ave}(v_c, whole\ FOV) = \left(\frac{1}{\Delta\Omega_{whole\ FOV}}\right)\sum_{j=1}^{l}\left[f_{ave}\left(v_c, \theta_{c,j}\ , \phi_{c,j}\right)\Delta\Omega_j\right] \tag{A2.80}$$

A2.2 Foil thickness calculations for FIPS forward model

The primary focus of this appendix is evaluate what carbon foil thickness for the FIPS instrument is best able to explain the observed TOF distributions from the flight data. This is accomplished by assuming a range of carbon foil thicknesses in the TRIM software package (Ziegler 2004; Ziegler et al. 2010), computing the forward modeled TOF distribution corresponding to that foil thickness and comparing that distribution to the flight data. In this appendix all flight data will come from the -13 kV PAHV period which spans from 12-Mar-2015 02:00:00 to 30-Apr-2015 17:30:00 and includes only time periods when MESSENGER was inside the planetary magnetopause. In parallel to selecting an appropriate foil thickness, it is also prudent to evaluate in a holistic sense how well forward modeled TOF distribution based on TRIM are able to reproduce the kind of distribution seen in the flight data. This targets the question of whether TRIM is an accurate enough model of carbon foil energy straggling for use in TOF instrument forward models.

A2.2.1 Varying carbon foil thickness

A range of carbon foil thickness is assumed, centered on a carbon foil thickness of 82 Å in accordance with previous modeling efforts (Raines et al. 2013). It is useful to know the rough conversion between carbon foil thickness expressed in terms of the areal density and the actual thickness normal to the foil surface. For a typical carbon foil the areal density, $\left[\frac{\mu g}{cm^2}\right]$, is related to the thickness, $\Delta x\ [\text{Å}]$, by

$$\sigma = \left(0.02\frac{\mu g}{cm^2\text{Å}}\right)\Delta x \tag{A2.81}$$

, where the scaling factor is just the volume density of carbon foil expressed in typical units for the field. We will specify all the foil thickness in terms of the thickness normal to the foil surface in this section.

To assess the appropriate foil thickness we select three representative E/q steps of the FIPS instrument and run a range of carbon foil thickness through TRIM at each step. The ions we run the TRIM simulation on are H^+, He^+, and He^{2+}, as these generally have the clearest peaks in the flight TOF data. The energy distribution after the carbon foil is the converted to a TOF distribution using the formulation given in Section 4.2. The resultant TOF distributions for the three energy steps chosen, 0.52 kV, 1.01 kV, and 6.92 kV are shown in Figure A2.2, Figure A2.3, and Figure A2.4, respectively.

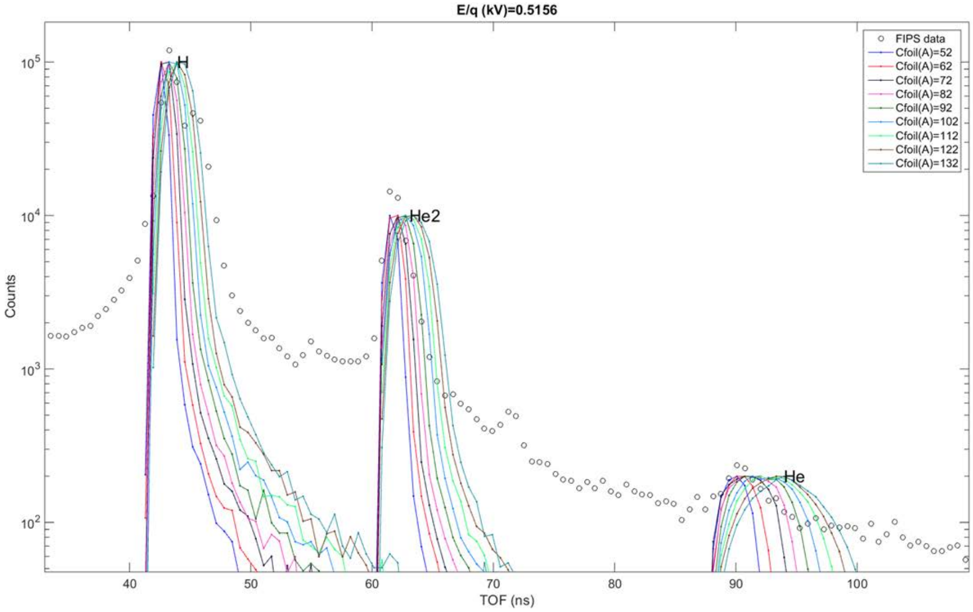

Figure A2.2: Comparison of the measured TOF distribution from flight data (open circles) and the TOF distributions predictions from TRIM simulations at several carbon foil thicknesses (indicated in the legend). The TOF range shown corresponds to the peak locations of incident H+ ions, He2+, and He+ ions (labeled as H, He2, and He, respectively). The E/q step that the TOF flight data is taken at and the TRIM simulations are match to is 0.5156 kV.

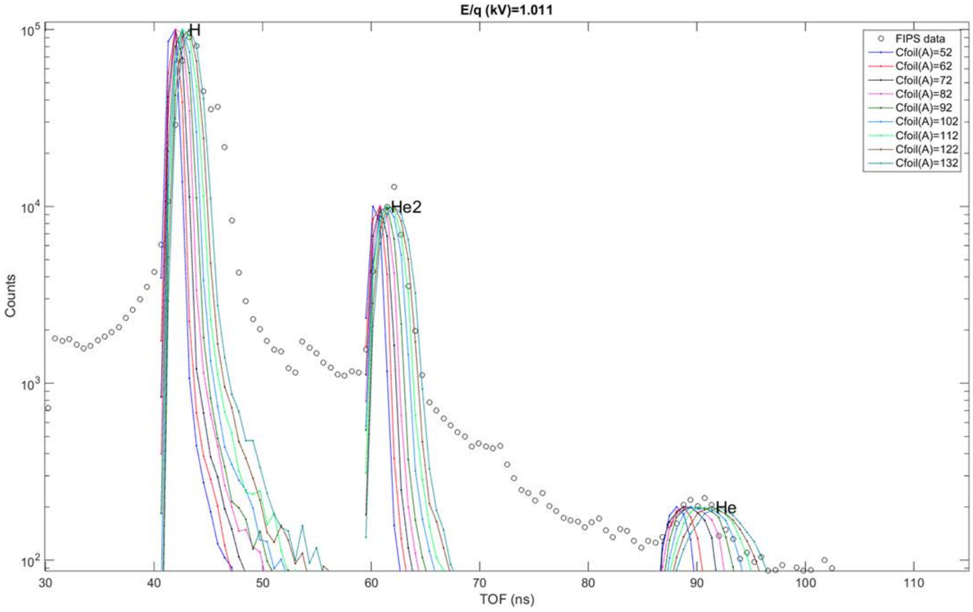

Figure A2.3: Comparison of the measured TOF distribution from flight data (open circles) and the TOF distributions predictions from TRIM simulations at several carbon foil thicknesses (indicated in the legend). The TOF range shown corresponds to the peak locations of incident H+ ions, He2+, and He+ ions (labeled as H, He2, and He, respectively). The E/q step that the TOF flight data is taken at and the TRIM simulations are match to is 1.011 kV.

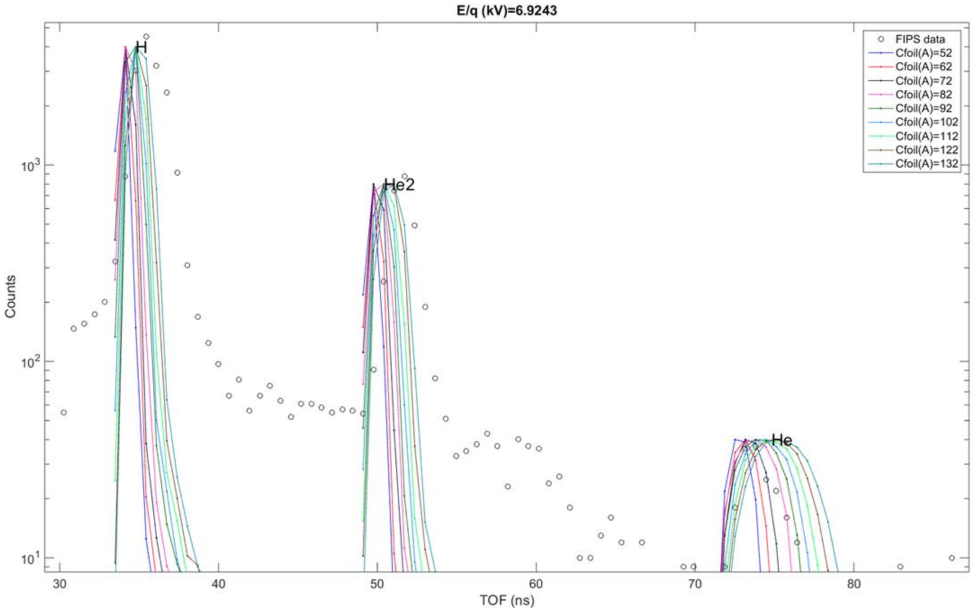

Figure A2.4: Comparison of the measured TOF distribution from flight data (open circles) and the TOF distributions predictions from TRIM simulations at several carbon foil thicknesses (indicated in the legend). The TOF range shown corresponds to the peak locations of incident H+ ions, He2+, and He+ ions (labeled as H, He2, and He, respectively). The E/q step that the TOF flight data is taken at and the TRIM simulations are match to is 6.9243 kV.

The objective with this figures is to see if a single carbon foil thickness matches the peak TOF location of the inflight FIPS data. For H^+ and He^{2+} we find there is no single foil thickness that matches the peak TOF location at all E/q values. Instead we see a progression from lower carbon foil thickness matching better at E/q = 0.52 kV to higher carbon foil thicknesses matching at E/q= 6.92 kV. The exception is He^+, which shows reasonable agreement with the 72 or 82 Å foil curves at all E/q values. Even for a given E/q step, we do not see agreement between the different ions on the best matching carbon foil thickness.

The fact that the proton curve in particular doesn't match well with a single foil thickness is disconcerting. The observation that the flight TOF distribution moves to steadily higher TOF relative to a single foil thickness TRIM prediction suggests one explanation for the cause. It is possible that protons are transmitted through the carbon foil and emerge with a charge. If the protons emerged with a positive charge then they would be decelerated slightly as they moved from the carbon foil to the stop MCP. This would result in a larger TOF and could help explain our observations.

A2.2.2 Investigating charged transmitted ions

There is some support in the literature for expected charge state distributions for atoms transmitted through carbon foils. One exceptional example is shown in Figure A2.5, which described the charge state distribution for protons as they pass through an amorphous carbon foil. It is clear that there is a cross over in energy, at about 40 keV in this case, where the majority of H atoms leave the carbon foil with a positive charge.

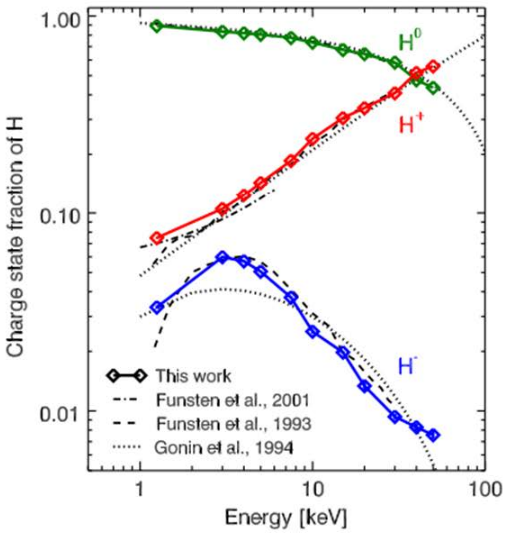

Figure A2.5: The charge state fractions of hydrogen after passing an amorphous carbon foil of nominal thickness of 25 Å. Adapted from Allegrini et al. (2014).

It is worth noting that with the PAHV at -13 kV for the data used in this appendix, the maximum incident energy of a proton in our analysis is about 20 keV (for the 6.92 kV step). However, the exit charge distribution can depend to some extent on the foil thickness and the impurities deposited on the foil surface. To test the theory of species leaving the foil with net charge we reprocess the TRIM simulation data from the previous section for each new charge state of interest. The results of this analysis are shown in

Figure A2.6, Figure A2.7, Figure A2.8, for the same E/q steps as the previous foil thickness analysis. For clarity we only include three foil thickness in these figures as they get too busy otherwise. Each post foil charge state considered manifests itself as another family of foil thickness curves. The different families of curves of segregated by the line style used to plot them. We see that the varying post foil charge states have a much larger impact on shifting the TOF peak of the model than variations between the carbon foil thickness. If we assume that the protons at E/q=0.52 kV are mostly neutral leaving the foil and that protons at E/q = 6.2 kV are mostly singly charged we can explain the apparent shift in the TOF peak of the flight proton data. The FWHM of the higher E/q proton peak still cannot be explained by singly charged protons.

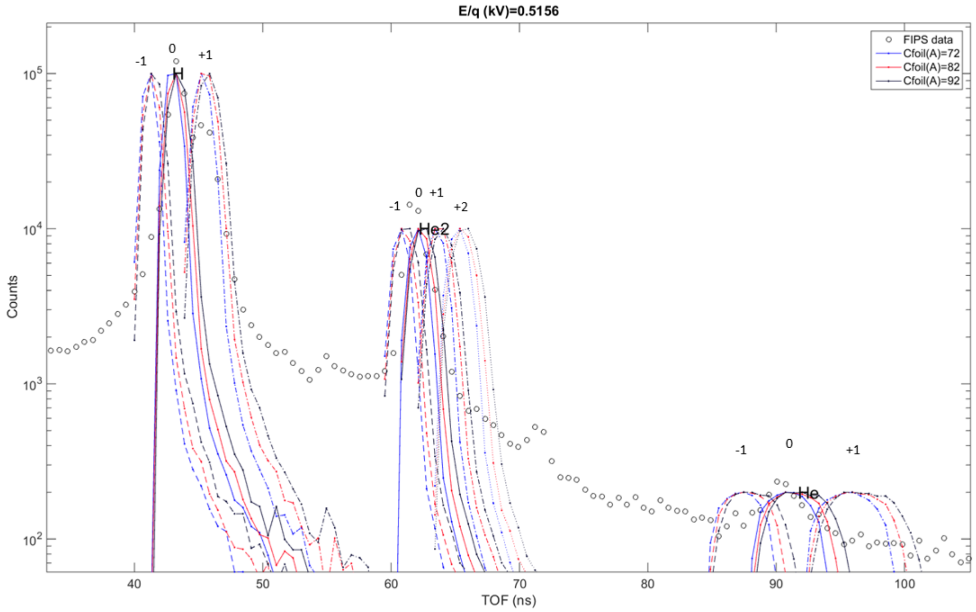

Figure A2.6: Comparison of FIPS TOF flight data and TOF TRIM simulation for ions that are transmitted through the carbon foil unneutralized. Three different carbon foil thickness are model with TRIM and are colored according to the plot legend. The different line styles for each foil thickness correspond to the charge state of the ion after it is transmitted through the carbon foil. The charge state is indication near the peak of the ion's TOF distribution for each ion species. The E/q step that the TOF flight data is taken at and the TRIM simulations are match to is 0.5156 kV.

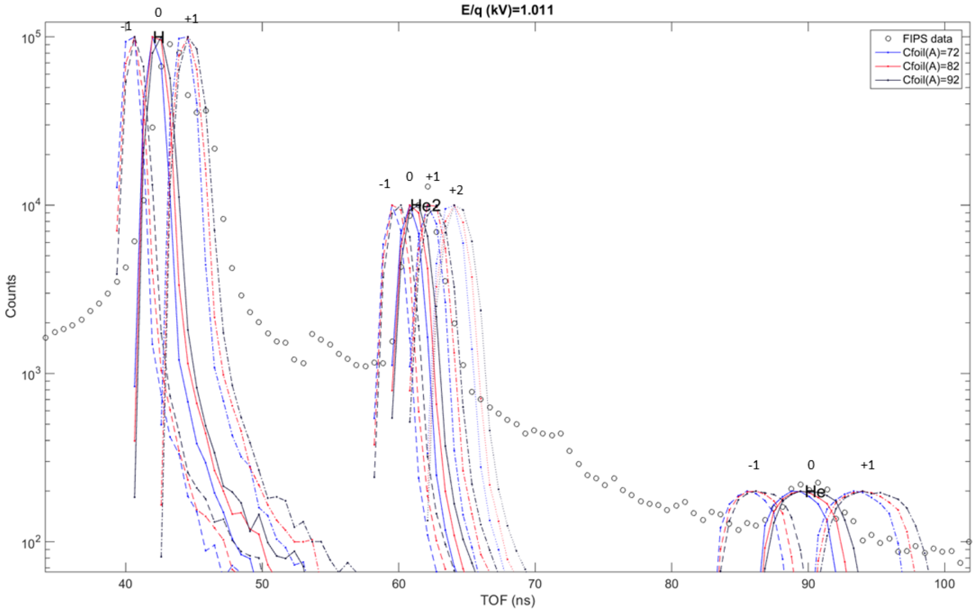

Figure A2.7: Comparison of FIPS TOF flight data and TOF TRIM simulation for ions that are transmitted through the carbon foil unneutralized. Three different carbon foil thickness are model with TRIM and are colored according to the plot legend. The different line styles for each foil thickness correspond to the charge state of the ion after it is transmitted through the carbon foil. The charge state is indication near the peak of the ion's TOF distribution for each ion species. The E/q step that the TOF flight data is taken at and the TRIM simulations are match to is 1.011 kV.

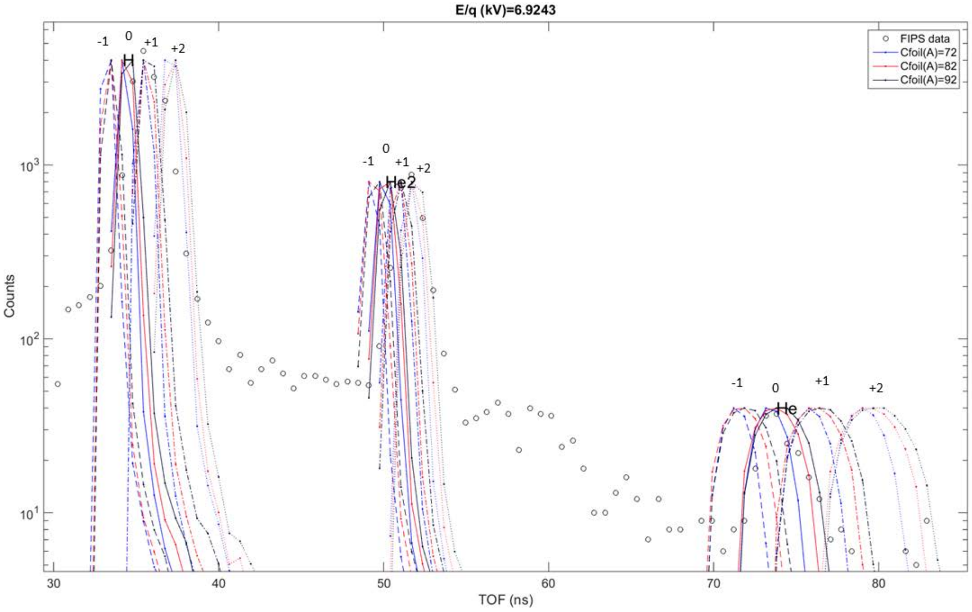

Figure A2.8: Comparison of FIPS TOF flight data and TOF TRIM simulation for ions that are transmitted through the carbon foil unneutralized. Three different carbon foil thickness are model with TRIM and are colored according to the plot legend. The different line styles for each foil thickness correspond to the charge state of the ion after it is transmitted through the carbon foil. The charge state is indication near the peak of the ion's TOF distribution for each ion species. The E/q step that the TOF flight data is taken at and the TRIM simulations are match to is 6.9243 kV.

For the case of incident He^{2+} ions the situation is a little harder to believe. In the lowest E/q step the He^{2+} peak is well fit by assuming the ion leave the foil as a neutral He. But as you move toward the E/q=6.92 kV step, the TOF distribution is best explained by He^{2+} leaving the carbon foil retaining a charge of 2+. This charge state distribution is not well supported by the results in Allegrini et al. 2014, which is the most complete data on post foil charge states found at the time of this work. Returning to the case of incident He^{+} ions we find that the flight data is pretty well matched by the neutralized post foil He atoms.

Thus we conclude that the unneutralized atoms leaving the carbon foil in the TOF section offer a promising explanation for some of the differences between the TRIM and flight TOF distributions, but cannot fully explain the discrepancy. It is certainly the case that the discrepancy between TRIM and flight data cannot be explained solely be choosing a single carbon foil thickness that matches all the data (see Figure A2.2-Figure A2.4). The post foil charge state model is the more promising of the two, but would require some more data that backs up the proposed post foil charge state distributions as they are not supported by current findings. Including different post foil charge states would also increase the uncertainties in the heavy ions recoveries, effectively smearing and widening all the TOF probability distributions. To close out this appendix we include a flavor of what including post foil charges states in the heavy ion TOF distributions would look like. This is shown in Figure A2.9-Figure A2.11. The main take away is that the overlap between heavy ions would be much worse if non-neutral post foil charge states turn out to be important for heavy ions. The findings of Allegrini et al. 2014 do cover some heavy ions like O, and indicate that the dominant post-foil charge state should be the neutral.

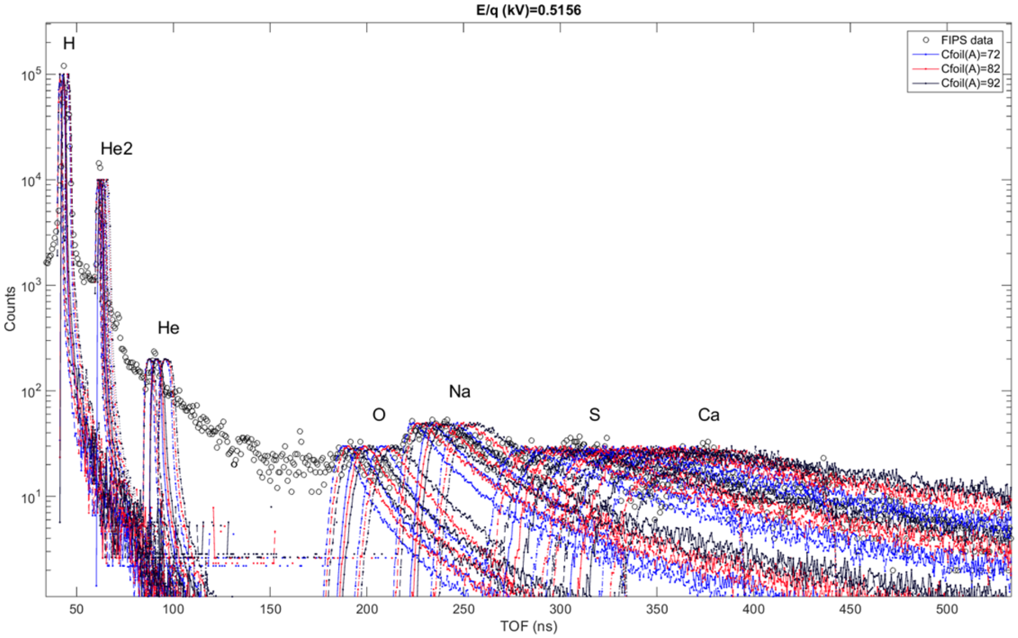

Figure A2.9: Same format as Figure A2.6, except a larger TOF range is shown along the x-axis. The charge state of the ion transmitted through the carbon foil is not indicated in this figure, but the line styles remain the same as in Figure #. The E/q step that the TOF flight data is taken at and the TRIM simulations are match to is 0.5156 kV.

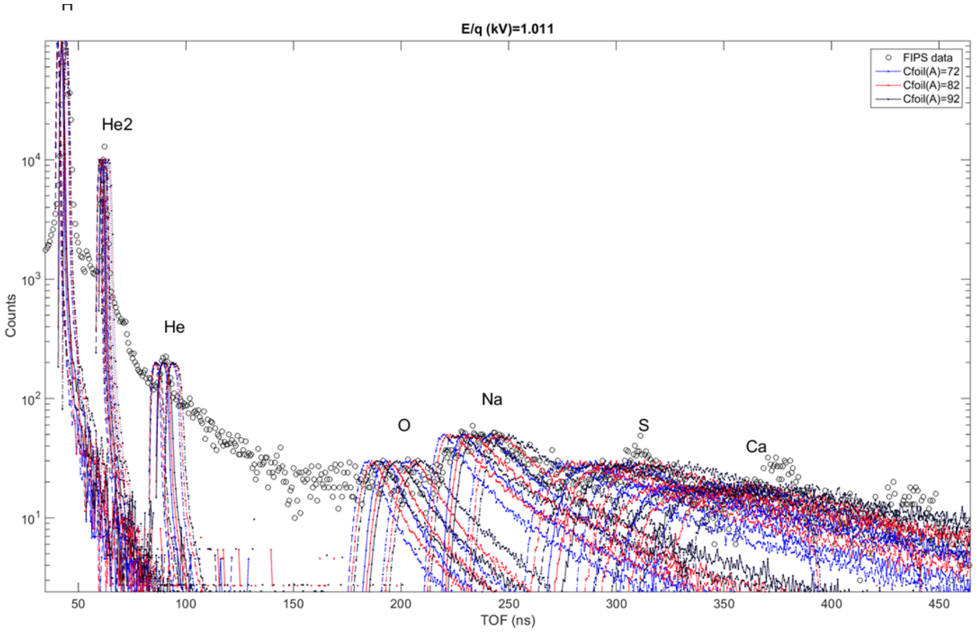

Figure A2.10: Same format as Figure A2.7, except a larger TOF range is shown along the x-axis. The charge state of the ion transmitted through the carbon foil is not indicated in this figure, but the line styles remain the same as in Figure #. The E/q step that the TOF flight data is taken at and the TRIM simulations are match to is 1.011 kV.

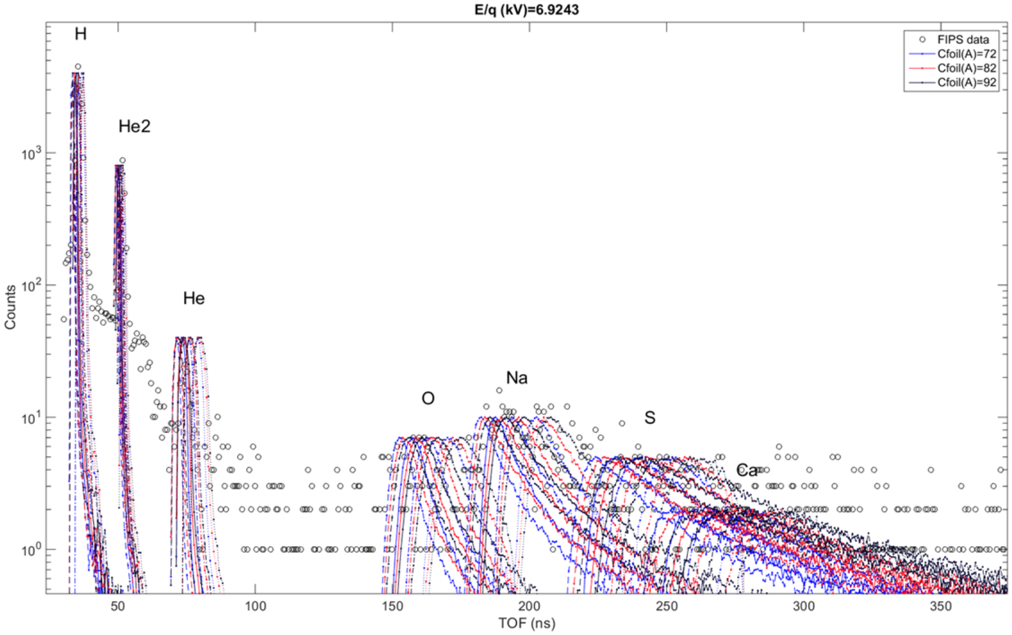

Figure A2.11: Same format as Figure A2.8, except a larger TOF range is shown along the x-axis. The charge state of the ion transmitted through the carbon foil is not indicated in this figure, but the line styles remain the same as in Figure #. The E/q step that the TOF flight data is taken at and the TRIM simulations are match to is 6.9243 kV.

A2.3 FIPS planetary ion forward model

Simulations of the FIPS measurement process require a comprehensive understanding of the system and are therefore a good place to start this analysis. Using simulated measurements of the ions of interest we will attempt to predict how measurements will manifest in the Energy per charge (E/q) vs. Time of Flight (TOF) space of the FIPS instrument. This will allow us to use a statistical model to assign measured ion counts to their most likely species. In the next few sections we step through modeling the TOF measurements made by the FIPS instrument, building on the discussion in Section 1.3.

A2.3.1 Carbon foil energy straggling simulations

The TOF measurement of the FIPS instrument hinges on the use of a carbon foil. This foil serves to neutralize an incident ion and also to release secondary electrons when the ion passes through the foil. These electrons act to trigger the start signal for the TOF measurement. Understanding the energy losses associated with an ion traversing the foil is crucial in understanding the recovered ion TOF.

The energy loss of an ion through the carbon foil is a complicated problem itself, and so we use the TRansport of Ions in Matter (TRIM) software package (Zeigler 2004, Zeigler et al. 2010) to estimate these energy losses. In Figure A2.12 we show the result of one such simulation, where 10^5 sulfur atoms with an initial energy of 15 keV were passed through a carbon foil with a thickness of 82 Å. This carbon foil thickness has been found to be the best match to the observed TOF distributions, and will be used for all subsequent calculations (see Appendix 2). These TRIM simulations have to be run for each ion for every combination of Post Acceleration High Voltage (PAHV) and E/q step that is to be analyzed. For each ion the energy incident on the foil will be the ion's energy incident on the entrance aperture, plus the energy received from the PAHV, which accelerates the ion before its impact with the carbon foil.

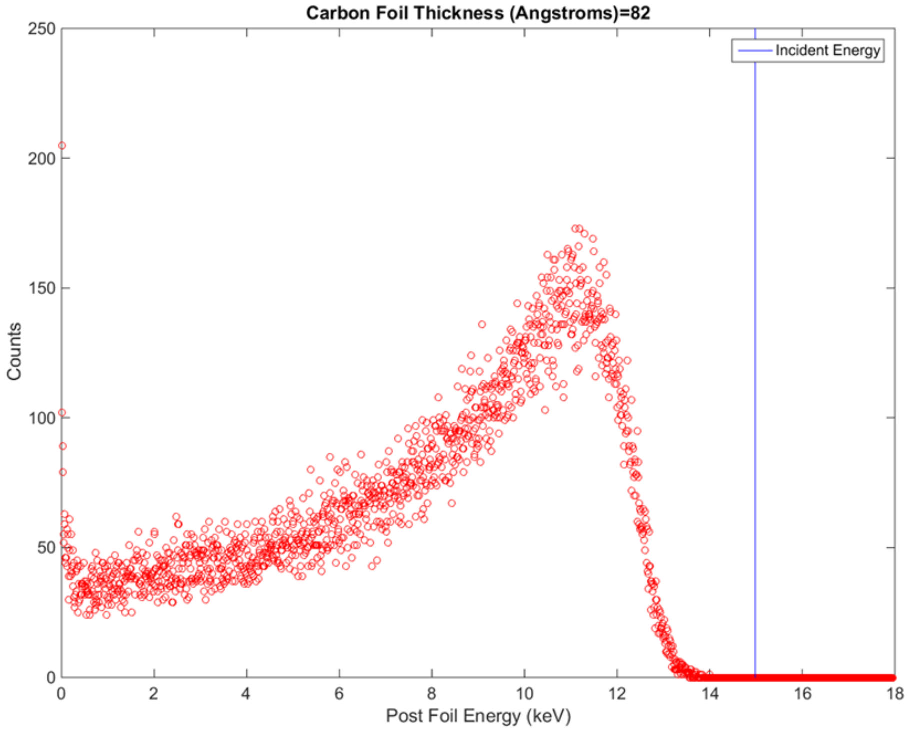

Figure A2.12 An example of the distribution of transmitted ion energies that is recovered from a TRIM simulation of an ion beam with incident energy of about 15 keV passing through a carbon foil with a thickness of 82 Angstroms.

The relationship between the energy incident on the carbon foil and the incident E/q of a given ion is

$$E_{prefoil} = q * \left(\left(\frac{E}{q}\right)_i - PAHV\right) \tag{A2.82}$$

, where $E_{prefoil}$ is the ion energy just before impacting the carbon foil, q is the ion charge, $\left(\frac{E}{q}\right)_i$ is the energy per charge value of the current energy per charge step, i, and $PAHV$ is the current post acceleration high voltage level (< 0). For the periods of interest in this work, FIPS was run with 60 logarithmically E/q steps ranging from 8 eV/e to 13.6 keV/e, and the PAHV was set at either -10.5 kV or -13 kV. For the 10 different incident ion species in this study (H+, He+, He2+, O+, Ne+, Na+, Mg+, Al+, Si+, S+, Ar+, Ca+, K+), this requires 60 x 13 x 2= 1560 different TRIM runs to produce the predicted post foil energy distributions required for this study.

A2.3.2 TOF forward modeling

With the TRIM simulations mentioned above, the energy distributions transmitted through the carbon foil of all ions species of interest were computed. Given the initial post foil energy we calculate the expected TOF for each ion as it traverses the TOF section of the FIPS instrument. In general, ions can leave the carbon foil still charged (though it is rare with the energies FIPS observes), so we must consider the voltages applied in the TOF section of the instrument. Figure A2.13 gives a rough schematic of how the voltages can vary through the TOF section of the FIPS instrument. Using this framework we construct the total time of flight for an ion leaving the foil.

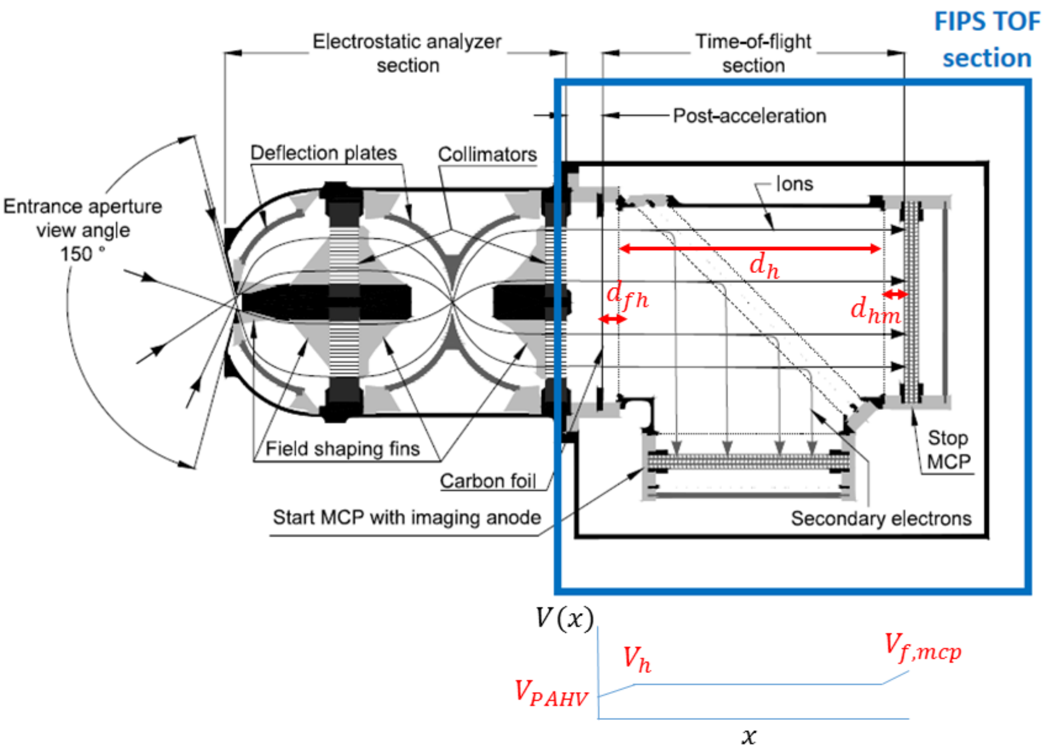

Figure A2.13 Schematic of the FIPS instrument with the TOF section indicated. Within the time of flight section the distance from the carbon foil to the TOF housing, the length of the TOF housing, and the distance from the TOF housing to the stop MCP are denoted with d_{fh}, d_h, and d_{hm}, respectively. A qualitative description of how the voltage varies through the TOF section is shown in the voltage vs distance plot below the TOF section.

An ion leaves the carbon foil with an initial energy E_0, and at an angle θ from the normal direction to the carbon foil. The component of velocity of the ion that determines the ion's TOF (assuming electric fields only in the x-direction in Figure A2.13) will be the x component in our coordinate system (the normal to the carbon foil is also in the x-direction). We will break the TOF section into three parts and calculate the time it takes the ion to pass through each section. Each section will be determined by a starting voltage, V_0 and an ending voltage, V_1. We assume that the voltage varies linearly through each section, implying a constant electric field. Therefore, in each section, the ion has a constant acceleration in the x direction given by

$$a = \frac{V_0 - V_1}{L} \frac{q}{m} \tag{A2.83}$$

, where L is the length of the section, q, is the ion charge, and m is the ion mass. The first section is defined as the distance between the carbon foil and the TOF section, $d_{fh} = 4\ mm$. For the first TOF section, the carbon foil was at the post-acceleration high voltage value, V_{PAHV}, and the TOF section was at a constant fraction of the PAHV, $V_{TOF} = \frac{14}{15} V_{PAHV}$. For our time periods of interest, V_{PAHV} was either -10.5 kV or -13 kV. Using basic kinematics for a mass under constant acceleration we calculate the TOF for this first section. The initial velocity of an ion in the x direction for this section is given by

$$u_1 = \sqrt{\frac{2E_0}{m}} cos\theta \tag{A2.84}$$

, and the acceleration is given by

$$a_1 = \frac{V_{PAHV} - V_{TOF}}{d_{fh}} \frac{q}{m} \tag{A2.85}$$

Thus the total time to traverse this section is given by

$$T_1 = \left(\frac{1}{a_1}\right)\left(-u_1 + \sqrt{u_1^2 + 2\, a_1\, d_{fh}}\right). \tag{A2.86}$$

The second section is defined as the distance through an approximately field free portion of the TOF section. The length of this section was $d_h = 65.5\ mm$, with both the start and ending voltage equal to V_{TOF}. The initial velocity in this section, u_2, can be found using conservation of energy from the initial velocity in section one,

$$u_2 = \sqrt{u_1^2 + \frac{2q}{m}\ (V_{PAHV} - V_{TOF})}. \tag{A2.87}$$

Since there was no acceleration in section two, the time to traverse this section is simply given by

$$T_2 = \frac{d_h}{u_2} \tag{A2.88}$$

, which is the limiting expression if one applies L'Hospital's rule to the expression for the traversal time for TOF section one as $a \rightarrow 0$.

The third and final section was the region between the field free section of the TOF section and the stop MCP. We call the starting voltage for this section V_{TOF}, and the ending voltage is the voltage at the front of the MCP, $V_{f,MCP}$. The voltage at the back of the MCP was a constant fraction of the PAHV, similar to the TOF section, such that $V_{b,MCP} = \frac{3.5}{15}\ V_{PAHV}$. The voltage across the MCP plates then defines the voltage at the front of the MCP.

$$V_{f,MCP} = \Delta V_{MCP} + V_{b,MCP} \tag{A2.89}$$

, where ΔV_{MCP} is the voltage across the MCP, typically -2600 V. With the starting and ending voltage for this section we can calculate the time to traverse this section in the same manner as for section one. The initial velocity for section three is again calculated from conservation of energy

$$u_3 = \sqrt{u_1^2 + \frac{2q}{m}\left(V_{PAHV} - V_{f,MCP}\right)} \tag{A2.90}$$

, and the acceleration through this section is given by

$$a_3 = \frac{V_{TOF} - V_{f,MCP}}{d_{hm}}\frac{q}{m}. \tag{A2.91}$$

Thus, the time through section three is

$$T_3 = \left(\frac{1}{a_3}\right)\left(-u_3 + \sqrt{u_3^2 + 2\,a_3\,d_{hm}}\right) \tag{A2.92}$$

, and the total time through the TOF section is given by

$$TOF = T_1 + T_2 + T_3 - T_e. \tag{A2.93}$$

, where T_e is the electron time of flight offset (about 4.8 ns). The secondary electrons must trigger the start MCP and they take a non-zero amount of time to move from the foil to the start MCP. The measured TOF value is simply the difference between when the stop and start MCP triggered, so we must account for this small offset.

In the case that an ion leaves the foil neutralized, this TOF expression simplifies to

$$TOF = \frac{d_{fm}}{u_1} - T_e \tag{A2.94}$$

, where d_{fm} is simply the sum of the lengths of the three section above ($d_{fm} = 74.5$ mm).

Using the expression described above we calculate what the measured TOF distribution would be for each TRIM simulation that we have run. This calculation leads to distributions like those shown in Figure A2.14. For each recovered TOF distribution the peak TOF value and the TOF value at both the lower Full Width Half Maximum (FWHM) and upper FWHM are recorded to help map out the region of TOF space that is occupied by each ion.

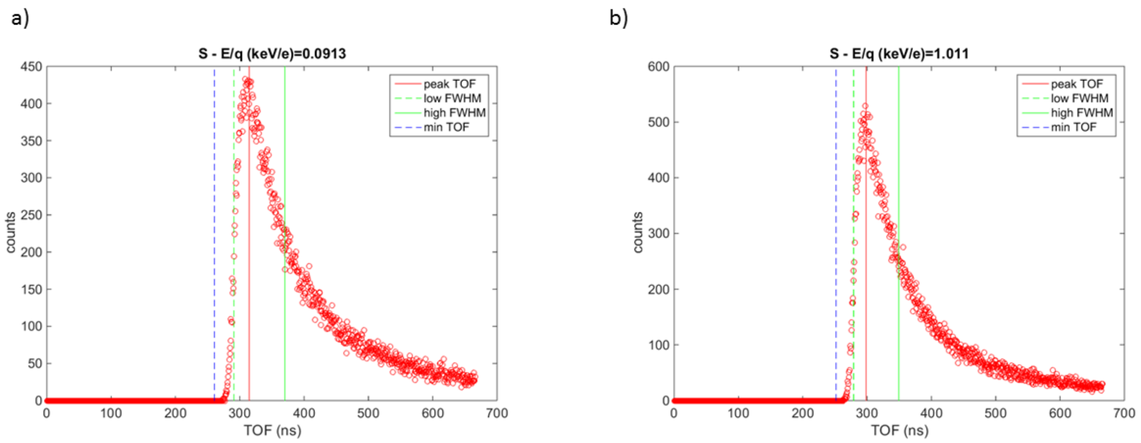

Figure A2.14: The model TOF distribution calculated from a TRIM simulation for sulfur ions passing through the TOF section of the FIPS instrument, with a Post Acceleration High Voltage (PAHV) equal to -13 kV. In a) the TOF distribution corresponds to an ion with incident E/q = 0.09 keV/e, and in b) incident E/q = 1.01 keV/e. The recovered peak TOF, and low and high full width half maximum values are shown with vertical lines. The blue vertical line indicates the expected TOF value if an ion didn't lose any energy to the carbon foil.

At each E/q step, each ion has a specific TOF distribution recovered from our forward model and the TRIM simulation results. These TOF distribution vary with E/q step, as the more energetic the incident ion, the lower the peak TOF value for that ion. The trend of each ion's TOF distribution with E/q will be referred to as that ion's "track". A depiction of how the tracks for our chosen ions occupy the E/q vs TOF space that FIPS observed is shown in Figure A2.15.

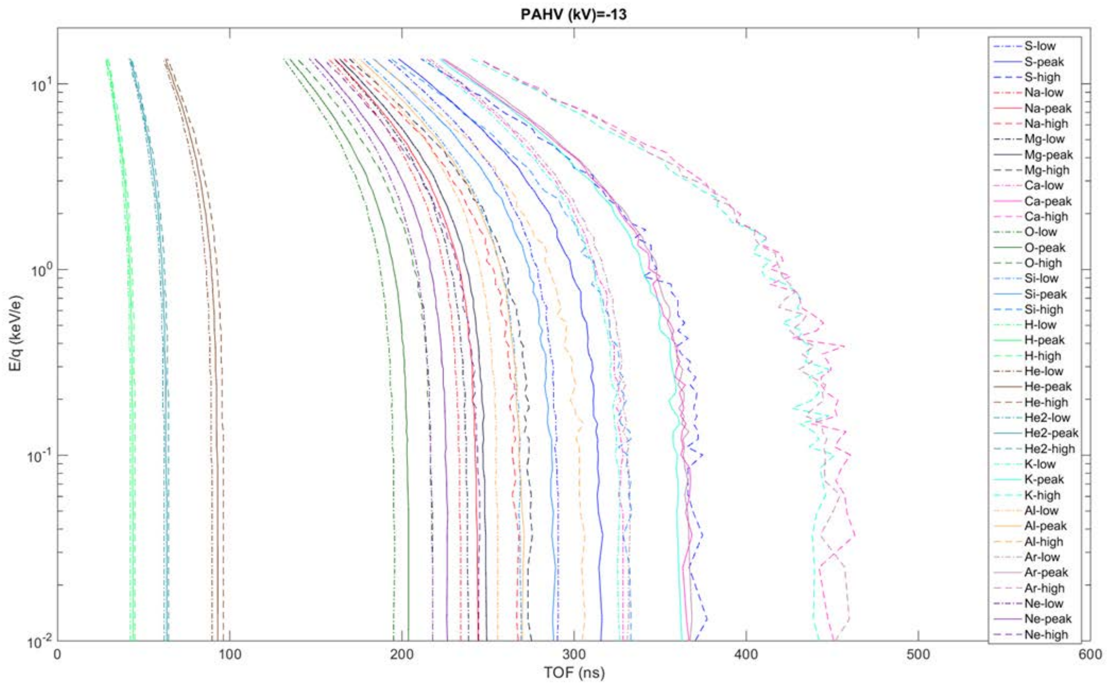

Figure A2.15 For each ion species of interest, the recovered peak, low TOF FWHM, and high TOF FWHM values are shown. These are recovered from the TOF distribution as shown in Figure A2.14 for PAHV = -13 kV.

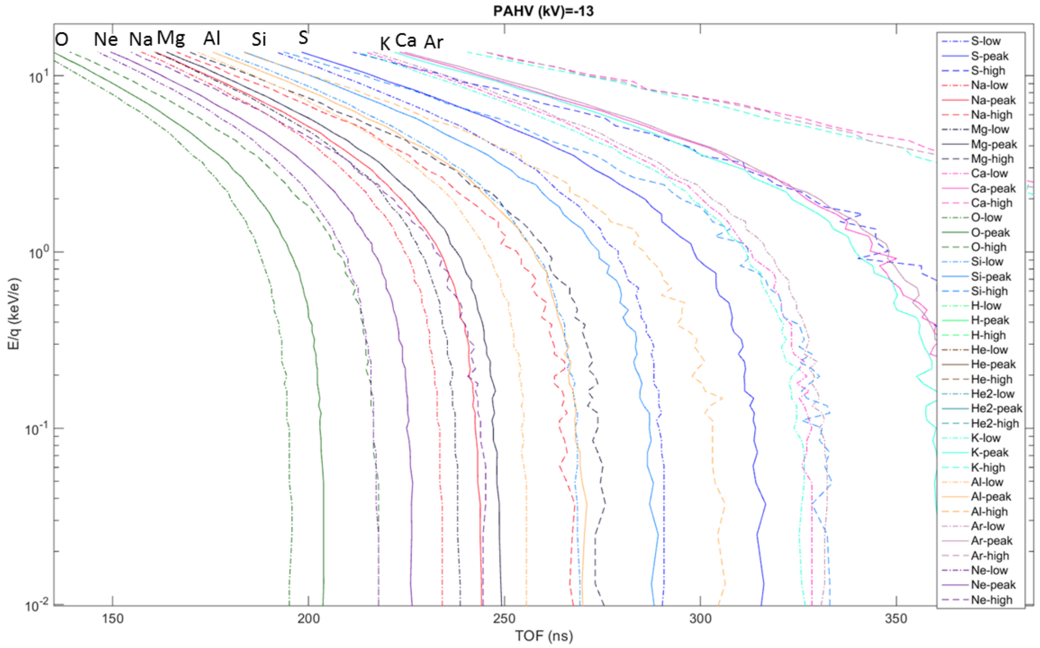

Figure A2.16 Same format as the previous Figure A2.15, except the TOF range has been narrowed to shown ions of interest. The peak E/q vs TOF track of each ion is also labeled with the ion name. These curves still correspond to PAHV =-13 kV.

From this figure it is apparent that H^+, He^+, He^{2+} are quite separated from the other heavier ion tracks. The recovery of the heavy ions will be the main focus of this work so a zoomed in version of Figure A2.15 is shown in Figure A2.16, to highlight the tracks of these heavy ions. In Figure A2.16 it is apparent that there is a large degree of overlap expected between certain heavy ions groups. In particular the Na and Mg tracks are very overlapped, and to a lesser extent Si and S are overlapped. These tracks only indicate where the FWHM values of the ion tracks lie relative to the peaks of other ion tracks, they do not full capture the extended tails to higher TOF values that are seen in Figure A2.14. Notice also that the degree of overlap between ion tracks varies slightly with E/q. For example, the high TOF FWHM of the Si distribution lies close to the peak of the S track at high E/q, but extend beyond the peak of S at lower E/q values. Therefore we may expect the deconvolution of these ion tracks to have some dependence on the E/q range analyzed.

A2.3.3 Noise Models

As is the case with all real instruments, there are certain considerations regarding noise. For FIPS this means measurements of a valid TOF start and stop signal that do not correspond to an actual measurement of an ion. These noise measurements will populate the same E/q vs TOF space as the ion tracks and further complicate the recovery process for these ions. Noise considerations relevant for the recovery of heavy ions will be discussed.

An example of the E/q vs TOF parameter space measured by FIPS is shown in Figure A2.17. This measurement space will be the central focus of all the heavy ion recovery analysis of this section. In Figure A2.17, the regions predominantly occupied by ion tracks are indicated, but equally useful are the regions occupied by noise sources. The region labeled “Background” is characteristic of the background noise rates and distributions experienced by the FIPS instrument. The region labeled “ESD” corresponds to noise sources that depend on incident particle flux measured by FIPS. During time of high incident particle flux, the electron-stimulated desorption (ESD) of material from the start MCP is enhanced. The main difference between the Background and ESD noise is the dependence on the incident flux. As it does not depend on incident flux, the

Background noise is considered a passive noise source whereas the ESD source is categorized as active (Gershman et al. 2013a).

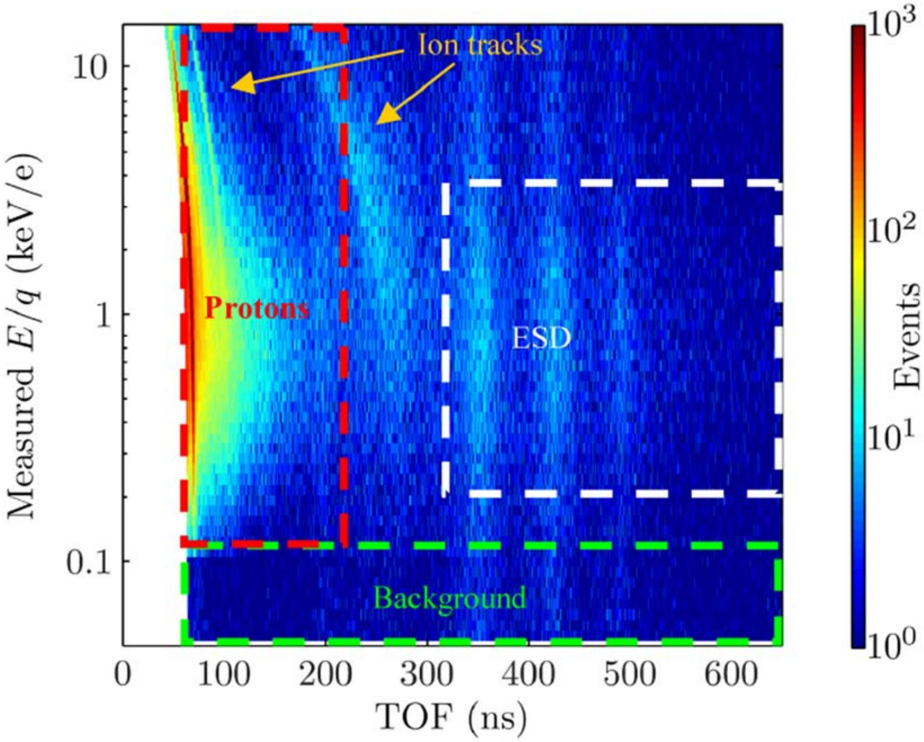

Figure A2.17 E/q vs TOF histogram of 50 days (day of year 100-149 in 2011) of orbital MESSENGER/FIPS heavy ion (m/q > 1 amu/e) measurements. Curved tracks roughly correspond to incident ions. Boxes marking the E/q vs TOF bins corresponding to background events, proton tail events, and induced electron stimulated desorption events are indicated as "Background", 'Protons", and "ESD", respectively. Adapted from Gershman, et al. (2013a).

The last major noise source is labeled as "Protons", and stems from the contamination of the H^+ mass peak into the peaks for species that occupy the higher TOF regions of the measurement space. This is primarily due to the energy straggling that occurs when the protons pass through the carbon foil during the TOF measurement process. Energy straggling results in a high TOF tail for the protons, which is not well represented by the TRIM simulations, as determined by comparison with real FIPS data. As the peak for H^+ has the smallest TOF of all the ions of interest, its high TOF tail has the greatest potential to contaminate the TOF channel corresponding to all other ion species. For more details on the origin and characteristics of these noise sources, the reader is referred to Gershman et al. (2013a) and Gilbert et al. (2014).

The characteristic TOF distribution will be the most important component of the noise sources for our heavy ion recovery schemes. We begin by introducing the Harp Emission (HE) and Field Emission (FE) TOF distributions in Figure A2.18. These two noise sources are essentially the building blocks to the Background and ESD noise sources discussed earlier. The HE distribution stems from electron emission from high-voltage wire harps in the FIPS TOF section, and the FE distribution from a localized field emission source near the edge of the start MCP active area (Gilbert et al. 2014). The location of the peaks in the HE distribution in Figure A2.18a correspond to the flight times of ions desorbed from the start MCP (by the impact of secondary electrons from the carbon foil or emission from wire harps) traveling to the top of the TOF chamber (Figure A2.13), where they cause electrons to be emitted which are then drawn to the stop MCP, triggering the stop signal. This results in a correlated start-stop signal pair that does not correspond to a real ion event.

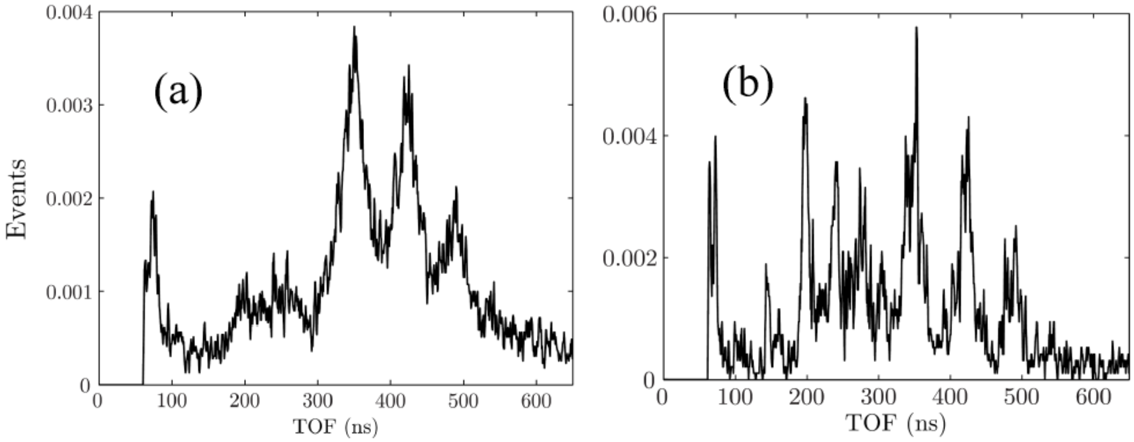

Figure A2.18 Normalized TOF distribution for background ESD events in MESSENGER/FIPS trigger by a) harp electrons (HE) and b) field emission electrons (FE). The harp emission TOF distribution corresponds to the flight times of desorbed species from the surface of the start MCP to the top of the TOF chamber. The field emission events include a contribution from desorbed ions that strike the side of the TOF chamber, leading to flight times at a constant fraction of the corresponding harp emission distribution peaks. Adapted from Gershman et al. (2013a).

The FE TOF distribution stems from a similar process, and is shown in Figure A2.18b. In this case electrons emitted from nearby voltage cables impact the start MCP, similar to the HE. However, for the FE case the MCP impact site is much more localized as a “hotspot” of sorts (see Gilbert et al. 2014 for details). Ions desorbed from this location on the MCP are more likely to strike the sides of the TOF section before reaching the top of the TOF section (due to the cylindrical geometry of the TOF section). This effectively shortens the travel distance of the desorbed ion before the stop MCP is triggered by the emission of secondary electrons when the desorbed ion impacts the TOF section wall. Thus the FE distribution has peaks that are a fraction of the HE TOF distribution in addition to TOF peaks that are similar to the HE distribution. The HE and FE TOF distributions are generated by examining the region of TOF space labeled as Background over time periods when very few heavy ion count are expected (i.e. outside Mercury's magnetosphere). Any measurements accumulated in this region are assumed to be noise and then used to create the distributions seen in Figure A2.18. These distributions are created for every 50 day period of FIPS data.

With the HE and FE distributions characterized we now define the Background (or passive) and ESD expected noise distributions in an identical fashion as Gershman et al. (2013a). The passive distribution is simply a weighted average of the HE and FE distributions. The weight is determined by the fraction of the MCP that corresponds to a "hotspot", characteristic of the FE distribution (see Gershman et al. 2013a for details). The ESD distribution is primarily determined from the HE TOF distribution. However, when incident particles are measured by FIPS, they produce secondary electrons from the carbon foil that tend to hit closer to the center of the MCP than events recorded during the Background period that generated the HE TOF distribution. This effects the distribution of locations that desorbed ions originate from on the start MCP. Thus the flight times of the desorbed ions differ slightly from the flight times observed during the Background period. This effect is approximated by shifting the HE TOF distribution so that the observed TOF peak around 325-375 ns (Figure A2.18a) lines up with the peak seen in each daily accumulation of real data (see Gershman et al. 2013a for details). The ESD distribution in then simply a slightly translated version of the HE distribution. This ESD distribution is generated for every E/q step of FIPS with a cadence of 1 day.

The last important noise distribution required for our analysis is the Proton Tail distribution. This distribution is determined by an empirical fit to the data between the expected proton track and the start of the heavy ion tracks. Based on the fit in this region, the Proton Tail distribution is extrapolated to the higher TOF regions. This process is depicted in Figure A2.19, where a subset of the TOF range corresponding to the Proton Tail is displayed.

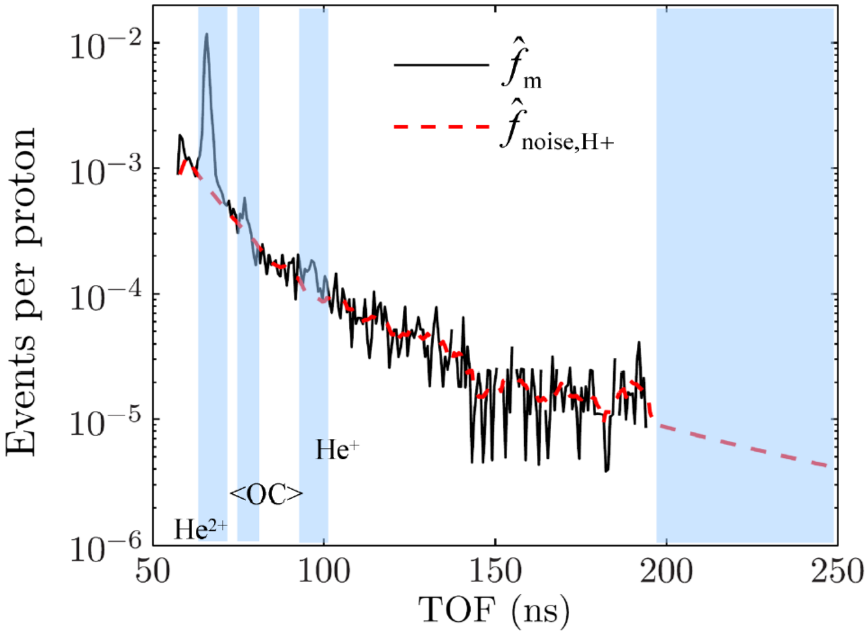

Figure A2.19 TOF distribution of proton tail events from E/q=1.5 keV/e for day of year 100-209 in 2011, normalized by the proton event rate. TOF value corresponding to solar wind ion tracks for He2+, He+, and an average oxygen and carbon group, are indicated. The black solid curve is the set of normalized raw measurements. The red dashed curve represents a smoothed curve that has been interpolated through ion track regions and extrapolated to higher TOF values with a power law. Adapted from Gershman et al. (2013a).

Note that the peak of the proton distribution not shown, it is at a lower TOF which is truncated in this image. The profile for the Proton Tail shown in the red-dashed line which is simply a smoothed interpolation of the raw TOF distribution shown in black. The vertical blue highlighting in Figure A2.19 with ion labels indicates the portion of the TOF distribution that is not included in this interpolation. For the region corresponding to heavy ion tracks (the blue shaded region above 200 ns) the interpolation of the raw TOF distribution is fit with a power law and then extrapolated to these higher TOF values. This recovery of the proton tail distribution is performed for the TOF distributions at every E/q of FIPS at a 10 day cadence. For reference, a summary block diagram of the relationship between the different noise models employed is shown in Figure A2.20.

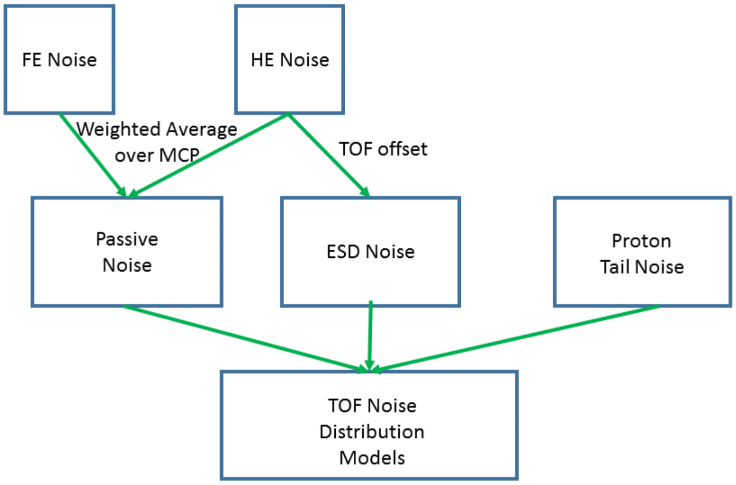

Figure A2.20 Block diagram indicating how the noise distributions for the FIPS instrument are categorized and contribute to generating a noise distribution model for use in the ion recovery scheme.

A2.4 Creating a spare FIPS

The forward modeling work in the previous section is based almost entirely on the results of the TRIM simulations (Ziegler 2004; Ziegler et al. 2010). TRIM does provide a robust tool for estimating energy loss and angular scattering in foils, but a large uncertainty exists in TRIM simulations due to the lack of quantitative knowledge of foil composition and thickness. Carbon foils are often not made of only carbon but contain elements such as, e.g., H, O, F, Na, and K (Gruntman 1997 and reference therein). Trying to model these impurities with TRIM still does not result in completely satisfactory results compared to laboratory measurements (see Allegrini et al. 2016 for details). In Allegrini et al. (2016), they recommend using empirical data of foil performance instead of TRIM, when available. As the in-flight FIPS is no longer available for further calibration, the next best alternative is to construct a comparable model of FIPS in a laboratory environment. This may allow for validation of the TRIM modeling performed or even help refine the forward modeled energy straggling and TOF distributions.

Thus a model of the TOF section of the FIPS instrument was assembled, essentially from spare parts found in the laboratory of its initial construction. The minutia pertaining to this model construction are quite involved, but are not the focus of this discussion. An assembled version of the FIPS TOF section can be seen in Figure A2.21, before the outer shell that covers the TOF section is affixed. This image should be very reminiscent of the sketch of the TOF section in Figure A2.13.

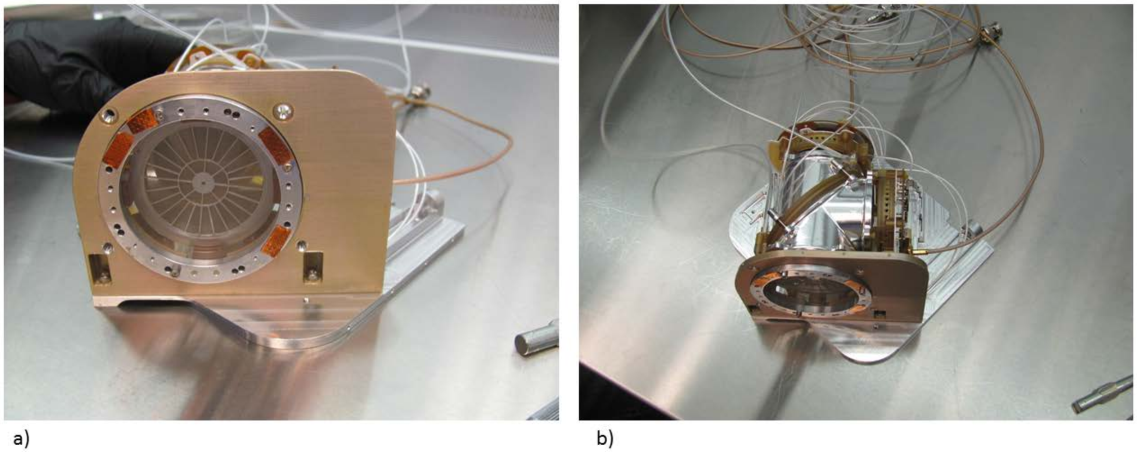

Figure A2.21 In a) the entrance aperture of the FIP TOF section is shown. In b) the TOF section is shown from above, apart from the covering, the TOF section is fully assembled.

In order to power this TOF section a very specific set of voltages have to be produced and applied. Some of these voltages are used in the forward model of the FIPS instrument presented in Section A2.3. While the actual flight instrument had a dedicated power supply with very stable voltage outputs are the required levels, for this lab effort we are limited to constructing a basic voltage divider. A schematic of the voltage divider utilized is presented in Figure A2.22. In Figure A2.22a-b pictures of the assembled voltage divider are shown, whereas in Figure A2.22c a more intelligible circuit diagram of how the PAHV and the MCP voltage supply were integrated into the resistive network is shown.

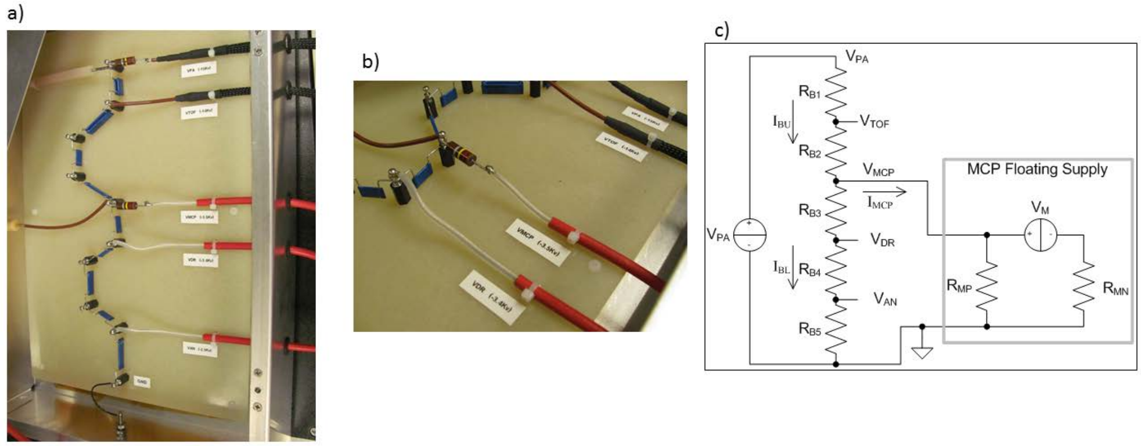

Figure A2.22 In a) and b) pictures of the assembled resistive divider network are shown, creating the voltages required to run the TOF assembly of FIPS. In c) we show the idealized sketch of the resistive divider network, and how it interfaces with the MCP voltage supply.

After a satisfactorily assembled and powered TOF section was achieved, the primary focus was to make TOF measurements analogous to the inflight data. To accomplish this the TOF section is placed in a vacuum chamber such that it can observe incident ions accelerated toward its entrance aperture. A picture of the actual lab setup is shown in Figure A2.23, where Figure A2.23a shows the vacuum chamber and a portion of the ion acceleration tube and Figure A2.23b shows the power supply used for the FIPS TOF section.

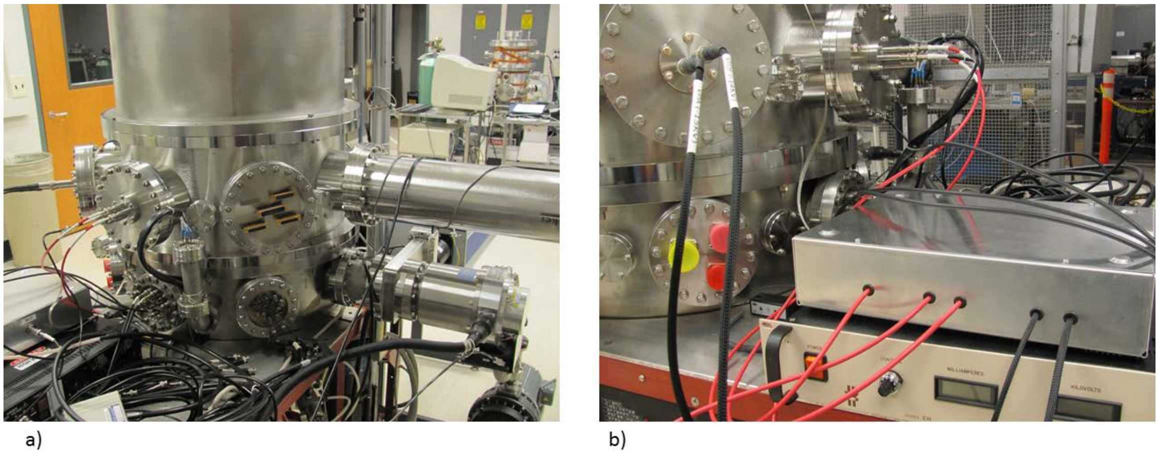

Figure A2.23 In a) we show the current experimental setup, the ion beam enters the vacuum chamber from the right where it is measured by our TOF assembly. In b) we show the resistive divider voltage taps that power the TOF assembly's electrostatic fields.

A rough schematic of the lab setup is also shown in Figure A2.24. Further details of the Mass Spectrometry Laboratory of the University of Michigan and the setup of this ion beam and vacuum chamber can be found in Gilbert et al. (2010). With the use of a Wien filter we are able to select different ion species based on their mass per charge ratio (m/q) and accelerate them toward the TOF section at energies from 1-13 keV. As the ions enter the TOF section they trigger the start and stop TOF signals as described previously. These signals are taken from the TOF section and sent to a computer (after some signal processing) for further analysis.

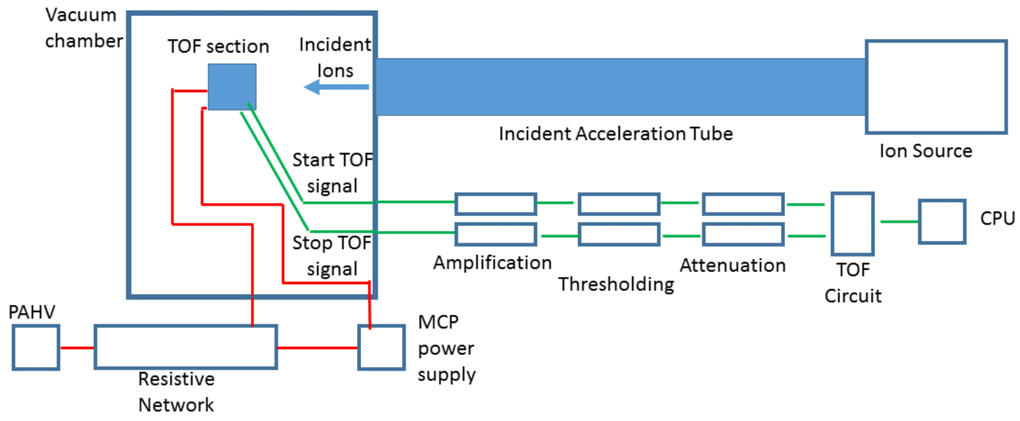

Figure A2.24 A block diagram of the ion measurement setup for testing the FIPS TOF section. Ions are sent from the ion source along the acceleration tube toward the TOF section. The TOF section records a start and stop TOF pulse corresponding to how long it takes an ion to traverse the TOF section. These pulse are sent out of the vacuum chamber and undergo some signal processing before being read into a TOF circuit and then sent to a computer terminal for analysis. The TOF section has its voltage points controlled by a resistive network powered by the post acceleration high voltage power supply. There is also a separate power supply for the MCPs that records the start and stop signals in the TOF section.

An example of the TOF distributions measured with the lab TOF section are shown in Figure A2.25, where the distribution measured for H, N, and O ions are histogrammed. The peak of each of these distributions is relatively clear, even if the distribution itself is a little noisy in sections. These TOF measurements were taken at an incident beam energy of 1 keV and serve as an excellent proof of concept for the reconstructed TOF section.

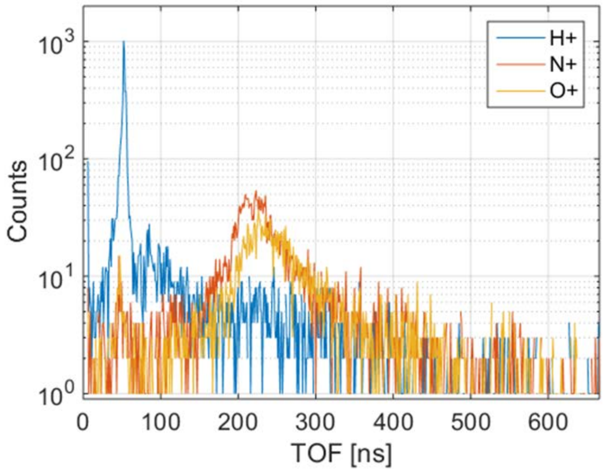

Figure A2.25 In a) we show preliminary time of flight (TOF) measurement made with our reassembled FIPS TOF assembly with an incident beam of 1 keV and PAHV=-10.5 kV.

To provide measurements that are useful for refining the forward modeled TOF distributions discussed in the previous section we must expand upon these initial measurements. This involves both measuring more ions relevant to Mercury's space environment and also measuring a range of incident energies for those ions. The ions useable with the current ion source must be relatively stable as a gas in order to be input into the ion source. Gases that are readily available in the lab are H_2, O_2, N_2, and Ar. Of these options only O_2 (and maybe Ar) produces heavy ions that are relevant at Mercury. Another option is to input SF_6 gas, which is quite stable, in order to produce sulfur ions. However, there will likely be several byproducts created when ionizing SF_6 and these may coat the inside of the vacuum chamber with unwanted depositions. Thus we must first verify the ability to make TOF distribution measurements across a range of incident energies, with the less complicated gases readily available in the lab.

These initial tests took the form of H^+, N^+, and O^+ ion measurements in the range of 1keV to 13 keV in incident energies. We show the post-processed results of these measurements as E/q vs TOF histograms in Figure A2.26, Figure A2.27, and Figure A2.28. Unfortunately, as we explain below, we find that the TOF histograms collected at 1 keV are not representative of the ability to collect useful TOF distributions at all incident energies.

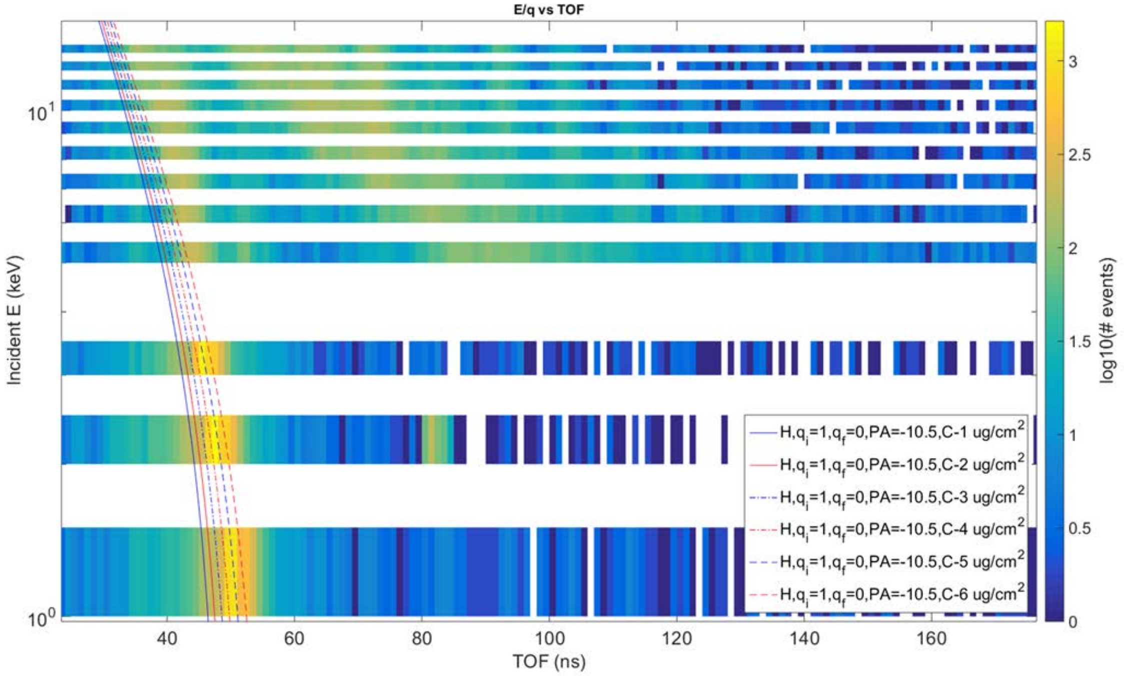

Figure A2.26 A histogram of the TOF distributions observed over a range of different beam energies. The beam energy is binned such that the lower bound of the bin on the plot is equal to the incident energy value corresponding to that bin. The "width" of the bins in the energy dimension is arbitrary and the white space between them emphasizes that they were collected on sequential experimental runs. Modeled E/q vs TOF curves for protons are overlaid as lines. The prefoil ion charge (q_i), postfoil ion charge (q_f), Post Acceleration (PA), and carbon foil thickness for each model curve are indicated in the plot legend.

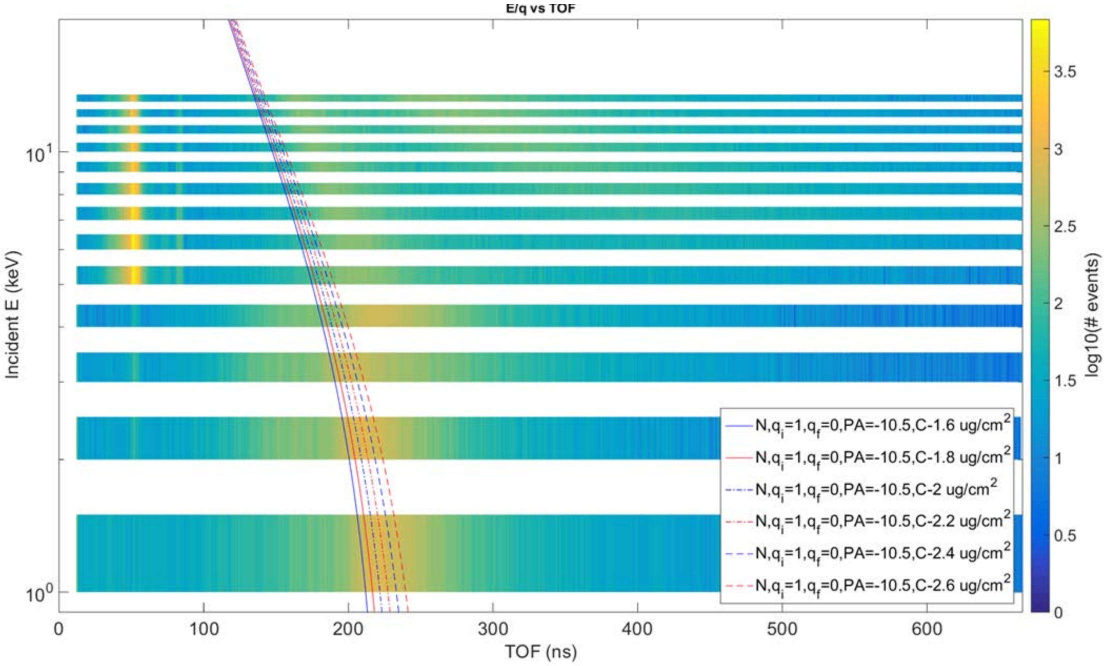

Figure A2.27 This figure is shown in the same format as the previous Figure A2.26. The difference is that N+ ions were selected via the Wien filter instead of H+ as in the previous figure. Modeled curves are overlaid as in the previous figure.

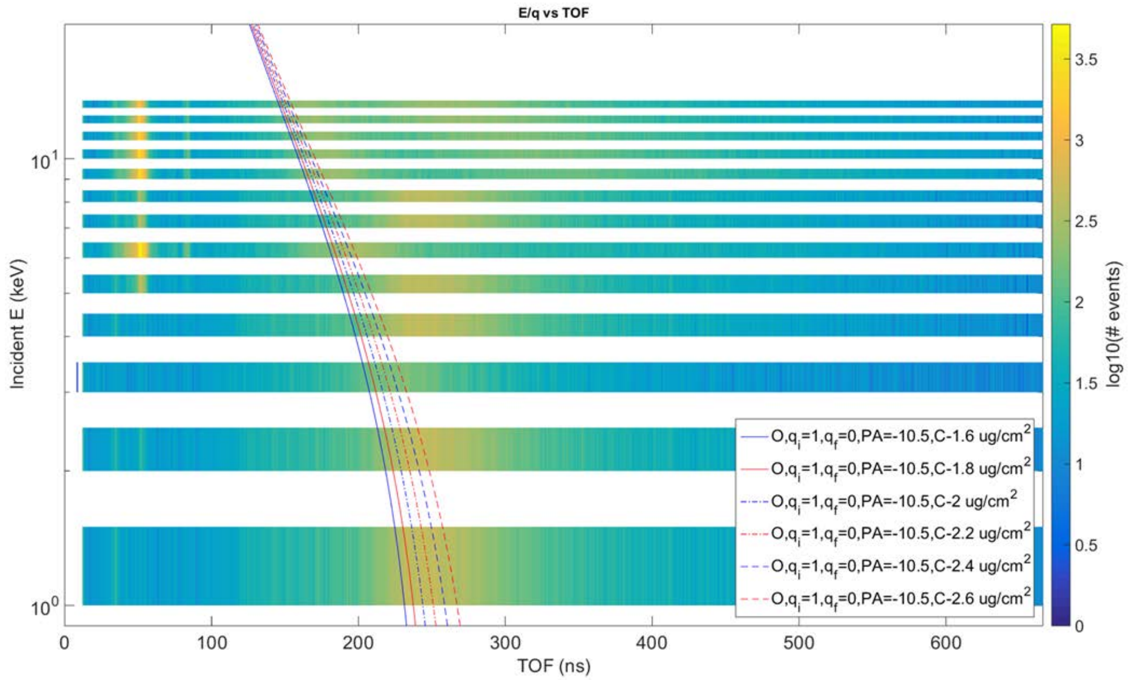

Figure A2.28 This figure is shown in the same format as the previous Figure A2.26. The difference is that O+ ions were selected via the Wien filter. Modeled curves are overlaid as in the previous figure.

In Figure A2.26, which are the measurements for the TOF distributions of H^+, there is a spurious second peak in the TOF distribution appears for incident energies above 4 keV. Furthermore, when our forward model for the E/q vs TOF behavior is overlaid on the same figure, we find that we cannot exactly reproduce the observed trend line for the peak of the TOF distribution at each energy. We overlay forward modeled trend lines for several carbon foil thicknesses and find that at lower energies a thickness of about 4 ug/cm^2 seems to best fit the data. However, this foil thickness does not match well at all with the behavior seen at higher incident energies, where the TOF peak is at higher TOF values than our model predicts.

In Figure A2.27, and Figure A2.28 we find similar inconsistencies in the measurements. In both the case of the N^+ and O^+ ions measurements we find significant deviations in the measured TOF distribution from the best fit modeled TOF distribution. The case for O+ is particularly telling as the TOF distribution peak appears to jump around non-monotonically with increasing incident energies. The spurious behavior suggest an issue with the experimental setup. In particular if the forward model for a single ion cannot match the observations, we must consider that we are actually measuring varying contributions from multiple ions. The ion source never has only one pure sample of gas in it, thus a Wien filter is the only way to select the desired species.

Despite the fact that the Wien filter should provide a filter for ion species by their m/q it appears that the TOF signature of multiple ions shows up in the measurements. This could mean that the spatial size of the TOF section entrance aperture is large relative to the separation of ion species by the Wien filter. I.e. the crossed electric and magnetic field of the Wien filter do not bend unwanted ion species far enough away from the central axis of the ion drift tube to avoid their entering the TOF section.

We verify this theory of multiple ions entering the TOF section by looking at several 1D cuts through the E/q vs TOF histograms presented in the previous figures. In Figure A2.29 we take three different E/q cuts at 1, 7, and 12 keV and overplot the measured TOF distributions when the Wien filter is set to filter only for N^+ (red) and only for O^+ (blue). It is clear that for the 1 keV case the TOF distribution agrees well with a forward model with a carbon foil area density of 2 ug/cm^2. However, for the higher energy cases we see clear deviation from the forward model TOF peak predictions. In particular, for the 12 keV case we see that the same measured TOF distribution is observed for both ions, even though the Wien filter is set to different values for each case!

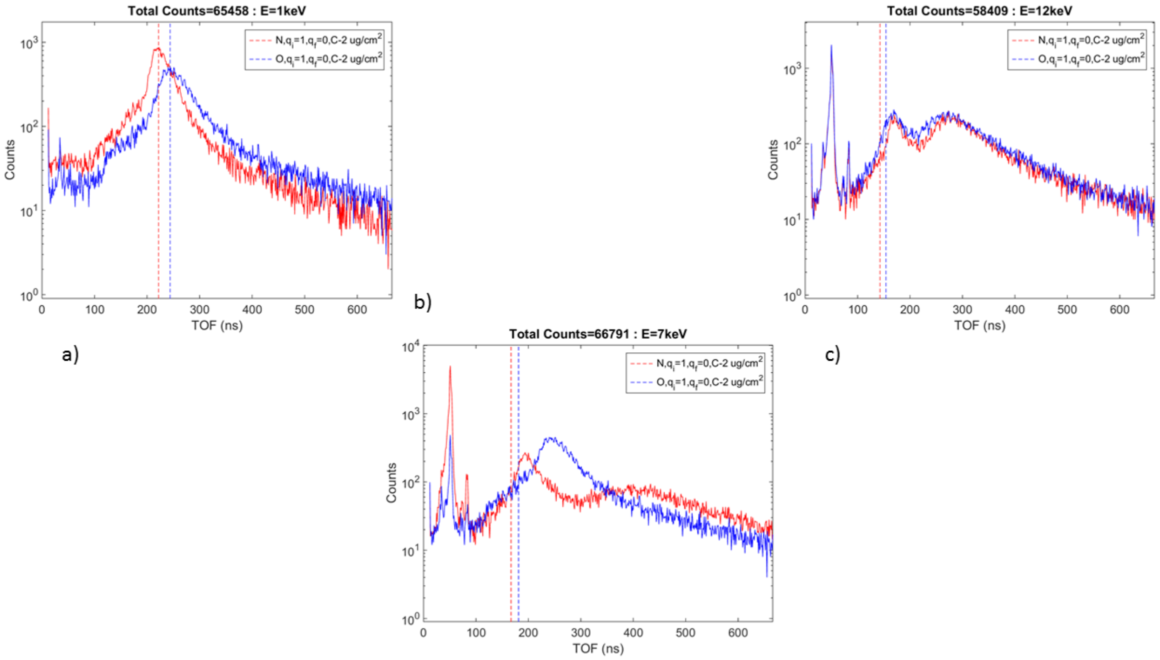

Figure A2.29 The measured TOF distribution for N+ and O+ at incident energies of 1, 7, and 12 keV are shown in panel a-c, respectively. The vertical lines indicate the expected peak of the TOF distribution from the best fit model for each ion.

These issues with validating the TOF measurements with the experimental setup persisted up to the time of the writing of this thesis. Future work will focus on identifying and solving this issue so that specific ion species can be selected with confidence and make sense with forward model predictions. When that milestone is achieved the testing of ions relevant to Mercury's space environment will proceed. If confidence can be established with those ions, the forward model TOF distributions created from TRIM simulations will be modified to include any significant changes.

A2.5 Identifying overlapping ion signatures

A2.5.1 Synthetic data validation of MLCA

Based on the lab measurements available at the time of this dissertation, the TRIM based forward model represents the most reliable method to separate ion tracks in the FIPS flight data. This section deals with developing a statistically robust scheme to separate overlapping ion tracks into their most probable sources, using the forward modeled TOF distributions for each ion.

We will begin with a sample of the FIPS E/q vs TOF data from the -13 kV period that is broken up into broad ion groups. In Figure A2.30, a histogram of the E/q and TOF of all the ion counts measured by FIPS with bounding tracks for several ion groups. These ion groups are representative of the models used in the works of Raines et al. 2013, where the ions were grouped into an O^+ group (O^+ and water group ions), a Na^+ group (including Na^+, Mg^+, Si^+), and a Ca^+ group (including S^+, Ca^+, K^+). Grouping the ions in this manner does not allow overlapping ions to be separating into distinct groups. Implementing a most probable separation of these overlying track should allow such a separation.

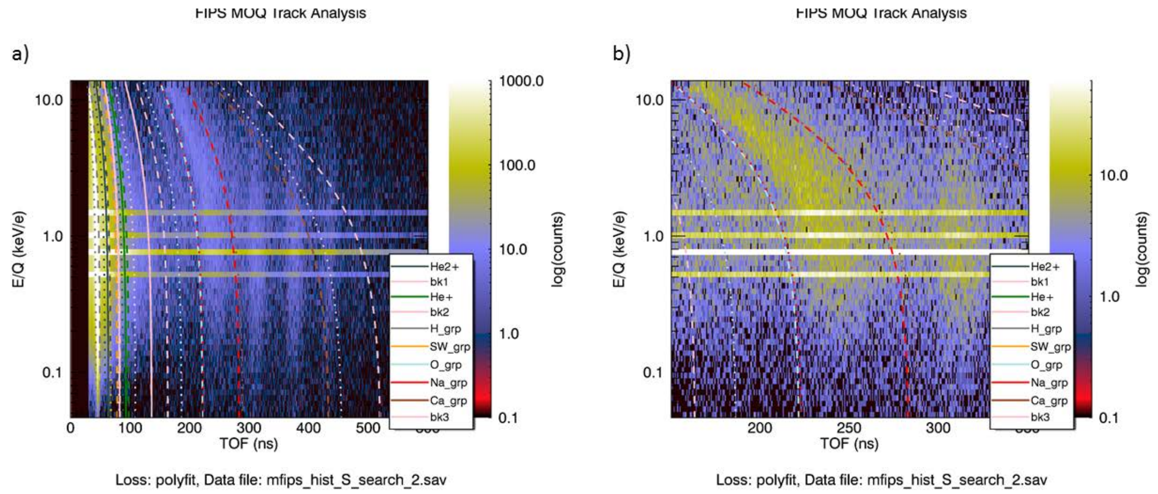

Figure A2.30 The measured counts in each Energy-per-Charge (E/q) and Time of Flight (TOF) bin measured by FIPS for the PAHV = -13 kV time period. The color scale indicates the number of counts in each bin and is logarithmically spaced. The predicted "tracks" for several ion species or ion groups are overlaid as colored lines. In panel a) we should the entire TOF space (0-666 ns) sampled by FIPS. In panel b) the TOF range is narrowed to focus on the region most relevant to the ion recovery analysis of this work.

As discussed in the main text a Maximum Likelihood Count Assignment scheme is implemented to statistically separate ion groups that overlap in the E/q versus TOF measurement space of the FIPS instrument. The end product of the MLCA scheme is a unique estimate of the number of counts attributable to each ion's probability distribution function in TOF space, at each E/q step of FIPS.

As a first check of the MLCA technique, synthetic TOF distributions were created from TRIM data and fed into the algorithm. Of particular interest was how well very overlapped peaks could be recovered. To this end, we assembled TRIM data with 1E5 incident counts of Si and Na and 1E3 counts of S and Mg. Sodium and magnesium are heavily overlapped in TOF space and silicon and sulfur also show moderate overlap. In Figure A2.31, the synthetic TOF distribution is shown with black open circles and the recovered TOF distributions are shown according to the legend.

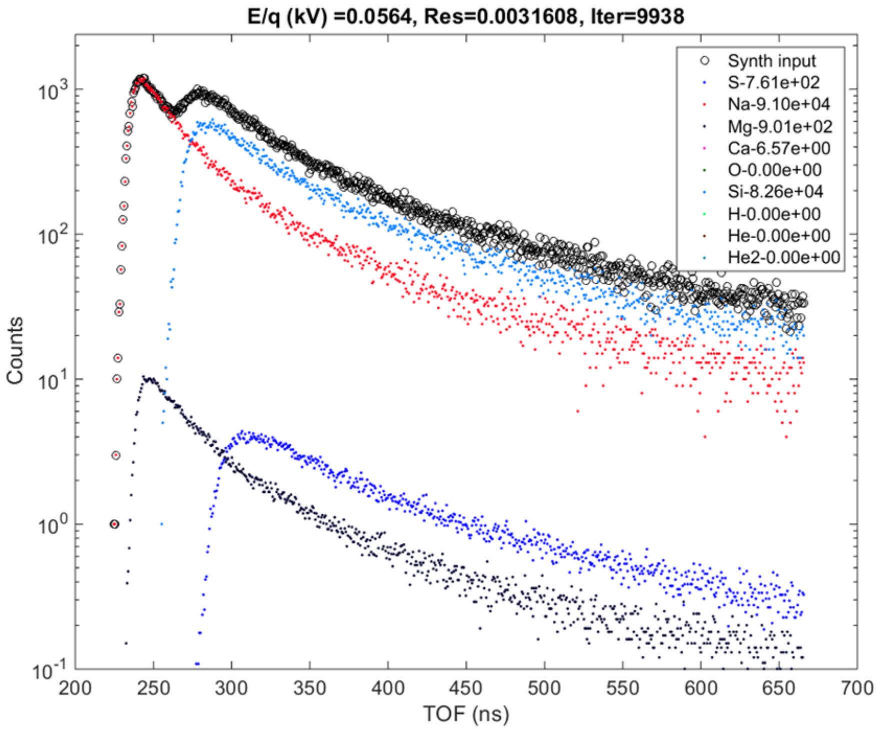

Figure A2.31 Graphical representation of how the MLE algorithm separates the contributions several different species in a synthetic data trail. The input TOF histogram was generated with a summation of Na, Mg, S, and Si ion TOF distributions. Input: 10^5 cnts Si, 10^3 cnts S, 10^5 cnts Na, 10^3 cnts Mg.

One potentially misleading feature of Figure A2.31 is that a TOF distribution of the recovered ion species is shown. From (4.14), it is clear that the TOF dimension is summed over during the recovery process, making is impossible to recover TOF resolved ions. The displayed distributions result from simply scaling the probability distribution of an ion species by the number of recovered counts. This is valid in the high count limit, but for sufficiently low counts, the actual TOF distribution will be some random sampling of the displayed distribution. It is also important to note that even though 1E5 counts are sent in to the TRIM simulation, not all of them will make it through the carbon foil and count in the TOF distribution. Therefore comparing the recovered counts to the number of ions launched in TRIM is not accurate. In Figure A2.32, a more detailed analysis of the MLCA recovery performance is shown. Furthermore, the recovery is shown for all 60 E/q steps with the same synthetic data input conditions for Si, Na, S, and Mg.

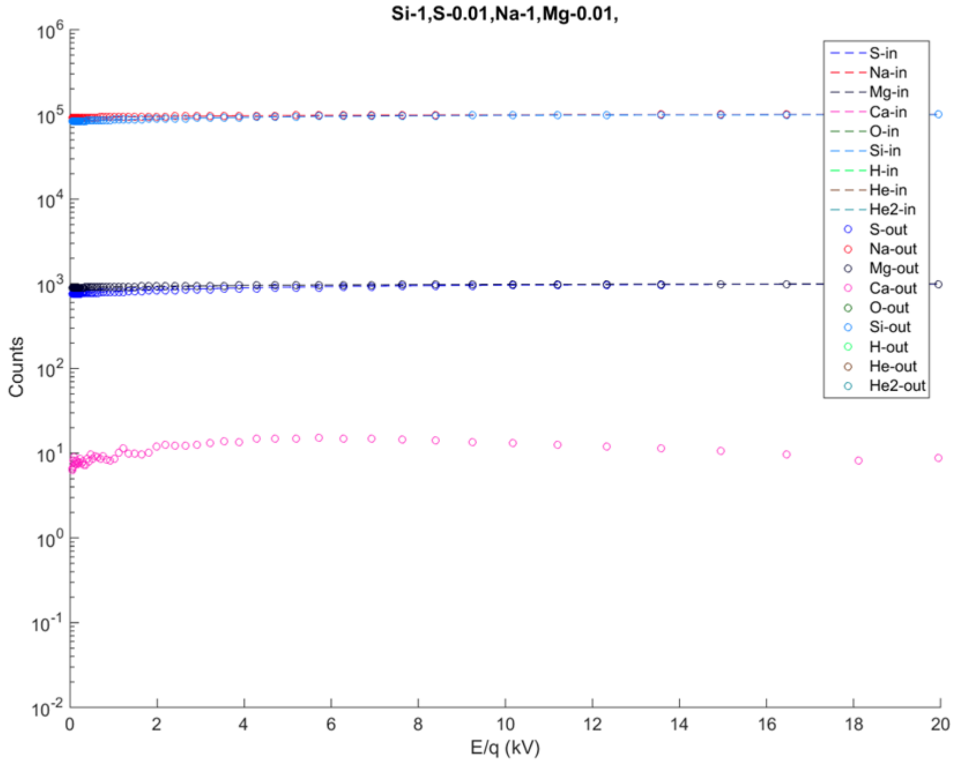

Figure A2.32 A comparison of the recovered vs input count totals in synthetic data evaluations of the MLE algorithm. For each E/q step of the FIPS instrument we sum together some amount of counts from S, Si, Na, Mg. The amount of counts input from each is shown in a dashed line. The output number of counts for each ion species is shown as colored circles at each E/q step, according to the legend. The recovered count totals essentially lie on top of the input count totals, indicating a near-perfect recovery. The exception is the Ca recovered counts, which had no corresponding input counts.

The dashed lines indicate the total number of ions of a given species that passed through the carbon foil and entered the TOF section in the synthetic data. The open circles indicate the recovered number of counts for a given ion species. This figure essentially shows a perfect recovery of even the heavily overlapped Na and Mg species, the only erroneous recovery is that some input counts are assigned to Ca, which was not included in the input synthetic data. However, the erroneously assigned Ca is a full two orders of magnitude below the count recovery levels for Si and S. This recovery indicates the power of the MLCA scheme, but one should note how dependent the recovery is on the assumed probability distributions. In the case of the synthetic data, the input data matched the TOF probability distributions for each ion perfectly, TRIM was used to derive both. For real inflight FIPS TOF distributions, this will no longer be the case.

A2.5.2 Application of MLCA to inflight data

The most important difference in the application of the MLCA scheme to synthetic versus flight data is the presence of a noise signature. The MLCA scheme can only assign counts based on the probability distribution given to it, therefore, with no knowledge of noise sources the model will assign noise counts as real ions. An example of this is shown in Figure A2.33, where the approximate recovered TOF distributions for each ion are shown relative to the flight data.

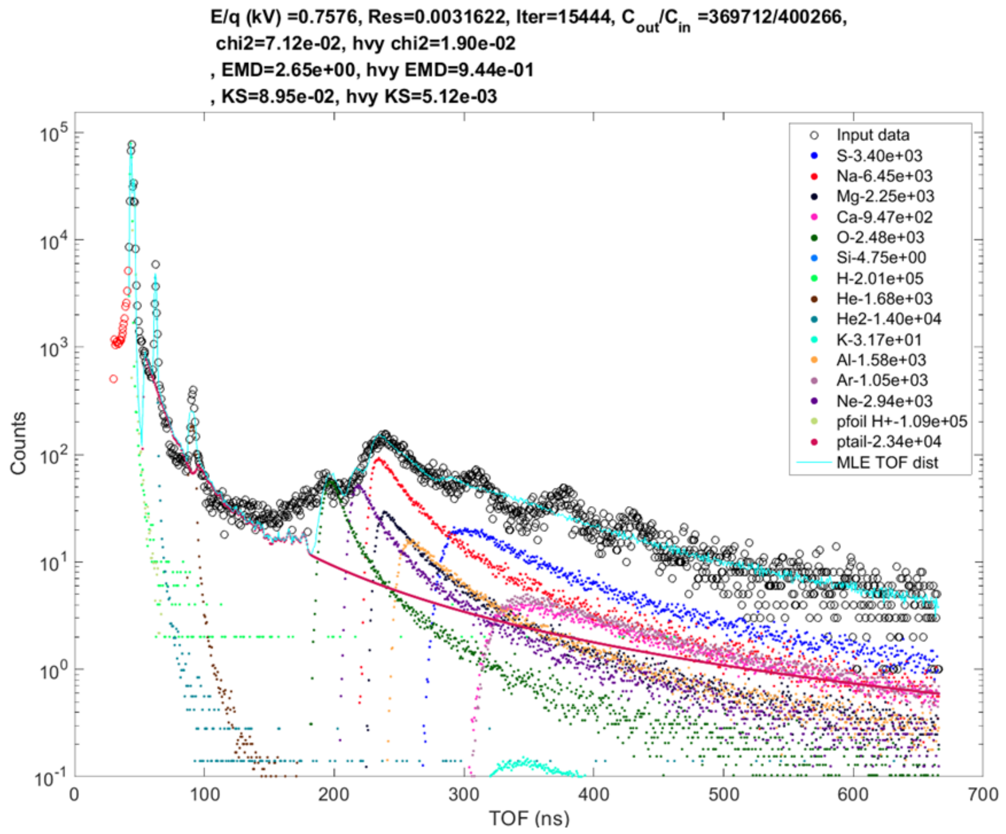

Figure A2.33 Example of the MLE recovery from a real in flight TOF distribution collected by FIPS. The noise distribution corresponding to dark counts is not included in the recovery to show the erroneous assignment of dark counts as real ions. The TOF distribution corresponds to an incident E/q of 0.5156 kV, and a PAHV of -13 kV. The red circles indicate points in the measured TOF distribution that were not assigned to any ion (no valid probability distributions in those TOF bins).

The region of interest in this figure is from TOF= 300 ns to 500 ns. From earlier in this section we know that the three peaks in this section are characteristic of the HE or FE noise distributions and are not signatures of real counts. However, as the MLCA model has only real ion distributions to work with, these peaks are assigned to ions such as S, K, and Ca which have the most pronounced distributions at high TOF values. The cyan line shows the sum of the recovered ion distributions and it is apparent that it does not match well with the three peak structure from 300-500 ns.

In an effort to include the effects of the noise sources present in the FIPS instruments, we add pseudo-ion distributions to the MLCA model that have TOF distributions consistent with the noise sources. In Figure A2.34, we show an example of the MLCA recovery with the Proton Tail, Electron Stimulated Desorption, and passive probability distributions included.

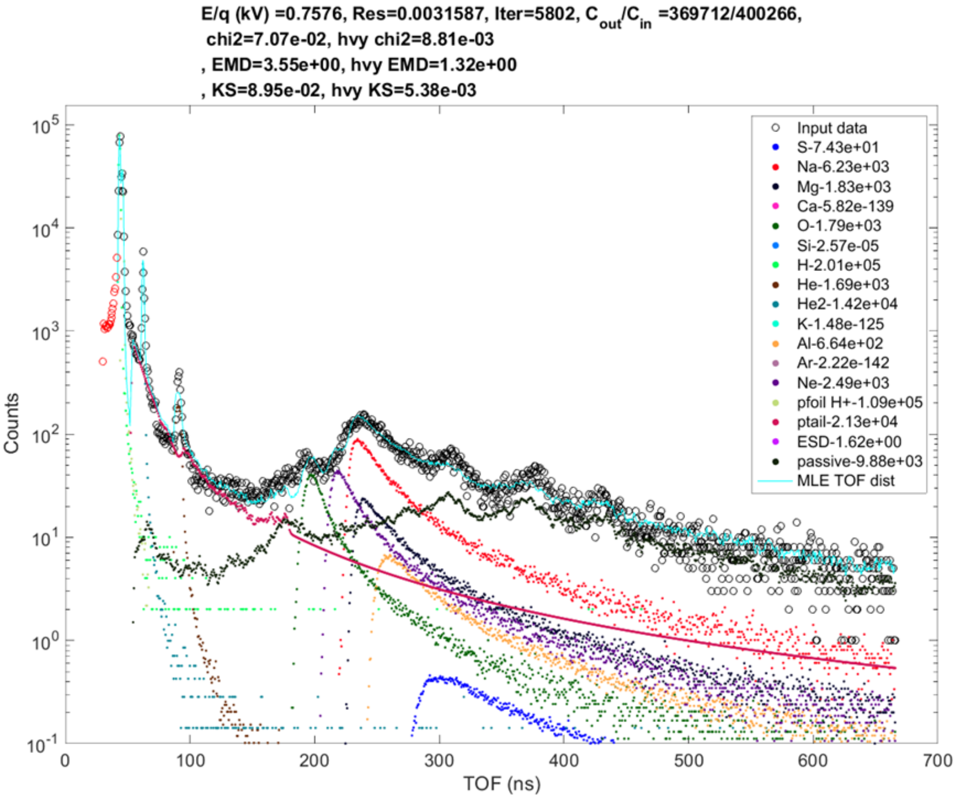

Figure A2.34 An MLE recovery for the -13 kV time period, E/q 1.011 kV. In this case a noise distribution for the dark counts is included in the MLE recovery. These distributions are the Proton Tail (ptail) Electron Stimulated Desorption (ESD) and passive distributions and are shown in the plot legend. The estimated total recovered count distribution is shown with the cyan line (details in text).

Examining how well the total recovered TOF distribution (cyan line) matches the measured TOF distribution (open black circles) we see that three peak distribution is matched slightly better than it was in the previous figure. However, the match is not perfect in the 300- 500 ns region, and so we also try another noise distribution in an attempt to better match this region. Instead of using the ESD and passive distributions we opt for the more basic building blocks of those distributions, the Field Emission (FE) and Harp Emission (HE) distributions. Recall the passive distribution is based on a weighted average of the FE and HE distributions, and the ESD distribution is basically a shifted version of the HE distribution. With the FE and HE (along with Proton Tail) distributions as inputs to the MLCA method, we are better able to reproduce the observed peaks in the 300-500 ns region. This is shown in Figure A2.35.

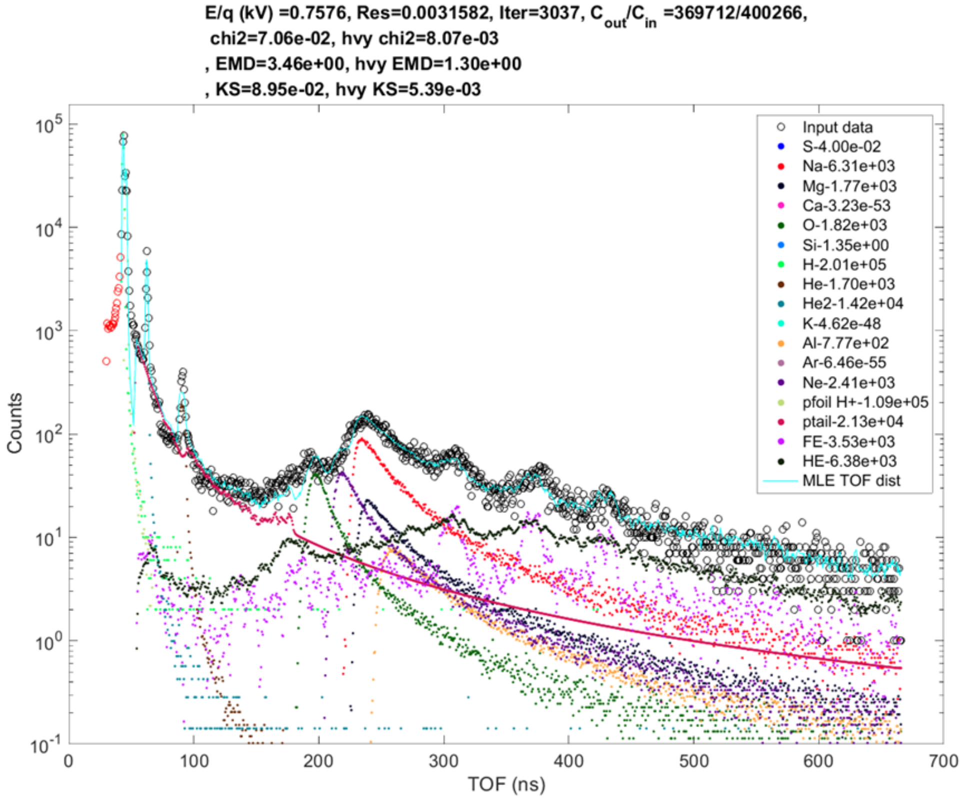

Figure A2.35 Same format as previous Figure A2.34. Exactly the same E/q step and time period as the previous figure, but the noise distribution is now modeled with the FE, and HE distributions. This creates a noticeably different recovered for some heavy ions.

The results for these particular E/q steps are a good start for characterizing the MLCA scheme, but we also desire an impartial method to evaluate the accuracy of the recovered ion count distributions relative to the observed TOF distribution. To accomplish this we will use several techniques to quantify the difference between the recovered TOF distribution and the measured TOF distribution. The first test is a symmetric version of the chi squared test. This is defined as

$$\chi^2 = \frac{1}{2}\sum_i \frac{(O_i - E_i)^2}{O_i + E_i} \tag{A2.95}$$

, where χ^2 is the recovered residual, O_i is the observed number of counts in TOF bin i, and E_i is the recovered number of counts in TOF bin *i*. The second test is the Earth Mover's Distance (EMD) (Rubner et al. 2000). This test is based on the cumulative distribution functions of the observed and recovered TOF distributions. We defined the (discrete) cumulative distribution function of the observed distribution as $C_i = \sum_{k=1}^{i} O_i$, and the cumulative distribution function of the recovered distribution function as $D_i = \sum_{k=1}^{i} E_i$. From these distributions, the EMD is defined as

$$EMD = \sum_i |C_i - D_i|. \tag{A2.96}$$

The last test we make use of is the Kolmogorov-Smirnov (KS) test, which ends up being quite similar to the EMD test (Lampariello 2000). The KS test statistic is defined as

$$KS = \max(|C_i - D_i|). \tag{A2.97}$$

, which is the maximum residual term from the cumulative distribution functions. An example of the computation of this statistic from the -13 kV period for E/q =0.5156 is shown in Figure A2.36. Here the individual terms of the χ^2 and EMD tests are shown as a function of TOF. The KS statistic is simply the maximum of the EMD statistics for each TOF value. In this case we are showing the recovery statistics for the case where the input noise distributions were Proton Tail, HE, and FE.

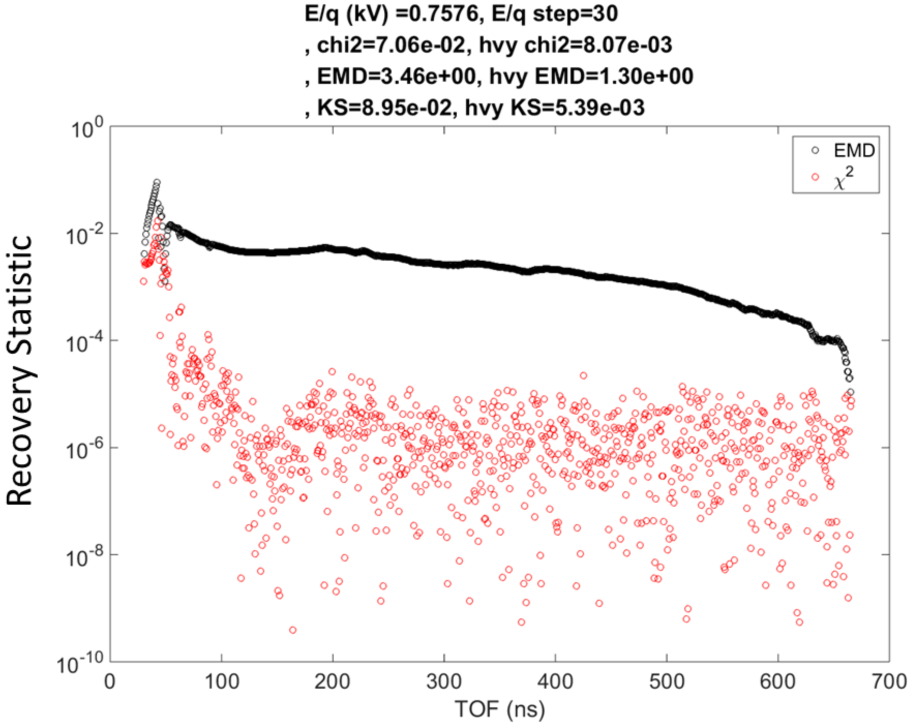

Figure A2.36 An example of the contribution of each TOF bin to the total residual statistic, for the three residual statistics computed. In the case of the EMD, and chi squared statistics, the total statistic is simply the sum of these contribution from each TOF bin. In the case of the KS statistics, the total statistic is the maximum value of the of contributions from each TOF bin.

It is clear from Figure A2.36 that the residuals from the proton peak at TOF values around 40 ns dominates the recovery statistic. Since the recovery of new heavy ions is of primary interest, we also define a heavy ion TOF range that computes the recovery parameters only over the reduced range of TOF = 150-400 ns. This should exclude the recovery of the proton peak from the goodness of fit metric.

For both the full TOF range and this new reduced heavy ion TOF range, we use these statistics to quantify the difference between the TOF distributions for three different noise model cases. In case 1 we only include the Proton Tail noise, this is meant as a control group for the heavy ion recovery evaluation. In case 2 we use the Proton Tail, ESD and passive noise sources, and in case 3 the Proton Tail, HE, and FE distributions are used. The results of these statistics for the whole TOF distribution are shown in Figure A2.37. We show the recovery statistics for six different permutations in this figure. The residual for the three different noise sources discussed above are computed for both the -10.5 kV and -13 kV time periods. As the proton peak dominates the recovery statistic, there is a lot of overlap between the different cases.

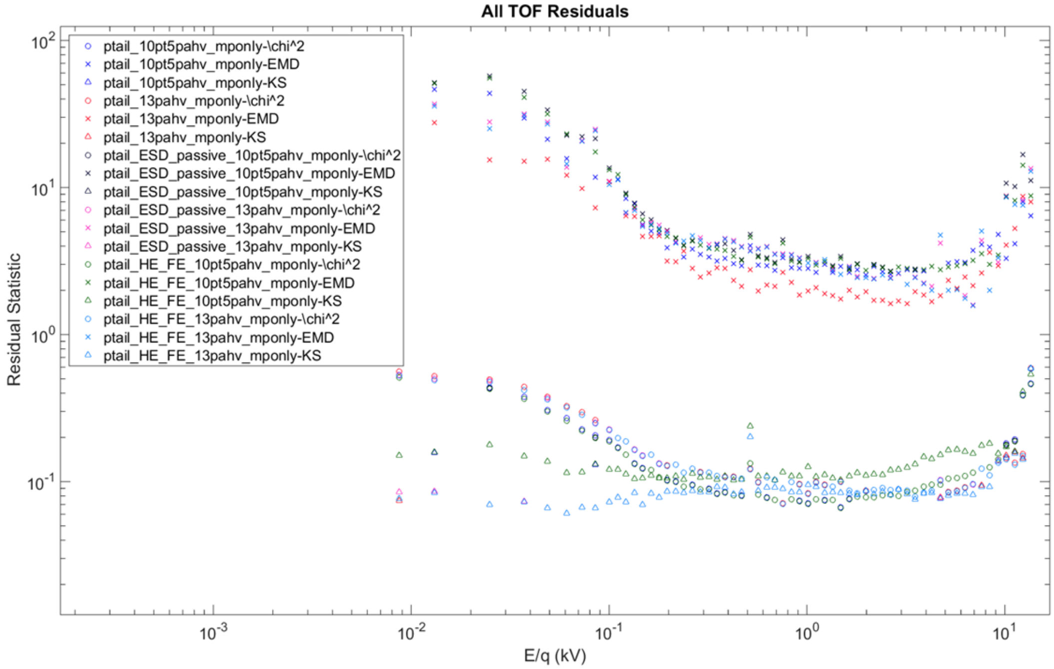

Figure A2.37 A plot of the calculated residual, using several different measures, for several different noise distributions. The lower the residual, the better the recovered TOF distribution at each E/q step matches the raw observed TOF distribution. Residuals over the entire TOF range, 0-666 ns are considered in this statistic.

Each residual method yields a very different value, but it is difficult to see much disparity between the different noise models within a particular residual statistic. There is a rough trend that the recoveries are better for all noise models between E/q =0.2 kV and about 7 kV, but no noise model completely outshines the others, for either the -10.5 kV or -13 kV cases. The heavy ion statistic should focus more on the recovery in the TOF region specific to the ions of interest, and is presented in Figure A2.38

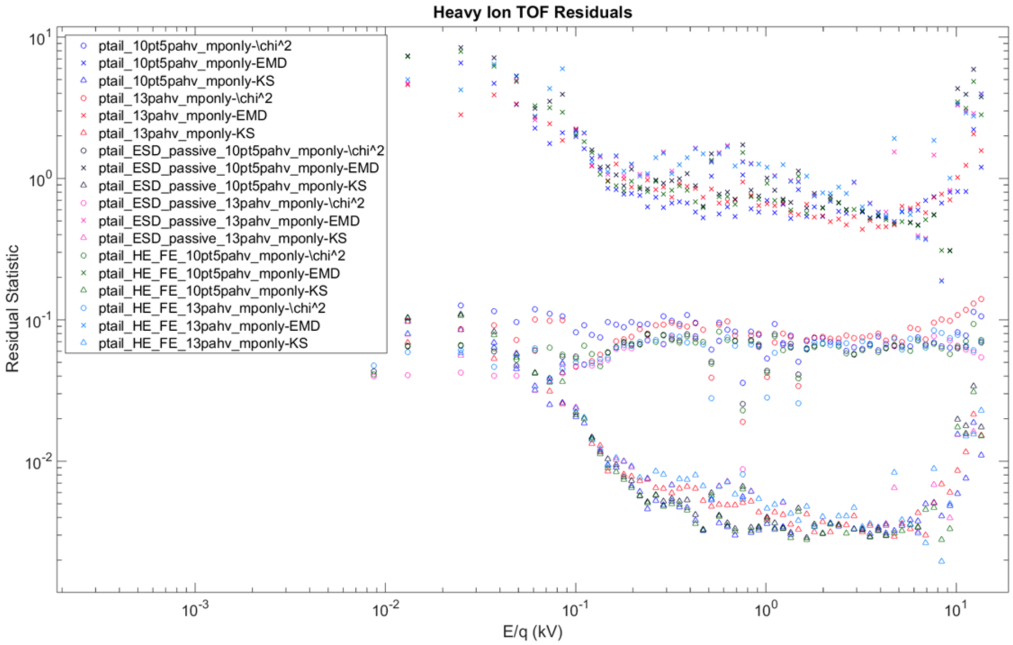

Figure A2.38 A plot of the calculated residual, using several different measures, for several different noise distributions. The lower the residual, the better the recovered TOF distribution at each E/q step matches the raw observed TOF distribution. Residuals over a subset of the TOF range, 150-400 ns are considered in this statistic.

Again, the discrepancies between the different models are not huge. Looking at the EMD and KS tests for both the -10.5 and -13 kV cases, it actually appears that the control case (just Proton Tail noise) has the lowest residual values. This does not make sense with the trends seen by eye in Figure A2.33-Figure A2.35, where it appeared that the HE and FE noise sources best matched the noise signature seen in the TOF distribution. We conclude that the EMD and KS noise metrics are dominated by features different than what is seen by visual inspection. In the case of the chi-squared residuals, the results in Figure A2.38 do at least seem consistent with what is seen by looking at the individual TOF recoveries. For both the -13 kV and -10.5 kV case the HE/FE and ESD/passive cases very similar, but are both lower than the control case. We don’t see large separation between the different noise models, which seems to defy the improved fit we see in comparing the ESD/passive and HE/FE noise distribution cases in Figure A2.34 and Figure A2.35.

Using a combination of the residual calculation and visual inspection of the recovered TOF distributions, we choose the HE/FE noise distributions for the two time periods of interest. Admittedly, there is some ambiguity as to which noise model best represents the noise associated with the measurements during our selected periods. With these noise distributions in place, the MLCA method will recover the most probable partition of counts between the ions (and noise distributions) at its disposal.

A2.6 Tracing foreshock plasma observations to a bow shock surface

This section describes how to find the location on a model bow shock surface that a plasma population observed in situ by FIPS, onboard MESSENGER, originated from. The model bow shock used is that described in Winslow et al. (2013). In the foreshock work performed, this tracing is done in one of two ways. In the first method, a trace is simply made along the in-situ measured magnetic field direction to find the intersection with a model bow shock surface. In the second method, the velocity vector of the observed plasma population is computed and a trace along this direction is used to find the intersection with the model bow shock. A trace along the velocity vector is only performed for the observed FAB populations, not for the diffuse populations as they do not have a recoverable bulk velocity.

Once a trace back to the bow shock surface is made, the angle between the IMF and the bow shock normal at that bow shock location, θ_{bn}, needs to be computed. The IMF vector at the bow shock location is assumed to be that same as that measured in-situ at the location of the MESSENGER spacecraft. The normal vector is computed from the analytic bow shock model.

A2.6.1 Recovery of population propagation direction

The analysis used in this section makes several assumptions about which parameters are available from measurements of the FIPS and MAG instruments on the MESSENGER spacecraft and the nature of the solar wind and IMF. It is assumed that the scalar value of the solar wind velocity is computed. For analysis of FAB populations it is also assumed that the FAB velocities are computed. The average magnetic field vector for a given foreshock event is assumed to be measured, and furthermore the magnetic vector at the bow shock surface is assumed to be equivalent to the in-situ magnetic field observed by the spacecraft. Last, the solar wind is assumed to flow radially outward from the Sun in an inertial frame centered on the Sun (Heliocentric Inertial Frame for our purposes).

We begin with the algorithm for tracing an observed FAB population, from its point of observation at the spacecraft, back along its foreshock propagation direction to the model bow shock surface. The first task of this recovery is to determine the velocity direction of the FAB, relative to the MSO coordinate system. As byproducts to this calculation, we will also determine the unaberrated solar wind velocity, the FAB velocity relative to the solar wind, and the flow direction of the solar wind relative to the MESSENGER spacecraft.

We begin by relating the FAB velocity relative to the solar wind to the FAB and solar wind velocities observed by the spacecraft. The calculation of these velocities in the spacecraft frame is described in Chapter 5. This relationship is expressed in (A2.98), where the notation A/B represents "A relative to B".

$$\vec{\boldsymbol{v}}_{FAB/SW} = \vec{\boldsymbol{v}}_{FAB/SC} - \vec{\boldsymbol{v}}_{SW/SC} \tag{A2.98}$$

We will assume that the FAB population flows along the IMF direction in the solar wind frame, letting us simplify the expression for $\vec{\boldsymbol{v}}_{FAB/SW}$. Only the scalar value of the FAB velocity in the spacecraft frame is recovered, so the full vector $\vec{\boldsymbol{v}}_{FAB/SC}$ is replaced by a scalar magnitude times an unknown unit vector. The magnitude of this unit vector, by definition, is unity, as represented in (A2.100).

$$v_{FAB/SW}\hat{\boldsymbol{b}} = v_{FAB/SC}\begin{bmatrix} x_1 \\ y_1 \\ z_1 \end{bmatrix} - \vec{\boldsymbol{v}}_{SW/SC} \tag{A2.99}$$

$$x_1^2 + y_1^2 + z_1^2 = 1 \tag{A2.100}$$

The solar wind velocity in (A2.99) is broken up to express its aberration from the radial direction due to MESSENGER's motion about the Sun. The vast majority of this aberration is due to Mercury's motion about the Sun as MESSENGER goes about its orbit around the planet.

$$\vec{\boldsymbol{v}}_{SW/SC} = \vec{\boldsymbol{v}}_{SW,HCI} - \vec{\boldsymbol{v}}_{SC,HCI} \tag{A2.101}$$

In the inertial HCI frame, the solar wind velocity direction is entirely antisunward, with some unknown magnitude. Only the magnitude of the solar wind velocity relative to the spacecraft is measured, so the full $\vec{\boldsymbol{v}}_{SW/SC}$ vector is broken into a magnitude and an unknown unit vector to express this. Finally, the spacecraft velocity relative to the Sun (its inertial velocity) is known from the CSPICE ephemeris data provided by NASA for the MESSENGER mission (https://naif.jpl.nasa.gov/naif/toolkit.html). These assumptions are expressed in (A2.102), and (A2.103) simply states that the unknown unit vector for the solar wind velocity relative to the spacecraft has a magnitude of unity.

$$v_{SW/SC}\begin{bmatrix} x_2 \\ y_2 \\ z_2 \end{bmatrix} = v_{SW}\begin{bmatrix} -1 \\ 0 \\ 0 \end{bmatrix} - \vec{\boldsymbol{v}}_{SC,HCI} \tag{A2.102}$$

$$x_2^2 + y_2^2 + z_2^2 = 1 \tag{A2.103}$$

Breaking up the vector expressions of (A2.99) and (A2.102) into their components yields six independent equations. Along with (A2.100) and (A2.103) this yields eight unknowns and eight equations, a fully determined system of equations. The unknowns we solve for are v_{SW}, $v_{FAB/SW}$, x_1, y_1, z_1, x_2, y_2, and z_2. This system of equations is solved using the nonlinear system of equations solver, *fsolve.m*, which comes in the standard MATLAB package.

With these equations, the direction of the FAB propagation in the spacecraft frame is determined. As the spacecraft velocity is small relative to Mercury's orbital velocity, the FAB velocity in the spacecraft frame is essentially the same as that in the MSO coordinate frame. However, for completeness, the FAB velocity vector in the MSO coordinate frame (relative to Mercury) is computed. Recall, the unit vector (x_1, y_1, z_1) is the direction of the FAB in the spacecraft frame, so the FAB velocity relative to Mercury is given by

$$\vec{\boldsymbol{v}}_{FAB,MSO} = v_{FAB/SC}\begin{bmatrix} x_1 \\ y_1 \\ z_1 \end{bmatrix} + \vec{\boldsymbol{v}}_{SC/Mercury} \tag{A2.104}$$

, where the velocity of the spacecraft relative to Mercury is determined by CSPICE.

The net result of the computations so far is the velocity direction of an observed FAB population, which is used to trace back to a model bow shock surface. This FAB velocity direction represents the slight aberration of the FAB population from the IMF direction by the solar wind velocity. If the foreshock population observed is a diffuse population, the tracing is simply performed along the measured average IMF direction for the event. This is because no bulk velocity is recoverable for the observed diffuse populations (see Chapter 5). For either the FAB or diffuse population, the recovered propagation direction in the MSO frame will be indicated with the unit vector $\hat{\boldsymbol{a}}$.

A2.6.2 Ray Tracing Algorithm

Tracing from the spacecraft location back to the model bow shock surface requires an analytic model for the bow shock. This model is taken from Winslow et al. (2013) and is based on a coordinate system that is a translation of the MSO coordinate system. The relation between the two coordinate systems is given by

$$\vec{\boldsymbol{r}}_{BS} = \vec{\boldsymbol{r}}_{MSO} - \begin{bmatrix} x_0 \\ 0 \\ z_0 \end{bmatrix} \tag{A2.105}$$

, where $\vec{\boldsymbol{r}}_{BS}$ is a position in the bow shock system, $\vec{\boldsymbol{r}}_{MSO}$ is a position in the MSO coordinate system, x_0= 1220 km (0.5 R_M), and z_0= 484 km (0.2 R_M). This translation between the coordinate systems accounts for a shift to the focus of the conic section that models the bow shock (x-direction shift) and a shift to account for the offset of the magnetic dipole of Mercury (z-direction shift). In the bow shock coordinate system, the bow shock surface is represented by the following

$$r = \frac{p\epsilon}{1 + \epsilon\, cos\theta} \tag{A2.106}$$

, where the radius, r, and the zenith angle, θ, have their usual meaning in spherical coordinates, p is the focal parameter, and ϵ is the eccentricity. The focal parameter is nominally 2.75 R_M, but is adjusted for each orbit to match the observed bow shock crossings (see Chapter 5). The eccentricity is taken to be 1.04 as calculated in Winslow et al. (2013). One important point for the bow shock surface is that the zenith angle θ is taken from the x-direction.

With the bow shock surface described, the intersection of that surface with a ray in the direction of propagation, $\hat{\boldsymbol{a}}$, must be computed. The ray has its origin at the spacecraft location and extends an arbitrary amount back along the propagation direction. As $\hat{\boldsymbol{a}}$ can represent either the FAB velocity direction, or the IMF direction, a ray in the direction of propagation may extend in the parallel or anti-parallel direction relative to $\hat{\boldsymbol{a}}$**.** The ray is modeled by (A2.107), where *s* is a free parameter to be solved for.

$$\vec{\boldsymbol{r}}_{ray}(s) = \vec{\boldsymbol{r}}_{SC} + s\, \hat{\boldsymbol{a}} \tag{A2.107}$$

The value of *s* that defines the point where the ray intersects the bow shock will satisfy (A2.106) such that

$$r_{ray,BS} - r_{model,BS} = 0 \tag{A2.108}$$

, where $r_{ray,BS}$ is the radial distance of the point on the ray corresponding to a given value of *s* from the origin of the bow shock coordinate system. The variable $r_{model,BS}$ is the radial distance from that same origin to the bow shock surface for the value of θ the corresponds to the current position on the ray, $\vec{\boldsymbol{r}}_{ray}$. Finding the value of *s* that satisfies this equation yields the position vector of the point of intersection of the ray with the shock surface. It is possible to get multiple valid intersections of the bow shock surface, but the most sunward intersection is the one that is physically relevant.

A2.6.3 Calculation of bow shock normal

After a successful tracing back to the bow shock surface, the most relevant quantity for shock acceleration processes and the formation of foreshock plasma populations is the angle between the bow shock normal and the IMF direction. Recall that the IMF vector direction at the point of intersection with the bow shock surface is assumed to be the same as the IMF vector measured in-situ at the spacecraft location. This is an inherent limitation of a single spacecraft mission. With this IMF vector determined, all that remains is to find an expression for the normal vector to our assumed bow shock surface model.

Writing the expression for our analytic surface in implicit form allows use to express the unit normal to the surface in terms of the gradient vector. This is seen in (A2.109) and (A2.110).

$$F(r, \theta, \phi) = r - \frac{p\epsilon}{1 + \epsilon \, cos\theta} \tag{A2.109}$$

$$\hat{\boldsymbol{n}} = \frac{\nabla F}{|\nabla F|} \tag{A2.110}$$

In spherical coordinates the del operator can be expressed as the following,

$$\nabla F = \frac{\partial F}{\partial r}\,\hat{\boldsymbol{r}} + \frac{1}{r}\frac{\partial F}{\partial \theta}\,\hat{\boldsymbol{\theta}} + \frac{1}{r\,sin\theta}\frac{\partial F}{\partial \phi}\,\hat{\boldsymbol{\phi}} \tag{A2.111}$$

, where θ is the zenith angle and ϕ is the azimuth angle. Note that we will temporarily assume that θ is the angle from the z-direction so that the standard formulas relating Cartesian and spherical unit vectors can be utilized. Recall that in our formulation of the bow shock model, θ is actually the angle from the x-direction. We will simply rotate our temporary axes to coincide with this convention after the expression for the normal vector is found.

Evaluating the expression for the gradient yields the expression shown in (A2.112).

$$\nabla F = \hat{\boldsymbol{r}} - \left(\frac{p\epsilon^2 sin\theta}{r(1+\epsilon cos\theta)^2}\right)\hat{\boldsymbol{\theta}} \tag{A2.112}$$

Using the usual relations between Cartesian and spherical unit vectors allows us to re-express (A2.112) as,

$$\begin{aligned}\nabla F = {} & (sin\theta cos\phi\,\hat{\boldsymbol{x}} + sin\theta sin\phi\,\hat{\boldsymbol{y}} + cos\theta\,\hat{\boldsymbol{z}}) \\ & - \left(\frac{p\epsilon^2 sin\theta}{r(1+\epsilon cos\theta)^2}\right)(cos\theta cos\phi\,\hat{\boldsymbol{x}} + cos\theta sin\phi\,\hat{\boldsymbol{y}} \\ & - sin\theta\,\hat{\boldsymbol{z}})\end{aligned} \tag{A2.113}$$

, where some simplification leads to the following expression (A2.114).

$$\nabla F = \hat{\boldsymbol{x}}\left(sin\theta cos\phi\left(1-\frac{p\epsilon^2 cos\theta}{r(1+\epsilon cos\theta)^2}\right)\right)+ \\ \hat{\boldsymbol{y}}\left(sin\theta sin\phi\left(1-\frac{p\epsilon^2 cos\theta}{r(1+\epsilon cos\theta)^2}\right)\right)+ \\ \hat{\boldsymbol{z}}\left(cos\theta+\frac{p\epsilon^2\sin^2\theta}{r(1+\epsilon cos\theta)^2}\right) \tag{A2.114}$$

To be consistent with the convention of our bow shock model, we must rotate from a coordinate system where θ is the angle from the z-axis to one where it is the angle from the x-axis. This is accomplished simply by a permutation of the unit vectors, x-> y’, y-> z’, z-> x’. We distinguish this new coordinate system by adding primes to the unit vectors. This is now an expression for a normal vector to the bow shock surface in the bow shock coordinate system.

$$\nabla F = \hat{\boldsymbol{y}}'\left(sin\theta cos\phi\left(1-\frac{p\epsilon^2 cos\theta}{r(1+\epsilon cos\theta)^2}\right)\right)+ \\ \hat{\boldsymbol{z}}'\left(sin\theta sin\phi\left(1-\frac{p\epsilon^2 cos\theta}{r(1+\epsilon cos\theta)^2}\right)\right)+ \\ \hat{\boldsymbol{x}}'\left(cos\theta+\frac{p\epsilon^2\sin^2\theta}{r(1+\epsilon cos\theta)^2}\right) \tag{A2.115}$$

This vector must be normalized as in (A2.110) and then can be used to calculate θ_{bn} at any location on the bow shock surface.

$$\theta_{bn} = \mathrm{acos}\left(\hat{\boldsymbol{b}}_{IMF}\cdot\hat{\boldsymbol{n}}_{BS}\right) \tag{A2.116}$$

References

Allegrini, F., Ebert, R.W., Fuselier, S.A., et al., 2014, Charge state of ~1 to 50 keV ions after passing through graphene and ultrathin carbon foils, Optical Engineering, **53**(2), 024101

Allegrini, F., Ebert, R.W., Funsten, H.O., 2016, Carbon foils for space plasma instrumentation, J. Geophys. Res. Space Phys., **121**, 3931-3950, doi:10.1002/2016JA022570

Anderson, B.J., Johnson, C.L., Korth, H., et al., 2011, The Global Magnetic Field of Mercury from MESSENGER Orbital Observations, Science, **333**, 1859

Andrews, G.B., Zurbuchen, T.H., Mauk, B.H., et al., 2007, The Energetic Particle and Plasma Spectrometer Instrument on the MESSENGER Spacecraft, Space Sci. Rev., **131**, 523

Bame, S.J., Hundhausen, A.J., Asbridge, J.R. & Strong, I.B. (1968), Solar Wind Ion Composition, Phys. Rev. Lett., **20**, 393-395

Bida, T.A., Killen, R.M., Morgan, T.H., 2000, Discovery of calcium in Mercury's atmosphere, **404**, 159-161

Broadfoot, A.L., Kumar, S., Belton, M.J.S., et al., 1974, Mercury's Atmosphere from Mariner 10: Preliminary Results, **185**, 4146, 166-169

Broadfoot, A.L., Shemansky, D.E., Kumar, S., 1976, Mariner 10-Mercury atmosphere, Geophys. Res. Lett., **3**, 577-580

Berger, L., & Wimmer-Schweingruber, R.F., 2011, Systematic Measurements of Ion-Proton Differential Streaming in the Solar Wind, Phys. Rev. Lett., **106**, 151103

Bochsler, P., 2007, Minor ions in the solar wind, Astron. & Astrophys. Rev., **14**, 1-40

Breech, B.A., Matthaeus, W.H., Cranmer, S.R., Kasper, J.C., & Oughton, S., 2009, Electron and proton heating by solar wind turbulence, J. Geophys. Res., **114**, A9

Burgess, D., 1987, Shock Drift Acceleration at Low Energies, J. Geophys. Res., **92**, 1119-1130

Burgess, D., 1989, Alpha particles in field-aligned beams upstream of the bow shock: Simulations, Geophys. Res. Lett., **16**, 163

Burgess, D., Möbius, E., Scholer, M., 2012, Ion Acceleration at the Earth's Bow Shock, Space Sci. Rev., **173**, 5-47, DOI 10.1007/s11214-012-9901-5

Chandran, B.D.G., Verscharen, D., Quataert, E., et al. 2013, Stochastic Heating Differential Flow, and the Alpha-to-proton Temperature Ratio in the Solar Wind, ApJ, **776**, 45

Cranmer, S.R., & van Ballegooijen, A.A., 2003, Alfvenic Turbulence in the Extended Solar Corona: Kinetic Effects and Proton Heating, ApJ, **594**, 573

Cranmer, S.R., Mattheaus, W.H., Breech, B.A., Kasper, J.C., 2009, Empirical Constraints on Proton and Electron Heating in the Fast Solar Wind, ApJ, **702**, 1604-1614

Cranmer, S.R., van Ballegooijen, A.A., 2012, Proton, Electron, and Ion Heating in the Fast Solar Wind from Nonlinear coupling between Alfvenic and Fast-Mode Turbulence, ApJ, **754**, 92

Delcourt, D.C., Moore, T.E., Orsini, S., et al., 2002, Centrifugal acceleration of ions near Mercury, Geophys. Res. Lett., **29**, L01591, doi:10.1029/2001GL013829

Delcourt, D.C., Grimald, S., Leblanc, F., et al., 2003, A quantitative model of the planetary Na+ contribution to Mercury's magnetosphere, Annal. Geophys., **21**, 1723-1736, doi:10.5194/angeo-21-1723-2003

Edmiston, J.P., Kennel, C.F., Eichler, D., 1982, Escape of heated ions upstream of quasi-parallel shocks, Geophys. Res. Lett., **9**, 531-534, doi:10.1029/GL009i005p00531

Ellison, D.C., Moebius, E., Paschmann, G., Particle injection and acceleration at earth's bow shock-Comparison of upstream and downstream events, Astrophys. J., **352**, 376-394

Evans, L.G., Peplowski, P.N., Rhodes, E.A., et al., 2012, Major-element abundances on the surface of Mercury: Results from the MESSENGER Gamma-Ray Spectrometer, J. Geophys. Res., **117**, E00L07

Fermi, E., 1949, On the Origin of the Cosmic Radiation, Phys. Rev., **75**, 1169

Fermi, E., 1954, Galactic Magnetic Fields and the Origin of Cosmic Radiation, Astrophys. J., **119**, 1

Fisk, L.A., Zurbuchen, T.H., & Schwadron, N.A., 1999, On the Coronal Magnetic Field: Consequences of Large-Scale Motions, ApJ, **521**, 868

Forman, A.M., 1981, First-order Fermi acceleration of the diffuse ion population near the Earth's bow shock, in *Proceedings of the 17th International Cosmic Ray Conference*, **3**, 467-470

Forman, A.M., Drury, L. O'C., 1983, Time-Dependent Shock Acceleration: Approximations and Exact Solutions, Proceedings from the 18th International Cosmic Ray Conference, **2**, 267

Gabriel, A.H., (1976), A magnetic model of the solar transition region, Phil. Trans. Royal Soc. London, A, **281**, 339.

Garrard, T.L., Davis, A.J., Hammond, J.S., & Sears, S.R., 1998, The ACE Science Center, Space Sci. Rev., **86**, 649

Geiss, J., Gloeckler, G., & von Steiger, R., 1995, Origin of the Solar Wind From Composition Data, Space Sci. Rev., **72**, 49

Gershman, D.J., Zurbuchen, T.H., Fisk, L.A., et al., 2012, Solar wind alpha particles and heavy ions in the inner heliosphere observed with MESSENGER, J. Geophys. Res. (Space Phys.), **117**, A00M02

Gershman, D.J., Gilbert, J.A., Raines, J.M., et al., 2013a, Post-processing modeling and removal of background noise in space-based time-of-flight sensors, Deep Blue, http://hdl.handle.net/2027.42/100358

Gershman, D.J., Slavin, J.A., Raines, J.M., et al., 2013b, Magnetic flux pileup and plasma depletion in Mercury's subsolar magnetosheath, J. Geophys. Res., **118**, 7181-7199

Gilbert, J.A., Gershman, D.J., Gleockler, G., et al., 2014, Characterization of background sources in space-based time-of-flight mass spectrometers, Review of Scientific Instruments, **85**, 091301

Gilbert, J.A., Lundgren, R.A., Panning, M.H., et al., 2010, An optimized three-dimensional linear-electric-field time-of-flight analyzier, Rev. Sci. Instrum., **81**, 053302, http://dx.doi.org/10.1063/1.3429941

Gloeckler, G., Geiss, J., Balsiger, H., et al., 1992, The Solar Wind Ion Composition Spectrometer, Astron. Astrophys. Suppl. Ser., **92**, 267-289.

Gloeckler, G., Ipavich, C. J., Tums, E.O., et al., 1998, Investigation of the Composition of Solar and Intersteller Matter Using Solar Wind and Pickup Ion Measurements with SWICS and SWINCS on the ACE Spacecraft, Space Sci. Rev., **86**, 497

Greco, A., Matthaeus, W.H., Servidio, S., Chuychai, P., Dmitruk, P., 2009, Statistical Analysis of Discontinuities in Solar Wind Ace Data and Comparison with Intermittent MHD Turbulence, ApJ, **691**, L111

Grevesse, N., Sauval, A.J., 1998, Standard Solar Composition, Space Sci. Rev., **85**, 161-174

Gombosi, T. I., 1998, Physics of the Space Environment, New York, Cambridge University Press

Gosling, J.T., Thomsen, M.F., Bame, S.J., et al., 1982, Evidence for specularly reflected ions upstream from the quasi-parallel bow shock, Geophys. Res. Lett., **9**, 1333

Gruntman, M. (1997), Energetic neutral atom imaging of space plasmas, Rev. Sci. Instrum., 68, 3617–3656, doi:10.1063/1.1148389.

Hammer, R. (1982), Energy Balance of Stellar Coronae. I. Methods and Examples, The Astophys. J. , **259**, 767-778

Hefti, S., Gründwaldt, H., Ipavich, F.M.., et al., 1998, Kinetic properties of solar wind minor ions and protons measured with SOHO/CELIAS, J. Geophys. Res. (Space Phys.), **103**, 29697

Hernandez, R., & Marsch, E., 1985, Collisional time scales for temperature and velocity exchange between drifting Maxwellians, J. Geophys. Res. (Space Phys.), **90**, 11062

Hoppe, M., Russel, C.T., 1981, On the Nature of ULF waves upstream of planetary bow shocks, Adv. Space Res., **1**, 327

Hovestadt, D., Hilchenbach, M., Bürgi, A., et al., 1995, CELIAS-Charge, Element, and Isotope Analysis System for SOHO, Sol. Phys., **162**, 441

Huebner, W.F., Mukherjee, J., 2015, Photoionization and photodissociation rates in solar and blackbody radiation fields, Planetary and Space Science, **106**, 11-45

Ipavich, F.M., Gloeckler, G., Fan, C.Y., et al., 1979, Initial observations of low energy charged particles near the earth's bow shock on ISEE-1, Space Sci. Rev., **23**, 93

Ipavich, F.M., Gosling, J.T., Scholer, M., 1984, Correlation between the He/H ratios in upstream particle events and in the solar wind, J. Geophys. Res., **89**, 1501-1507

Ipavich, F.M., Gloeckler, G., Hamilton, D.C., et al., 1988, Protons and Alpha Particles in Field-Aligned Beams Upstream of the Bow Shock, Geophys. Res. Lett., **15**, 1153-1156

Isenberg, P.A., 1984, The ion cyclotron dispersion relation in a proton-alpha solar wind, J. Geophys. Res., **89**, 2133

Isenberg, P.A., & Vasquez, B. J., 2007, Preferential Perpendicular Heating of Coronal Hole Minor Ions by the Fermi Mechanism, ApJ, **668**, 546

Isenberg, P.A., & Vasquez, B.J., 2009, Preferential Acceleration and Perpendicular Heating of Minor Ions in a Collisionless Coronal Hole, ApJ, **696**, 591

Johnson, R.E., 1990, Energetic Charged-Particle Interactions with Atmospheres and Surfaces, Physics and chemistry in space, vol. 19, Springer-Verlag, Berlin

Kasper, J.C., Lazarus, A.J., Steinberg, J.T., Ogilvie, K.W., Szabo, A., 2006, Physics-based tests to identify the accuracy of solar wind ion measurements: A case study with the Wind Faraday Cups, J. Geophys. Res. (Space Phys.), **111**, A03105

Kasper, J.C., Lazarus, A.J., Gary, S.P., 2008, Hot Solar-Wind Helium: Direct Evidence for Local Heating by Alfvén-Cyclotron Dissipation, Phys. Rev. Lett., **101**, 261103

Kasper, J.C., Bennett, M.A., Stevens, M.L., Zaslavsky, A., 2013, Sensitive Test for Ion-Cyclotron Resonant Heating in the Solar Wind, Phys. Rev. Lett., **110**, 091102

Kasper, J.C., Abiad, R., Austin, G., et al., 2015, Solar Wind Electrons Alphas and Protons (SWEAP) Investigation: Design of the Solar Wind and Coronal Plasma Instrument Suite for Solar Probe, SSRv, doi:10.1007/s11214-015-0206-3

Killen, R.M., Ip, W.H., 1999, The surface-bounded atmospheres of Mercury and the Moon, Reviews of Geophysics, **37**, 361-406

Killen, R.M., Shemansky, D., Mouawad, N., 2009, Expected Emission from Mercury's Exospheric Species, and their Ultravoilet-Visible Signatures, Astrophys. J. Supplement, **181**, 351-359

Killen, R.M., Potter, A.E., Vervack, R.J., et al., 2010, Observations of metallic species in Mercury's exosphere, **209**, 75-87

Killen, R.M., Hahn, J.M., 2015, Impact vaporization as a possible source of Mercury's calcium exosphere, Icarus, **250**, 230-237

Kis, A., Scholer, M., Klecker, B., et al., 2004, Multi-spacecraft observations of diffuse ions upstream of Earth's bow shock, Geophys. Res. Lett., **312**, 20801

Kis, A., Scholer, M., Klecker, B., et al., 2007, Scattering of field-aligned beam ions upstream of Earth's bow shock, Ann. Geophys., **25**, 785-799

Kohl, J.L., et al., 1998, UVCS/SOHO Empirical Determinations of Anisotropic Velocity Distributions in the Solar Corona, ApJ, **501**, L127-L131, doi:10.1086/311434 (1998)

Kohl, J.L., Noci, G., Cranmer, S.R., et al., 2006, Ultraviolet spectroscopy of the extended solar corona, Astron. Astroph. Rev., **13**, 31.

Kronberg, E.A., Kis, A., Klecker, B., et al., 2009, Multipoint observations of ions in the 30-160 keV energy range upstream of the Earth's bow shock, J. Geophys. Res. (Space Phys.), **114**, 3221

Kucharek, H., Möbius, E., Scholer, M., et al., 2004, On the origin of field-aligned beams at the quasi-perpendicular bow shock: multi-spacecraft observations by Cluster, Ann. Geophys., **22**, 2301-2308, doi:10.5194/angeo-22-2301-2004

Kuperus, M., Ionson, J.A., Spicer, D.S., 1981, On the Theory of Coronal Heating Mechanisms, Ann. Rev. Astron. Astrophys., **19**, 7-40.

Lampariello, F., 2000, On the Use of the Kolmogorov-Smirnov Statistical Test for Immunofluorescence Histogram Comparison, Cytometry, **39**, 179-188.

Landi, E. 2007, Ion Temperatures in the Quiet Solar Corona, ApJ, **663**, 1363-1368

Landi, E., & Cranmer, S.R., 2009, Ion Temperatures in the Low Solar Corona: Polar Coronal Holes at Solar Minimum, ApJ, **691**, 794-805

Le, G., Chi, P.J., Blanco-Cano, X., et al., 2013, Upstream ultra-low frequency waves in Mercury's foreshock region: MESSENGER magnetic field observations

Leblanc, F., Johnson, R.E., 2003, Mercury's sodium exosphere, Icarus, **164**, 261-281

Leblanc, F., Johnson, R.E., 2010, Mercury exosphere I. Global circulation model of its sodium component, Icarus, **209**, 280-300

Leblanc, F., Doressoundiram, A., 2011, Mercury exosphere. II. The sodium/potassium ratio, Icarus, **211**, 10-20

Lee, M.A., 1982, Coupled hydromagnetic wave excitation and ion acceleration upstream of the earth's bow shock, J. Geophys. Res., **87**, 5063-5080

Lee, M.A., Skadron, G., 1985, A Simple Model for the Formation of "Reflected", "Intermediate", and "Diffuse" Ion Distributions Upstream of Earth's Bow Shock, J. Geophys. Res., **90**, 39-45

Livadiotis, G., McComas, D.J., 2013, Understandings Kappa Distributions: A Toolbox for Space Science and Astrophysics, Space Sci. Rev., **175**, 183-214

Marsch, E., Rosenbauer, H., Schwenn, R., Muehlhaesuer, K.H., Neubauer, F.M., 1982a, Solar wind helium ions- Observations of the HELIOS solar probes between 0.3 and 1 AU, J. Geophys. Res., **87**, 35

Marsch, E., Schwenn, R., Rosenbauer, H., et al., 1982b, Solar wind protons – Three dimensional velocity distribution and derived plasma parameters measured between 0.3 and 1 AU, J. Geophys. Res., **87**, 52

Maruca, B.A., Bale, S.D., Sorriso-Valvo, L., Kasper, J.C., Stevens, M.L., 2013, Collisional Thermalization of Hydrogen and Helium in Solar-Wind Plasma, Phys. Rev. Lett., **111**, 241101

McClintock, W.E., Vervack Jr., R.J., Bradley, E.T., et al., 2009, MESSENGER Observations of Mercury's Exosphere: Detection of Magnesium and Distribution of Constituents, Science, **324**, 610

McComas, D.J., Bame, S.J., Barker, P., et al., 1998, Solar Wind Electron Proton Alpha Monitor (SWEPAM) for the Advanced Composition Explorer, Space Sci. Rev., **86**, 563

McKenzie, J.F., Banaszkiewicz, M., and Axford, W.I., 1995, Acceleration of the high speed solar wind, Astron. and Astrophys., **303**, L45-L48.

Möbius, E., Kucharek, H., Mouikis, C., et al., 2001, Observations of the spatial and temporal structure of field-aligned beam and gyrating ring distributions at the quasi-perpendicular bow shock with Cluster CIS, Ann. Geophys., **19**, 1411-1420

Ness, N.F., Behannon, K.W., Lepping, R.P., et al., 1974, Magnetic field observations near Mercury: Preliminary results from Mariner 10, Science, **185**, 151-160

Neugebauer, M., Goldstein, B.E., Smith, E.J., Feldman, W.C., 1996, Ulysses observations of differential alpha-proton streaming in the solar wind, J. Geophys. Res., **101**, 17047

Newbury, J.A., Russell, C.T., Phillips, J.L., Gary, S.P., 1998, Electron temperature in the ambient solar wind: Typcial properties and a lower bound at 1 AU, J. Geophys. Res., **103**, 9553

Nittler, L.R., Starr, R.D., Weider, S.Z., et al., 2011, The Major-Element Composition of Mercury's Surface from MESSENGER X-ray Spectrometry, Science, **333**, 1847

Ogilvie, K.W., Chornay, D.J., Fritzenreiter, R.J., et al., 1995, SWE, A Comprehensive Plasma Instrument for the Wind Spacecraft, Space Sci. Rev., **71**, 55

Ogilvie, K.W., Scudder, J.D., Vasyliunas, V.M., et al., 1977, Observations at the planet Mercury by the plasma electron experiment: Mariner 10, J. Geophys. Res., **82**, 13, 1807-1824

Oka, M., Terasawa, T., Saito, Y., et al., 2005, Field-aligned beam observations at the quasi-perpendicular bow shock: Generation and shock angle dependence, J. Geophys. Res., **110**, A05101

Osman, K.T., Matthaeus, W.H., Greco, A., Servidio, S., 2011, Evidence for Inhomogenous Heating in the Solar Wind, ApJ, **727**, L11

Osman, K.T., Matthaeus, W.H., Wan, M., Rappazzo, A.F.,2012, Intermittency and Local Heating in the Solar Wind, Phys. Rev. Lett., **108**, 261102

Parker, E.N., 1958, Dynamics of the Interplanetary Gas and Magnetic Fields, ApJ, **128**, 664

Parker, E.N. (1988), Dynamics of the Interplanetary Gas and Magnetic Fields, The Astrophys. J., **128**, 664-676

Paschmann, G., Sckopke, N., Bame, S.J., et al., 1979, Association of low-frequency waves with suprathermal ions in the upstream solar wind, Geophys. Res. Lett., **6**, 209-212

Paschmann, G., Sckopke, N., 1980, Energization of Solar Wind Ions by Reflection From the Earth's Bow Shock, J. Geophys. Res., **85**, 4689-4693

Paschmann, G., Sckopke, H., Papamastrorakis, I., et al., 1981, Characteristics of Reflected and Diffuse Ions Upstream From the Earth's Bow Shock, J. Geophys. Res., **86**, 4355-4364

Perry, G.W., 2006, A First Course in Atmospheric Radiation, 2nd Ed., Madison, Sundog Publishing

Potter, A., Morgan, T., 1985, Discovery of sodium in the atmosphere of Mercury, **229**, 651-653

Priest, E.R., Foley, C.R., Heyvaerts, J., et al. (2000), A Method to Determine the Heating Mechanisms of the Solar Corona, The Astrophys. J., **539**, 1002-1022

Raines, J.M., Slavin, J.A., Zurbuchen, T.H., et al., 2011, MESSENGER observations of the plasma environment near Mercury, Planetary and Space Science, **59**, 2004-2015

Raines, J.M., Gershman, D.J., Zurbuchen, T.H., et al., 2013, Distribution and compositional variations of plasma ions in Mercury's space environment: The first three Mercury years of MESSENGER observations, J. Geophys. Res. Space Phys., **118**, 1604-1619.

Raymond, J.C., Kohl, J.L., Noci, G., et al., 1997, Composition of Coronal Streamers from the SOHO Ultraviolet Coronagraph Spectrometer, Solar Phys., **175**, 645

Richardson and Cane, 2010, Near-Earth Interplanetary Coronal Mass Ejections During Solar Cycle 23 (1996-2009): Catalog and Summary of Properties, Solar Physics **264**, 189

Romero, G.E., Vieyro, F.L., and Vila G.S., 2010, Non-thermal processes around accreting galactic black holes, Astron. and Astrophys., **519**, A109

Rubner, Y., Tomasi, C. and Guibas, L.J., 2000, The earth mover's distance as a metric for image retrieval. *International journal of computer vision*, *40*(2), pp.99-121.

Safi-Harb, S., et al., 2000, A Broadband X-Ray Study of Supernova Remnant 3C 397, ApJ, **545**, 922-938

Saito, Y., Sauvaud, J.A., Hirahara, M., et al., 2010, Scientific objectives and instrumentation of Mercury Plasma Particle Experiment (MPPE) onboard MMO, Planetary and Space Science, **58**, 182-200

Sarantos, M., Slavin, J.A., Benna, Mehdi, 2009, Sodium-ion pickup observed above the magnetopause during MESSENGER's first Mercury flyby: Constraints on neutral exospheric models, Geophys. Res. Lett., **36**, L04106

Scholer, M., 1985, Diffusive Acceleration, Geophys. Monograph Series, **35**, 287

Scholer, M., Kucharek, H., Trattner, K.-H., 1999, Injection and acceleration of H^+ and He^{2+} at Earth's bow shock, Ann. Geophys., **17**, 583-594

Shearer, P., von Steiger, R., Raines, J.M., et al., 2014, The Solar Wind Neon Abundance Observed with ACE/SWICS and ULYSSES/SWICS, ApJ, **789:60** (10pp)

Slavin, J.A., Holzer, R.E. (1981), Solar wind flow about the terrestrial planets, 1. Modeling bow shock position and shape, J. Geophys. Res., **86**, 11401-11418, doi:10.1029/JA086iA13p11401

Smith, C.W., Lee, M.A., 1986, Coupled Hydromagnetic Wave Excitation and Ion Acceleration Upstream of the Jovian Bow Shock, J. Geophys. Res., **91**, 81-90

Solomon, S.C., McNutt Jr., R.L., Gold, R.E., et al., 2007, MESSENGER mission overview, Space Sci. Rev., **131**, 3-39, doi:10.1007/s11214-007-9247-6

Sonnerup, B.U.Ö, 1969, Acceleration of particles reflected at shock front, J. Geophys. Res., **74**, 1301-1304

Spitzer, L., Jr., 1967, Physics of Fully Ionized Gases, (2nd ed.; Interscience, NewYork)

Sundberg, T., Boardsen, S.A., Slavin, J.A., et al., 2013, Cyclic reformation of a quasi-parellel bow shock at Mercury: MESSENGER observations

Tanaka, M., Goodrich, C.C., Winske, D., et al., 1983, A source of the backstreaming ion beams in the foreshock region, J. Geophys. Res., **88**, 3046-3054, doi:10.1029/JA088iA04p03046

Tracy, P.J., Kasper, J.C., Zurbuchen, T.H., et al., 2015, Thermalization of Heavy Ions in the Solar Wind, ApJ, **812**, 170

Tracy, P.J., Kasper, J.C., Raines, J.M., et al., 2016, Constraining Solar Wind Heating Processes by Kinetic Properties of Heavy Ions, Phys. Rev. Lett., **116**, 255101.

Vervack, R.J., McClintock, W.E., Killen, R.M., et al., 2010, Mercury’s Complex Exosphere: Results from MESSENGER’s Third Flyby, Science, **329**, 672

von Steiger, R., Geiss, J., Gloeckler, G., & Galvin, A.B., 1995, Kinetic Properties of Heavy Ions in the Solar Wind From SWICS/Ulysses, Space Sci. Rev., **72**, 71

von Steiger, R., Schwardron, N.A., Fisk, L.A., et al., 2000, Composition of quasi-stationary solar wind flows from Ulysses/Solar Wind Ion Composition Spectrometer, J. Geophys. Res. (Space Phys.), **105**, 27217

von Steiger, R., & Zurbuchen, T.H., 2006, Kinetic properties of heavy solar wind ions from Ulysses-SWICS, Geophys. Res. Lett., **33**, L09103

von Steiger, R., & Zurbuchen, T.H., 2011, Polar coronal holes during the past solar cycle: Ulysses observations, J. Geophys. Res., **116**, A01105

von Steiger, R., & Zurbuchen, T.H., 2016, Solar Metallicity derived from in situ solar wind composition, ApJ, **816:13** (8pp)

Wibberenze, G., Fischer, H.M., Zoellich, F., et al., 1985, Dynamics of intense upstream ion events, J. Geophys. Res., **90**, 283-301

Wimmer-Schweingruber, R.F., von Steiger, R., Geiss, J., et al., 1998, O^{5+} in High Speed Solar Wind Streams: SWISC/Ulysses Results, Space Sci. Rev., **85**, 387-396

Winslow, R.M., Anderson, B.J., Johnson, C.L., et al., 2013, Mercury’s magnetopause and bow shock from MESSENGER Magnetometer observations, J. Geophys. Res., **118**, 2213-2227, doi:10.1002/jgra.50237

Wurz, P., Whitby, J.A., Rohner, U., et al., 2010, Self-consistent modelling of Mercury’s exosphere by sputtering, micro-meteorite impact and photon-stimulated desorption, Planet. Space Sci., **58**, 1599-1616

Ziegler, J.F., 2004, SRIM-2003, *Nucl. Instrum. Methods Phys. Res. B*, **219**, 1027

Ziegler, J.F., et al., 2010, SRIM-The Stopping and Range of Ions in Solids, *Nucl. Instrum. Methods Phys. Res. B*, **268,** 1818-1823

Zurbuchen, T.H., Gloeckler, G., Cain, J.C., et al., 1998, A low-weight Plasma Instrument to be used in the Inner Heliosphere, Conference on Missions to the Sun II, **3442**, 217

Zurbuchen, T.H., 2007, A New View of the Coupling of the Sun and the Heliosphere, Annu. Rev. Astron. Astophys., **45**, 297-338

Zurbuchen, T.H., Raines, J.M., Gloeckler, G., et al., 2008, MESSENGER observations of the composition of Mercury's ionized exosphere and plasma environment, Science, **321**, 90-92

Zurbuchen, T.H., Raines, J.M., Slavin, J.A., et al., 2011, MESSENGER observations of the spatial distribution of planetary ions neary Mercury, Science, **333**, 1862